DESIGN AND APPLICATION OF FLUORESCENT SENSING SCAFFOLDS BASED UPON AND ORIGINATING FROM CONJUGATED ARYL-ETHYNYL SYSTEMS

by

CHRISGEN LEE VONNEGUT

A DISSERTATION

Presented to the Department of Chemistry and Biochemistry
and the Graduate School of the University of Oregon
in partial fulfillment of the requirements
for the degree of
Doctor of Philosophy

March 2016

DISSERTATION APPROVAL PAGE

Student: Chrisgen Lee Vonnegut

Title: Design and Application of Fluorescent Sensing Scaffolds Based upon and Originating from Conjugated Aryl-ethynyl Systems

This dissertation has been accepted and approved in partial fulfillment of the requirements for the Doctor of Philosophy degree in the Department of Chemistry and Biochemistry by:

Dr. Kenneth Doxsee	Chairperson
Dr. Michael Haley	Co-Advisor
Dr. Darren Johnson	Co-Advisor
Dr. Mark Lonergan	Core Member
Dr. James Remington	Institutional Representative

and

Dr. Scott L. Pratt	Dean of the Graduate School

Original approval signatures are on file with the University of Oregon Graduate School.

Degree awarded March 2016

© 2016 Chrisgen Lee Vonnegut

DISSERTATION ABSTRACT

Chrisgen Lee Vonnegut

Doctor of Philosophy

Department of Chemistry and Biochemistry

March 2016

Title: Design and Application of Fluorescent Sensing Scaffolds Based upon and Originating from Conjugated Aryl-ethynyl Systems

The utility of fluorophores for sensing applications in the current state of the art of biological imaging hardly needs to be stated. The use of fluorophores in exploring and determining the internal structure and active dynamics of cellular processes has been pivotal, allowing us to explore areas of study inaccessible through other means. A simple search of fluorophores in Scifinder© demonstrates their popularity, as the number of hits increases year after year, until the year of 2015 when there were 1400+ journal articles published with the phrase. Fluorophore applications range far and wide, from sensing applications related to environmental concerns, to public health, to clinical usage. Fluorophores have been developed to detect explosive residues, to monitor environmental pollutants, and even to detect illicit substances.

In cellular applications, a fluorophore needs to be well suited to examining the relevant processes, including participating in the cellular milieu, and actively signifying the phenomena that are desired. Chapter I examines the usage of alkynes in fluorescent sensing scaffolds and gives a survey of their applicability in the field. Chapter II demonstrates the utility of disulfide-based macrocyclic scaffolds in the design of supramolecular hosts for chloride anions and their use as solid-state sensors for these anions. Chapter III explores the synthesis and application of an alkyne-based scaffold in the reversible detection of dithiol/disulfide redox flux and a new mode of quantification of dithiol-disulfide redox couples, a classically difficult area of study. Chapter IV focuses on methods utilized to improve the disulfide-based redox sensing capabilities. Chapters V and VI explore the properties of a new fluorophore scaffold discovered during research into another sensing scaffold, demonstrating a new reaction which yields a heretofore underexplored heterocycle with novel photophysical and supramolecular behaviors.

This dissertation contains both previously published and unpublished co-authored material.

CURRICULUM VITAE

NAME OF AUTHOR: Chrisgen Lee Vonnegut

GRADUATE AND UNDERGRADUATE SCHOOLS ATTENDED:

University of Oregon, Eugene, OR

Benedictine College, Atchison, KS

DEGREES AWARDED:

Doctor of Philosophy, Chemistry, 2016, University of Oregon

Bachelor of Science, Chemistry, 2007, Benedictine College

AREAS OF SPECIAL INTEREST:

Organic Synthesis

Fluorescence

Supramolecular Chemistry

PROFESSIONAL EXPERIENCE:

Scientist, Analytical R&D, Thermo Fisher Scientific

Eugene, Oregon, 2015

Graduate Teaching Assistant, Department of Chemistry, University of Oregon

Eugene, Oregon, 2015-2014, 2013-2012, 2011-2010

Graduate Research Assistant, Department of Chemistry, University of Oregon

Eugene, Oregon, 2010-2016

Chemist, Analytical R&D, Boehringer Ingelheim

Saint Joseph, Missouri, 2008-2009

Lead Laboratory Technician, Albaugh Inc.

Saint Joseph, Missouri, 2007-2008

Undergraduate Research Assistant, Benedictine College

Atchison, Kansas, 2003-2007

PUBLICATIONS:

Vonnegut, C. L.; Shonkwiler, A. M.; Khalifa, M. M.; Zakharov, L. N.; Johnson, D. W.; Haley, M. M. Facile Synthesis and Properties of 2-λ^5-Phosphaquinolines and 2-λ^5-Phosphaquinolin-2-ones. Angew. Chem. Int. Ed. **2015**, *54*, 13318–13322.

Marshall, J. L.; Rudebusch, G. E.; Vonnegut, C. L.; Zakharov, L. N.; Haley, M. M. Synthesis and properties of fully conjugated indacenediselenophene and diindenoselenophene derivatives. Tet. Letters **2015**, *56*, 3235-3239.

Berryman, O. B.; Johnson, C. A.; Vonnegut, C. L.; Fajardo, K. A.; Zakharov, L. N.; Johnson, D. W.; Haley, M. M. Solid-State Examination of Conformationally Diverse Sulfonamide Receptors Based on Bis(2-anilinoethynyl)pyridine, -Bipyridine, and –Thiophene. Cryst. Growth Des. **2015***, 15,* 1502-1511.

Vonnegut, C. L.; Tresca, B. W.; Johnson, D. W.; Haley, M. M. Ion and Molecular Recognition Using Aryl–Ethynyl Scaffolding. Chem. Asian J. **2015**, *10*, 522-535.

Young, B. S.; Chase, D. T.; Marshall, J. L.; Vonnegut, C. L.; Zakharov, L. N.; Haley, M. M. Synthesis and properties of fully-conjugated indacenedithiophenes. Chem. Sci. **2014**, *5*, 1008-1014.

J. M. Engle, P. S. Singh, C. L. Vonnegut, L. N. Zakharov, D. W. Johnson and M. M. Haley. Synthesis and solid-state structures of a macrocyclic receptor based on the 2,6-bis(2-anilinoethynyl)pyridine scaffold. CrystEngComm. **2014**, *16*, 3703-3706.

Fix, A. G.; Deal, P. E.; Vonnegut, C. L.; Rose, B. D.; Zakharov, L. N.; Haley, M. M. Indeno[2,1-c]fluorene: A New Electron-Accepting Scaffold for Organic Electronics. *Org. Lett.* **2013**. *15*, 1362–1365.

Rose, B. D.; Vonnegut, C. L.; Zakharov, L. N.; Haley, M. M. Fluoreno[4,3-c]fluorene: A Closed-Shell, Fully Conjugated Hydrocarbon. *Org. Lett.* **2012**, *14*, 2426–2429.

Young, B. S.; Marshall, J. L.; MacDonald, E.; Vonnegut, C. L.; Haley, M. M. Diazaheterocycle analogues of tetracene: synthesis and properties of a naphtho-fused cinnoline and a naphtho-fused isoindazole. *Chem. Commun.* **2012**, *48*, 5166-5168.

Weber, C. D.; Robinson, S. G.; Stay, D. P.; Vonnegut, C. L.; Lonergan, M. C. Ionic Stabilization of the Polythiophene-Oxygen Charge-Transfer Complex. *ACS Macro Lett.* **2012**, *1*, 499–503.

PATENTS

Phosphorus-Containing Heterocycles and A Method for Making and Using. Chris Vonnegut, Airlia Shonkwiler, Michael Haley, Darren Johnson; Provisional application, #62/183,477.

ACKNOWLEDGMENTS

I would like to thank the NIH for research funding and stipend support during my time at the University of Oregon (GM087398). I would also like to thank everyone who helped me throughout the years, my family back home who I visited too rarely, the students I taught that inspired me, my labmates, coworkers, friends, and companions.

This dissertation is dedicated to Airlia Shonkwiler, who started as an undergraduate researcher and blossomed into an impressive scientist in her own right. This research wouldn't have been possible without her.

TABLE OF CONTENTS

Chapter Page

LIST OF FIGURES

LIST OF TABLES

LIST OF SCHEMES

CHAPTER I

ION AND MOLECULAR RECOGNITION USING ARYL-ETHYNYL SCAFFOLDING

This introductory chapter was published with Blakely W. Tresca, Darren W. Johnson and Michael M. Haley in *Chemistry, an Asian Journal* as a review on pages 522–535 of Volume 10, Issue 3 in March 2015. Both Blakely and I contributed significantly to the main text of the review, while Profs. Johnson and Haley provided editorial support. This introduction leads heavily into both anion host design and fluorophore mechanisms as a theme throughout the dissertation.

INTRODUCTION

The use of defined, preorganized scaffolds for host-guest chemistry originates in the discovery of cyclodextrins, and the recognition of their rich intermolecular interactions in the earlier half of the 20th century.[1] Quickly thereafter, the field of inclusion chemistry exploded with the advent of crown ethers, cryptands, and cavitands, which defined the discipline of supramolecular chemistry.[2] Since their inception, synthetic molecular hosts have utilized a variety of linkers to elaborate their binding cavities. Oftentimes, structural rigidity must be considered as a design principle in host construction. For example, a large segment of macrocyclic receptors use the rigidity inherent in aryl-aryl linkages to create the appropriate geometries for suitable guest inclusion.[3] Alternatively, inclusion of an alkyne linkage between

aryl groups has been utilized within synthetic molecular hosts, both for its ability to directly connect two units by an essentially inflexible spacer, and for the electronic conjugation it enables between the two aryl units.[4] Alkynes are installed synthetically via a variety of well proven techniques. Classically, the alkyne functionality can be formed through dehydrohalogenation reactions or via nucleophilic attack of an acetylide anion. There are also a number of routes to access the alkyne unit from carbonyls, via the Corey Fuchs reaction, the Colvin rearrangement, or the Seyferth-Gilbert homologation.[5] These methods all suffer from harsh reaction conditions, typically requiring a strong base and thus precluding the use of more functionally diverse starting materials. Some work has been done to extend the scope of these reactions to gentler conditions, such as the modified Bestmann-Ohira homologation, though this route is still limited to the formation of terminal alkynes.[6] For the preparation of arylethynyl linkages, however, few reactions can match the robustness and versatility of the Sonogashira cross-coupling reaction.[7-9] A large variety of aryl-ethynyl scaffolds are now easily accessible because of the gentle conditions, high yields, and wide functional group tolerance of this reaction.

As the supramolecular chemistry field has grown and the need for new receptors has increased, the alkyne linkage has emerged as a useful rigid unit for construction of receptors with designed cavities. In addition, this motif allows spatial separation of the binding site and a spectroscopic handle, yet still confers the electronic effects of the binding event. In this way, the binding event and the spectroscopic changes can act independently, with the alkyne acting as a wire to convey the electronic perturbations of the binding event to the spectroscopic site.

In this Focus Review, we explore recent advances in the use of aryl-ethynyl receptors in the host-guest chemistry of analyte sensing. The major families of analytes are covered,

from cationic metal species to anionic or neutral species prevalent in biological systems. As well, we cover usage of these hosts in development of sensor molecules for a variety of applications, such as detection of chemical weapons. This is not intended to be a comprehensive review, but rather a survey of recent literature exemplifying the utility and versatility of the aryl-ethynyl unit as a structural and/or sensing motif in the construction of molecular receptors. This review focuses mostly on the use of small-molecule synthetic hosts. Except for a few specific examples, the vast, well-studied area of arylene-ethynylene polymers in such sensing applications will not be covered as it has already garnered multiple reviews.[10]

SENSING STRATEGIES

Numerous strategies for the detection of analytes have been employed in recent years. The classic observable changes utilized are either colorimetric or fluorometric, although sensors based upon a gelation response or other physical state changes have also been developed.[12-13] Chiroptical changes measured by circular dichroism (CD) enhancement is emerging as a new method for analyte detection.[14-15] Fluorescence remains the most commonly utilized spectroscopic change because of the enhanced sensitivity compared to colorimetric changes. Fluorescence also lends itself well to sensing within biological microenvironments, such as those inside cells, as native fluorescence of cells can be filtered out by selecting a fluorophore possessing non-competitive emission or excitation.[16-17] As well, the variety of fluorescence mechanisms aids in the design of sensor molecules. The more common and more widely understood mechanisms are photo-induced electron transfer (PET), intramolecular charge transfer (ICT), metal-ligand charge transfer (MLCT), twisted intramolecular charge transfer (TICT),[18] electronic energy transfer (EET),

fluorescence resonance energy transfer (FRET), and excimer/exciplex formation. Some of the more recently developed fluorescent mechanisms are aggregation-induced emission (AIE)[19] and excited-state intramolecular proton transfer (ESIPT). All of these methods have been utilized for detection of analytes, with particular attention paid to AIE and ESIPT in recent years.[20-21]

The aryl-ethynyl scaffold can readily participate in many of these mechanisms, as it provides a rigid structural unit for the formation of an appropriate binding cavity, allows for conjugative communication between aryl units for appropriate fluorescent responses, and has fewer degrees of freedom than an alkyl chain, disfavoring non-radiative decay. While free rotation around an alkyne-arene C-C single bond can lead to detrimental non-radiative decay, this conformational flexibility provides a useful handle for sensing purposes utilizing AIE or TICT (**Figure 1.1**), where inclusion of an appropriate guest can restrict rotation and yield a spectroscopic response through either twisted relaxation of the excited state, or aggregation of the now-hindered fluorophore to initiate an AIE process.[22]

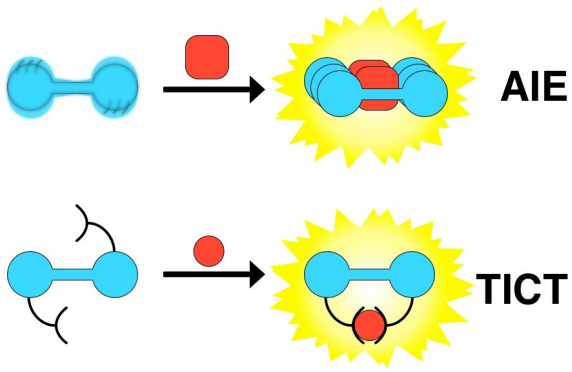

Figure 1.1. Two common fluorescence mechanisms used in sensing: AIE, here hindrance of internal rotation via aggregation reduces non-radiative relaxation, and TICT, where interaction of a suitable guest causes the TICT state to no longer inhibit fluorescence.

Classically, sensor molecules were built utilizing principles outlined in de Silva's seminal review of fluorescent recognition events. For a PET-based response (**Figure 1.2**), the common method of sensor design utilizes an electron-rich donor site (D) as the recognition element tethered to a fluorophore (F). Until the binding event occurs, PET from the donor to the fluorophore quenches fluorescence; however, upon coordination of a cationic or suitably electron-poor guest (G), electron donation ceases and fluorescence turns on. This technique has been utilized since the early 1970s to build sensor molecules, and can be related conceptually to the original complexone sensors first described in the 1950s.[23]

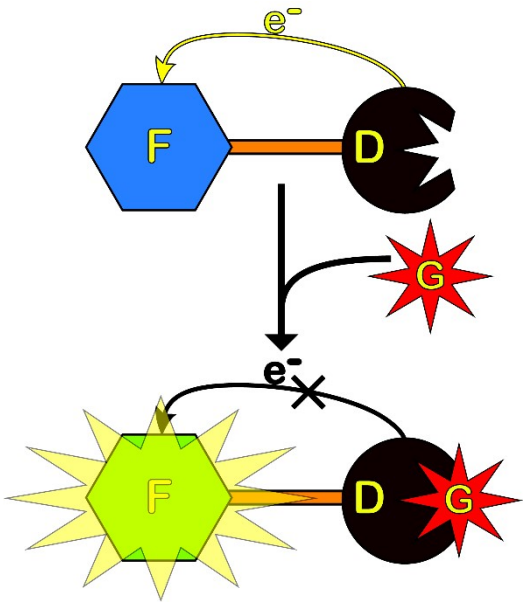

Figure 1.2. Illustration of PET mechanism for sensing. Coordination of a guest (G) diminishes the electron-donation of the chelating group/electron donor (D), thus stopping quenching and enabling the native fluorescence of fluorophore (F).

For many fluorescent sensing mechanisms, the aryl-ethynyl functionality confers the three concepts of the so-called 'magic triangle' of sensor design: rigidification, to confer a large photoluminescent quantum yield (PLQY); preorganization, to build a binding site

already tailored to the intended guest; and electronic decoupling, where the binding subunit and fluorophore are spatially separated enough to inhibit direct interaction of the guest.[24] To control the signaling response of the host molecule, modification of electron-withdrawing/donating groups attached to a fluorophore significantly affects the spectroscopic changes of the binding event. For example, in our studies, changing the appended groups alters the electron density within an anion sensor and thus the nature of the fluorescent response from different anionic guests (see below).[25-26]

Conformational changes upon a binding event can also play a large role in spectroscopic sensing responses. Alkyne linkers provide an axle about which the host molecule can rotate, affording differing conformations upon inclusion of diverse guests. Within our group we have found that an aryl-ethynyl scaffold can adopt varying conformations in the solid state or in solution when influenced by a guest (see below).[27-29] These conformational changes have a direct effect on the conjugation throughout the system, giving rise to differences in the emission spectra.

CHARGED SPECIES

Cations

Sensing and quantification of metal cations in solution and complex media are needed due to their environmental prevalence and human health relevance (both beneficial and detrimental). In humans the three most common transition metal cations are Fe, Zn, and Cu.[30] Since disruption of homeostasis by these metal ions is causative in many diseases, a more complete understanding of their roles in the body would be beneficial to the medical field[30-31] In addition, the detection of heavy metal cations such as Cd, Hg, Cr, and Pb is an

integral research area due to their presence in waste streams and their detrimental effects on living organisms. Molecules selective for these metal ions are thus essential for both environmental and biological sciences. To this end, many sensors based upon aryl-ethynyl scaffolding have been developed to detect metal ions in recent years, with some key examples outlined below. While there are many mechanisms to sense metal cations based upon the variety of interactions with the host molecule, that subject is not broached here as a number of comprehensive reviews are available in the literature.[30-37]

A tris-phenanthrolyl oligomer connected via ethynyl linkers was used to selectively sense Cr^{III} over other metal cations.[38] Upon full occupation of the three phenanthroline units, the emission spectrum was shifted by 100 nm, allowing quantification across a range of concentrations. An OFF-ON assay to determine the concentration of Cr^{III} in solution was realized through the Cu^{II} complex with quenched fluorescence; in the presence of Cr^{III} the emission was restored. In addition, a ratiometric assay of Cr^{II} and Cr^{III} was possible through the use of monomeric **1** (**Figure 1.3**).

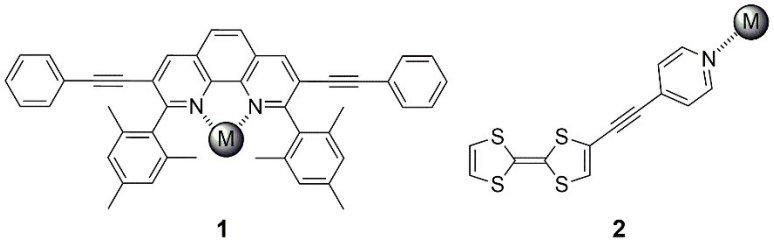

Figure 1.3. Two examples of metal coordination by nitrogen lone pairs in conjugated fluorophores: an alkyne substituted phenanthroline monomer (**1**) for fluorescent detection of Cr^{II} and a donor-acceptor (D-A) fluorophore with a 4-pyridyl receptor (**2**).

Similar utilization of an acetylene unit as a conjugative linker was realized by Tung, who employed a D-A dyad connected via an alkyne bridge to detect Pb^{II} in solution (**2**,

Figure 1.3).[39] The 4-pyridyl unit coordinated to Pb^{II} ions and changed the nature of the D-A interaction to give a measurable UV/Vis spectral response, with a binding constant of $\log(K_a)$ -3.76 in acetonitrile. Interaction between Pb^{II} and the donor tetrathiafulvalene (TTF) led to no spectroscopic change, as demonstrated with a phenyl analogue.

TTFs are widely used as donors in sensing scaffolds. In one example, a crown-ether-fused π-expanded tetrathiafulvalene (**3**, exTTF) attached to ethynyl anthracenes experienced PET quenching of the anthracene fluorophores (**Figure 1.4**) similar to classical complexone-type sensors. [41] Upon binding a cation, the donor ability decreases and disables PET to yield an OFF-ON fluorescent sensor for cations. Receptor **3** displayed a selective spectroscopic response for large, soft cations such as Ba^{2+} ,with a $\log(K_a)$ of 4.11 in THF.

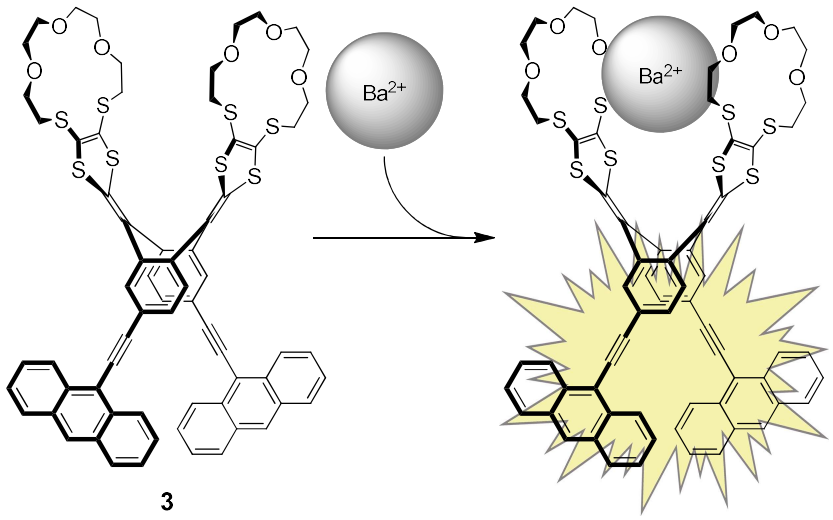

Figure 1.4. Structure of a crown-ether functionalized π-expanded fluorophore for the detection of large, soft metal cations. Inclusion of a cation within the crown-ether pincer limits PET between the exTTF donor and anthracene fluorophore, recovering the anthracene fluorescence of **3**.

Alkynes define the binding pocket with naphthalene walls in cation sensor **4** (**Figure 1.5**), allowing selective fluorometric detection of Fe^{III} ions over a variety of other metal cations.[42] The alkyne linker provided facile synthetic access to the target sensor molecules (through Sonogashira methodologies) and rigidified the binding site.

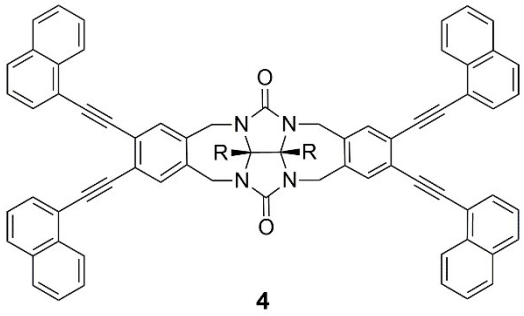

4

Figure 1.5. Pincer-like molecule **4** with conjugated aromatic walls selectively senses Fe^{III} via an ON-OFF quenching response.

Cruciform-shaped molecules have been extensively employed as sensors for metal cations as well as for neutral molecules. Bunz et al. found that a series of structures such as **5** and **6** (**Figure 1.6**), when utilized in a differential sensing array, could discriminate between a variety of metal cations and amines via both colorimetric and fluorometric responses and solvatochromic behaviors.[44-46] Variants with non-conjugated amine substituents selectively interacted with Zn^{2+} cations over other metals, while those with conjugated coordinating groups had differing responses.[47] These structurally simple systems provide superior HOMO-LUMO separation along the X and Y axes, yielding distinctive solvatochromic and analyte-sensitive spectroscopic changes.

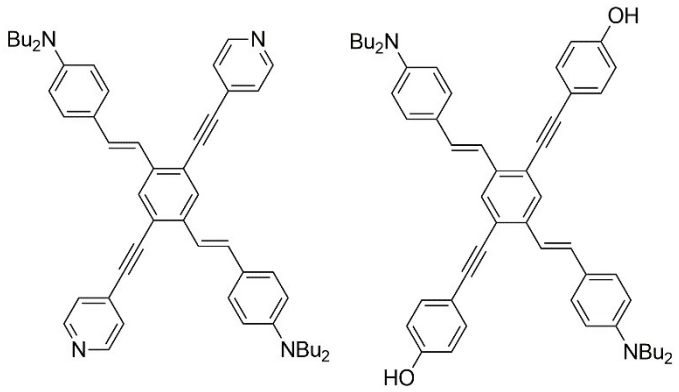

5 **6**

Figure 1.6. Cruciform molecules **5** and **6** with donor and acceptor groups or differing coordination groups.

Another class of cruciform sensors based on 1,2,4,5-tetrakis(arylethynyl)benzenes is exemplified by the work of Haley et al. [48] where the molecules were found to have selective responses to a variety of metal ions. This class of aryl-ethynyl cruciforms has seen extensive exploration in the literature from fundamental structure-property studies as substructures of larger dehydrobenzannulene derivatives,[49-50] as well as by the group of Baxter in their work on strained- and oligo-cruciform aryl-alkynyl systems.[51-52]

Anions

Anion Sensing Mechanisms

In recent years, anion recognition has begun to compete with cation sensing in the literature as a major research thrust. Cation sensor development was spurred in the mid-1960s by the advent of crown ethers and continues to be quite thoroughly explored [31,53] Anion recognition has been slower to progress because of the difficulties of sensing anions over other analytes, with numerous books and reviews citing poorly-defined solvation

geometries, low basicity, and high hydration energies among the limitations in coordinating anionic species.[54-58] A wide variety of mechanisms have been employed to produce a sensing response for an anion over competing analytes.[59]

Fluorophore collisional quenching (CQ) is the most easily accessed mechanism for anion sensing, with a variety of neutral and cationic fluorophores having been developed based on this mechanism. Fluorescent polymers are able to maximize the resulting fluorogenic response by providing multiple binding sites. Bringing the anion closer to the fluorophore, as in guanidinium probe 7 a, can also increase the degree of emission quenching (**Figure 1.7**) [60] The enhanced proximity produced a four-fold improvement in CQ response compared to a similar ammonium probe.

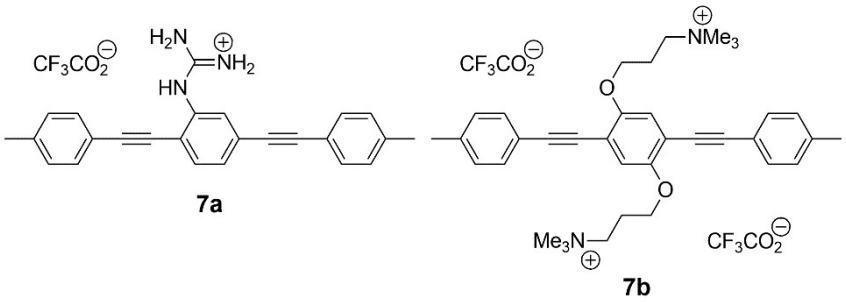

Figure 1.7. Demonstration of CQ in anion receptor design. Guanidinium appended fluorophore **7a** provides hydrogen bonding and ion pairing in close proximity to the fluorophore for a more robust quenching response compared to ammonium probe **7b**.

Another method utilized in the design of fluorogenic anion sensors relied on PET induction. Unlike the turn-on response commonly encountered with cations, anions produce a turn-off fluorescence response when the mechanism is PET-based, as anion chelation induces in increase in electron density, and thus a more efficient PET process. This mechanism has been used extensively to produce sensors for the common anionic water

contaminant fluoride. [61] In the BODIPY-based probe **8** (**Figure 1.8**), the terminal triaryl-borane sites are able to selectively coordinate F^- in the presence of competing anions due to the strength of the B-F bond. The additional electron density of the ArBMes2F^- subunit then quenches the appended BODIPY dye upon excitation via PET. [62]

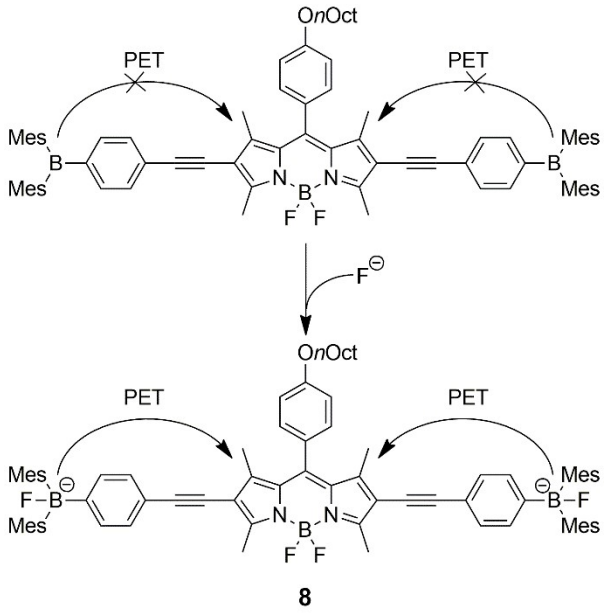

8

Figure 1.8. Addition of fluoride to aryl-ethynyl BODIPY fluorophore **8** quenches the BODIPY fluorescence via a PET mechanism.

PET anion sensors also utilize protons as messengers to detect anions, especially in the case of more basic anions such as F^-. A solution of hemi-cruciform **9** (**Figure 1.9**) exhibits a large bathochromic shift and quenched emission upon addition of excess tetrabutylammonium fluoride (TBAF), likely due to deprotonation of the benzimidazole core.[63] A similar response to acids, bases, and differing anions was also observed with cruciform **10**. [64] Gratifyingly, through the analysis of a combination of PET effects on emission and solvatochromism allowed the absolute identification of numerous amines, boronic acids, and anions through differential analysis. [65] As with all cruciform structures,

their interesting fluorescent behavior is attributed to the excellent orbital separation of the HOMO and LUMO, enabled by alkyne structural units, which facilitates energy transfer during fluorescence and is easily perturbed by analytes.

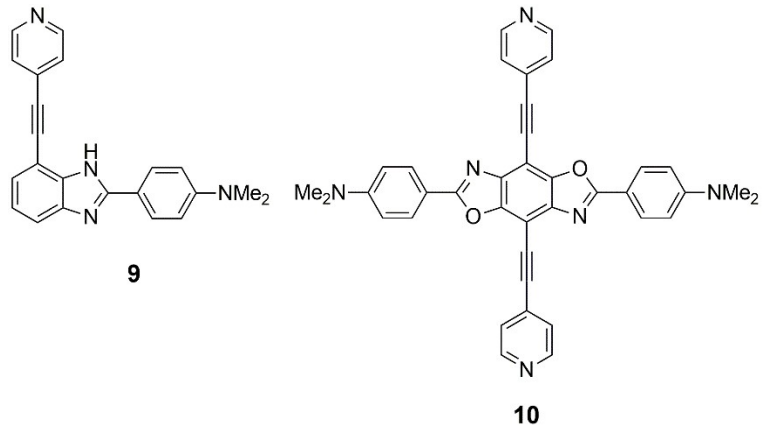

Figure 1.9. Cruciform architectures **9** and **10** used for the identification of whole structural families by differential analysis.

Altering the angle or freedom of rotation about the alkyne can also cause a change in fluorescence upon anion binding, reminiscent of the aforementioned sensing strategy utilizing TICT.[22] The first examples of such a system were bis-ureas **11** and **12** with a mono- or di-yne linker (**Figure 1.10**). [66] A low barrier to rotation provides easy access to the desired syn binding conformation from the stable unbound anti conformer. In addition, anion induced planarity increases the barrier for non-radiative internal conversion, and the result is an OFF-ON fluorescent response to Cl^-. The effect of induced planarity is reinforced by titrating in AcO^-, which binds 1:2 to a solution of **12**•Cl^-, and observing a decreased PLQY as the AcO^- displaces Cl^-. Whereas both PET and collisional quenching mechanisms result in ON-OFF fluorescent responses, the free-rotation around an alkyne enables an OFF-ON

response, which is a boon for analytical purposes due to the dramatic enhancements in signal to noise ratios.

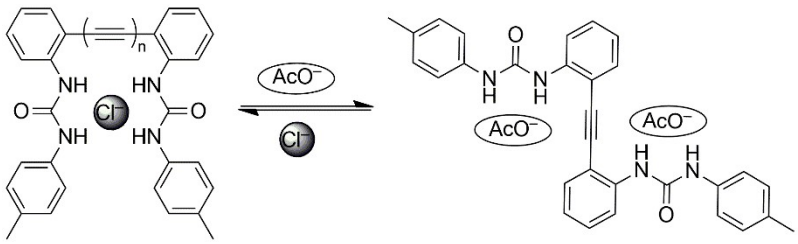

Figure 1.10. The ability of aryl-ethynyl receptors to provide a desirable turn-on response to anions was discovered using bis-ureas **11** and **12**. Cl^- binds 1:1 and turns on fluorescence, while AcO^- binds 1:2 and turns off fluorescence.

Insight into the OFF-ON response can be found in the parallel field of molecular switches. The lowest energy conformation of molecular rotors **13** and **14** is 'closed' in the unbound state with two intramolecular hydrogen bonds (**Figure 1.11**)[67] The alkyne can be switched to a second 'closed' state by introducing Cl^-, and the rotor now forms a stable complex with two intermolecular and one intramolecular hydrogen bond. A new Na^+ complex has been observed by cryogenic ion vibrational predissociation spectroscopy that is analogous to the rotational transition state between the two 'closed' states.[68] The 'open' state can also be considered similar to the unbound state of an alkyne anion host that lacks preorganization.

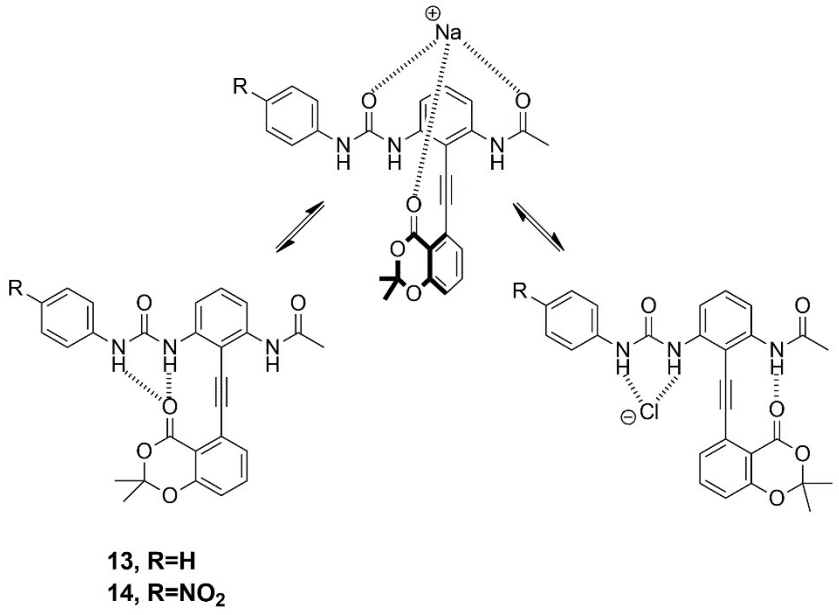

Figure 1.11. Cryogenic ion vibrational predissociation experiments reveal three distinct states of aryl-ethynyl molecular switches **13** and **14**.

AIE is another promising mechanism in the design of OFF-ON fluorescent sensors. The close packing of fluorophores into aggregates blocks non-radiative relaxation pathways through intramolecular motion, similar to the alkyne rotors. The Allen group's synthesis of a series of fluorescent lipid mimics incorporating both an anion coordination site and the zwitterionic phosphocholine group (**15**, **Figure 1.12**) is one application of AIE in anion sensing.[69] The urea and phosphate groups form emissive head-to-tail dimer aggregates in non-coordinating solvents, and fluorescence studies revealed that while weakly basic anions (Cl^- or NO_3^-) do not disrupt aggregation, more basic anions ($H_2PO_4^-$ or HCO_3^-) cause dissociation and quenching.

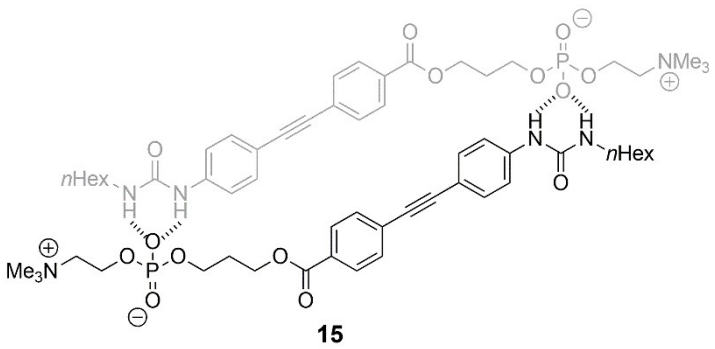

15

Figure 1.12. Phospholipid mimic **15** forms head-to-tail aggregates that are emissive through an AIE mechanism.

Selectivity

Considerable effort has gone into the design of reporting mechanisms for anion sensing, which is only one half of the necessary design principles. The other aspect of anion detection is providing these sensors with anion selectivity as well. To accomplish this, a variety of methods have been used to develop catalogs of discriminating hosts by altering selectivity within a single structural family. The most direct method is to alter the size or shape of a rigid binding pocket. For example, the constrictive binding pocket in bis-indolocarbazole macrocycle **16** forces N_3^- to bind upright, or perpendicular to the plane of the host (**Figure 1.13**) The N_3^- can rotate 90° to bind parallel to the plane of the host simply by expanding the pocket to 1,3-diyne **17**.

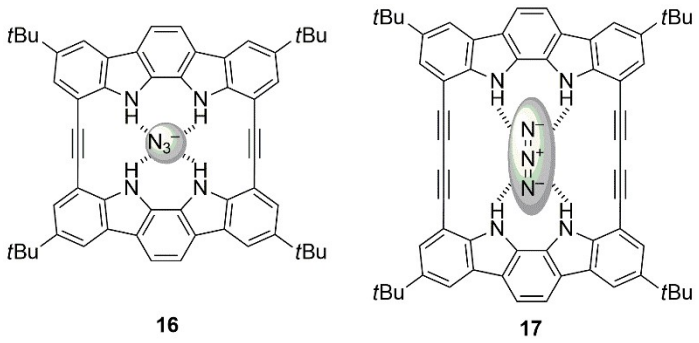

Figure 1.13. Ethynyl-linked bis-indolyl host **16** binds N_3^- in an upright fashion, perpendicular to the host plane. Extended diethynyl-linked bisindolyl host **17** is able to accommodate linear N_3^- inside the binding pocket, parallel to the host plane.

Selectivity through bottom-up design can nonetheless be time-consuming. As a result, several groups have developed methods for quickly modifying existing hosts to equip a trusted scaffold with new selectivity, for instance, molecular self-assembly, post-synthetic modification, and photoswitching. A particularly ambitious method for quickly building a library of hosts is through the anion-templated assembly of coordination complexes. Two $[M2L4]^{4+}$ monomers, with M = Pd^{II} and L = **18** (**Figure 1.14**), assemble around a single BF_4^- into an interlocked structure, $[M2L4]_2^{8+}$, with two additional binding pockets.[71] The interlocked structure encapsulates BF_4^-, as observed in ^{19}F NMR and ESI-MS data. The $[M2L4]_2^{8+}$ complex also exhibited allostery in Cl^- binding, where the first Cl^- equivalent caused a collapse of the outer cavities and facilitated the binding of a second Cl^-.

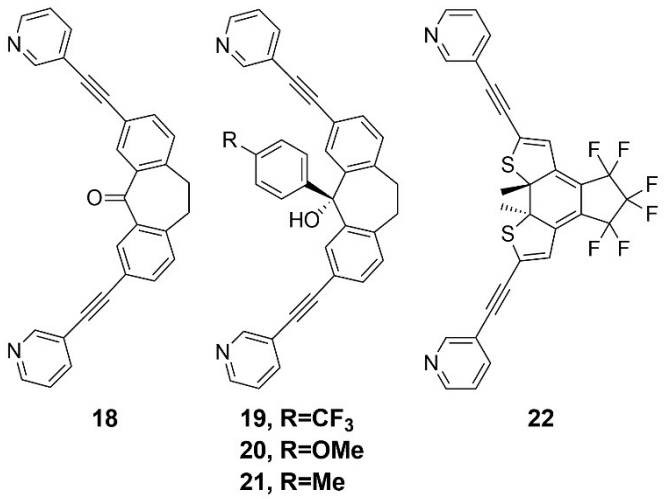

Figure 1.14. A variety of acetylene linked pyridine ligands employed for constructing $[M2L4]^{2+}$ and $[M2L4]_2^{4+}$ cages for anion recognition.

A single step modification of **18** led to more sterically demanding ligands **19-21** (**Figure 1.14**), which formed stable $[M2L4]^{4+}$ complexes with BF_4^- templates. Adding Cl^- drove formation of a $[M2L4]_2^{8+}$ interlocked cage with Cl^- trapped inside the smaller central cavity.[72] The smaller central cavity leaves more space in the outer cavities, and the weakly bound BF_4^- undergoes ion exchange with ReO_4^- , to give the final structure $[Pd2L4]_2[Cl][ReO4]_2^{5+}$. Photoswitchable ligand **22** forms a stable $[M2L4]^{4+}$ cage upon addition of Pd^{II} [73] This structure reversibly switches between open and closed conformations upon irradiation with UV (open→closed) or visible light (closed→open). The open cage has a 47-fold higher affinity for $B_{12}F_{12}^{2-}$ than the closed cage, likely due to increased rigidity preventing Pd^{II} to $B_{12}F_{12}^{2-}$ close contacts. The ability to control anion binding or selectivity through light stimulus is an exciting opportunity for controlling anion concentration or removing harmful anions with a recyclable host.

Not surprisingly, the complex host-guest interactions that are important for efficient anion coordination can also be used to quickly change anion selectivity. In systems large enough to bind multiple guests, such as ditopic receptors, the first guest can be used to tune selectivity. The 1,3-diyne macrocyclic host **23** (**Figure 1.15**) is capable of exhibiting two separate binding modes dependent on anion geometry.[74]

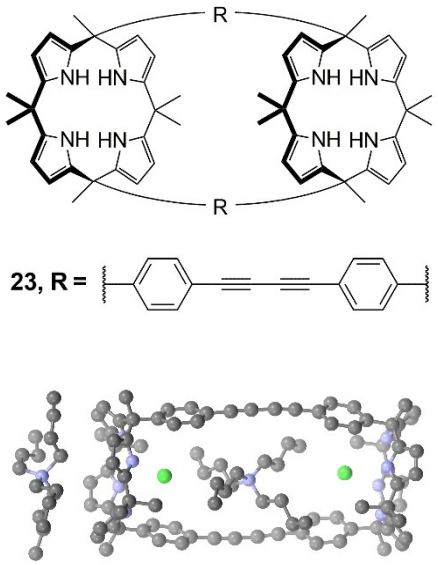

Figure 1.15. A tricyclic calix[4]pyrrole macrocyclic host (top) and the x-ray crystal structure of tricyclic host **23** (bottom) reveals the supramolecular assembly of a [1:2:2] ditopic receptor with $TBA^{+}Cl^{-}$. Hydrogen atoms have been omitted for clarity.

First, two independent binding sites coordinate anions inside through hydrogen bonds with one cation external and a second found between the anions. Enclosing a cation inside the binding pocket leads Cl^{-} to be favored over linear anions and a large cooperativity factor for binding Cl^{-}. Interestingly, host **23** also assembles into a pseudorotaxane by hydrogen bonding with 3,5-pyridinecarboxamide-N-oxide. [75] The smaller binding pocket still provides six hydrogen bond donors and is selective for the linear anions cyanate and azide.

In this case, three distinct binding modes have been demonstrated with a single rigid host molecule.

Rigid host molecules provide the greatest degree of control over the size and shape of the anion binding pocket. While they can be tuned through synthetic modification and secondary guest-guest interactions, sometimes the best method is to provide the host with a certain degree of flexibility to choose its own best guest. Bis-indolocarbazole host **24** (**Figure 1.16**) binds SO_4^{2-} (K_a = 25,000 M^{-1}) with a 2500-fold selectivity over other anions in 10% (v/v) MeOH/acetone. Conformationally free hosts can exhibit weaker anion binding than their rigid counterparts; however, this can be overcome by using noncovalent interactions to favor a preorganized binding pocket. Internal hydrogen bonds organize **24** into a pocket too large for halides, but one that embraces SO_4^{2-} comfortably through eight hydrogen bonds. [76]

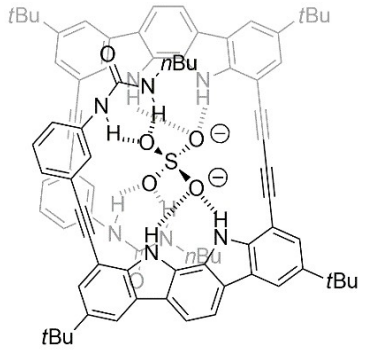

24

Figure 1.16. Urea appended indolocarbazole **24** forms an internal hydrogen-bond supported helix, which binds SO_4^{2-} selectively over other common anions.

Non-rigid hosts can also be tuned for a desired anion by changing the size and shape of the binding pocket. We have developed a research program utilizing a modular approach to synthesize highly conjugated arylethynyl receptors for anion recognition. Unlike many fluorescent anion sensors, these sensors contain an inherently fluorescent arylethynyl backbone as opposed to a pendant fluorophore unit. We have previously described a series of both bis(sulfonamido)- and bis(urea)-ethynylpyridines that exhibit positive fluorescent responses to anions with the right combination of electron-donating and/or electron-withdrawing substituents on the pendant phenyl rings. The bis-ureas (e.g., **25**-**28**, **Figure 1.17**) exhibit a rich solvent-based conformational dependence, showing in the solid state that "S"-, "U"- and "W"-type conformations are all possible depending on solvent guests (for instance, "S" shown in 28, "U" shown in **25**-**27**). [27]

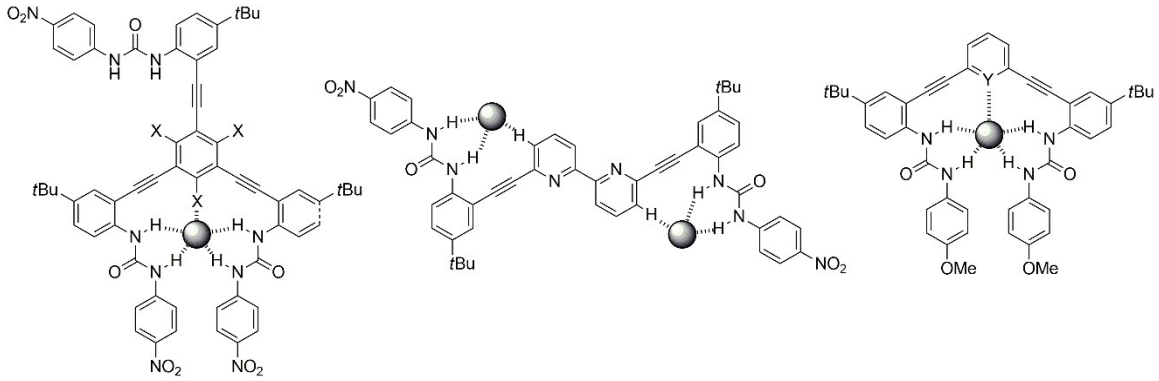

Figure 1.17. A family of aryl-ethynyl-urea receptors for selective anion recognition.

More recently we designed a NO_3^- selective probe, realized by modification of the bis-urea scaffold to add an additional binding site to form an idealized pocket for trigonal planar anions (e.g., **29**-**30**). [78] The selectivity of **29** for NO_3^- over halides was supported by ^{1}H NMR titrations in 10% DMSO/$CDCl_3$. The X-ray crystal structure favors an uncommon

explanation for selectivity, namely an anion-π type interaction between NO_3^- and the alkyne attached to the central arene, where the anion rests offset from the center of the tripodal binding pocket. Whereas the anion-π interaction is engendered by electron-poor receptor **29**, it is not observed in the protic receptor **30**, which also loses NO_3^- selectivity over the halogens. ^{1}H NMR spectroscopy titrations reveal a large shift in the central arene protons of **30** upon complexation to Cl^-, suggesting a hydrogen bonding interaction (as depicted in **Figure 1.17**) not observed in the presence of NO_3^-.

The formation of a C-H•••X hydrogen bond is not unique to the tripodal ligand. Two-armed host **27** (**Figure 1.17**) also forms strong C-H•••X hydrogen bonds, both in solution and in the solid state.[89] X-ray crystal structure determination of the **27**•Cl^- complex showed a short and nearly linear C-H•••Cl^- contact. The hydrogen bonding interaction was also evident in solution by a large downfield shift of the core proton upon the addition of anions. The additional hydrogen bond resulted in a 10-fold increase of the association constant over the free-base form of the pyridine host **25**.

Another example of binding in one of our bis-urea hosts surprisingly led to an anion controlled, three-way molecular switch. Bipy-based ligand **28** (**Figure 1.17**) was designed as a selective probe for the complexation of $H_2PO_4^-$ over halides and other oxoanions. [29, 80] Including hydrogen bond acceptors and donors in the binding pocket improved the selectivity by matching the two-donor, two-acceptor architecture of $H_2PO_4^-$ and allowed the host to bind this guest in a "U" conformation. Titrations and X-ray crystal structures revealed an alternative "S" binding mode for the halides, wherein a urea arm rotates about the alkyne linkage to form a C-H•••X hydrogen bond at the 3-position of the bipy subunit. The two distinct binding modes can be accessed sequentially, making the bipy ligand a three-way switchable probe.

An extreme case of a conformationally flexible anion host not only requires internal organization but also relies on two or more host molecules to assemble around a guest. A family of bis-diketodipyrrole receptors (**Figure 1.18**) was synthesized to study anion-templated assemblies. [81] Diyne **31** formed a [2+2] double helix as the major species under controlled conditions (l x 10^{-3} M, low [Cl-], -50°). Appending additional arenes stabilized the dimeric complex and facilitated observation in solution at room temperature. A cis-Pt linked ligand was also of a suitable geometry to form [2+2] complexes with Cl^- under specific conditions.

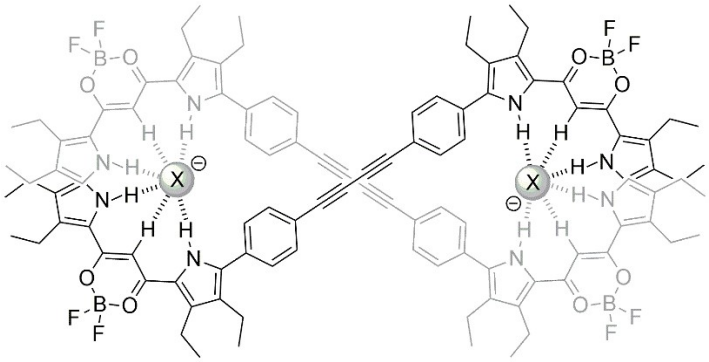

31

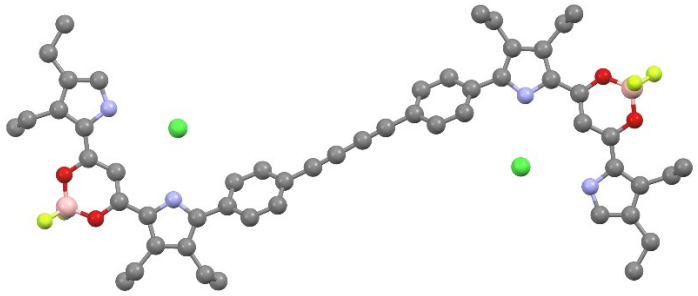

Figure 1.18. Dipyrrole-diketo anion receptor **31** designed to have two anion binding pockets (top); x-ray crystal structure of **31** complexed with Cl^- (bottom). TBA^+ counter ions and hydrogen atoms have been omitted.

Despite the numerous hurdles set up by anions to hinder efforts in designing potent and selective hosts, complex coordination events that were previously only possible with metals have been achieved. The ability of aryl-ethynyl hosts to act as building blocks or foldamers is not restricted to anions as templates. Methods for using the aryl-ethynyl scaffold for chiral sensing and even more complex architectures have also been achieved.

EMERGING AREAS

Chirality

Chirality sensing is the basis of many biological processes and an emerging field for synthetic receptor design. Novel arylethynyl sensors have been synthesized which report the absolute chirality of analytes. Sensors have also been developed that use circular dichroism spectroscopy as a mechanism for selective reporting of non-chiral analytes. Polymeric receptors in the burgeoning field of chiral detection have intriguing prospects for the assembly of supramolecular architectures to mimic natural structures such as proteins and enzymes. Though a detailed discussion on the use of polymeric receptors is beyond this review, a few notable examples will be highlighted in the context of chirality sensing.

Fluorescent aryl-ethynyl polymers have been modified for chiral detection by incorporating chiral binding sites. The Zhu group used a binaphthalene derivative with axial chirality, in conjunction with a Schiff base binding site, to give sensor **32**, which has selectivity for (D)-phenylalaninol (**Figure 1.19**). [82]

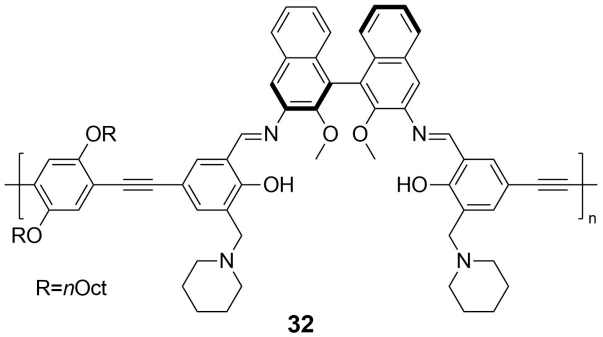

32

Figure 1.19. Aryl-ethynyl polymer **32** with an integrated chiral receptor unit.

Another interesting area of research for aryl-ethynyl oligomers and polymers is reproducing the double-stranded helix of DNA with synthetic precursors, which can then be used as induced chiral reporters. In solution and in the solid state, m-terphenyl polymers and oligomers such as **33** were found to form an achiral mixture of double helices through carboxylate salt bridges (**Figure 1.20**) The addition of chiral secondary amines induced the dimers to refold into chiral double helices, held together via a salt bridge. The handedness is dependent on the chirality of the amine and could be measured both in solution by CD and in the solid state by AFM. Further studies elucidated a large "sergeant and soldiers" effect, as well as a "majority rules" effect on the chirality.

An oligomeric double-helix was prepared by ring-closing metathesis of salt-bridged m-terphenyl monomeric derivatives of **33** appended with alkenes. [84] The dimeric helix produced a large CD response with little solvent dependence, compared to a model dimer that displayed a small CD signal. The addition of TFA or Zn^{2+} caused a near complete loss of the observed chirality in the helix due to disruption of the salt bridges. In addition, Zn^{2+} produced a turn-on fluorescence response. The chirality could be returned by addition of sequestering agents for the initial stimuli, addition of DIPEA for acid or [2.2.1] cryptand for Zn^{2+}.

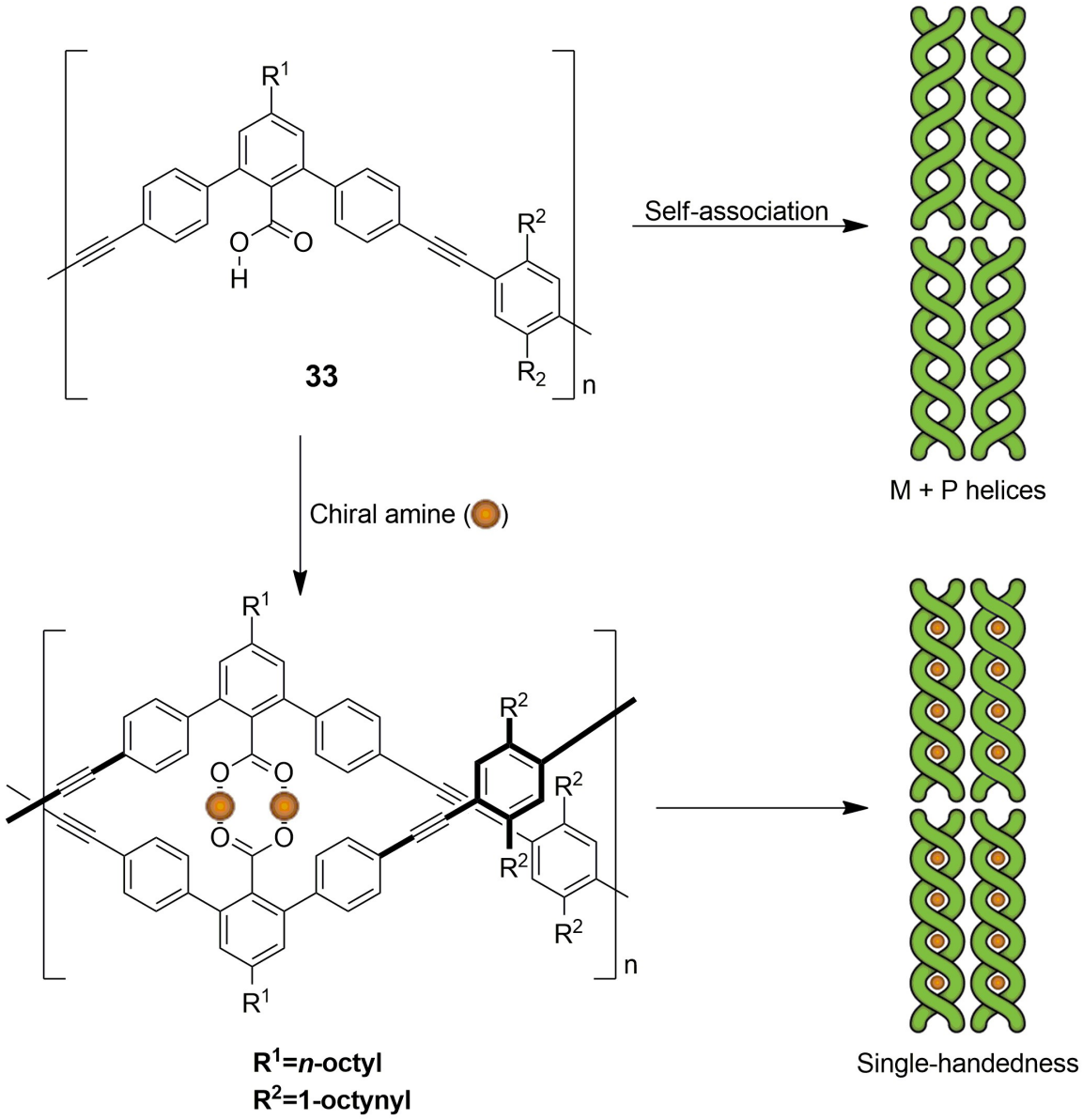

Figure 1.20. Foldamer **33** acts as a chiral reporter in the presence of chiral amines, generating helices of a single handedness due to the amine's chirality.

The design strategy of combining a fluorescent molecule with a probe group has also been used for modular, fluorescent chirality sensors. A phenothiazine fluorophore linked with both a chiral amine and boronic acid binding sites furnished **34** (**Figure 1.21**). The resulting aryl-ethynyl sensor provided enantioselective determination of a variety of sugars and organic acids.

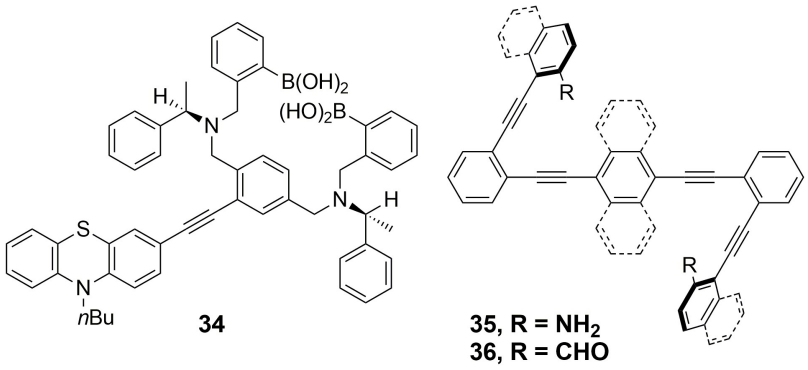

Figure 1.21. Examples of probes for determining chirality. **34**, a fluorescent sensor with chiral binding sites, shows chirally-selective recognition of chiral analytes. An achiral rotor within **35** and **36** can be induced to chiral conformations via imine formation.

The Wolf group has developed a chirality sensing scaffold by appending aryl-amines or aldehydes to a central aryl-ethynyl rod, giving sensors with the general scaffold of **35**-**36** (**Figure 1.21**). The functionalized aryl-ethynyl rotors form imines upon reaction with amine or aldehyde analytes. Chiral diamines or dialdehydes lock the probe in a single chiral conformer, which leads to a large Cotton effect, and quantitative determination of ee is possible. Further studies with mono-substituted chiral analytes revealed similar large Cotton effects and linear calibration curves for ee determination via CD analysis.

The ethynyl-indolocarbazole anion sensors of Jeong have also been reengineered to act as both a chiral reporter for achiral analytes and an enantiomer-selective sensor for chiral analytes (**Figure 1.22**). [89] The addition of chiral methylene groups to a known indolocarbazole anion probe produced foldamer **37** with a strong helicity preference measured by CD in nonpolar solvents. The chiral response of this probe is affected by both the solvent polarity and the presence of anions in solution. For instance, changing the solvent from toluene to CH_2Cl_2 or $CHCl_3$ resulted in a decrease of the CD signal by half; further increasing solvent polarity to DMSO or CH_3CN caused a near complete loss of chirality. Notably, the switchable chirality could also be used to detect anions by noting the CD signal inversion in the presence of Cl^-, Br^-, or AcO^-.

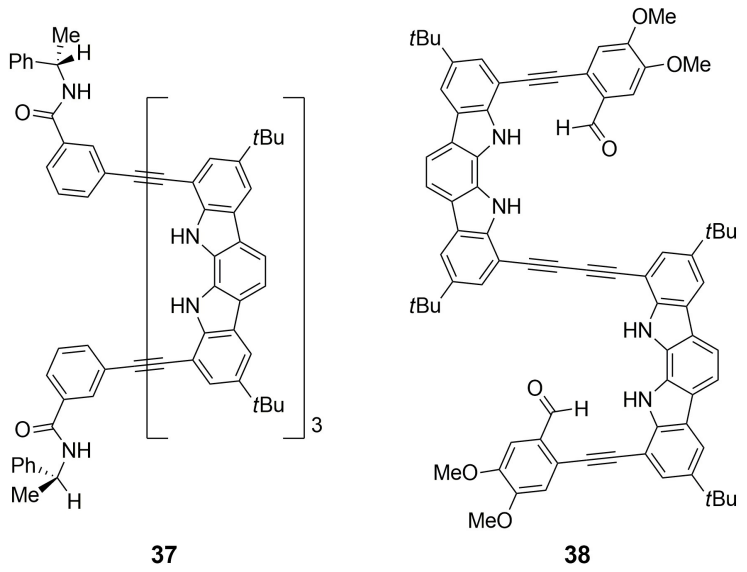

Figure 1.22. Foldamers **37** and **38** have been engineered to act as hosts for chiral guests using the aryl-ethynyl scaffolding.

The absolute configuration and ee of amino acids can also be determined using indolocarbazole foldamers.[90-91] Bis(ethynyl-indolocarbazole)s with appended aryl-aldehydes

such as **38** form chiral helices in the presence of N-Boc protected amino acids; these helices can subsequently be locked in place by imine formation with ethylene-1,2-diamine. The resulting chiral macrocycles produce a large CD response, and calibration with mixtures of isomers permits rapid determination of ee for a given sample. Analysis of X-ray crystal structures and computational models revealed that this stereoselectivity is likely due to steric interactions between amino acid side chains and the bis-alkyne. The development of novel chirality sensors brings supramolecular chemistry closer to its roots in biology and biomolecules.

Biological Species

One of the primary purposes for synthesizing anion-selective fluorescent probes is to provide biologists and biochemists with better tools for studying anion-regulated cellular processes. A corollary to this purpose is the synthesis of small molecule-based anion transporters or anion channel mimics. These mimics are useful for studying the mechanisms of cellular anion transport and as possible treatments for anion transport protein deficiencies. The Jeong group was successfully able to design a synthetic chloride channel to mimic the S. typhimurium protein.[92] The combination of four hydrogen-bond donors in an anion-binding pocket with judicious side-chain selection produced a potent anion binder and anion transporter. The presence of both a greasy side-chain and activated alcohols was necessary for efficient anion transport.

Ion transport across cell membranes has also been achieved by designing synthetic molecules to form porous channels.[93] Oligomers with alternating regions of hydrophilic and hydrophobic chains interpenetrate the lipid bilayer and form supramolecular assemblies. The timescale of the ion transport, measured by time-dependent conductance, indicates a pore

formation mechanism, not flip-flopping. Transport rates with various alkali metals allowed for rough determination of the pore size as 0.53 nm.

The work of Moore et al. has gone a long way in proving the viability of designing artificial protein mimics from arylethynyl scaffolds.[94] Oligomers of phenylacetylene form a helical structure with a well-defined hydrophobic cavity that is able to bind guests in water. Replacement of a single phenyl with a pyridine in the chain provides a reactive site for guest modification either by protonation or methylation reactions. Arylethynyl foldamers have also been used to selectively bind saccharides. [95-97] A pyridineacetylene foldamer offers multiple hydrogen bond acceptors and provides good shape complimentarity. Covalent linkage of the foldamer with a coherent saccharide allows for the synthesis of stable, chiral aryl-ethynyl foldamers (**Figure 1.23**). This method of covalent linkage also allows for the possibility of a displacement assay for other guests.

Water-soluble aryl-ethynyl probes have also been applied as selective binders and stabilizers for G-quadruplex DNA structures. A series of bisamide (39) and trisamide (40) functionalized aryl-ethynylpyridines were studied for the effects of structural modifications on G-quadruplex stabilization and sequence selectivity (**Figure 1.24**) [98] The trisamide was found to be the most potent ligand at stabilizing a range of G-quadruplex sequences with a 2-fold increase in ΔT_m over the parent bisamide ligand. Addition of a triazole to the bisamide by click chemistry improved the ΔT_m, albeit less than the trisamide. Surface plasmon resonance (SPR) was used to elucidate the kinetics and equilibrium binding constants, K_d, for each ligand. The triazole ligand was found to have good selectivity for one G-quadruplex sequence over others; however, the trisamide was found to have lower sequence selectivity, and both ligands displayed non-specific or multiple binding at high [L].

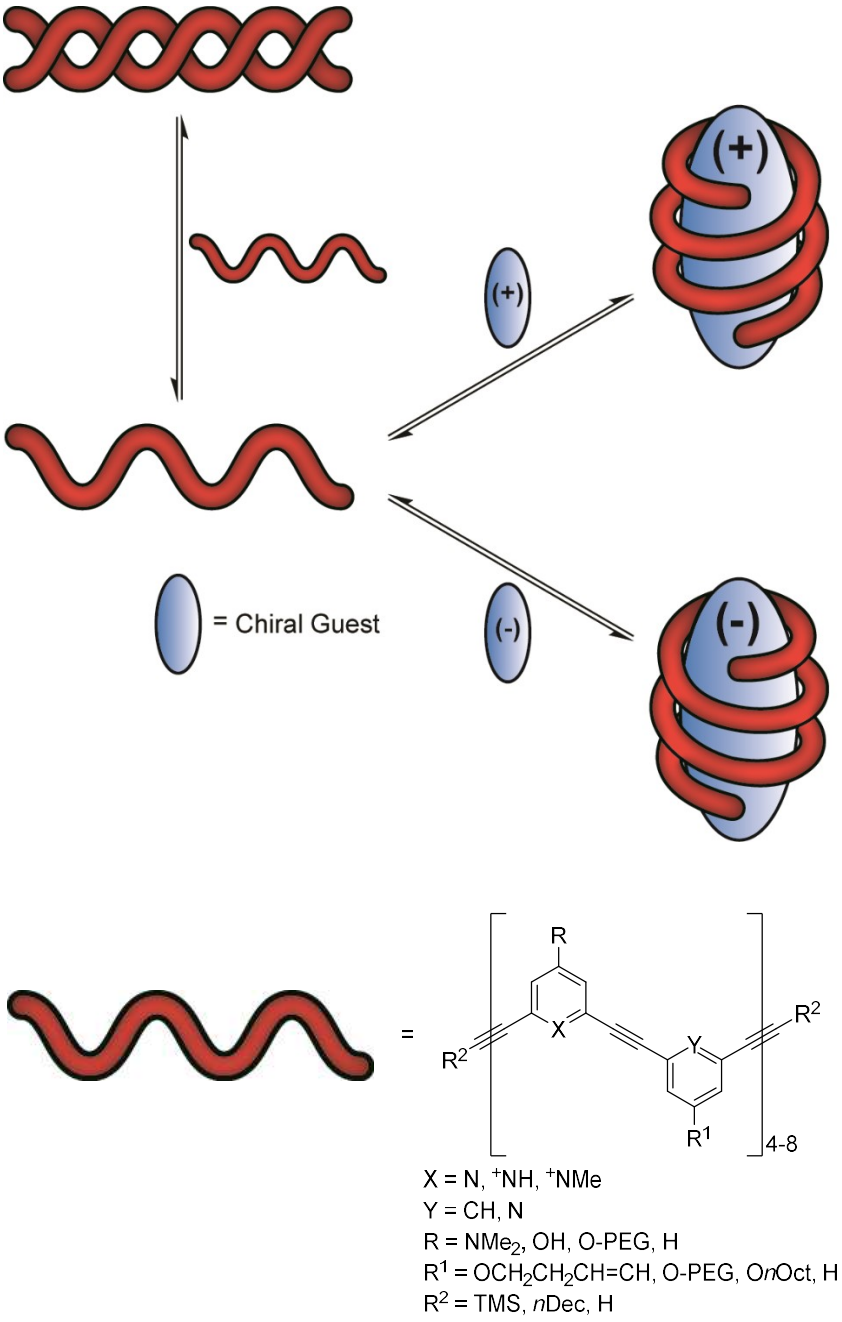

Figure 1.23. Aryl-ethynyl foldamers form complimentary binding pockets to provide guest selectivity, in conjunction with specific binding motifs.

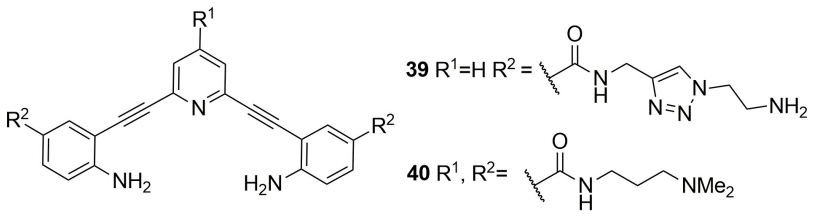

Figure 1.24. Side-chain engineering provides both water solubility and G-quadruplex selectivity for bisethynylanilinopyridines.

Chemical Warfare Agents

Another targeted application where aryl-ethynyls have proven their utility is the sensing of chemical warfare agents and high energy organic compounds. Recent events have reemphasized these compounds as an important area for sensor development. The principles of aryl-ethynyl sensor design pioneered with simple metals and halides, and including structure design, -conjugation, it-stacking, and metal coordination have been invaluable when applied to more dangerous compounds.

Stang et al. and Mukherjee et al. have developed a series of cages utilizing alkyne linkers and various metal centers whose native fluorescence is quenched in the presence of nitro-aromatics. [99-100] The quenching response of cages such as 41-43 (**Figure 1.25**) was selective for nitrated aromatics typical to explosives manufacture over other electron-poor aromatic molecules. A similar quenching response was found in a series of alkyne-linked dendrimers, based upon a silole core. These fully conjugated dendrimers exhibited a fluorescence emission which was selectively quenched in the presence of nitrated aromatics.[101]

In addition to sensing mechanisms utilizing the quenching abilities of nitrated aromatics, Wild et al. developed a series of alkyne-linked terpyridine Zn complexes such as

44 (**Figure 1.26**) These complexes responded selectively to organophosphate model compounds that are representative of the G-series of nerve agents. These sensor compounds were loaded on a solid support to create a test strip for nerve agents in the gaseous phase.

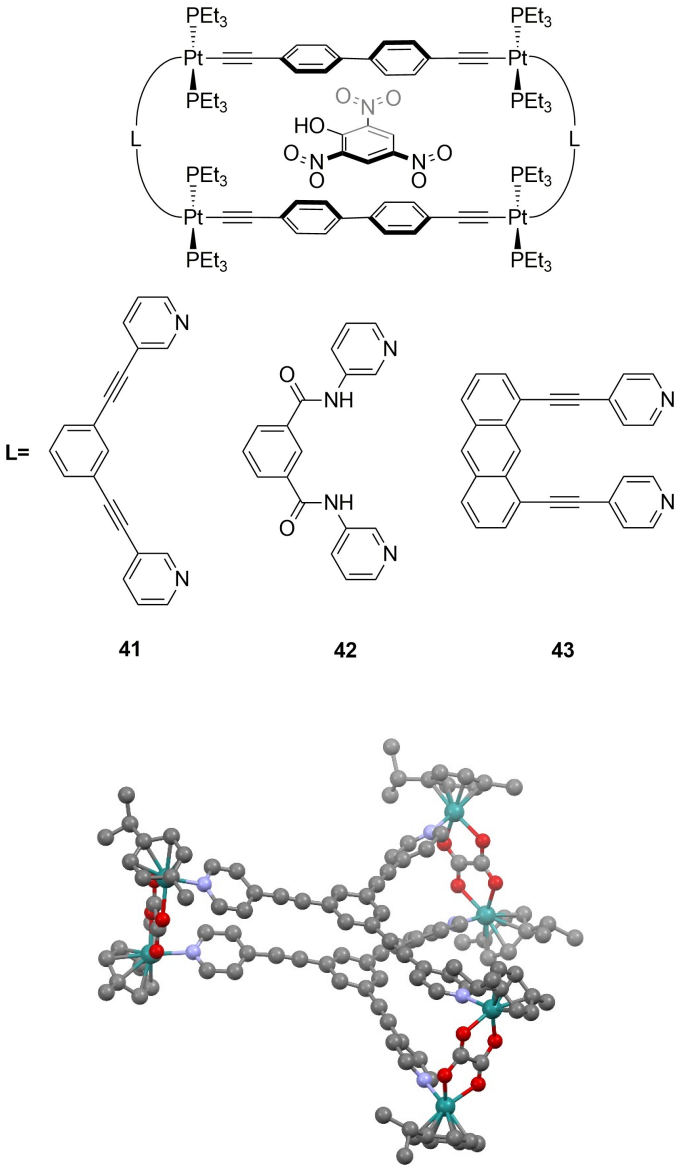

Figure 1.25. A family of macrocyclic hosts based on Pt (top) and x-ray crystal structure of another macrocyclic host based on Ru (bottom) for the detection of nitrated aromatics.

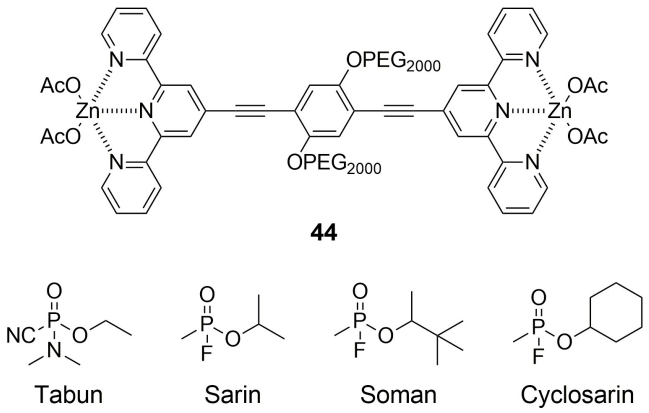

Figure 1.26. Zn complex (top) utilized in the detection of common nerve agents (bottom).

Gas Storage

In addition to their use in sensing nitrated aromatics, macrocyclic cage structures assembled from aryl-ethynyl linkages have been used for the selective storage and subsequent release of gases such as CO_2 over other atmospheric gases. The Zhang group has developed a family of organic molecular cages assembled with aryl-ethynyl linkages (**Figure 1.27**). These cages demonstrate selective adsorption of CO_2 in the presence of N_2, which shows promise in carbon capture applications; the ability to filter out and separate CO_2 in the presence of N_2 carrier gas is a potent method for the reduction of carbon emissions from industrial processes.[103] By assembly through dynamic covalent chemistry, formation of the cages 45 and 46 proceeded with exceedingly good yields. Comparison of alkyne-based 46 against previously developed anthracene-based cage 45 showed over a twofold increase in CO_2 selectivity versus N_2 in the solid phase (1 38/1 for 46 vs. 62/1 for 45) [104-105] Crosslinking 46 via Sonogashira cross-coupling with p-diethynylbenzene formed an all-organic framework which demonstrated lower CO_2 selectivity (63/1) over N_2, but higher absorption of CO_2 by weight than all other cages studied (8.01 cm^3/g vs. 5.58-3.32 cm^3/g).

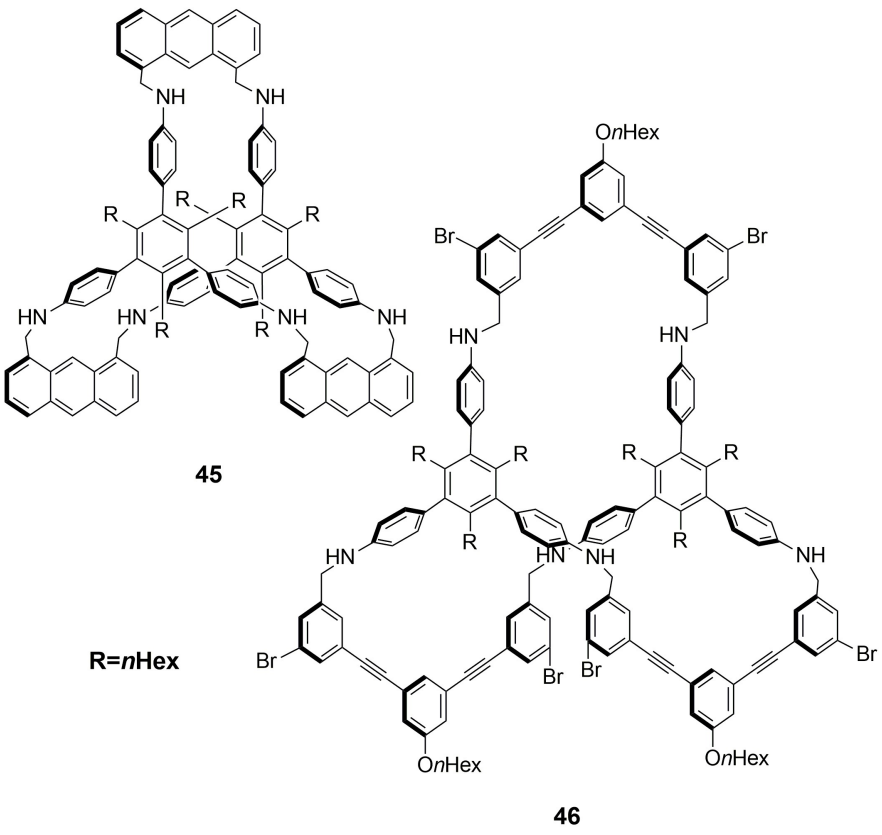

Figure 1.27. Large molecular cages **45** and **46** demonstrate selective adsorption of CO_2 over other atmospheric gases.

CONCLUSION

In summary, a variety of methods for incorporating aryl-ethynyl groups into recognition scaffolds, and their unique roles as both rigid structural units and conjugative linkers have been summarized. The methods covered utilize the unique characteristics of the ethynyl group to provide selectivity and responsiveness to designed sensors. The simplest usage relies only on acetylenes as rigid, conjugated linkers for reporter and recognition units. However, the complexity of possible aryl-ethynyl based systems is limited only by the designer's imagination. This has been demonstrated by such a variety of uses as multianalyte

responsiveness from a single probe and analyte-responsive mimics of large biomolecules, proteins, and DNA, in addition to the classical guests such as the inorganic anions and cations.

The future directions of aryl-ethynyl compounds in sensing and recognition purposes shows a strong potential for artificial protein mimics, where the alkyne-linked foldamers can construct a chiral structure with a hydrophobic central cavity for stereoselective supramolecular catalysis. When appended with water-solubilizing groups, this can yield a powerful methodology for water-based supramolecular chemistry. As the field of supramolecular chemistry grows, the aryl-ethynyl linkage is showing itself to be a privileged scaffold for the construction of both molecular machines and supramolecular architectures.

BRIDGE TO CHAPTER II

This introduction chapter delved into the myriad uses of the aryl-ethynyl scaffolds for the sequestration and host-guest chemistry for a large variety of analytes. Here we laid out the various mechanisms that the sensor molecules use for fluorescence changes and other spectral changes. In addition, we sample the variety of hosts built upon these scaffolds specifically for anionic guests. In Chapter II the use of an aryl-ethynyl scaffold as a macrocyclic anion host is explored, building upon the myriad applications presented here, and lays the groundwork for the remainder of the dissertation.

Chapter II includes material that will be published with coauthors Airlia M. Shonkwiler, Charles A. Johnson II, Lev N. Zakharov, Darren W. Johnson and Michael M. Haley. Chapter III includes material that will be published with coauthors Calden N. Carroll, Daisuke Inokuchi, Lev N. Zakharov, Michael M. Haley and Darren W. Johnson. Chapters IV

and VI include material that will be published with coauthors Airlia M. Shonkwiler, Lev N. Zakharov, Darren W. Johnson and Michael M. Haley.

Chapter V includes material that has been published with coauthors Airlia M. Shonkwiler, M. M. Khalifa, Lev N. Zakharov, Darren W. Johnson and Michael M. Haley.

CHAPTER II

TUNING THE SIZE OF A FLUORESCENT MACROCYCLE FOR TARGETED GUEST INCLUSION – SOLUTION STATE AND SOLID STATE INTERACTIONS

This manuscript is prepared for submission to *Chemical Science*, an RSC journal, with coauthors Airlia M. Shonkwiler, Charles A. Johnson II, Lev N. Zakharov, Darren W. Johnson and Michael M. Haley. Airlia Shonkwiler and I performed synthetic and analytical investigations throughout the course of this manuscript, while Dr. Johnson performed initial investigations into the scaffolds utilized. Dr. Zakharov provided crystallographic support for the manuscript, while Profs. Haley and Johnson provided editorial support and directed the course of the research.

INTRODUCTION

Classically, macrocyclic scaffolds have been used in a large variety of applications, ranging from pharmaceuticals and chemical sensing to synthetic receptors and materials for organic electronics. Macrocycles in drug design have been extensively employed, due to their conformational rigidity, with the entropic cost of binding already paid because of a locked structure and a higher theoretical ligand efficiency. [1–4] Assembly of these macrocycles has typically been a difficult task, with an extensive number of synthetic techniques utilized to prepare these compounds in good yield and fight the entropic constraints inherent in the cyclization step.[5–7] Depending on the macrocyclization employed, these methods can utilize

either high dilution/pseudo-high dilution, pre-organization, or templation by a suitable guest in the case of receptor-type macrocycles. There are a number of reactions that lend themselves to macrocycle formation such as ring-closing metathesis and disulfide bond formation. These have benefits over some of the other methods employed, such as peptide bond formation, due to their symmetric nature, allowing easier synthesis of the two sides of the cycle.

One important tool in macrocyclization reactions has been the concept of preorganization, where the entropic cost of creating a large cyclic molecule is alleviated somewhat by pre-shaping the scaffold into a curved form, yielding a preferential macrocyclization over other reaction geometries.[8] While there have been some poignant examples of high-yielding macrocyclic hosts prepared through exceedingly simple synthetic techniques, these scaffolds are, by necessity, quite symmetric, and the synthesis of these scaffolds would tend to be highly sensitive to their functionality.[9] Such a route represents an excellent example of synthetic design and the potential for complex products arising from structurally simple starting materials, although such a strategy does not allow for a modular design or inclusion of electron-rich and electron-poor regions into the scaffold design for spectroscopic tunability.

In our group we have extensively used a 1,3-bis(2-anilinoethynyl)arene-based scaffold as an effective, tunable fluorescent host for a variety of anionic analytes.[10–21] We found that this backbone provides a suitable geometry as a rotationally flexible receptor for the halides, phosphate, sulfate, and nitrate in our examinations of conjugated hosts for biologically and environmentally relevant analytes. It was posited in our studies that use of a pre-organized macrocyclic receptor could pay some of the entropic costs of the binding event, creating a much more energetically favorable association event. Although we

successfully obtained such a system, it had some limitations: (i) the scaffold showed a poor fluorescence response, (ii) its binding interactions with halides in solution were weak, (iii) its synthesis proceeded in a low 11% yield for the key macrocyclization step, and (iv) the final product required extensive purification.[11] Attempts to improve the yield through pseudo-high dilution conditions were unsuccessful, demonstrating the difficulty inherent in this step. Still in pursuit of a macrocyclic anion host to take advantage of the aforementioned benefits, we redesigned the structure to contain a disulfide linkage. Macrocycles **1a**-c, our new targets, would possess the suitable functionalities for anionic guest inclusion: hydrogen-bond donors within the cleft, and a pyridine nitrogen atom suitable for protonation to form a strong, hydrogen-bonding binding pocket. To understand the different effects of linker size on the binding cavity, we elected to vary the number of methylene units between the carbonyl and the S-atom effectively changing only the size of the binding pocket, without changing the number or arrangement of hydrogen bonding functionalities. We also sought to study how well the anionic guest fit inside each of the binding pockets by obtaining their solid state structures, thus allowing direct measurement of the size and shape of the cavity, in addition to allowing an examination of the hydrogen bond "anion coordination geometry" of the hydrogen-bond donors which line the cavity.[22] Herein we report the synthesis, solid-state structures, binding studies and optoelectronic properties of disulfide macrocycles **1a-c** (**Figure 2.1**).

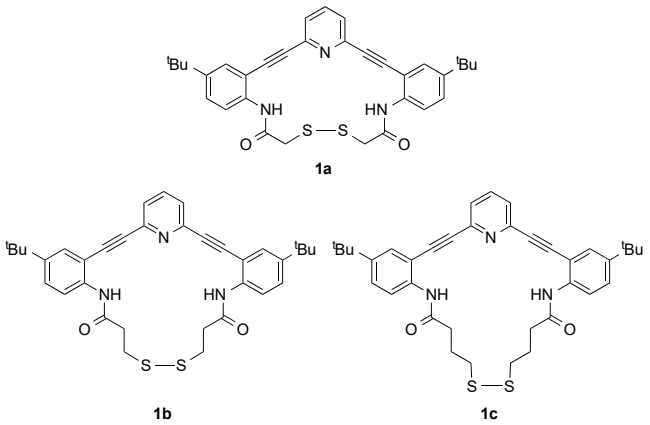

Figure 2.1. Family of disulfide-based macrocyclic hosts in this study.

RESULTS AND DISCUSSION

Synthesis

Preparation of **1a**-**c** started with our previously reported key intermediate **2** (**Scheme 2.1**). Reaction with the requisite chloroalkanoyl chlorides provided chloroamide derivatives **3**a**-c** in 89-97% yield. Subsequent treatment with KSAc produced thioacetyl-functionalized **4a-c** in yields from 85-92%. Under air-free conditions K_2CO_3 unmasked each thioacetate derivative giving the thiolate forms, which were subsequently oxidized by treatment with elemental I2 after minimal workup, resulting in formation of the target disulfide macrocycles **1a-c** in good isolated yields (59-77%). Interestingly, the macrocyclization step displayed high sensitivity to the reaction conditions. If the I_2 oxidation of the thiol was performed in the presence of added Et3N, then the yield of the macrocycle was often quite low (20-40%), with extensive oligomer and polymer formation.

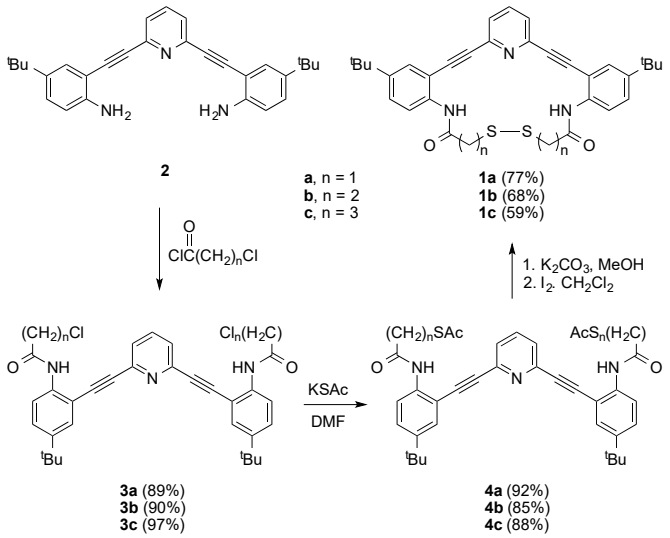

Scheme 2.1. Synthesis of disulfide macrocycles **1a-c**. **3** and **4** are shown in a "W" conformation; **1** is shown in the "U" conformation which is pre-organized for guest binding.

If the reaction was performed in the absence of external base and at low concentrations, however, then the reaction proceeded quite well, with significantly higher yields of the target macrocycle and reduced formation of higher-order oligomers and polymeric species. We posit that in the absence of external base, the internal pyridine provides a basic site to form the necessary thiolate for oxidation, and due to the ion-pair formation and concomitant association of pyridinium and thiolate, results in a self-templated reaction. The stability of the thiolate is likely enhanced within the cleft due to the ring of hydrogen-bond donors of the scaffold. In addition, the reaction is likely further templated due to the formation of iodide anions during the course of the oxidation. As we have designed these scaffolds to be proficient anion-binders, it is no surprise that the presence of anions could help stabilize the U-conformer (**Scheme 2.1**) of the aryl-ethynyl scaffold necessary for cyclization to occur. The conjugated scaffold is thus beneficial for macrocyclization on two fronts: not only does it provide a preorganized scaffold already

curved for favorable cyclization conditions; it also provides an internal pyridine to direct the cyclization to occur favoring monomeric macrocycles over larger structures.

Solid-State Structures

The smallest member of the family, **1a**, yielded diffraction-quality crystals by slow evaporation from a mixture of CH_2Cl_2/hexanes. Previous experience suggested this class of hosts will crystallize with a solvent guest (or even adventitious water) in the binding pocket;[10–18,23] however, in this case, neither solvent nor water guest was present in the structure. Rather, the disulfide bond folded up into the binding pocket, preventing any guests from occupying the space, making a close contact between the sulfur atoms and the pyridine nitrogen (N•••S distance: 3.437 Å, sum of Van der Waals radii: 3.35 Å, **Figure 2.2**). As a result, there was no room for guest encapsulation. It appears that with the short linker length, the disulfide is stabilized by an intramolecular hydrogen bond with the amide N-H (distance N-H•••S: 2.555 Å), preventing access to the cavity. Attempts to force guest encapsulation via treatment with HCl gas yielded the protonated species as witnessed by changes in the fluorescence and absorption spectra, but the HCl salt of this macrocycle resisted all attempts of crystallization and instead decomposed to polymeric species upon concentration.

The crystal packing of macrocycle **1a** is dominated by van der Waals interactions with no intermolecular hydrogen bonds present. There is some evidence for π-π stacking between the alkynes and the amide carbonyl, but the closest non-bonding contact between molecules is 3.471 Å, just outside the sum of van der Waals radii for the two carbon atoms. The packing motif demonstrated 1D stacks, with alternating head-to-tail packing (**Figure 2.2**).

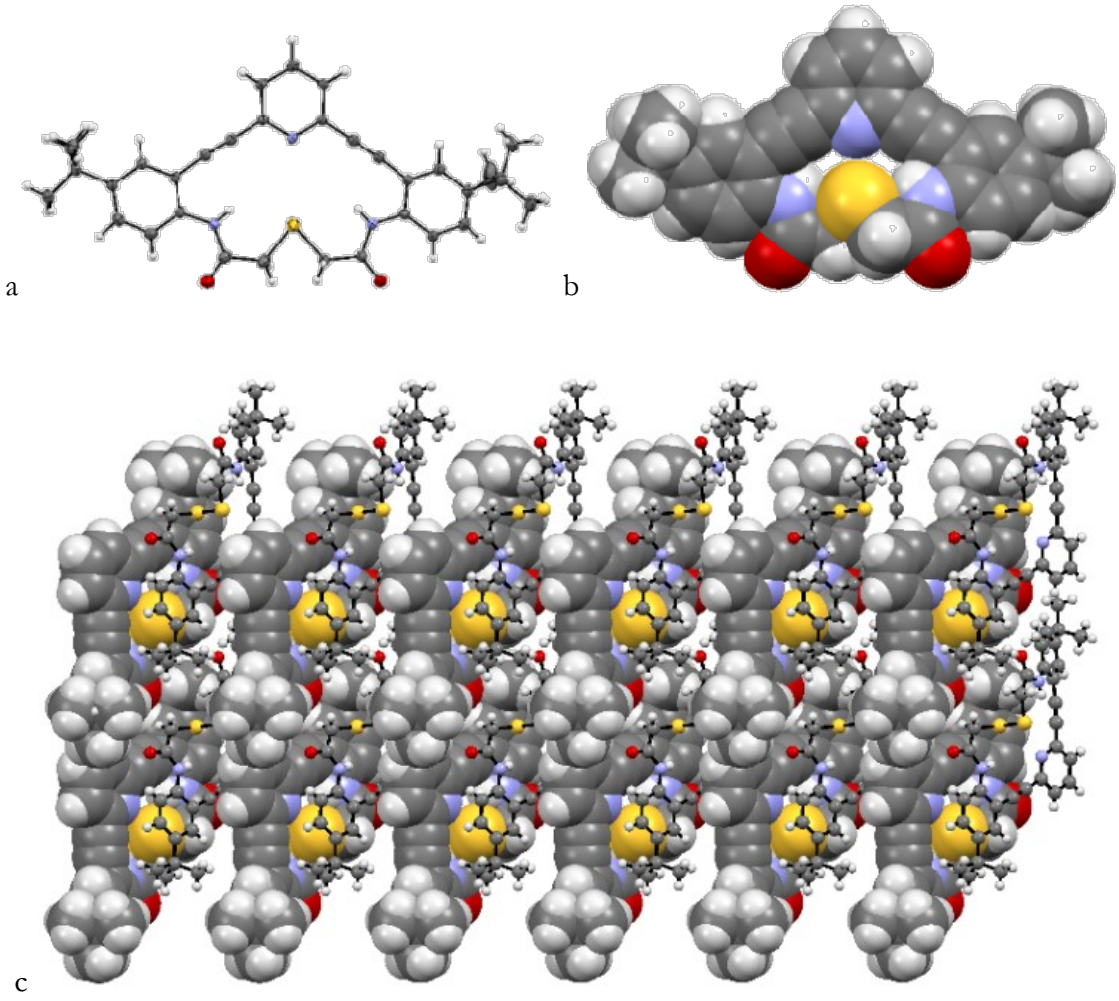

Figure 2.2. (a) ORTEP of **1a**, ellipsoids drawn at 50% probability. (b) Space-filling model of solid-state structure of **1a**, showing filled central cavity. (c) Solid-state crystal packing of **1a**, with alternating molecules drawn in ball-and-stick and space-filling models for clarity. In all structures disordered atoms in one t-butyl group are removed for clarity.

Examination of the solid-state structure of the macrocycle extended by two carbon atoms, **1b**, demonstrated a cavity more than suitable for guest inclusion. This structure included H_2O in the binding pocket, even though the crystals were grown by slow evaporation of a hexanes solution of **1b**. This was an encouraging result, as our previous studies revealed that hosts which bound water in the neutral form typically also acted as excellent hosts for halides in the protonated form.[10,11] In the case of **1b**, only one of the amide N-H functionalities forms a hydrogen bond to the encapsulated guest, so that the H_2O molecule is not quite in the center of the cavity (**Figure 2.3a**). As the space-filling structure indicates, H_2O does not quite fill the interior of the binding pocket (**Figure 2.3b**).

As is typical in compounds of this type that bind water, the H_2O molecule donates a hydrogen bond to the amide oxygen of a neighboring molecule in the crystal structure, forming dimers (**Figure 2.3c**). Each dimer was then held to the next molecule in the chain by another hydrogen bond between the amide N-H not involved in binding to the guest, forming a hydrogen bond with an amide oxygen of a neighboring molecule.

The HCl salt of macrocycle **1b**, formed by bubbling HCl gas through a CH_2Cl_2 solution, afforded X-ray quality single crystals, allowing us to examine the solid state structure of the ionic host-guest complex. Protonation of the pyridine defined the cavity with a ring of hydrogen-bond donors in which chloride fits snugly (**Figure 2.4a-b**), suggesting that chloride better fills the host cavity rather than being shifted to the side as with a water guest.

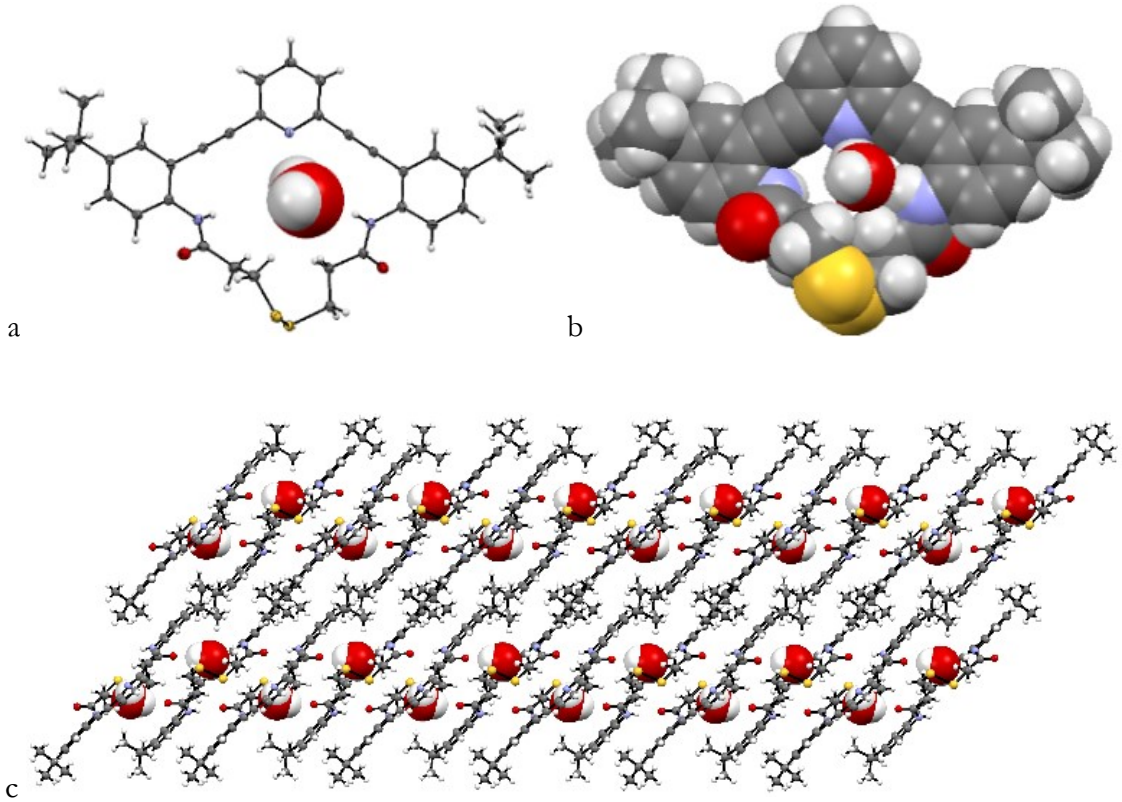

Figure 2.3. (a) ORTEP of **1b•H_2O**, ellipsoids drawn at 50% probability. (b) Space-filling model of solid-state structure of **1b•H_2O**, showing central cavity occupied with water guest. (c) Solid-state crystal packing of **1b•H_2O**, host molecules drawn as ball-and-stick models, guest drawn in space-filling mode, exemplifying the water-assisted intermolecular interactions.

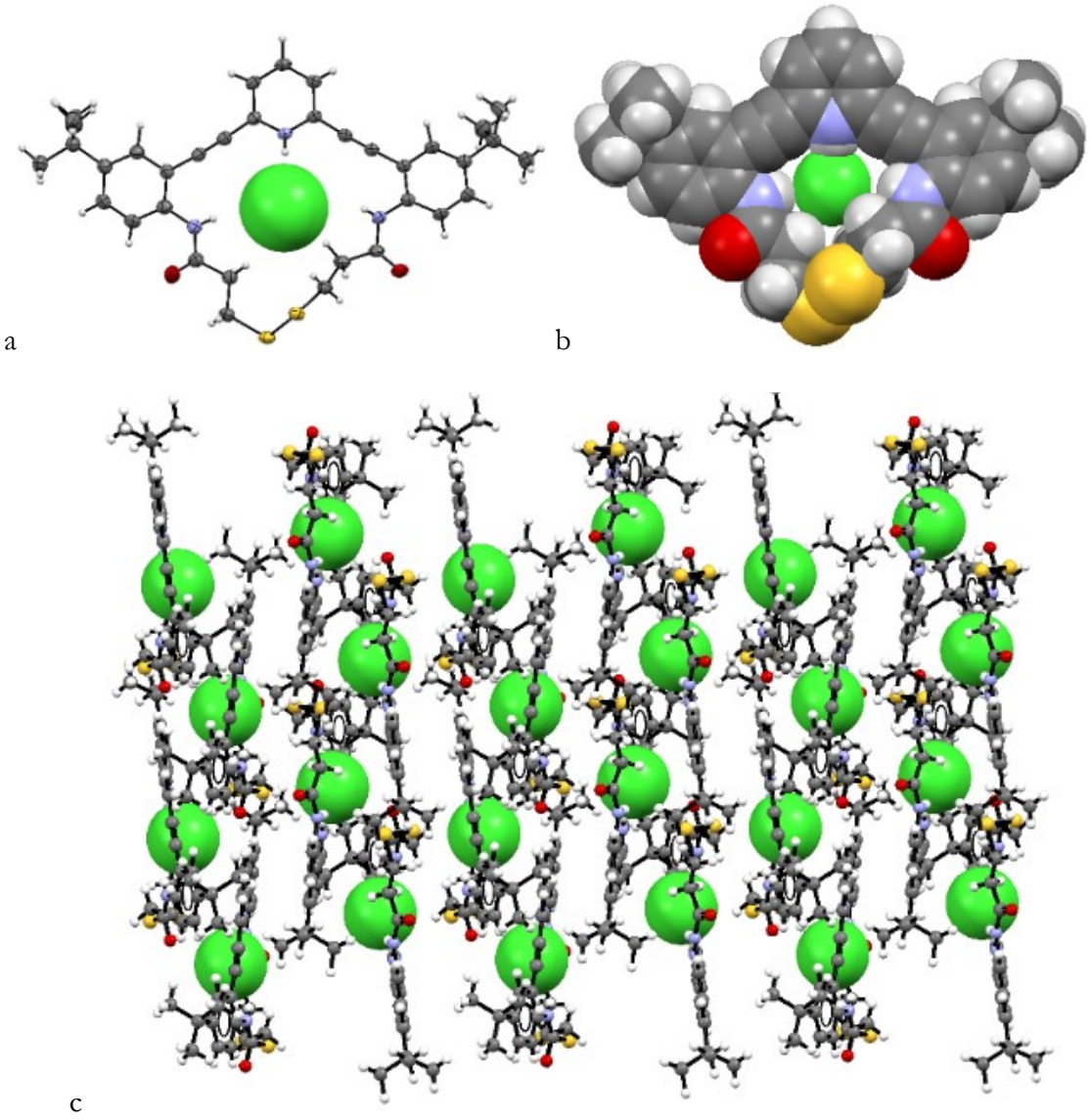

Figure 2.4. (a) ORTEP of **1b•HCl**, ellipsoids drawn at 50% probability. (b) Space-filling model of solid-state structure of **1b•HCl**, showing central cavity occupied with chloride guest. (c) Solid-state crystal packing of **1b•HCl**, host molecules drawn as ball-and-stick models, guest drawn in space-filling mode, exemplifying the brick-and-mortar type packing once the additional hydrogen-bond donor of water is no longer present. Solvent molecules (CH_2Cl_2) removed for clarity.

Interestingly, one of the α CH bonds also participated in the association with the anionic guest, which is not unheard of in the literature; [24,25] however, only one of the amide N-H bonds forms a short, linear contact with the chloride. The other amide N-H remained uninvolved in additional hydrogen bonds between host molecules (**Table 2.1**). Examination of the packing in the solid state demonstrated a CH-O hydrogen bond from the 4-position of the pyridinium to an amide oxygen of a neighboring molecule as the primary intermolecular contact (**Figure 2.4c**). Loss of the additional hydrogen-bond found in **1b•H_2O** resulted in a different packing motif, similar to brick-and-mortar type packing, as individual molecules were no longer held in 1D stacks via intermolecular hydrogen bonds.

As only one of the two amides participated as a good hydrogen bond donor, we reasoned that the macrocyclic cavity was a little too rigid with the spacer size that we had chosen. Host flexibility that allows the structure to fit the guest can be a beneficial design strategy, exemplified by induced fit molecular recognition seen principally in many biological systems. [26] We therefore examined more flexible macrocycle **1c** with an additional two carbons in the ring. Slow evaporation of a CH_2Cl_2/hexanes solution of **1c** provided diffraction quality crystals, allowing study of the binding cavity within the size-expanded host.

As before, adventitious H_2O was incorporated into the host cavity even though the crystallization was performed in hydrophobic solvents (**Figure 2.5**). This structure also appeared to fit H_2O quite well though the host is quite flexible with a $(CH_2)_3SS(CH_2)_3$ tether.

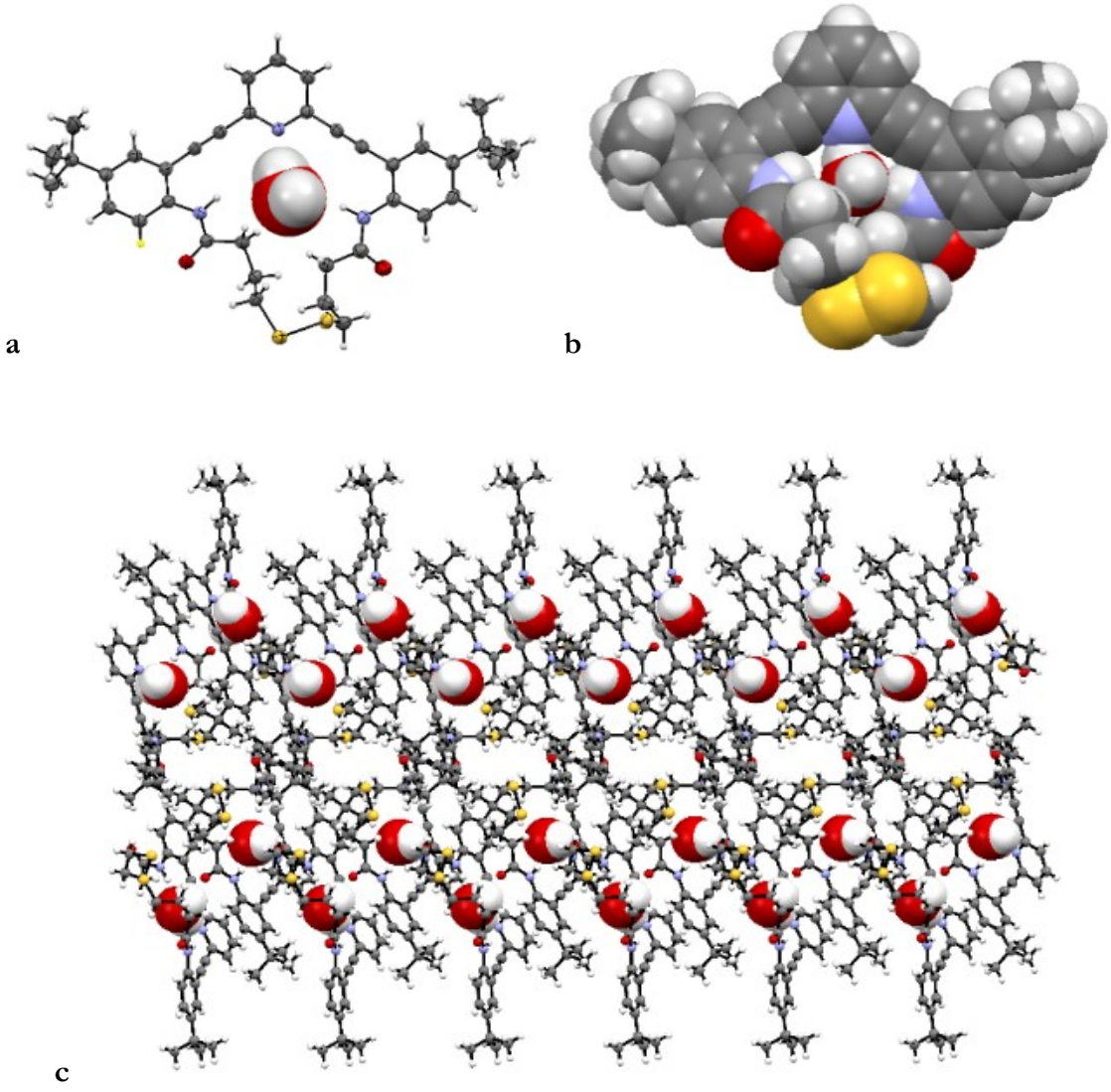

Figure 2.5. (a) ORTEP of **1c•H_2O**, ellipsoids drawn at 50% probability. (b) Space-filling model of solid-state structure of **1c•H_2O**, showing central cavity occupied with water guest. (c) Solid-state crystal packing of **1c•H_2O**, host molecules drawn as ball-and-stick models, guest drawn in space-filling mode, exemplifying the water-assisted intermolecular interactions.

Analogous to **1b•H_2O**, the solid-state structure of **1c•H_2O** is held together through H_2O donating a hydrogen bond to an amide oxygen of a neighboring molecule, forming 1D stacks in the crystal lattice (**Figure 2.5c**). Similar to the other structures, the water guest in **1c•H_2O** is slipped to one side, experiencing a hydrogen bond with only one amide N-H; however, unlike **1b•H_2O**, the remaining amide N-H stays directed within the cleft, and does not donate an additional hydrogen-bond to another molecule. This suggests promise for this macrocycle as an ideal host for chloride since it is large enough to allow all hydrogen-bond donors to comfortably direct into the center of the cavity, yet small enough to still exhibit selectivity for the smaller halides.

By employing similar conditions for the formation of the other HCl complexes, we obtained the solid-state structure of **1c•HCl**. The extra linker flexibility allowed the cavity to collapse slightly to fully encapsulate the chloride guest. This tether flexibility also resulted in the crystal structure having four crystallographically independent molecules in the unit cell, however, with slightly varying degrees of cavity size. One of the molecules, pictured in **Figure 2.6a-b**, demonstrated complete occupation of the cavity by chloride, with each amide N-H donating a hydrogen-bond to the same chloride in the pocket. Due to the flexibility of this linker size, however, there were two different binding modes in the same solid-state structure, with one demonstrating an ideal full coordination of chloride by three hydrogen-bond donors with support from α-CH donors, and another demonstrating only two internal N-H hydrogen bonds to a single chloride (**Table 2.1**).

Interestingly, this packing motif resulted in fairly close-spacing between the chloride atoms, with a closest distance of 4.035 Å, demonstrating effective charge screening by the pyridinium host, similar to previously observed dimers in sulfonamide-based hosts (**Figure 2.6c**). [10,19]

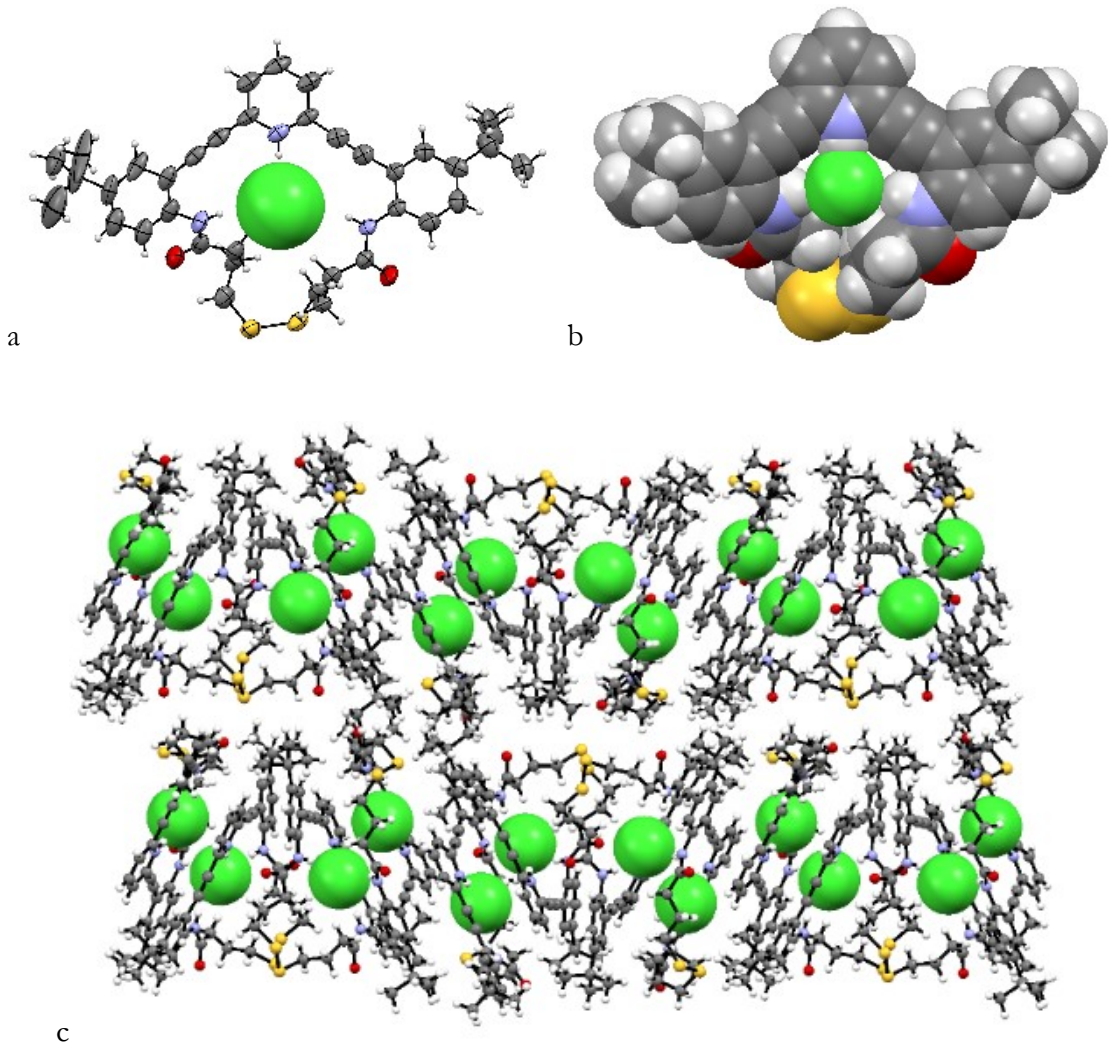

Figure 2.6. (a) ORTEP of **1c•HCl**, ellipsoids drawn at 50% probability. (b) Space-filling model of solid-state structure of **1c•HCl**, showing central cavity occupied with chloride guest. (c) Solid-state crystal packing of **1c•HCl**, host molecules drawn as ball-and-stick models, guest drawn in space-filling mode, exemplifying the alternate nature of the structure, where one molecule utilizes all three amide bonds in the cleft, and the next shares one with an additional molecule. Solvent molecules (CH_2Cl_2) removed for clarity.

This structure appears to demonstrate ideal chloride interactions, and as the flexibility seemed to be on the cusp of becoming detrimental, we elected not to pursue larger macrocycles. The packing differences in the solid state structure of the two macrocycles due to the small change of addition two methylene groups was intriguing, and indicated potential use in the solid-state.

Relevant bond lengths, bond angles, and structural features are given in **Table 2.1** to enable a full analysis of each structure's ability to act as a host. Examination of the data reveals several noteworthy trends. It is well known that RSSR functionalities are most stable at 90° dihedral angles;[27] however, among the various structures, only three are within 5° of that value. The smallest macrocycle (**1a**) shows one of the larger deviations from ideal (13.1°), while the larger macrocycles tend toward angles closer to 90°. While **1a** appears to have the most strained disulfide, it is additionally stabilized by the amide N-H. Forcing a guest into the macrocycle through protonation likely destabilizes the disulfide through loss of the N-H interactions, resulting in its decomposition. Neutral **1b•H_2O** is very close to the ideal disulfide dihedral angle, although upon protonation and inclusion of chloride, the

Entry	RSSR dihedral	Distance from guest to α-C	Distance from guest to pyridine N	Distance from guest to amide N	Angle between guest and α-CH	Angle between guest and pyridine N-H	Angle between guest and amide N-H
1b•H_2O	89.3	2.966, 3.249	2.966	3.010, 4.501	159.1, 135.6, 112.6, 24.0	159.1	164.1, 109.3
1b•HCl	103.4	2.956, 3.511	2.956	3.609, 3.961	175.4, 127.3, 126.7, 25.9	175.4	159.7, 142.9
1c•H_2O	93.3	2.833, 3.127	2.833	3.176, 3.818	170.4, 161.7, 107.6, 63.1	161.7	162.6, 135.4
1c•HCl	90.0	2.953, 3.513	2.953	3.341, 3.521	177.6, 148.7, 126.7, 86.2	177.6	166.3, 161.7
1a	76.9	n/a	n/a	n/a	n/a	n/a	n/a

Distances reported in Å; angles reported in °.

Table 2.1. Structural features derived from solid-state data

disulfide is forced to adopt a 13.4° shift from the ideal 90°, resulting in host strain. Expanded cycle **1c**, however, displays only a 3° deviation from 90° in the neutral state, and upon protonation, adopts the ideal angle upon encapsulation of a chloride atom. This again

demonstrates that **1c** is likely the best host size for a chloride atom, due to its increased stability upon binding the guest.

The participation of the α C-H atoms in the host-guest interaction demonstrated the utility of C-H bonds as hydrogen bond donors. Such an interaction is implicated as a major structural feature in the stabilization of tertiary structure in proteins.[24-25,28-29] Their participation was more involved in the neutral host-guest complexes, where the guest shifted to one side in the macrocycle cleft allowing extra stabilization from the C-H donor. In the ionic complexes, however, the protonated pyridinium is a much stronger hydrogen-bond donor, and as a result the chloride guest was held closer to the center of the macrocycle, resulting in smaller contribution of the significantly weaker amide α C-H hydrogen bond donors.

The amide N-H hydrogen bond donors, however, were strong participants in all of the determined structures. A similar effect to the interaction of the amide α C-H bonds was also seen, where in the neutral state the encapsulated water guest was shifted toward one side of the cavity, while in the protonated state the anionic guest was held in the center due to the strong pyridinium hydrogen-bond donor. As a result, the ionic complexes demonstrate central guest encapsulation, with the larger host **1c** demonstrating a perfectly central encapsulation of the chloride anion, with both N-H•••Cl contacts fairly close in distance.

All of these structural aspects indicate that **1c** has the best combination of sufficient flexibility to incorporate the chloride guest, while remaining rigid enough to support the binding pocket and avoiding the entropic cost of rigidifying a flexible scaffold. **1c** also exhibits the least strain in the disulfide upon protonation and incorporation of the anionic guest, it utilizes all three strong hydrogen-bond donors in stabilization of the guest, and it

incorporates some stabilization due to weak hydrogen-bonds from the neighboring α-CH groups.

Calculated Structures

With flexible hosts, the effects on molecular structure due to crystal-packing can be significant.[30–32] To examine these effects, we turned to computational models to scrutinise the structural features absent intermolecular interactions. A solvation model would be necessary for quantitative energetic determinations, for structural considerations and comparison to solid-state calculations performed in gas-phase are sufficient. Additionally, as these structures interact with solvent through hydrogen bond formation, an explicit solvent model would be required, which was beyond the scope of this cursory analysis.

This allowed us to explore the structure of **1a**-**1c** without encapsulated guest, which was not possible experimentally. Macrocycle **1a** demonstrated approximately the same conformation computationally as it did in solid-state (**Figure 2.7**); however, to fit a guest, the disulfide needed to invert its orientation. This transition is energetically unfavorable, as the disulfide must planarize, a transition state that in unhindered systems possesses a barrier of ~7.5 kcal mol^{-1}.[33] It is unsurprising, then, that this structure did not incorporate water into its solid-state structure. Computationally, **1b** has many of the same structural features determined crystallographically, with a few differences (**Figure 2.8**). In contrast to **1a**, **1b** did not exhibit any large changes in conformation upon incorporation of a guest. The computed structures exhibited a lesser tendency for the guest to occupy one side of the macrocycle compared to the solid state. In the case of water as a guest, this is likely due to water donating its additional hydrogen bond to neighbours in the solid-state.

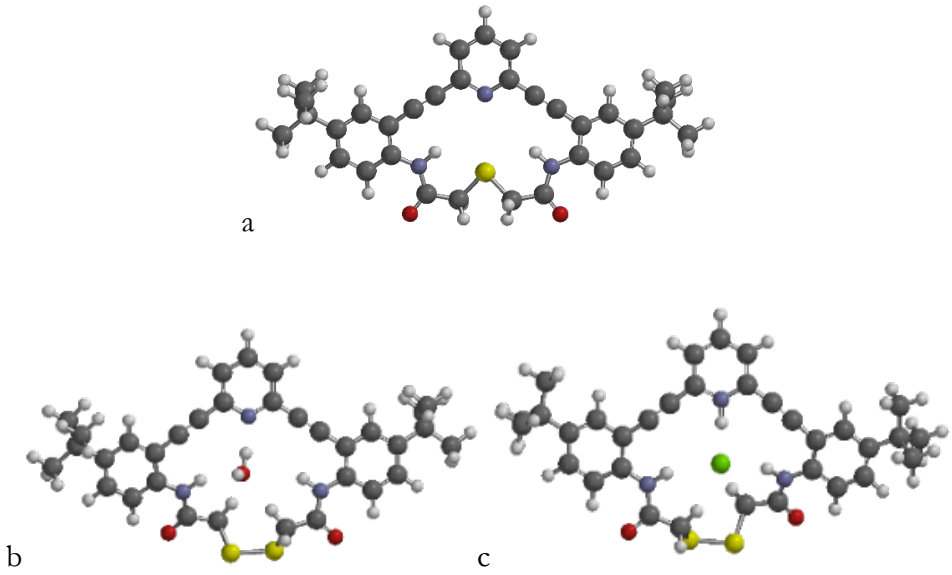

Figure 2.7. Calculated structures of **1a** (a), **1a•H₂O** (b), and **1a•**HCl (c).

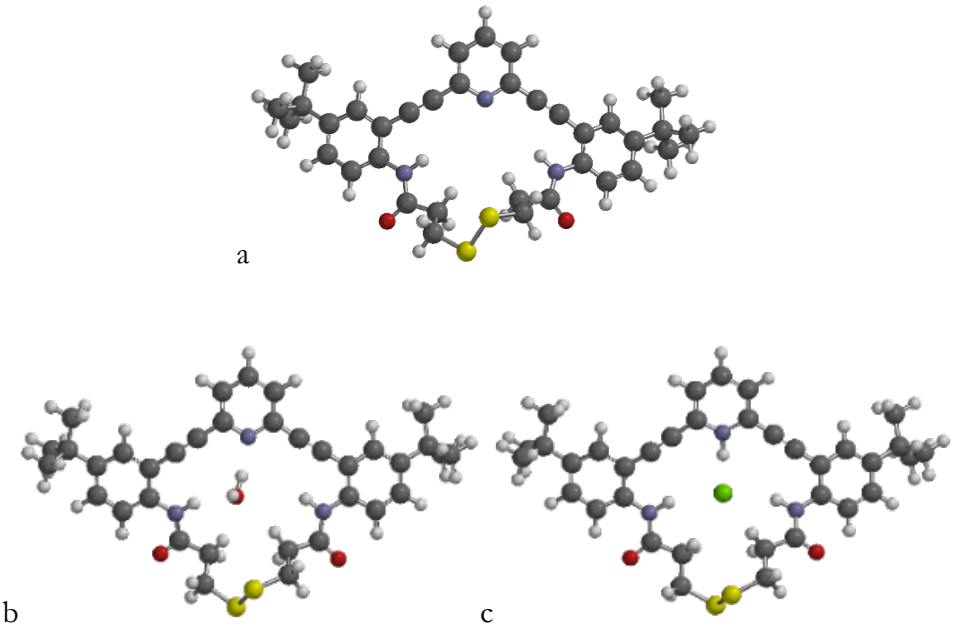

Figure 2.8. Calculated structures of **1b** (a), **1b•H₂O** (b), and **1b•HCl** (c).

Interestingly, α-CH participation in guest incorporation is more prevalent in solid-state structures than the computed structures. The disulphide dihedral angle in computed structures shows much more deviation in medium sized macrocycle **1b** compared to the solid-state, though it still indicates the same deviation from the ideal angle upon protonation and inclusion of chloride. It predicts the opposite trend for the disulphide bond in **1c** upon protonation, however, though it does indicate that the largest macrocycle is closest to ideal in both bound and unbound states (**Figure 2.9**, **Table 2.2**).

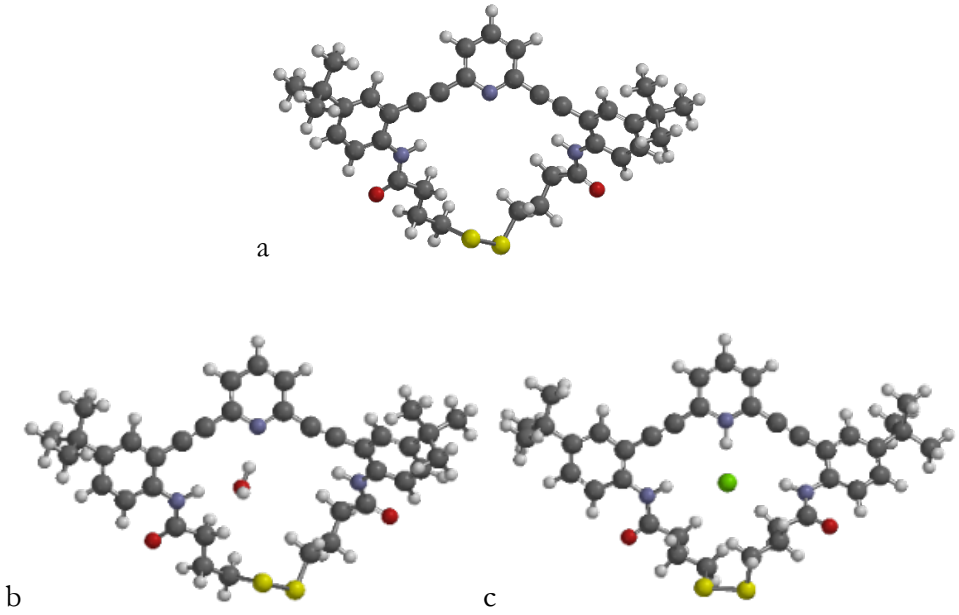

Figure 2.9. Calculated structures of **1c** (a), **1c•H_2O** (b), and **1c•HCl** (c).

Though there were some discrepancies between the calculated values and those derived from solid-state structures, overall they both indicated that the expanded macrocycles **1b** and **1c** act as excellent hosts for chloride in solution, and the solid-state structures are representative of the solution-state.

Entry	RSSR dihedral	Distance from guest to α-C	Distance from guest to pyridine N	Distance from guest to amide N	Angle between guest and α-CH	Angle between guest and pyridine N-H	Angle between guest and amide N-H
1a	83.4	n/a	n/a	n/a	n/a	n/a	n/a
1a•H_2O	85.8	3.248, 3.314	2.773	3.068, 3.807	175, 141, 52, 33	173	156, 150
1a•HCl	86.7	3.490, 3.575	2.950	3.425, 3.550	160, 149, 45, 38	174	160, 159
1b	114.2	n/a	n/a	n/a	n/a	n/a	n/a
1b•H_2O	115.2	3.283, 3.503	2.839	3.109, 4.172	160, 150, 70, 57	168	163, 148
1b•HCl	120.5	3.449, 3.497	2.950	3.502, 3.534	111, 109, 104, 102	178	160, 156
1c	86.5	n/a	n/a	n/a	n/a	n/a	n/a
1c•H_2O	89.8	3.305, 5.567	2.928	3.000, 5.430	132, 129, 77, 30	170	159, 141
1c•HCl	86.9	3.649, 3.702	2.958	3.725, 3.898	156, 141, 79, 43	178	161, 158

[a] Distances reported in Å.; angles reported in °, calculations performed at B3LYP, 6-31* level of theory.

Table 2.2. Structural features derived in silico

Spectroscopic Properties – Solution State

Our group has worked extensively with aryl-ethynyl scaffolds as structural directors for both definition of the binding pocket and providing a conjugated system for photoluminescent sensing applications. Thus, we then proceeded to determine any differences in the absorption/emission spectra based upon guest inclusion in the differing sized macrocycles. An overlaid fluorescence spectrum of all three macrocycles at the same concentration in the neutral and protonated states is shown in **Figure 2.10**.

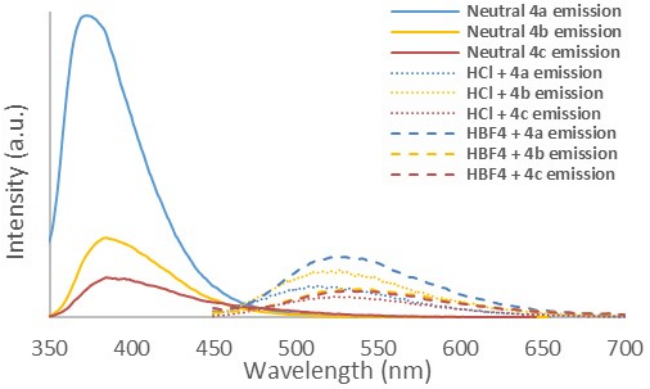

Figure 2.10. Emission spectra of equimolar solutions of **1a**-c in $CHCl_3$, neutral and in the presence of HCl and HBF_4, demonstrating the difference in emission intensities as a function of added anion.

All of the macrocycles are fluorescent in the neutral state; **1a** has an emission band at 370 nm, while both **1b** and **1c** possess slightly red-shifted emission maxima, emitting at 383 nm. This red-shifting as linker length increases indicates greater planarity of the conjugated scaffold upon increasing the macrocycle's size, which increases the efficiency of charge transfer between the electron poor pyridine in the center and the two appended acetanilide rings. The intensity of fluorescence emitted by **1a**, however, is much greater than for **1b** and **1c**, which is expected due to the rigid nature of the scaffold helping to inhibit non-radiative vibrational relaxation pathways.

When dry HCl gas is bubbled through the solutions of macrocycles **1a-c**, the fluorescence emission red-shifts to ca. 530 nm, indicating facile protonation of the pyridyl subunit. This dramatic change in emission wavelength is representative of greater charge transfer between the now positively-charged pyridinium ring and the acetanilide rings. The red-shifting of the fluorescent emission as due to pyridine protonation was reflected in the protonation of the macrocycle by HBF_4 as well, which demonstrated that the emissive properties were due mainly to the protonation event, and not from host-guest complexation.

As expected, the fluorescence of the macrocycle significantly quenches upon protonation. Interestingly, the quenching behaviour is reflected not only in the HCl salt, as would be expected due to the propensity for halides to diminish fluorescence due to collisional quenching, but also in the presence of HBF_4, indicating that the pyridinium is the likely culprit for the quenching behaviour. The percent decrease in emission intensity of the macrocycle upon addition of HCl is much less in the larger members of the family compared to the smallest member, **1a**. This phenomenon is likely due to the preferential coordination of chloride within the cavities of the larger molecules, which prevents inter-system crossing

(ISC) by collision with the host's π-system (collisional quenching is typically encountered in the presence of halides).

This reduced quenching behaviour in the larger systems indicates that the macrocycles are likely hosting chloride in the binding pocket more efficiently than is the smallest member. A smaller difference in quenching proficiency than would be expected due to the anion in solution was also seen in the larger macrocyclic hosts reported by our group.[11] Interestingly, when the macrocycles are protonated with an acid with a non-coordinating counter ion (BF_4^- typically has a lower quenching proficiency than other anions), the fluorescence is quenched to almost the same degree as the neutral macrocyclic species. This suggests that protonation of all three macrocyclic hosts, rather than the nature of the guest, plays the predominant role in fluorescence quenching in solution.

Solution State Anion Binding

Examination of the structural features of each macrocycle in the solid state and gas-phase indicated the potential for these cycles to act as excellent hosts for chloride. We attempted to determine the binding constant of chloride for both **1b** and **1c**, ignoring the use of **1a** for solution state determinations due to its inherent instability in the protonated state. To start with the protonated host, acids with non-coordinating counter ions were explored, using either trifluoroacetic acid (TFA) or tetrafluoroboric acid (HBF_4) to protonate the receptor. Initial determinations of the association constant (K_a) between either **1b•HBF$_4$** or **1b•TFA** and tetrabutylammonium chloride (TBACl) in water-saturated $CDCl_3$ via NMR titrations revealed a K_a much too large to determine via this method.[34] As this association constant was $>>10^6$ M^{-1}, we altered tactics twofold, by changing to a determination via

UV/Vis spectroscopy the concentration could be reduced by orders of magnitude, and by changing the solvent to a more competitive one, MeCN, K_a could be dampened.

We were then able to measure association constants for the macrocycle **1b•TFA** in MeCN/15% H_2O. The best fit model for the association in solution was as a 2:1 H:G complex, with $K_{11}=10\ M^{-1}$, and $K_{21}=1x10^{10}$ for association constants. We were pleased to see such a large association constant even for a dimeric complex, however, the macrocycles were poorly behaved in aqueous solutions, and their performance changed over time suggesting that disulphide shuffling occurred and higher order oligomers were being formed. This complicated determination of association constants and acquisition of reliable solution state data, thus this route for the exploration of their performance as anionophores was not pursued further.

Although these macrocycles demonstrated little sensing behaviour for chloride in the solution state, they still performed as excellent anionophores in solution. However, there were some intriguing features in the solid state for these macrocycles and the alignment of the conjugated scaffold depending on the presence or absence of an anionic guest. We thus decided to examine the spectroscopic behaviour of these compounds in the solid state.

Spectroscopic Properties – Solid State

The macrocycles exhibited a stark difference in their emissive properties in the solid-state upon both protonation and inclusion of different guests. Compounds **1b** and **1c**, when dissolved in CH_2Cl_2 and dropcast onto glass slides, displayed slightly red-shifted fluorescence compared to the solution state, as is typical for fluorophores; however, when the solid films were dipped into a 10% aqueous TFA solution, the compounds exhibited a red-shifted emission. When the neutral films were treated with HCl, interestingly, an enhancement of

the emission was displayed, along with a different emission wavelength between the different sized macrocycles (**Figures 2.11, 2.13**).

a 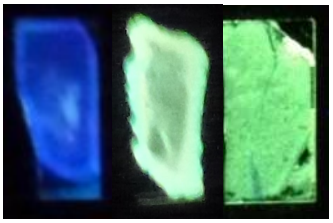 b 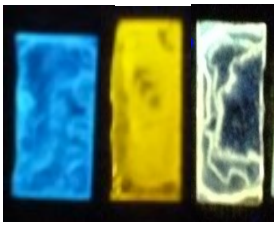

Figure 2.11. Demonstration of emission change of (a) **1b** and (b) **1c** in the solid state as a film on glass slides. For each set of slides, the conditions are as follows: Left, neutral compound film. Middle, neutral compound film exposed to HCl vapours. Right, neutral compound film exposed to TFA vapours.

This was an intriguing result, especially since there was practically no difference in emission between the macrocyclic species in the solution state. This difference in emission must solely be due to the intermolecular interactions in the solid-state, as **1b•**HCl and **1c•**HCl demonstrated dramatically different solid-state structures.

The crystal structures indicate a difference in the closest contact between the electron-rich and electron-poor portions of the conjugated backbone. The macrocycle **1c**, upon protonation and incorporation of chloride, arranges to form close contacts between the pyridinium and acetanilide rings, while **1b** arranges with the alkyl functionality acting as spacers between iterations of the conjugated scaffold so that there are no close contacts between conjugated portions of differing electron density, only close contacts between the pyridine/pyridinium (**Figure 2.12**). The closest non-bonding contact between pyridinium rings and acetanilide rings in **1c** is 3.501 Å, allowing for excitation transfer between

molecules in the solid state, resulting in a more dramatically red-shifted emission compared to **1b**.

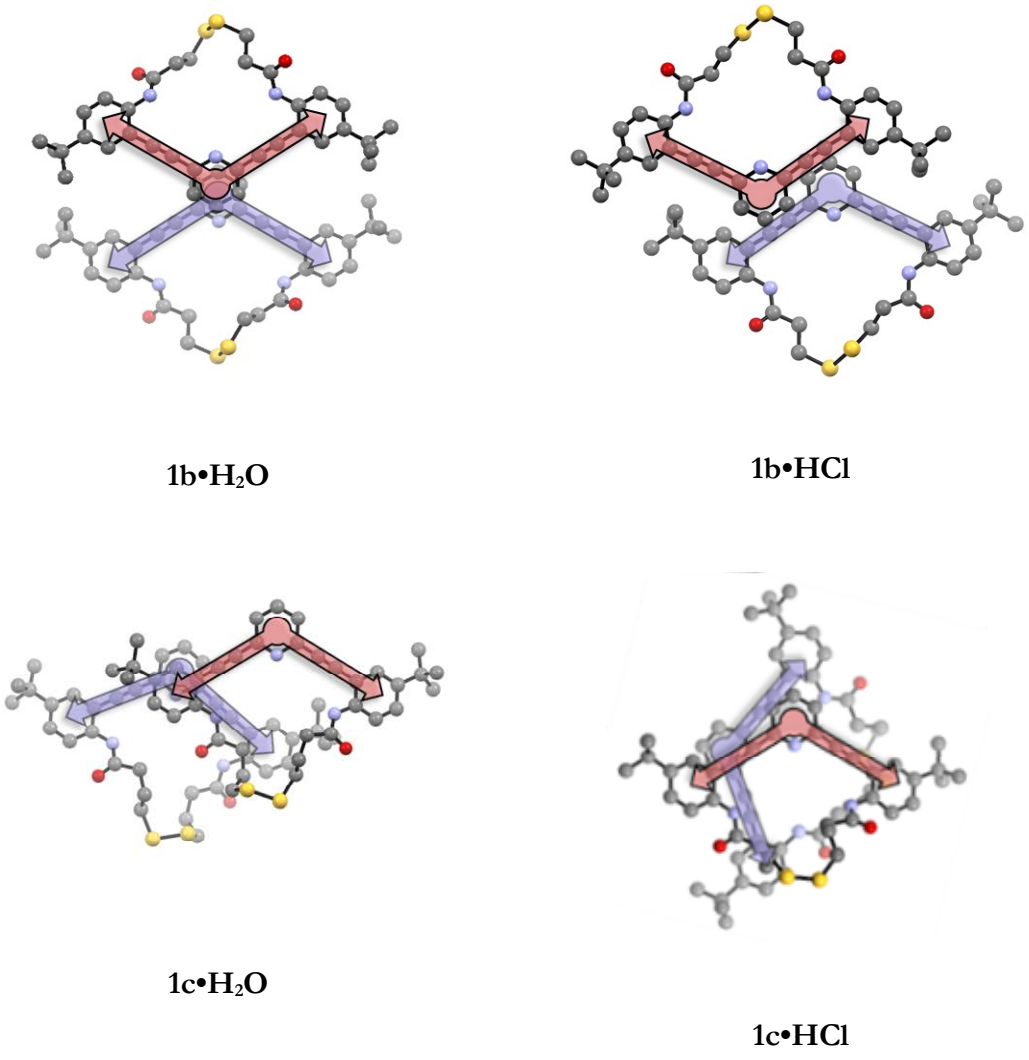

Figure 2.12. Illustration demonstrating the differing alignments of π-stacked dimers in the solid state structures of **1b** (top) and **1c** (bottom). Hydrogen atoms, solvent molecules, and encapsulated guests omitted for clarity, models shown as ball and stick. The two degenerate transition dipole moment vectors are shown for the two molecules in each dimer, with the two sets of vectors coloured red and blue as a visual aid to see their alignment.

This is schematically similar to the formation of J-aggregates and H-aggregates.[35,36] In the bis(2-ethynylacetanilido)pyridine scaffold there are two degenerate first excited states, each corresponding to transfer of electron density to the central pyridine/pyridinium from the acetanilide ring. As a result, the overall transition dipole moment of the fluorophore backbone can be viewed as two separate vectors, originating in the pyridine and terminating in the centroid of each of the acetanilide rings. For each of the macrocycle solid state structures, the scaffolds crystallized as π-stacked dimers. However, in both **1b•H_2O** and **1b•**HCl, the dimers stacked in such a way that the transition dipole moments are all anti-parallel, resulting in only minor wavelength shifts in the solid-state as compared to the solution state. Thus, in the solid state, this compound displays some characteristics of H-aggregates.

In **1c•H_2O** and **1c•HCl**, however, the solid state demonstrates a partially parallel alignment between transition moment dipole vectors. This is indicative of J-aggregate dimer formation in the solid-state. This is exemplified by red-shifted emission in the solid-state compared to solution state, and somewhat sharp emission bands. As these are amorphous thin-films, neither macrocycle demonstrates perfect J-aggregate or H-aggregate formation and spectral behaviours when cast. However, the dominant spectral changes due to these aggregate formations still occur.

This response proved to be specific for chloride, due to the need for a small, spherical guest to allow for this crystal packing motif. The response due to TFA was not as intense of an emission change, and the brightness of the film upon incorporation of chloride guest was much more intense than that formed upon treatment with TFA (**Figure 2.13**).

a 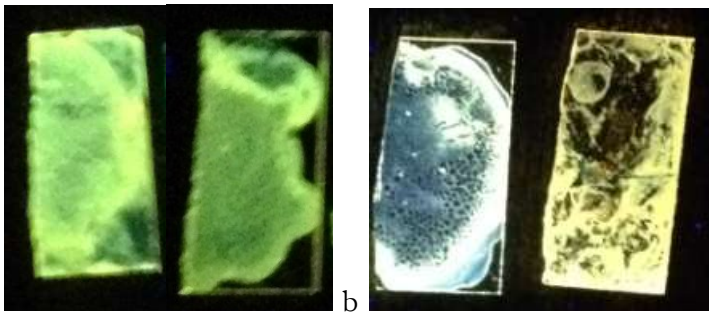 b

Figure 2.13. Demonstration of emission change of (a) **4b** and (b) **4c** in the solid state as a film on glass slides upon exposure to anions. A film cast of the neutral species was exposed to TFA vapour for 10 seconds (a,b), left), then soaked in a saturated solution of KCl for 1 hour, with only **4c** showing a spectral change from soaking (b), right).

This demonstrated a novel sensing method, where the change in solid-state interactions due to incorporation of a specific guest results in a measurable spectroscopic change. To explore this as an applicable sensor for chloride, the neutral film was exposed to TFA to form the protonated species. Then, this film was dipped into a 2M aqueous solution of KCl. Upon exposure to this solution for one hour, the change in emission due to chloride incorporation was apparent. Interestingly, performing the same test with a 2M solution of KBr resulted no spectroscopic change compared to that seen with chloride, demonstrating the sensitivity of emission of the solid films toward the nature of the anionic guest. Our laboratory is exploring the use of this mechanism for quantitation of anions in solution as a test strip. The same change in spectral properties demonstrated in **Figure 2.11** and **2.10** is demonstrated through the fluorescence spectra of the thin films (**Figure 2.14**). It should be noted that the peak for **1c•TFA** after soaking in KCl solution does not redshift quite as far as does the peak for the cast **1c•HCl** film. This is likely due to incomplete incorporation of

chloride within the films, as the peak of the film's emission possesses a shoulder that extends to 450 nm, representative of remaining **1c•TFA** in the film.

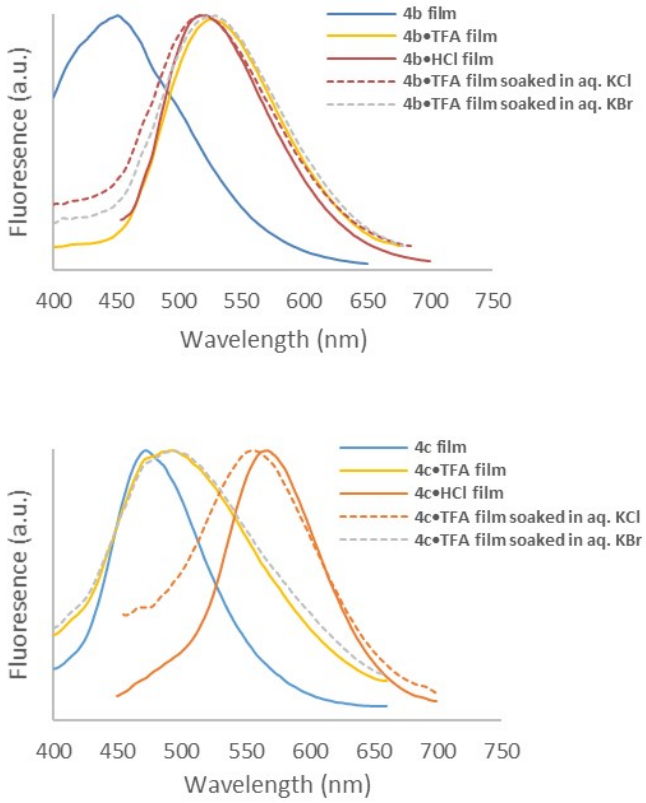

Figure 2.14. Fluorescent emission of macrocycle films (**1b**, top, **1c**, bottom) and their response to acids and anionic analytes. Films prepared by drop casting 1mL of a 1 mg/mL solution of macrocycle in dichloromethane on glass slide. To obtain protonated films, neutral cast films were exposed to vapours of relevant acid.

Noteworthy is the lack of a spectroscopic response of **1c** films in the solid state in the presence of bromide as opposed to chloride. The structural arrangements resulting in the dramatic red shift were not amenable to the larger size of bromide as opposed to chloride, lending halide selectivity through the solid-state structure. Though there are a number of notable examples in the literature of solid-state anion sensors using either thin films or

anionophores loaded onto a solid support,[37–43] to the best of our knowledge this is the first example of a solid state spectroscopic anion sensing mechanism that is selective for chloride over bromide.

CONCLUSION

In summary, a family of fluorescent disulfide-based macrocycles was synthesized using the facile disulfide bond formation as a mechanism for macrocyclization. This allowed for the formation of large rings with a high yield atypical for macrocycle formation. The solid-state structures of the neutral forms, which acted as hosts for water, were determined alongside their complexes with HCl. The structural features were contrasted with calculated structures, demonstrating the differences in the solid state compared to those in a vacuum. These fluorescent hosts, though they did not display differing emission upon complexation in the solution state, displayed a novel difference in the solid state based upon guest incorporation. The solid films are being investigated as a solid state sensor for halides, and demonstrated proficiency in the application as a potential dipstick test for the presence of chloride.

EXPERIMENTAL

Synthesis of Compounds 3a-c

General Amide Synthesis. The appropriate acid chloride (5 equiv.) was added to a solution of 2 (100 mg, 0.237 mmol) in dry THF (10 mL). The reaction was allowed to stir for 1 h at 25 °C before being quenched with MeOH (15 mL). The volatiles were removed *in vacuo* and

filtration of the crude solid through a 3 inch silica plug (1:1 hexanes:EtOAc) afforded the desired product.

3a – See reference 2 for synthesis and characterization.

3b – 90% yield. ^{1}H NMR (500 MHz, $CDCl_3$) δ 8.31 (d, *J* = 8.6 Hz, 2H), 8.09 (s, 2H), 7.77 (t, *J* = 7.9 Hz, 1H), 7.59 (d, *J* = 1.8 Hz, 2H), 7.54 (d, *J* = 7.8 Hz, 2H), 7.45 (dd, *J* = 8.8, 2.2 Hz, 2H), 3.91 (t, *J* = 6.4 Hz, 4H), 2.94 (t, *J* = 6.4 Hz, 4H), 1.32 (s, 18H). ^{13}C NMR (126 MHz, $CDCl_3$) δ 167.92, 147.13, 143.46, 137.09, 136.86, 129.33, 128.19, 126.63, 120.15, 110.82, 94.44, 85.87, 40.88, 39.98, 34.59, 31.33. HRMS (EI+) calcd for $C_{35}H_{38}N_3O_2Cl_2$ [MH^+]: 602.2342, found 602.2355.

3c – 97% yield. ^{1}H NMR (500 MHz,$CDCl_3$) δ 8.28 (d, *J* = 8.8 Hz, 2H), 8.04 (s, 2H), 7.76 (t, *J* = 7.8 Hz, 1H), 7.58 (d, *J* = 2.4 Hz, 2H), 7.54 (d, *J* = 7.8 Hz, 2H), 7.43 (dd, *J* = 8.8, 2.4 Hz, 2H), 3.67 (t, *J* = 6.2 Hz, 4H), 2.67 (t, *J* = 7.1 Hz, 4H), 2.23 (p, *J* = 6.7 Hz, 4H), 1.31 (s, 18H).^{13}C NMR (126 MHz, $CDCl_3$) δ 170.14, 146.89, 143.50, 137.04, 137.00, 129.30, 128.15, 126.63, 119.93, 110.68, 94.46, 85.77, 44.53, 34.58, 34.56, 31.33, 28.21. HRMS (EI+) calcd for $C_{37}H_{42}N_3O_2Cl_2$ [MH^+]: 630.2654, found 630.2667.

Synthesis of Compounds 4a-c

General Thioacetate Synthesis. Potassium thioacetate (5 equiv.) was added to a solution of 2a-c (0.2157 mmol) in anhydrous DMF (10 mL). After stirring for 4 h at rt, the reaction was quenched with saturated aqueous NH_4Cl soln (20 mL). The reaction mixture was extracted with EtOAc (40 mL), washed with brine (3 x 30mL), dried ($MgSO_4$) and filtered. The volatiles were removed *in vacuo* and filtration of the crude solid through a 3 inch silica plug (3:1 hexanes: EtOAc) afforded the desired product as an orange solid.

4a – See reference 2 for synthesis and characterization.

4b – 85% yield. ^{1}H NMR (500 MHz, $CDCl_3$) δ 8.27 (d, *J* = 8.6 Hz, 2H), 8.09 (s, 2H), 7.74 (t, *J* = 7.8 Hz, 1H), 7.58 (d, *J* = 2.1 Hz, 2H), 7.54 (d, *J* = 7.8 Hz, 2H), 7.42 (dd, *J* = 8.8, 2.3 Hz, 2H), 3.23 (t, *J* = 6.9 Hz, 4H), 2.79 (t, *J* = 6.9 Hz, 4H), 2.25 (s, 6H), 1.30 (s, 18H). ^{13}C NMR (126 MHz, $CDCl_3$) δ 196.18, 169.19, 146.94, 143.52, 136.99, 136.93, 129.36, 128.14, 126.69, 120.10, 110.82, 94.46, 85.79, 37.66, 34.57, 31.34, 30.70, 25.07. HRMS (EI+) calcd for $C_{39}H_{44}N_3O_4S_2$ [MH^+]: 682.2773, found 682.2770.

4c – 88% yield**.** ^{1}H NMR (500 MHz, $CDCl_3$) δ 8.28 (d, *J* = 8.7 Hz, 2H), 7.98 (s, 2H), 7.79 (t, *J* = 7.8 Hz, 1H), 7.58 (d, *J* = 1.9 Hz, 2H), 7.55 (d, *J* = 7.8 Hz, 2H), 7.43 (dd, *J* = 8.8, 2.2 Hz, 2H), 2.99 (t, *J* = 7.1 Hz, 4H), 2.54 (t, *J* = 7.3 Hz, 4H), 2.27 (s, 6H), 2.06 (p, *J* = 7.2 Hz, 4H), 1.31 (s, 18H).^{13}C NMR (126 MHz, $CDCl_3$) δ 195.83, 170.29, 146.83, 143.63, 137.04, 136.99, 129.30, 128.17, 126.68, 119.99, 110.68, 94.48, 85.83, 36.51, 34.56, 31.34, 30.73, 28.56, 25.67. HRMS (EI+) calcd for $C_{41}H_{48}N_3O_4S_2$ [MH^+]: 710.3086, found 710.3112.

Synthesis of Compounds 1a-c

General Thioacetate Deprotection & Subsequent Disulfide Formation. To a stirred solution of 3a-c (0.18 mmol) in rigorously degassed MeOH (120 mL) was added K_2CO_3 (5 equiv.) under an N_2 atmosphere. After stirring for 1 h at rt, a N_2-degassed solution of 20% aqueous NH_4Cl solution (120 mL) was cannula transferred into the flask under inert conditions to precipitate the intermediate thiol. The solid was collected and washed thoroughly with deionized water, dried, and immediately dissolved in CH_2Cl_2 (1.7 mM). Iodine was then added until iodine coloration remained. The reaction was quenched with 10% Na_2SO_3 (15 mL), washed with brine soln (2 x 30 mL), and dried over $MgSO_4$. The volatiles were removed *in vacuo* and the crude product purified via flash chromatography (3:1 hexanes:EtOAc) affording the desired product. Further purification by preparative HPLC

with a gel permeation column was sometimes needed to remove trace oligomers and small polymers.

1a – 77% yield. ^{1}H NMR (500 MHz, DMSO-d6) δ 9.80 (s, 2H), 8.14 (d, *J* = 8.4 Hz, 2H), 7.97 (t, *J* = 7.8 Hz, 1H), 7.73 (d, *J* = 7.8 Hz, 2H), 7.65 (d, *J* = 2.3 Hz, 2H), 7.56 (dd, *J* = 8.9, 2.4 Hz, 2H), 3.91 (s, 4H), 1.32 (s, 18H). ^{13}C NMR (126 MHz, DMSO-d6) δ 166.76, 147.31, 143.00, 137.54, 129.04, 129.02, 128.38, 126.65, 120.58, 112.11, 95.22, 84.86, 41.74, 34.70, 31.41. HRMS (EI+) calcd for $C_{33}H_{34}N_3O_2S_2$ [MH^+]: 568.2092, found 568.2077.

1b – 68% yield. ^{1}H NMR (500 MHz, $CDCl_3$) δ 8.43 (s, 2H), 8.27 (d, *J* = 8.6 Hz, 2H), 7.75 (t, *J* = 7.8 Hz, 1H), 7.58–7.49 (m, 4H), 7.44 (dd, *J* = 8.6, 2.2 Hz, 2H), 3.09 (t, *J* = 7.2 Hz, 4H), 2.97 (t, *J* = 7.0 Hz, 4H), 1.33 (s, 18H). ^{13}C NMR (126 MHz, $CDCl_3$) δ 169.49, 146.92, 143.21, 137.24, 137.18, 129.00, 128.30, 126.58, 120.39, 110.81, 94.27, 86.33, 37.49, 34.54, 33.67, 31.33. HRMS (EI+) calcd for $C_{35}H_{38}N_3O_2S_2$ [MH^+]: 596.2405, found 596.2415.

1c – 59% yield. ^{1}H NMR (500 MHz, $CDCl_3$) δ 8.30 (d, *J* = 8.7 Hz, 2H), 8.19 (s, 2H), 7.76 (t, *J* = 7.8 Hz, 1H), 7.56 (d, *J* = 7.8 Hz, 2H), 7.54 (d, *J* = 2.0 Hz, 2H), 7.43 (dd, *J* = 8.8, 2.3 Hz, 2H), 2.78 (t, *J* = 6.6 Hz, 4H), 2.64 (t, *J* = 6.8 Hz, 4H), 2.17 (q, *J* = 6.8 Hz, 4H), 1.32 (s, 18H). ^{13}C NMR (126 MHz, $CDCl_3$) δ 170.81, 146.69, 143.43, 137.15, 136.93, 129.05, 128.12, 127.03, 119.96, 110.65, 94.25, 85.91, 37.91, 35.79, 34.51, 31.32, 24.79. HRMS (EI+) calcd for $C_{37}H_{42}N_3O_2S_2$ [MH^+]: 624.2718, found 624.2747.

BRIDGE TO CHAPTER III

In this chapter we explored the facile macrocyclization reaction through the formation of a disulfide linkage to enable a high-yielding synthesis of a family of macrocyclic

anionophores. While these inherently fluorescent anion hosts did not display any spectroscopic detection selectivity in the solution state, they did display an intriguing electivity for chloride over bromide in the solid state, for only one of the macrocycles. This demonstrates the power of solid-state packing in sensor design, as the two macrocycles have widely differing spectral behaviors in thin films, though their structure differs by only two carbon atoms.

In Chapter III, this same facile macrocyclization is instead employed to spectroscopically detect the change in oxidation state of the disulfide linkage. Due to its high tendency to form intramolecular cycles, it preferentially closes the macrocycle opposed to polymerization, and thus can be used in the detection of redox poise of mixed thiol-disulfide systems. We then continue to explore methods of measurement of the redox potentials of disulfide bonds, enabling the use of electrochemistry to quickly determine the disulfide reduction potential, as opposed to the often time-consuming equilibration type measurements.

CHAPTER III

ELECTROCHEMICAL DETERMINATION OF DISULFIDE REDOX POTENTIALS: A CORRELATED STUDY RELATING IRREVERSIBLE NON-NERNSTIAN TWO-ELECTRON PROCESSES TO STANDARD DISULFIDE REDOX POTENTIALS

This chapter is prepared for publication with coauthors Calden N. Carroll, Daisuke Inokuchi, Lev N. Zakharov, Michael M. Haley and Darren W. Johnson. Drs. Carroll and Inokuchi initiated the studies into this area, while I performed the majority of the synthetic and analytical investigations. Dr. Zakharov provided crystallographic support, and professors Haley and Johnson provided editorial support and research directions. This chapter is formatted for submission to an ACS journal.

INTRODUCTION

Within cells aerobic respiration, derived from reduction of oxygen to water, generates reactive oxygen species (ROS) as byproducts. These ROS, if unmanaged, have detrimental effects on internal cellular processes by degrading proteins, lipids, and nucleic acids alike.[1] This degradation is implicated in many diseases where age is a major factor.[2,3] Due to the ubiquitous nature of redox agents in living systems, the study of redox processes

is integral to our understanding of cellular processes as a whole. Toward this end, fluorescent imaging with redox sensors is a powerful tool to visualize fluctuations in redox poise. Most reversible fluorescent sensors employed to visualize redox potentials have been protein or peptide based,[4-5] though a few small molecules capable of reversibly changing their fluorescence profile in response to a redox potential change have been produced.[6-7] However, full sensor characterization, such as determination of redox potential response, is typically not performed. A full suite of fluorescent sensors have been developed to detect the presence of individual ROSs such as hydrogen peroxide (H_2O_2), peroxynitrite (ONOO-), superoxide (O_2^-), or hypochlorite (^-OCl).[8] Though these sensors all show distinct changes with respect to the various ROSs, their major drawback is irreversibility of the sensing event. It has been suggested that one of the great contributions of supramolecular chemistry to sensing is the reversibility of its binding events; this is shown through macrocycles such as the crown ethers and cryptands for chelation of cations,[9] or katapinands for binding anions.[10] Sadly, due to inherent reactivities and short lifespans in the biological milieu, the use of such sensing motifs for ROSs is not feasible.

However, the cell's redox system (the glutathione/glutathione-disulfide redox couple) is driven through the reversible formation of a disulfide bond. If a sensor can be designed which participates in the native redox systems to yield a reversible change, then a probe for redox poise can be developed that benefits from the reversibility provided by supramolecular sensors without the need to directly interact with ROS. We demonstrate the synthesis, redox characterization, and reversible sensing behavior of a fluorescent small molecule based on dithiol/disulfide equilibria.

RESULTS/DISCUSSION

The aryl-ethynyl pyridine framework 1 has been used extensively as a rigid, fluorescent scaffold for sensing different analytes.[11–22] In this instance, a thiol containing group was appended to the aryl-ethynyl core (**Scheme 3.1**); the dithiol/disulfide redox couple is utilized in biological systems as the native redox management system, so its use within a synthetic sensor to probe said systems is a logical choice. Addition of α-halo acid halides to **1** furnished substituted amides **2a-d**. Substitution of the halide with potassium thioacetate yielded the masked thiols **3a-c**, which were revealed under basic conditions to give the desired sensors **4a-c** in 52-56% yield from **1**.

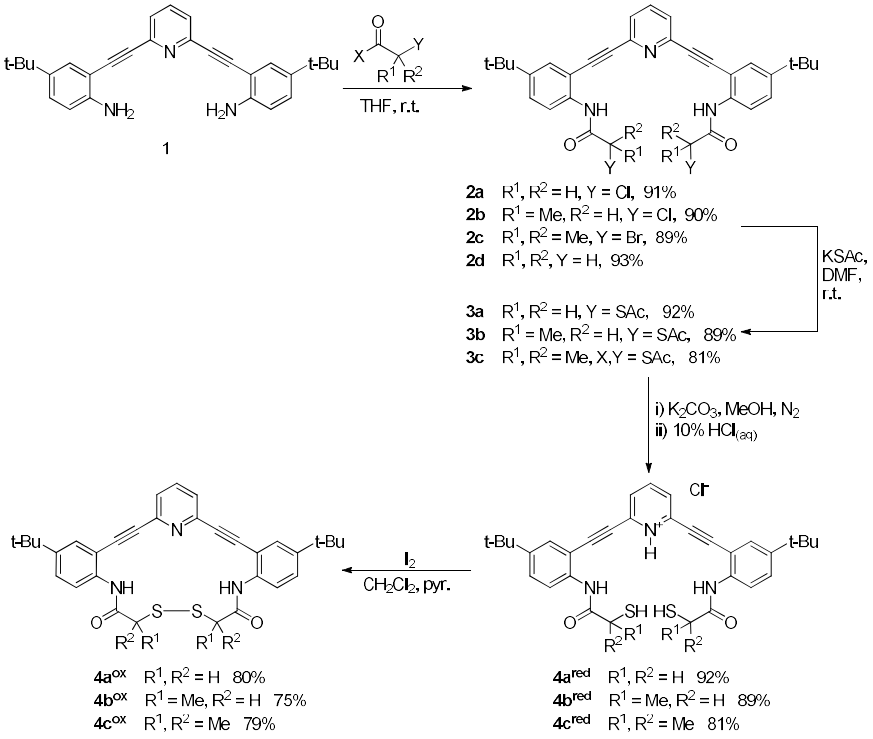

Scheme 3.1. Synthesis of sensors **4a-c**

Compounds **4a-c** are isolated as the dithiol if the deprotection is performed under rigorous air-free conditions and quenched with degassed aq. HCl to isolate the dithiol HCl

salt; reactions performed under ambient atmosphere result in thiolate oxidation to the disulfide. Except for the most sterically hindered **4c**, the dithiols could not be reliably isolated as the pure freebase under ambient atmosphere due to autooxidation. Interestingly, few polymeric byproducts are observed in the iodine oxidation step unless the reaction is performed at high concentrations. The tendency for preorganized cyclic dithiols to deter polymer formation is known for simpler dithiols, our rigid scaffold allows preferential monomer formation upon oxidation.[23] This is seen in the larger macrocyclic members of this family of compounds as well, as utilized in Chapter II.

The disulfide and dithiol forms of the sensor molecules display similar emission wavelengths, though the fluorescence emission intensity of the redox couple differ significantly. We noted a distinct quenching of the fluorescence in the oxidized state, compared to the reduced state, lending credence to sensing applications. (**Figure 3.1**)

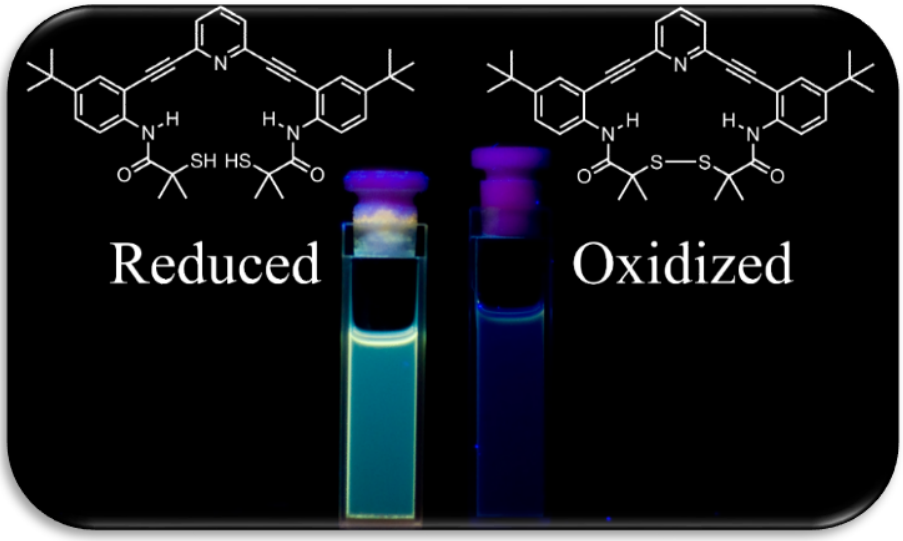

Figure 3.1. Demonstration of differing emission of the reduced and oxidized forms of compound **4c**; Visual demonstration of a solution of **4c**^{ox} (right) and **4c**^{red} (left) when excited by a handheld UV lamp.

Once we determined that our scaffold could act as a sensor for redox potential, we turned to quantitation of the redox potentials. Though there are a fair number of redox sensors in the literature, the number that are reversible are few,[8,28–33] and the number that have quantified redox potentials are limited to those based on polypeptides or proteins. There are few methods for determination of redox potentials of organic molecules, but the most frequently employed is cyclic voltammetry. (**Figure 3.2**)

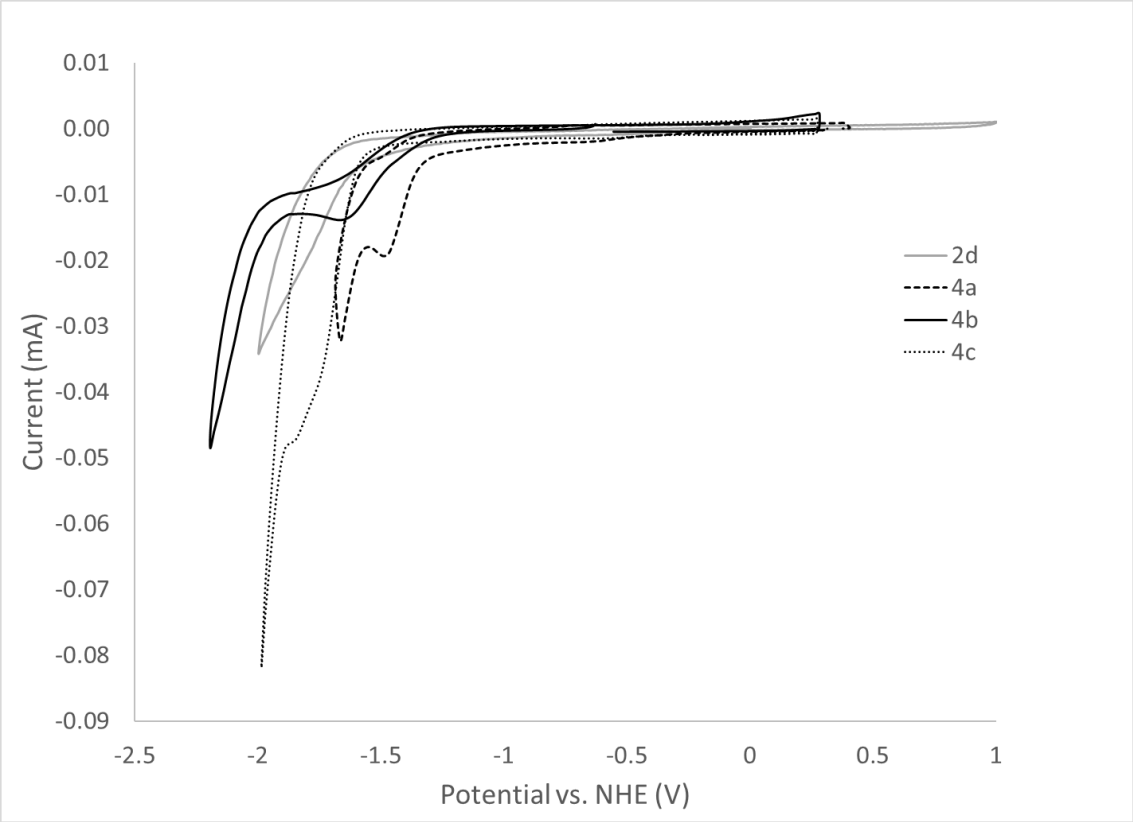

Figure 3.2. Cyclic voltammograms of sensors **4a**^{ox}-**4c**^{ox} and diamide **2d**. Performed in DMSO, with 0.1 M tetrabutylammonium tetrafluoroborate as supporting electrolyte, 3 mm glassy carbon working electrode, Pt-coil counter electrode, Ag wire pseudoreference with Fc/Fc^+ as internal standard, scan rate of 50 mV/sec.

Gratifyingly, it was found that the more sterically hindered disulfide within compound **4c^{ox}** exhibited a less negative reduction potential than the less substituted derivatives **4b^{ox}** and **4a^{ox}**, as is established in protein residues,[30,31] demonstrating the tunability of the redox sensing behavior. Control compound **2d** presented no peaks corresponding to electron transfer, showing that the conjugated backbone has no redox activity within the potential window of the experiment.

Classically, the determination of disulfide redox couples was coupled to the measurement of other biologically relevant redox couples, the historic one being the $NADP^+$-NADPH couple. Typical approaches to measure the redox potential of disulfide/dithiol couples utilize other biologically relevant redox couples, relating the values back to the potential of the NADP+/NADPH couple. There are a handful of disulfides with known redox potential, and the reducing ability of the redox couple of these disulfides has been determined and referenced back to the values known for standard reducing compounds.[32,33] Direct comparison of the disulfide within our family of sensors can thus be obtained through equilibration with DTT, whose redox potential in comparison with $NADP/NADPH^+$ has been known for some time.[33]

To perform this examination, disulfides **4a^{ox}-4c^{ox}** were mixed with dithiothreitol (DTT) in 50% CD_3OD/DMF-d^7 under nitrogen atmosphere. Equilibrium conditions were reached, then the equilibrium concentrations of DTT and trans-4,5-dihydroxy-1,2-dithiane (DTT^{ox}) and the oxidized and reduced forms of the sensor were measured via NMR and utilized to determine the standard redox potential through the Nernst equation. (**Table 3.1**). Though the redox potentials determined via equilibration with DTT allow direct comparison to biological systems, the analysis time is unwieldy, typically requiring 3-5 days to reach equilibrium concentrations.

Sensor	E_0 - voltammetry	E_0 - equilibration
4a^{ox}	-1850 mV	-295 mV
4b^{ox}	-1660 mV	-284 mV
4c^{ox}	-1510 mV	-255 mV

Table 3.1. Comparison of different reduction potentials of sensors **4a^{ox}-4c^{ox}**, as determined by equilibration with DTT and voltammetry.

In order to explore this relationship between voltammetric measurements and equilibration with other dithiols, we then decided to compare the known standard redox potentials of disulfides, determined via a well-accepted method, to the redox potentials determined by electrochemistry. Even though the electrode kinetics are not ideal, it was thought that a linear free energy relationship might exist between the potentials of the anodic disulfide reduction peaks and determined via electrochemistry and those from equilibration studies.

The key reduction step in the two mechanisms is quite different, where electrochemically the disulfide first must form the anion radical, which then dissociates to give the thiolate and thiyl radical. The remaining thiyl radical is then reduced to give the required dithiolate, overall following an ECE type mechanism.† (**Figure 3.3**) For solution equilibration, however, one thiolate displaces a second thiolate from a disulfide, forming a new mixed disulfide, eventually reaching an equilibrium mixture of disulfide/dithiol, where the relative concentrations of the two components are dictated by their relative redox potentials.

† In electrochemistry parlance, the nature of electrode reactions is typically differentiated as electrochemical steps (labeled as E), involving electron transfer to/from the electrode, and chemical steps (labeled as C), involving reaction steps separate from the electrode. In this case, there is an electron transfer to form the radical anion, followed by bond cleavage to form the thiyl radical and thiolate anion, followed by another electron transfer forming two thiolates overall, thus an ECE mechanism.

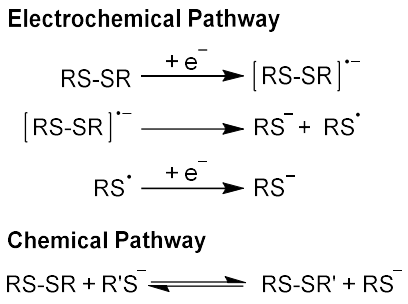

Figure 3.3. Different processes dictating a change in redox pathways as a function of measurement method.

The strongest correlation of voltammetric data with equilibration results of our sensors is found through analysis of the anodic peak in the reduction of the oxidized disulfide form, which represents the initial reduction of the disulfide to form the radical anion, followed by cleavage and a second reduction to produce the dithiolate pair. (**Figure 3.4**)

There are two values obtained from cyclic voltammetry of the disulfides which can be correlated with the known reduction potentials of disulfides, either the anodic initial reduction peak, or the following cathodic oxidation. In our laboratory, the most well behaved process is reduction of the disulfide form. Alternatively, one could start from the reduced dithiol form, though processes that take place for dithiol oxidation are much more complex than disulfide reduction, and are dramatically influenced by solvation. (**Figure 3.4**)

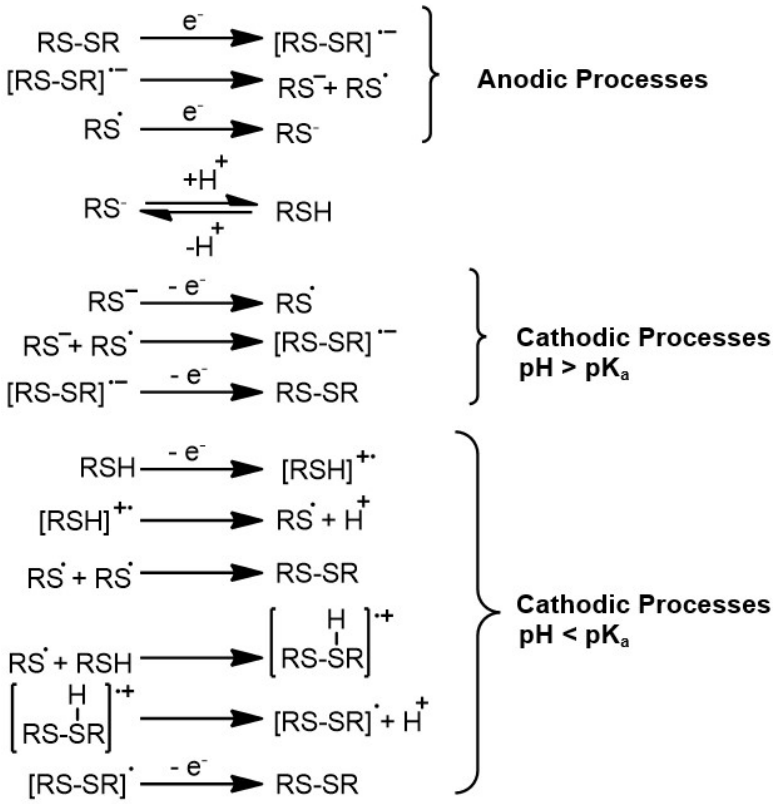

Figure 3.4. Outline of the electrode redox processes for electrochemical dithiol oxidation/disulfide reduction.

In attempts to determine the redox potential of organic dithiols, oxidation of the thiol form electrochemically yields ill-defined peaks, with large variances in any peak potentials determined. This is not surprising, as all of the electrochemical oxidation and reduction processes involving charge transfer to and from the electrode are highly dependent on proton transfer, except for one. The oxidation of thiols requires the anionic thiolate form, thus the pathway for re-oxidation of a thiol/thiolate is a much more convoluted process than the reduction of a disulfide, depending on numerous proton transfer steps. As a result, the process is pH dependent in relation to the pKa of the thiol in question, both of which are poorly defined quantities in organic, aprotic solvents.

pKa of the thiols in question have been correlated to the standard reduction potential of the dithiol/disulfide redox couple, with significant success. However, there is one aspect of the redox couple which cannot be correlated by the thiol pKa. That effect is the steric clash of substituents at the α position. Steric effects at this position result in a lengthening of the disulfide bond, which gives a concomitant increase in the energies of the S-S σ-bond and a decrease in energy of the S-S σ* orbital. This effectively increases the propensity of the disulfide to accept an electron into the σ* orbital, resulting in a less negative redox potential. As this phenomenon exists only in the disulfide form, any correlation between the standard potential and an aspect of only the thiol form will, by necessity, be incomplete.

The treatment of thiol pK_a correlating directly with the reduction potential of the thiol has been used most successfully in the determination of reduction potentials of cysteine residues within proteins. The success, here, is due to the structural homogeneity of sulfur-containing residues; all disulfides in a protein structure are due to a cysteine subunit. However, the changes in pK_a experienced by different proteins are a result of secondary and tertiary structure, where there can be residues present around the thiol which stabilize the anionic form and can therefore result in the more nucleophilic thiolate form being formed preferentially.

The reduction of disulfide bonds at the electrode surface typically result in the formation of a σ* radical anion initially, which then undergoes cleavage to form the thiyl radical and a thiolate (**Figure 3.5-6**). This σ* radical before the cleavage has the SOMO localized where the LUMO was previously, and in fact occupies that same orbital, assuming there is limited delocalization of the radical into the substituents on the sulfur atoms, as is the case in aryl-substituted disulfides.[34,35] Incidentally, the geometry change upon reduction to the anion radical typically is exemplified by a lengthening of the disulfide bond by ~0.8 Å,

which corresponds well to the change in geometry upon formation of the transition state apparent in thiol-disulfide interchange.[36] In addition, in the transition state of thiol-disulfide interchange, the negative charge is shared equally between the two external sulfur atoms of the three atom chain, resulting in approximately ½ additional electron occupation spread over two sulfur atoms, similar to the disulfide radical anion. As a result, the potential required to inject an electron into a disulfide is inherently linked with its ability to act as an electrophile in thiol-disulfide interchange, and there must be a linear relationship between the ability of a disulfide to accept an electron through electron transfer (which, fundamentally, is related to its electrophilicity) and the reduction potential as measured by equilibration with other disulfide/dithiol couples.

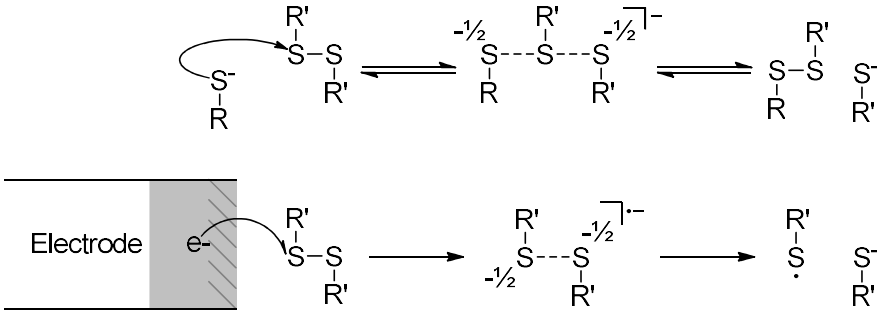

Figure 3.5. Demonstration of the mechanistic interpretation of both dithiol/disulfide interchange and electrochemical reduction of disulfides. As demonstrated here, the mechanistic steps for the two separate processes are similar, and both include a distribution of charge across the sulfur atoms in a fundamentally similar manner.

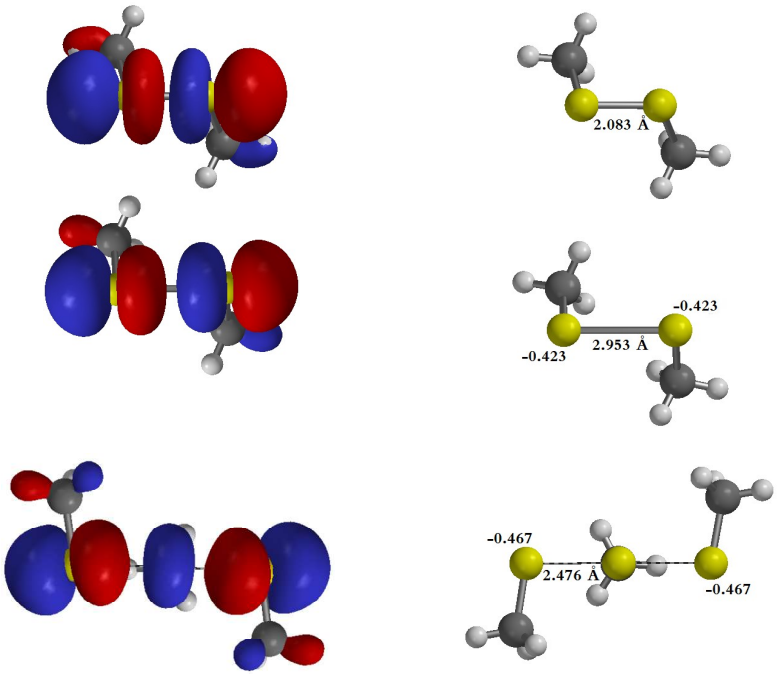

Figure 3.6. A comparison of LUMO of dimethyl disulfide (left, top) and the SOMO of the radical anion of dimethyl disulfide (left, middle) demonstrating the σ* nature of the radical anion; this is compared to the HOMO of the transition state of thiol disulfide interchange (left, bottom). This shows the similarity between the radical anion and the transition state of thiol-disulfide interchange, with significant anion localization across the sulfur atoms. The structure of neutral dimethyldisulfide (right, top) and the radical anion of dimethyl disulfide (right, middle) show the 0.87 Å increase in bond length upon reduction. The structure of the transition state of dithiol/disulfide interchange (right, bottom) showing bond lengths and electrostatic charges developed on each terminal sulfur atom, compared to the charges on each sulfur atom of the disulfide radical anion (right, middle). This shows how the bond lengths change upon reaction/reduction, and indicates their similarity. All calculations performed at B3LYP, 6-31g* level of theory.

There are some inherent differences in the mechanism of electron transfer from the electrode, which is frequently cited to follow an outer-sphere type mechanism, and that of dithiol-disulfide interchange, which must be an inner-sphere type process. One aspect of the dithiol/disulfide redox couple cannot be captured in the electrochemical measurements, and that is the rate of the redox process. This rate is most frequently affected by steric factors related to physical access of the redox site, which is circumvented by the outer-sphere type process utilized electrochemically. This allows us to avoid many energetic terms relating to solvation/desolvation of the intermediates, and examine the ideal, standard reduction potentials.

To explore this LFER between electrochemical and solution equilibration of disulfides, a series of other simple disulfides with known redox potentials were also explored voltammetrically. These disulfides' redox potentials had been previously determined via solution equilibration methods in Whitesides' group.[23,37]

Examination of the processes for oxidation and reduction of disulfide/dithiol redox couples shows that the main pathways of interest in the current study, those that gave the most linear correlation between aqueous/protic conditions and organic/aprotic conditions are the initial reductive processes that occur without a necessary proton transfer, the reduction of a disulfide to form the radical anion. (**Figure 3.4-6**) Attempts to correlate other quantities (half-wave potential, thiol oxidation peaks) with predetermined reduction potentials yielded correlation coefficients < 0.5, while the anodic peak potential resulted in a correlation of ~0.9. (**Figure 3.7**)

With a linear free-energy relationship between the reduction potential determined via voltammetry and the absolute potential determined through solution equilibration studies, easy access to the absolute potential of disulfides of note is now available through well-

known voltammetric techniques. This enables study of relevant redox potentials of disulfides typically not amenable to study in aqueous solutions, where the measurement of the redox potential depends on dithiol-disulfide interchange, a proton-transfer influenced process.

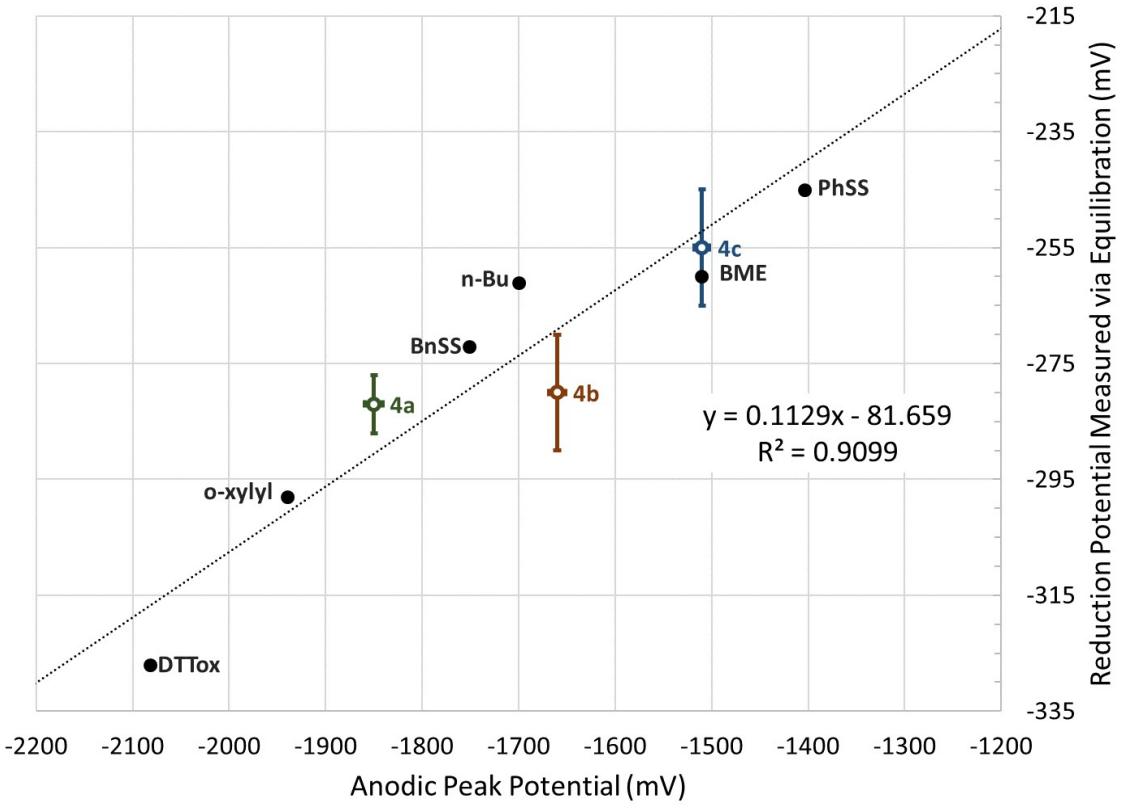

Figure 3.7. Linear relationship between values obtained via solution state equilibration measurements, and anodic peak potentials upon disulfide reduction. DTTox = trans-4,5-dihydroxy-1,2-dithiane, BnSS = dibenzyl disulfide, BME = betamercaptoethanoldisulfide, n-Bu = di-n-butyl disulfide, PhSS = diphenyl disulfide, o-xylyl = 6,7-dimethyl-1,4-dihydrobenzo[d][1,2]dithiine.

The LFER relates the energy of the transient radical anion back to the transition state of dithiol-disulfide interchange, and allows the comparison between the direct measure

of the electrophilicity of the disulfide, determined by cyclic voltammetry, and the redox potential values determined via solution-state equilibration.

CONCLUSION

In conclusion, a family of fluorescent ON-OFF redox sensors was developed. The redox potential of the sensors was measured both via cyclic voltammetry, and by equilibration with DTT, which allowed for comparison of the relevant redox potentials with potentials commonly cited in the literature.

The voltammetric assay was expanded to be comparable with disulfide redox potentials obtained from other assay methodologies. These results are now broadly applicable to disulfide-based redox probes, allowing simple determination of standard disulfide redox potentials through electrochemistry, values which can be correlated to those determined throughout the biochemical literature. This helps to bring together two disparate worlds, one of the biochemical community and the electrochemical community.

In addition, the demonstration of the correlation between the electrophilicity of disulfides and their voltammetric reduction potential opens up the potential for performing quantitative evaluation of both electrophiles and potentially nucleophiles through the measurement of their electrochemical behaviors, reminiscent of pioneering work by Saveant in the early 1990s.

EXPERIMENTAL

General Methods: ^{1}H and ^{13}C NMR spectra were obtained on a Varian 300 MHz spectrometer (^{1}H: 299.95 Hz, ^{13}C: 75.43 Hz), Inova 500 MHz spectrometer (^{1}H: 500.10 MHz, ^{13}C: 125.75 MHz) or Varian 600 MHz spectrometer (^{1}H: 599.98 MHz, ^{13}C: 150.87

MHz). Chemical shifts (δ) are expressed in ppm using non-deuterated solvent present in the bulk deuterated solvent ($CDCl_3$: ^1H 7.26 ppm, ^{13}C 77.16 ppm; $(CD_3)_2SO$: ^1H 2.5 ppm, ^{13}C 39.52 ppm). Solvents and reagents were used as purchased from suppliers, unless anhydrous conditions were employed, in which solvents were distilled from sodium/benzophenone under N_2 atmosphere (THF) or as purchased in sealed, DriSolv containers (DMF). Mass spectra were acquired with a Waters LCT Premier ESI-MS in positive mode using acetone as a solvent. UV-Vis spectra were acquired with a Hewlett-Packard 8453 UV-Visible spectrophotometer equipped with a 250 nm cutoff filter. Fluorescence data was acquired with a Horiba Jobin-Yvon FluoroMax-4 fluorescence spectrophotometer. HPLC performed using a JAI Recycling Preparative HPLC (Model LC-9101) with a JAIGEL-1H preparative column.

Synthesis of Compounds 2-4

General Amide Synthesis: To a 25 mM solution of bisaniline **1** in anhydrous THF under nitrogen atmosphere was added 5 equiv. acid halide via syringe. Solution was stirred for 2 hours, at which point reaction was quenched with 1 mL methanol. After stirring for 10 minutes post methanol addition, solvents were removed under reduced pressure to isolate the amide as the halide salt. To obtain the free-base, bis-amide was dissolved in DCM, treated with pyridine, filtered through a silica plug with 1:1 hexanes:ethyl acetate as mobile phase, and reduced under vacuum. The yield for compound **2b** decreased by ~50% if isolated as the freebase. Bis(2-chloroacetanilide) **2a** was prepared as previously reported in Chapter II.

Bis(2-chloropropanamide) 2b:

Prepared from **1** via General Amide Synthesis, in 90% yield, as HCl salt.

^{1}H NMR (300 MHz, $CDCl_3$) δ 9.30 (s, 2H), 8.33 (d, J = 8.8 Hz, 2H), 7.76 (t, J = 7.8, Hz, 1H), 7.67 (d, J = 2.3 Hz, 2H), 7.55 (d, J = 7.8 Hz, 2H), 7.47 (dd, J = 8.9, 2.4 Hz, 2H), 4.66 (q, J = 7.1 Hz, 2H), 1.90 (d, J = 7.0 Hz, 6H), 1.33 (s, 18H).

^{13}C NMR (126 MHz, $CDCl_3$) δ 167.35, 147.38, 143.30, 136.88, 136.22, 129.38, 127.90, 126.25, 119.10, 111.31, 94.87, 85.01, 56.70, 34.49, 31.20, 22.83.

HRMS (EI+) calcd for $C_{35}H_{38}N_3O_2Cl_2^+$ [MH^+] 602.2341, found 602.2328.

Bis(2-bromo-2-methylpropanamide) 2c:

Prepared from **1** via General Amide Synthesis, in 89% yield, as freebase.

^{1}H NMR (300 MHz, CDCl3) δ 9.46 (s, 2H), 8.34 (d, J = 8.8 Hz, 2H), 7.77 (t, J = 7.8, 1H), 7.70 (d, J = 1.4 Hz, 2H), 7.60 (d, J = 7.8 Hz, 2H), 7.49 (dd, j = 8.8, 1.4 Hz, 2H), 2.14 (s, 12H), 1.37 (s, 18H).

^{13}C NMR (126 MHz, $CDCl_3$) δ 170.15, 147.41, 143.56, 136.99, 129.61, 128.04, 126.38, 119.09, 111.50, 95.09, 85.34, 77.48, 77.23, 76.98, 63.52, 34.69, 32.87, 31.42.

HRMS (EI+) calcd for $C_{37}H_{42}N_3O_2Br_2^+$ [MH^+] 718.1644, found 718.1614.

Bisacetanilide 2d:

Prepared from **1** via General Amide Synthesis, in 93% yield, as freebase.

^{1}H NMR (500 MHz, DMSO-d^6) δ 9.60 (s, 2H), 7.97 (t, J = 7.8, Hz, 1H), 7.73 (d, J = 7.8 Hz, 2H), 7.68 (d, J = 8.6 Hz, 2H), 7.58 (d, J = 2.3 Hz, 2H), 7.50 (dd, J = 8.6, 2.4 Hz, 2H), 2.14 (s, 6H), 1.32 (s, 18H).

^{13}C NMR (126 MHz, DMSO-d^6) δ 169.02, 147.63, 143.42, 137.93, 137.73, 129.54, 127.75, 127.50, 124.53, 114.90, 93.21, 86.91, 34.65, 31.41, 23.97.

HRMS (EI+) calcd for $C_{33}H_{35}N_3O_2^+$ [MH^+] 506.2808, found 506.2809.

General Thioacetate Synthesis: To a 12.5 mM solution of bis(α-haloamide) in anhydrous DMF under nitrogen atmosphere was added 5 equivalents potassium thioacetate. Solution

was stirred for 6 hours, at which point reaction was poured into a volume of 15% aqueous ammonium chloride equivalent to 2 reaction volumes. The thioacetate product precipitates as an orange solid, which was collected by filtration. The solid is then dissolved in dichloromethane, loaded onto a silica plug, and eluted with 1:1 hexanes:ethyl acetate. Removal of solvent under vacuum yielded the freebase product as a yellow-orange solid. Compound 3a was prepared as previously reported in Chapter II.

Bis(2-thioacetylpropanamide) 3b:

Prepared from **2b** via General Thioacetate Synthesis, in 89% yield, as freebase.

^{1}H NMR (300 MHz, $CDCl_3$) δ 8.76 (s, 2H), 8.35 (d, J = 8.9 Hz, 2H), 7.91 – 7.74 (m, 3H), 7.64 (d, J = 2.3 Hz, 2H), 7.42 (dd, J = 8.8, 2.4 Hz, 2H), 4.35 (q, J = 7.2 Hz, 2H), 2.36 (s, 6H), 1.59 (d, J = 7.1 Hz, 6H), 1.32 (s, 18H).

^{13}C NMR (126 MHz, $CDCl_3$) δ 196.09, 169.52, 146.78, 143.57, 136.94, 136.55, 129.65, 127.75, 126.70, 119.52, 110.97, 94.60, 85.20, 41.63, 34.42, 31.21, 30.26, 15.86.

HRMS (EI+) calcd for $C_{39}H_{44}N_3O_4S_2^+$ [MH^+] 682.2773, found 682.2760.

Bis(2-thioacetyl-2-methylpropanamide) 3c:

Prepared from **2c** via General Thioacetate Synthesis, in 81% yield, as freebase.

^{1}H NMR (300 MHz, $CDCl_3$) δ 9.20 (s, 2H), 8.37 (d, J = 8.8 Hz, 2H), 7.67 – 7.59 (m, 4H), 7.46 (dd, J = 8.8, 2.4 Hz, 2H), 2.28 (s, 6H), 1.75 (s, 12H), 1.33 (s, 18H).

^{13}C NMR (151 MHz, $CDCl_3$): δ 195.20, 166.16, 146.18, 143.31, 136.59, 136.54, 29.38, 127.68, 126.57, 119.45, 110.79, 94.31, 85.15, 34.27, 33.99, 31.05, 30.13.

HRMS (EI+) calcd for $C_{41}H_{48}N_3O_4S_2^+$ [MH^+] 710.3081, found 710.3075.

General Thiol Deprotection: To a 1.5 mM solution of bis(thioacetate) in *thoroughly* nitrogen sparged methanol under nitrogen atmosphere is added 5 equivalents of potassium carbonate. After stirring for 1 hour, an amount of *thoroughly* nitrogen sparged 10% $HCl_{(aq)}$ or 20% w/v

$NH_4Cl_{(aq)}$ equal to one reaction volume is cannulated into the reaction vessel. The target product precipitates as an orange solid and can be collected via filtration. Note: Compound **4a** and **4b** are not stable in atmosphere as the freebase, and must be isolated as the HCl salt by quenching with degassed 10% HCl. Compound **4c** is air-stable, and can be isolated as the freebase by quenching the reaction with ammonium chloride.

Bis(2-thioacetanilide) 4a^{red}:

Prepared from **3a** via General Thiol Deprotection, in 92% yield, as chloride salt.

^{1}H NMR (300 MHz, $CDCl_3$): δ 9.73 (br s, 2H), 8.37 (d, *J* = 9.3, 2H), 7.68 (t, *J* = 7.8 Hz, 1H), 7.50 (d, *J* = 2.4 Hz, 2H), 7.47 (d, *J* = 8.1 Hz, 2H), 7.39 (dd, *J* = 2.4 Hz, 8.7 Hz, 2H), 3.49 (d, *J* = 9.3 Hz, 2H), 2.31 (t, *J* = 9.3 Hz, 2H), 1.32 (s, 18H).

^{13}C NMR (126 MHz, $CDCl_3$): 169.47, 148.83, 147.58, 143.39, 129.89, 130.04, 128.31, 128.50, 125.39, 116.48, 93.46, 86.82, 27.54, 34.97, 34.61.

HRMS (EI+) calcd for $C_{33}H_{36}N_3O_4S_2^+$ [MH^+] 570.2243, found 570.2265.

Bis(2-thiopropanamide) 4b^{red}:

Prepared from **3b** via General Thiol Deprotection, in 89% yield, as chloride salt.

^{1}H NMR (300 MHz, $CDCl_3$) δ 9.40 (s, 1H), 8.32 (d, J = 8.6 Hz, 1H), 7.81 (br m, 1H), 7.64 (m, 4H), 7.48 (dd, J = 9.0 Hz, 1.8 Hz, 2H), 3.81 (br m, 2H), 2.46 (d, J = 8.1 Hz, 2H), 1.71 (d, J = 7.5 Hz, 6H), 1.34 (s, 18H).

^{13}C NMR (126 MHz, DMSO-d^6) δ 172.18, 148.29, 147.91, 143.27, 137.29, 129.52, 127.92, 127.25, 123.88, 114.75, 93.59, 86.50, 37.11, 34.70, 31.41, 21.93.

HRMS (EI+) calcd for $C_{37}H_{44}N_3O_2S_2^+$ [MH^+] 598.2556, found 598.2546.

Bis(2-thio-2-methylpropanamide) 4c^{red}:

Prepared from **3c** via General Thiol Deprotection, in 91% yield, as freebase.

^{1}H NMR (300 MHz, $CDCl_3$) δ 9.86 (s, 2H), 8.35 (d, J = 8.7 Hz, 2H), 7.75 (t, J = 7.7 Hz, 1H), 7.67 (d, J = 2.2 Hz, 2H), 7.57 (d, J = 8.0 Hz, 2H), 7.46 (dd, J = 8.0, 2.2 Hz, 2H), 2.64 (s, 1H), 1.76 (s, 9H), 1.34 (s, 24H).

^{13}C NMR (151 MHz, $CDCl_3$) δ 173.36, 146.86, 137.16, 136.88, 129.26, 127.95, 126.00, 118.92, 111.07, 99.23, 94.69, 85.67, 48.92, 34.47, 31.23, 30.49.

HRMS (EI+) calcd for $C_{37}H_{44}N_3O_2S_2^+$ [MH^+] 626.2875, found 626.2891.

General Thiol Oxidation: To a 1.0 mM solution of dithiol in dichloromethane was added 5 equivalents of iodine and 5 equivalents of pyridine, in that order. The solution was stirred for 30 minutes, and then washed with 10% Na_2SO_3 (3x). The organic layer was dried over $MgSO_4$, filtered, and reduced under vacuum. The isolated solid, which contained small amounts of oligomers/polymer, was then filtered through a 4cm silica plug, with 1:1 EtOAc:Hexanes as eluent. Full purification from smaller oligomers required preparative HPLC (mp: $CHCl_3$). Disulfide **4a^{ox}** prepared as previously reported in Chapter II.

Disulfide 4b^{ox}:

Prepared from **4b^{red}** via General Thiol Oxidation as an inseparable mix of diastereomers in 75% yield.

^{1}H NMR (500 MHz, $CDCl_3$) δ 9.67 (s, 2H), 9.44 (s, 2H), 8.46 (d, J = 8.8 Hz, 2H), 8.40 (d, J = 8.8 Hz, 2H), 7.72 (m, 4H), 7.57 (m,4H), 7.51 (d, J = 3.4 Hz, 2H), 7.50 (d, J = 3.4 Hz, 2H), 7.48 – 7.44 (m, 4H), 3.97 – 3.88 (m, 4H), 1.69 (d, J = 7.3 Hz, 2H), 1.55 (d, J = 7.5 Hz, 2H), 1.34 (s, 36H).

^{13}C NMR (126 MHz, $CDCl_3$) δ 169.79, 169.15, 146.77, 143.33, 137.45, 137.39, 136.45, 136.44, 128.53, 128.48, 128.02, 127.96, 125.43, 125.37, 119.21, 118.93, 110.77, 109.99, 95.35, 84.54, 51.57, 51.05, 34.43, 31.22, 29.71, 18.80, 18.67.

HRMS (EI+) calcd for $C_{35}H_{38}N_3O_2S_2^+$ [MH^+] 596.2400, found 596.2405.

Disulfide 4c^{ox}:

Prepared from **4c^{red}** via General Thiol Oxidation in 79% yield.

^{1}H NMR (300 MHz, $CDCl_3$) δ 9.18 (s, 2H), 8.38 (d, J = 8.8 Hz, 2H), 7.74 (t, J = 7.8, 7.8 Hz, 1H), 7.57 (d, J = 2.3 Hz, 2H), 7.52 (d, J = 7.8 Hz, 2H), 7.46 (dd, J = 8.5, 2.4 Hz, 2H), 1.71 (s, 12H), 1.35 (s, 18H).

^{13}C NMR (126 MHz, $CDCl_3$) δ 170.65, 145.34, 132.58, 131.03, 128.42, 126.94, 126.07, 117.07, 106.26, 94.86, 96.45, 83.71, 63.12, 34.20, 30.29, 27.30.

HRMS (EI+) calcd for $C_{37}H_{42}N_3O_2S_2^+$ [MH^+] 624.2718, found 624.2720.

BRIDGE TO CHAPTER IV

Chapter IV continues with the applications of the disulfide sensors explored in Chapters II and III, exploring methods to increase the breadth of redox potentials that can be accessed for sensing applications, as well as structural modifications to be applied to the scaffolds to improve fluorescence and the sensing behavior. As witnessed in Chapter III, increasing the steric bulk around the disulfide bond increased the redox potential significantly; as a result of this observation the investigation of various synthetic modifications that would be able to both increase this steric bulk and modify the electron-accepting abilities of the disulfide bond was undertaken. Additionally, modification of the substituents on the central core of the scaffold can alter the sensing behaviors, and potentially allow access to a change in fluorescence that is OFF-ON in nature. Aryl disulfide-dithiol redox couples have been shown to operate differently than alkyl-based systems, and utilizing this difference in functionality is explored as well. The majority of the following chapter will be devoted to the strategies employed in the attempts to modify the sensor in these ways.

CHAPTER IV

VARIATIONS TO IMPROVE AND MODULATE BEHAVIORS OF THE MACROCYCLIC DISULFIDE SCAFFOLD

The studies in this chapter were performed by both Airlia Shonkwiler and myself. Dr. Lev Zakharov was invaluable in determination of solid-state structures, while Professors Darren W. Johnson and Michael M. Haley provided editorial assistance and directed the research in this chapter as it proceeded.

INTRODUCTION

As seen in Chapters II and III, the ethynylaniline scaffold cyclized through the use of a disulfide linker demonstrates multiple applications ranging from a redox sensor to a macrocyclic anion host. There have been multiple efforts to modify this scaffold to both improve its fluorescence behaviors, further tune the redox potentials attainable, and explore different modes of redox control in the scaffold.

Here we summarize the attempts to modify the scaffold and improve the ability of the scaffold to sense redox potentials. These attempts, while mostly unsuccessful, resulted in an improvement of the knowledge of these systems, further increasing our understanding of what structural modifications would or would not improve the properties we were optimizing.

We start with discussions of attempts to improve the steric bulk or electronic properties around the disulfide in the redox reporters demonstrated in Chapter III. We then demonstrate the effects of substitution of the pyridine in the central arene for a phenyl ring,

and show how the increased steric pressure of the central C-H atom affected the behavior of the disulfide bond, along with some synthetic queries into modifications of the central phenyl arene.

Further, we show the results of some attempts to improve the water solubility of the disulfide scaffold, through decoration of the conjugated scaffold with ionizable groups. These attempts were ultimately unsuccessful, though they did demonstrate the functionality which the scaffold could endure.

Finally, we discuss the attempts to improve the redox behavior of the system through modification of the sulfur containing portion of the molecule, and the results of these studies.

DISCUSSION

Improving Redox Control Through Steric Modifications

As demonstrated in Chapter III, steric modification in the positions of the disulfide scaffold results in a modification of the redox potentials of the disulfide-dithiol redox couple. As is noted in protein chemistry, the increased steric pressure on a disulfide bond will weaken it, and result in a less negative redox potential. This is, in large part, due to the increased S-S bond lengths, which destabilize the bonding orbitals, and the strain induced in the C-S-S-C dihedral angle deviating from the ideal 90° angle.

Synthetic attempts to increase the steric bulk at the α-position proceeded through the synthesis of small, sterically congested carboxylic acids. Increasing the steric bulk beyond that of the most hindered disulfide reported in Chapter III proved challenging, as all of the substrates required activation through formation of an acyl chloride at the final step. The

presence of the tertiary alcohol in the hindered carboxylic acid resulted in a position that was exceedingly acid sensitive, and all attempts to utilize these small sterically hindered acids resulted in decomposition at the acyl chloride formation step.

Increasing Steric Pressure on Disulfide Through Modification of the Central Arene

In addition to the exploration of differing functionalization of the α-position of the disulfide, the effect of changing the center aromatic ring of the conjugated scaffold was investigated (**Scheme 4.1**). Thiol **4**/disulfide **5** was thus prepared, where an unsubstituted phenyl ring was in place of the pyridine from previous sensors.

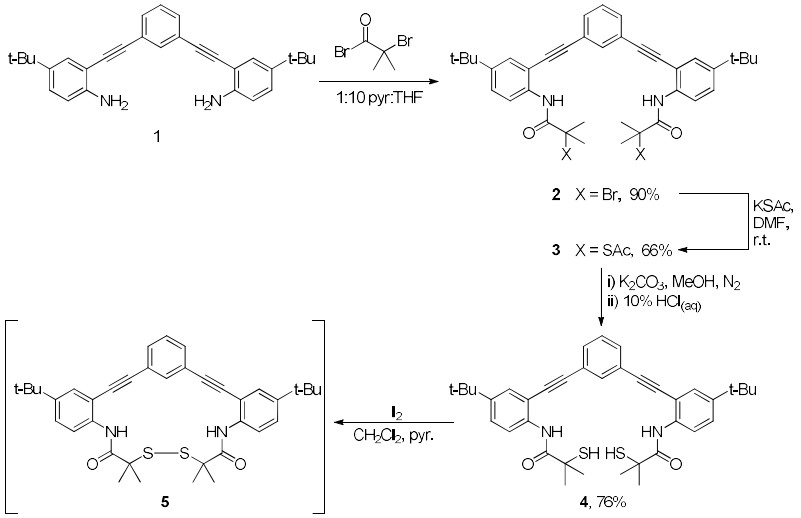

Scheme 4.1. Synthetic scheme for the synthesis of phenyl core disulfide **5**.

The oxidized form of this sensor proved difficult to isolate. Oxidation of the reduced dithiol with molecular iodine under basic conditions demonstrated conversion to the disulfide via crude NMR; however, upon purification, either via flash chromatography or HPLC purification with a polystyrene-based column, only the dithiol could be isolated reliably, recovered from what initially was predominately the disulfide form. This indicated

that the disulfide bond within this sensor was especially labile. A diffraction quality crystal of disulfide **5** was obtained by slow evaporation of a solution of **5** in hexanes. The solid-state structure demonstrated a surprisingly close contact between the central C-H bond and the disulfide bond (**Figure 4.1**).

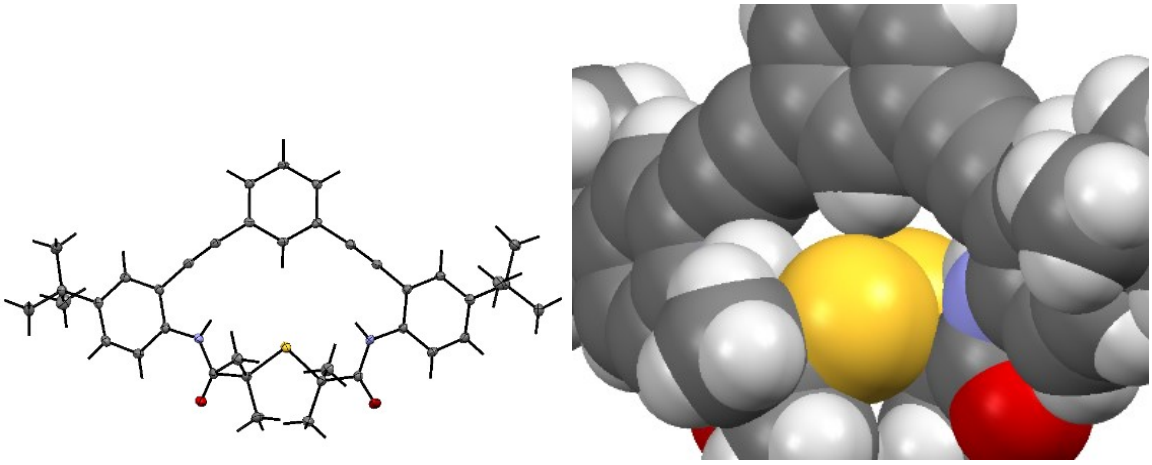

Figure 4.1. ORTEP of disulfide **5**, ellipsoids drawn at 50% probability (left), spacefilling model of disulfide C-H interaction (right). All H atoms were found from the diffraction data.

This seemed to indicate the partial stabilization of the disulfide bond via a bifurcated hydrogen bond between the disulfide and the phenyl hydrogen. Such a bifurcated hydrogen bond involving disulfides is known in proteins.[3]

Interestingly, UV/Vis and fluorescence measurements of the disulfide form of this compound indicated sensing behavior, with a 40nm emission shift in fluorescence between the oxidized and reduced forms when excited at 289nm (**Figure 4.2**). This would be greatly beneficial, as a ratiometric response is ideal for sensing phenomena such as oxidative stress, allowing for direct measurement of the ratio between oxidized and reduced forms. Unfortunately, after repeated fluorescence measurements with excitation at 289nm, disulfide degradation was observed, and an emission corresponding to the thiol form started growing

in. This phenomenon is also noted in proteins, where disulfides that are located near tryptophan residues can experience photolytic reduction when irradiated at 280nm; presumably a similar phenomenon is seen here, where the fluorophore sensitizes homolytic cleavage of the disulfide moiety.[4]

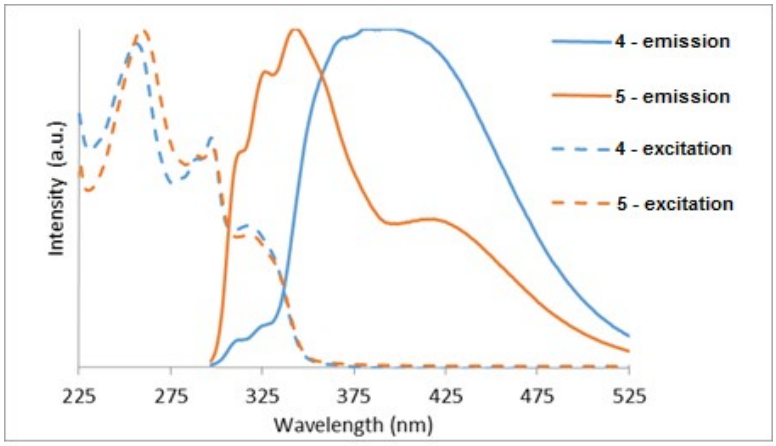

Figure 4.2. Absorption and emission of dithiol **4** and disulfide **5**.

Due to the lability of the disulphide bond in **5**, further pursuit of this functionality was abandoned. The inherent instability of the disulphide bond indicated, to a first approximation, that the oxidized form would be too unstable, and thus unlikely to form in solution as a part of dithiol/disulphide interchange. Additionally, the extremely blue-shifted emission and excitation of the scaffold without the pyridine unit (**Figure 4.2**) did not bode well for use in biological systems.

Attempts to Improve Water Solubility of Sensing Scaffold

We also needed to know the potential effects of a change in solvent on the reduction potentials we were measuring. In order to determine the effects of aqueous solvent on the

reduction potentials of the disulfide functionality, the scaffold needed more polar functional groups.

As other members in our laboratory were pursuing the synthesis of a variety of amidines for medicinal chemistry, this ionic functional group was explored as a potential solubilizing functionality for the disulfide (**Figure 4.3**).

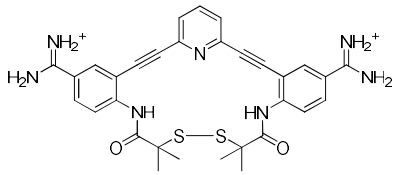

6

Figure 4.3. Target amidine containing disulfide.

Amidines possess a $pK_a = 14$, so they are effectively permanently ionized in aqueous solution. In our laboratory, a new route to amidines was developed using deprotonated amines as a nucleophile to add to nitrile groups to form the amidine.[4] Thus, we proceeded through the synthesis utilizing a cyano functionalized aniline as the starting material, in the hopes of forming a late stage amidine as a solubilizing group (**Scheme 4.2**). The synthesis proceeded as planned, however, upon deprotection of the thioacetate **10** to form the free thiolate, a polymeric product was formed. This likely was due to resultant attack of the thiolate functionality on the cyano group.

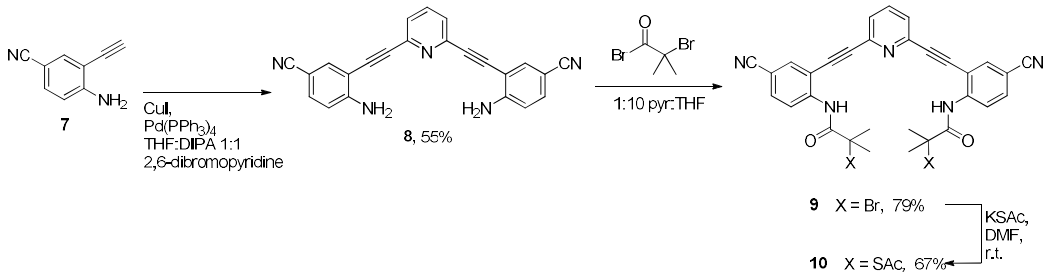

Scheme 4.2. Synthesis of cyano functionalized protected dithioacetate **10**.

A few other routes to functionalize the scaffold with ionic groups were attempted as well. A scaffold with an inverted pyridine ring in the scaffold was employed, in the hopes of alkylating it and providing ionic functionality (**Scheme 4.3**). The pyridine unit in this case resisted alkylation with most common alkylating agents. Though the target disulfide was not obtained in the course of this synthesis, it would likely have suffered from the same instability seen in **5** as a result of the steric pressure of the C-H bond within the cleft.

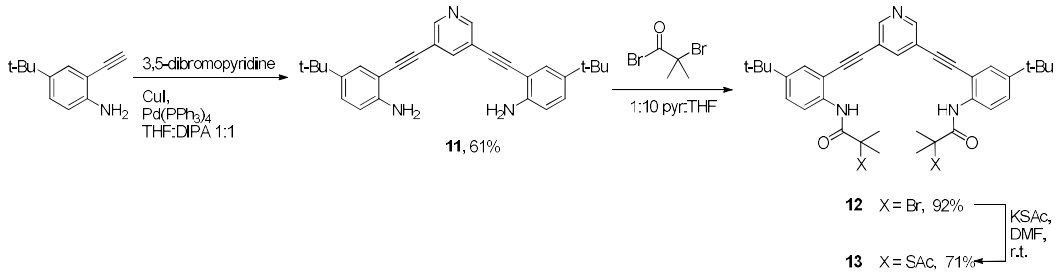

Scheme 4.3. Synthesis of 3,5-pyridyl functionalized protected dithioacetate **13**.

Though the water solubility would need to be improved in order to pursue these compounds as biological imaging agents, they resisted many of the attempts to functionalize them with ionic water-solubilizing groups. Another route to improve their sensing behavior that was investigated was modification of the redox couple functionality.

Modulation of Redox Properties Through Alteration of Redox Couple

In addition to the dithiol/disulfide redox couple, other potential redox functionalities were examined in order to explore different redox couples that would still behave in a reversible manner. Dithiocarbamates are another family of redox-active sulfur containing groups, whose redox properties have been examined previously.[5] It is known in the

literature that the dithiocarbamate/thiuram disulfide couple has a redox potential close to that of glutathione/glutathione disulfide, and that the oxidized and reduced forms can participate in thiol/disulfide interchange. The geometry around the disulfide linkage in thiuram disulfides is not constrained to that of the typical organic disulfide, and thus doesn't have the same dependence on dihedral angle that disulfides experience. As a result, it was thought that dithiocarbamates may have a more favorable behavior in equilibration with a dithiol/disulfide based redox couple, in addition to exhibiting a much easier synthetic route than the dithiol/disulfide based sensors, originating from a precursor common to the project (**Scheme 4.4**).

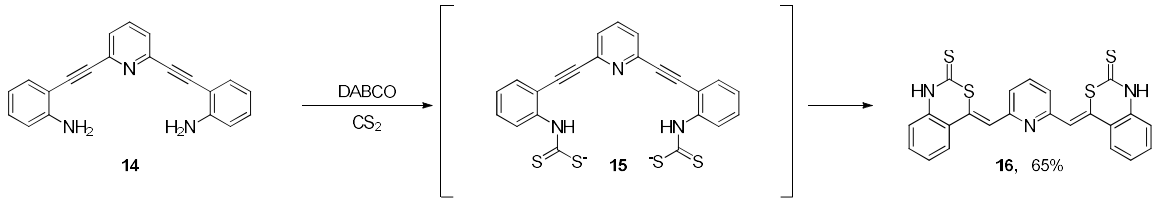

Scheme 4.4. Attempted synthesis of dithiocarbamate derivative **15**, resulting in cyclized product **16**.

However, when the reaction was carried out, it was found that the formed dithiocarbamate **15** immediately performed a 6-exo-dig cyclization, resulting in a 1,3-thiazine-2-thione product **16** (**Scheme 4.5**). Though this compound was not the intended product, it still had potential as a redox couple (**Scheme 4.6**). However, the fluorescence was quenched both in the reduced state and upon treatment with hydrogen peroxide.

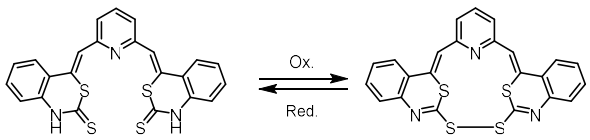

Scheme 4.5. Potential redox couple based upon 1,3-thiazine-2-thione scaffold.

Dithione **16** exhibits poor solubility in all solvents examined except for DMSO, and also demonstrated a quenched fluorescence. Though it could be utilized as a novel ligand for metals, due to its lack of fluorescence, it was not explored further. It appears that if fluorescent behavior is desired with a sulfur-based redox active functionality, then the sulfur atom must not be in direct conjugation with the fluorophore, so that the system can avoid heavy-atom quenching, but must affect the scaffold in such a way as to change the fluorescence profile upon its formation/cleavage.

This derivative is potentially available in one step from commercially available materials and commonly used precursors within the project.

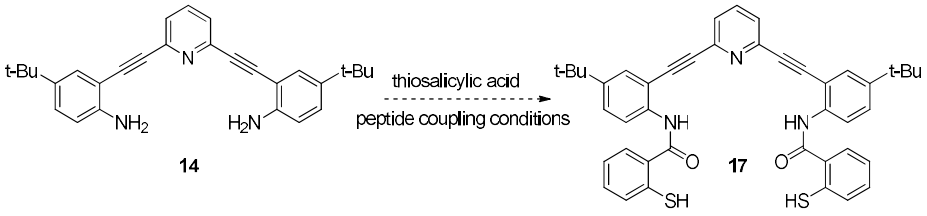

Scheme 4.6. Proposed synthesis of thiosalicylamide-based redox probe **17**.

The oxo analog of the target thiosalicylamide-based probe was found to have an exceedingly high fluorescence due to the intramolecular hydrogen bond between the hydroxyl group and the neighboring amide carbonyl. This rigidified the scaffold and resulted in a dramatic increase in quantum yield.

Computationally the redox couple shows promise for a TURN-ON response upon oxidation, as the thiol is directly in conjugation with the fluorophore backbone while reduced, but is bent out of conjugation with the phenyl ring upon oxidation (**Scheme 4.7, Figure 4.4**).

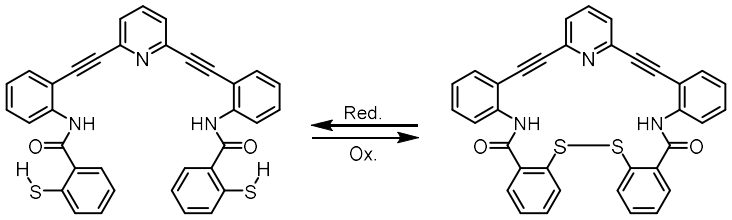

Scheme 4.7. Redox couple based on thiosalicylamide scaffold.

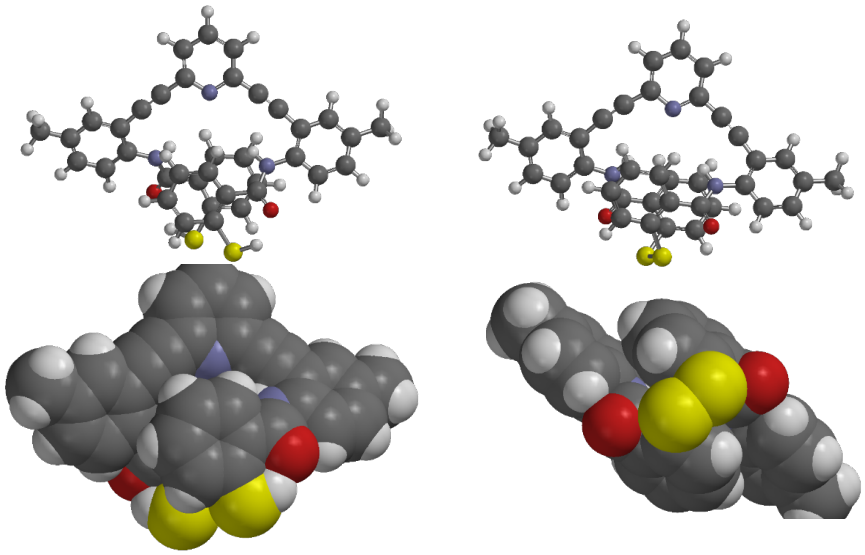

Figure 4.4. Optimized structures of reduced and oxidized variants of **17**, calculated at the B3LYP, 6-311G* level of theory.

Though this thiosalicylamide scaffold appeared to be theoretically promising, it proved difficult to synthesize, with all peptide coupling conditions producing only polymeric products with the thiol functionality attacking the activated carboxylate. An interesting side reaction occurred, however, when triphenylphosphite was used as a peptide coupling reagent (**Scheme 4.8**).

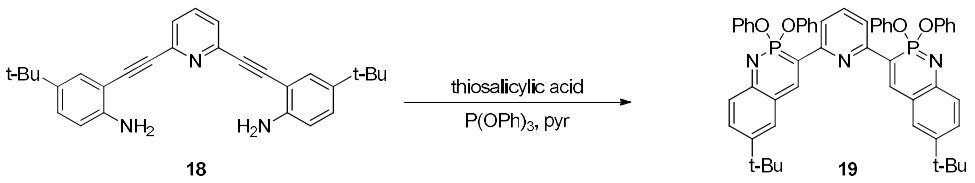

Scheme 4.8. Attempted synthesis of thiosalicylamide derivative, which formed an azaphosphinine, compound **19**.

This reaction produced a number of products, one of which displayed a bright, red-shifted fluorescence. We were able to obtain a crystal structure of the compound in question to assist in the identification, showing it to unambiguously be a 2-λ^5-azaphosphinine derivative resulting from a cyclization within our conjugated scaffold (**Figure 4.5**).

This heterocycle, with a tetra-coordinate phosphorus, at the time was not known in the literature. It features an in-ring nitrogen phosphorous double bond, with phosphorous in the +5 oxidation state. We posited that the triphenylphosphite used in the reaction formed a bond with the aniline nitrogen, and then cyclized with the alkyne to form the new six-membered heterocycle. An extensive literature search yielded no other examples of this reaction.

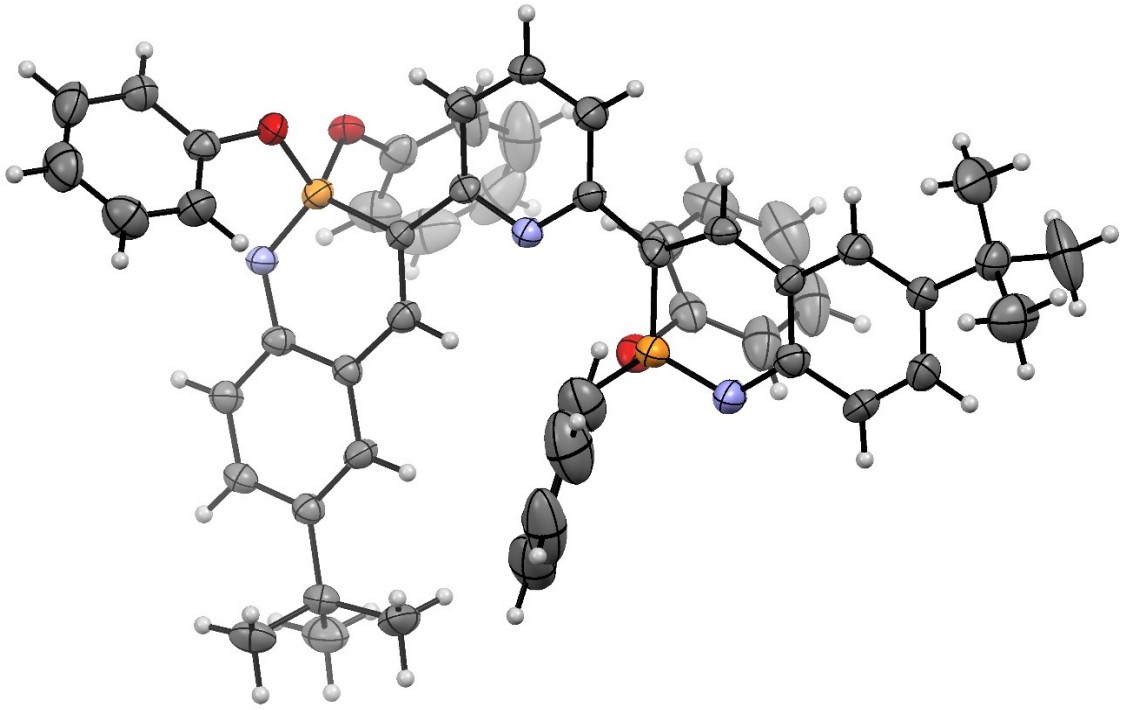

Figure 4.5. ORTEP of bis-azaphosphinine resulting from initial cyclization reaction, ellipsoids drawn at 50% probability.

CONCLUSION

In conclusion, we attempted a number of methodologies to improve the redox behavior and aqueous solubility of the redox sensor. It proved to be extensively sensitive to reaction conditions amenable to post-synthesis modification, as a result the majority of these attempts failed. The structure with a phenyl group as the central arene displayed some interesting properties, though it proved too unstable for general use.

While the thiosalicylamide derivative showed promise as a synthetic target, the cyclization to form an azaphosphinine ring system discovered in the course of the investigations displayed some interesting properties, and warrants further exploration.

EXPERIMENTAL

General Methods: ^{1}H and ^{13}C NMR spectra were obtained on a Varian 300 MHz spectrometer (^{1}H: 299.95 Hz, ^{13}C: 75.43 Hz), Inova 500 MHz spectrometer (^{1}H: 500.10 MHz, ^{13}C: 125.75 MHz) or Varian 600 MHz spectrometer (^{1}H: 599.98 MHz, ^{13}C: 150.87 MHz). Chemical shifts (δ) are expressed in ppm using non-deuterated solvent present in the bulk deuterated solvent ($CDCl_3$: ^{1}H 7.26 ppm, ^{13}C 77.16 ppm; $(CD_3)_2SO$: ^{1}H 2.5 ppm, ^{13}C 39.52 ppm). Solvents and reagents were used as purchased from suppliers, unless anhydrous conditions were employed, in which solvents were distilled from sodium/benzophenone under N_2 atmosphere (THF) or as purchased in sealed, DriSolv containers (DMF). Mass spectra were acquired with a Waters LCT Premier ESI-MS in positive mode using acetone as a solvent. UV-Vis spectra were acquired with a Hewlett-Packard 8453 UV-Visible spectrophotometer equipped with a 250 nm cutoff filter. Fluorescence data was acquired with a Horiba Jobin-Yvon FluoroMax-4 fluorescence spectrophotometer. HPLC performed using a JAI Recycling Preparative HPLC (Model LC-9101) with a JAIGEL-1H preparative column.

Synthesis of Compounds 2-19

General amide synthesis: To a 25 mM solution of dianiline in anhydrous 1:10 pyridine:THF under nitrogen atmosphere was added 5 equiv. 2-bromoisobutyryl bromide via syringe. Solution was stirred for 2 hours, at which point reaction was quenched with 1 mL methanol. After stirring for 10 minutes post methanol addition, solvents were removed under reduced pressure to isolate the amide. The amide was then dissolved in DCM, filtered

through a silica plug with 1:1 hexanes:ethyl acetate as mobile phase, and reduced under vacuum to yield the bisamide.

Bisamide 2: Synthesized via general amide synthesis, to give **2** in 90% yield. ^{1}H NMR (300 MHz, cdcl$_3$) δ 9.45 (s, 2H), 8.35 (d, *J* = 8.8 Hz, 2H), 7.87 (s, 1H), 7.68 – 7.53 (m, 4H), 7.53 – 7.36 (m, 3H), 2.12 (s, 12H), 1.37 (s, 18H).

General thioacetate synthesis: To a 12.5 mM solution of bisamide in anhydrous DMF under nitrogen atmosphere was added 5 equivalents potassium thioacetate. Solution was stirred for 6 hours, at which point reaction was poured into a volume of 15% aqueous ammonium chloride equivalent to 2 reaction volumes. The thioacetate product precipitates as a brown solid, which is collected by filtration. The solid is then dissolved in dichloromethane, loaded onto a silica plug, and eluted with 1:1 hexanes:ethyl acetate. Removal of solvent under vacuum yields the target thioacetate.

Thioacetate 3: Synthesized via general thioacetate synthesis, to give **3** in 66% yield as an off-white solid. 1H NMR (300 MHz, cdcl3) δ 9.17 (s, 1H), 8.36 (d, J = 8.9 Hz, 2H), 7.91 (s, 1H), 7.66 (dd, J = 7.7, 1.7 Hz, 2H), 7.61 – 7.40 (m, 6H), 2.19 (s, 6H), 1.74 (s, 12H), 1.35 (s, 18H).

General thiol deprotection: To a 1.5 mM solution of bis(thioacetate) in *thoroughly* nitrogen sparged methanol under nitrogen atmosphere is added 5 equivalents of potassium carbonate. After stirring for 1 hour, an amount of *thoroughly* nitrogen sparged 10% $HCl_{(aq)}$ or 20% w/v $NH_4Cl_{(aq)}$ equal to one reaction volume is cannulated into the reaction vessel. The dithiol precipitates as an off-white solid and is collected via filtration.

Dithiol 4: Following general thiol deprotection, yielded **4** in 76% yield. ^{1}H NMR (300 MHz, cdcl$_3$) δ 9.83 (s, 2H), 8.36 (d, *J* = 8.0 Hz, 2H), 7.84 (s, 1H) 7.66 – 7.51 (m, 3H), 7.48-7.35 (m, 4H), 2.41 (s, 2H), 1.75 (s, 12H), 1.75 (s, 18H).

Dianiline 8: To a N_2 sparged solution of **7** and 2,6-dibromopyridine in 10mL 1:1 THF:DIPA was added 0.5 mol% $Pd(PPh_3)_4$ and 0.5 mol% CuI, and stirred overnight. Filtered reaction mixture through a silica plug with CH_2Cl_2 as mobile phase, and removed volatiles. Purified via mixed solvent recrystallization from CH_2Cl_2 and hexanes to give **8** as a yellow solid in 55% yield. ^{1}H NMR (300 MHz, cdcl$_3$) δ 7.78 (t, *J* = 7.8 Hz, 1H), 7.70 (s, 2H), 7.54 (d, *J* = 7.8 Hz, 2H), 7.43 (d, *J* = 8.4 Hz, 2H), 6.75 (d, *J* = 8.4 Hz, 3H), 4.98 (s, 2H).

Bisamide 9: Synthesized via General Amide Synthesis, to give **9** in 79% yield as an off-white solid. ^{1}H NMR (300 MHz, cdcl$_3$) δ 9.55 (s, 2H), 8.66-8.55 (m, 3H), 7.85 (d, *J* = 1.9 Hz, 2H), 7.778-7.67 (m, 4H), 2.11 (s, 12H).

Thioacetate 10: Synthesized via general thioacetate synthesis, to give **10** in 67% yield as an orange solid. ^{1}H NMR (300 MHz, cdcl$_3$) δ 9.55 (s, 2H), 8.60-8.51 (m, 3H), 7.80 (d, *J* = 1.9 Hz, 2H), 7.60-7.47 (m, 4H), 2.21 (s, 6H), 1.85 (s, 12H).

Dianiline 11: To a N_2 sparged solution of 2-ethynyl-4-t-butylaniline and 3,5-dibromopyridine in 10mL 1:1 THF:DIPA was added 0.5 mol% $Pd(PPh_3)_4$ and 0.5 mol% CuI, and stirred overnight. Filtered reaction mixture through a silica plug with CH_2Cl_2 as mobile phase, and removed volatiles. Purified via mixed solvent recrystallization from CH_2Cl_2 and hexanes to give **11** as an off-white solid in 61% yield. ^{1}H NMR (300 MHz, cdcl$_3$) δ 8.68 (d, *J* = 1.9z Hz, 2H), 7.95 (t, *J* = 2.0 Hz, 1H), 7.40 (d, *J* = 2.3 Hz, 2H), 7.24 (dd, *J* = 8.5, 2.4 Hz, 3H), 6.72 (dd, *J* = 8.6, 1.9 Hz, 2H), 4.20 (s, 4H), 1.29 (s, 18H).

Bisamide 12: Synthesized via General Amide Synthesis to give **12** as an off-white solid in 92% yield. ^{1}H NMR (300 MHz, cdcl$_3$) δ 9.37 (s, 2H), 8.85 – 8.75 (m, 2H), 8.31 (d, *J* = 8.8 Hz, 2H), 8.05 (t, *J* = 2.0, Hz, 1H), 7.56 (d, *J* = 2.3 Hz, 2H), 7.45 (dd, *J* = 8.8, 2.3 Hz, 2H), 2.08 (s, 12H), 1.34 (s, 18H).

Thioacetate 13: Synthesized via general thioacetate synthesis, to give **13** in 71% yield as an orange solid. ^{1}H NMR (300 MHz, cdcl$_3$) δ 9.14 (s, 2H), 8.85 (d, *J* = 2.1 Hz, 2H), 8.36 (d, *J* = 8.8 Hz, 2H), 8.12 (t, *J* = 2.0 Hz, 1H), 7.52 (d, *J* = 2.4 Hz, 2H), 7.44 (dd, *J* = 8.8, 2.4 Hz, 2H), 2.22 (s, 6H), 1.73 (s, 12H), 1.32 (s, 18H).

Bisamide 14: To a N_2 sparged solution of 2-ethynyl-aniline and 3,5-dibromopyridine in 10mL 1:1 THF:DIPA was added 0.5 mol% $Pd(PPh_3)_4$ and 0.5 mol% CuI, and stirred overnight. Filtered reaction mixture through a silica plug with CH_2Cl_2 as mobile phase, and removed volatiles. Purified via mixed solvent recrystallization from CH_2Cl_2 and hexanes to give **14** as a yellow solid in 77% yield. ^{1}H NMR (300 MHz, dmso) δ 7.87 (t, *J* = 7.1 Hz, 1H), 7.72 (d, *J* = 7.3 Hz, 2H), 7.29 (dd, *J* = 7.7, 1.6 Hz, 2H), 7.14 (t, *J* = 7.8 Hz, 2H), 6.76 (d, *J* = 8.3 Hz, 2H), 6.57 (t, *J* = 7.3 Hz, 2H), 5.63 (s, 4H).

Bisthione 16: To a solution of bisaniline **14** in CS_2 was added 4 equivalents DABCO. The product precipitated over 2 hours as an orange-yellow solid, which was collected by filtration to give a 65% overall yield. ^{1}H NMR (300 MHz, dmso) δ 12.92 (s, 2H), 7.97 – 7.87 (m, 4H), 7.56 – 7.43 (m, 7H), 7.37 – 7.33 (m, 2H).

Azaphosphinine 19: To a solution of thiosalicylic acid in pyridine was added 1.2 equivalents of triphenylphosphite. This was heated to 100˚C for 8 hours, at which point 0.5 equivalents of **18** were added, and solution heated at 100˚C for an additional 12 hours. No yield is given, as the reaction suffered from numerous polymeric products and isolation of the target compound proved problematic from the complex reaction mixture. ^{1}H NMR (500 MHz, $CDCl_3$) δ 8.94 (d, *J* = 41.5 Hz, 2H), 7.86 (s, 2H), 7.47 (d, *J* = 8.5 Hz, 2H), 7.24 - 7.18 (m, 5H), 7.17 - 7.09 (m, 10H), 7.06-6.98 (m, 10H), 1.33 (s, 18H).

BRIDGE TO CHAPTER V

In this chapter we explored a variety of different functionalities to enable a larger range of redox potentials, differing solubility of the redox sensors, and improve the fluorescent response. Though these efforts were largely unsuccessful, they did demonstrate which reaction conditions the disulfide scaffold could tolerate. The scaffold is highly sensitive toward fluoride, electrophiles, and functionality more nucleophilic than the standard pyridine. Increasing the steric bulk around the disulfide functionality results in a much more unstable disulfide linkage, and although increasing the electron withdrawing character of the functionality near the disulfide would likely improve the reduction potential, it resulted in additional peaks electrochemically, convoluting the redox potentials obtained through that method.

Other functionality was explored as redox couples to be appended to the scaffold, though they demonstrated a tendency to react with the alkyne scaffold and/or quench the fluorescence in both oxidized and reduced states. Though the thiosalicylamide derivative shows a lot of promise in its fluorescence profiles, the synthesis proved very problematic, and no simple solutions are available.

While exploring the synthesis of this scaffold, however, it resulted in the discovery of an entirely new reaction to access a heretofore underexplored heterocycle. This heterocycle demonstrated a novel fluorescence, so the reaction to form the heterocycle was explored and expanded upon to demonstrate the properties of both the heterocycle itself and the new reaction to form it. In Chapter V, we demonstrate the functional group tolerance of this reaction and the various applications of the resultant heterocycle containing both phosphorous and nitrogen.

CHAPTER V

INITIAL INVESTIGATIONS INTO THE FORMATION AND APPLICATIONS OF 2-Λ^5-PHOSPHAQUINOLINES

This work was published in volume 54 of *Angewandte Chemie* in November of 2015. Airlia Shonkwiler performed the synthesis and isolation of a number of the compounds disclosed within, in addition to the supramolecular titration studies. Muhammad Khalifa provided synthetic support for production of a number of starting materials. Dr. Lev N. Zakharov solved diffraction data for the x-ray crystallographic structures disclosed within. Principle investigators Dr. Darren W. Johnson and Dr. Michael M. Haley, facilitated the research of this heterocycle and the new reaction to form it discovered herein.

INTRODUCTION

The azaphosphinine scaffold has been explored as an analogue of hydrocarbon-based molecules for nearly half a century. The simplest six-membered ring systems, analogous to benzene, are comprised of three structural isomers: 1,4-λ^3-azaphosphinine (**1**) was first made in 1972,[1] followed by the 1,3- (**2**) and 1,2- (**3**) λ^3-azaphosphinine congeners in 1987 (**Figure 5.1**).[2] Until recently, nearly all azaphosphinines have featured phosphorus atoms formally in the +3 oxidation state,[3] except for one notable example, compound **4**, which has phosphorus in the +5 oxidation state and was prepared in 1991.[4] The pioneering studies of Dewar and Campbell on 1,2-azaphosphinines in the early 1960s, however, met with varying degrees of success.[5] While Dewar was able to prepare the HI salt of **5**, attempts

by both groups to isolate the corresponding λ^3-derivatives yielded unstable systems that required isolation as λ^5-phosphonamidates such as **6**. While there have since been a handful of other investigations of 1,2-azaphosphinine structure and reactivity, the difficulty in synthesizing them has precluded rigorous investigations.[6] On the other hand, examination of the fully inorganic variants has proceeded extensively, with cyclotriphosphazenes such as **7** being one of the most studied inorganic heterocycles.[7] For example, the first cyclotriphosphazene was described in 1834 by Liebig, though the exact structure remained contested until the 1860s.[8]

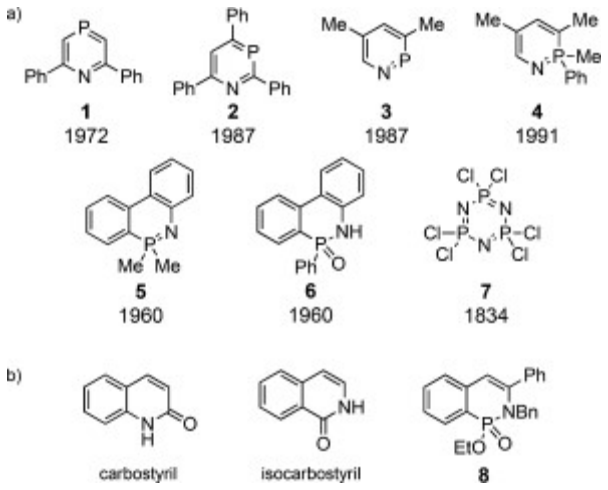

Figure 5.1. a) Early examples of azaphosphinines. b) Carbostryril and isocarbostyril and their structural similarity to bioisosteres like phosphonamidate **8**.

The choice of substituents on the phosphorous atom can significantly affect the stability and reactivity of the 1,2-λ^5-azaphosphinine scaffold. P-C_{alkyl} and P-C_{aryl} derivatives such as **4** and **5** are very sensitive to oxygen and water and decompose readily upon atmospheric exposure.[4–6] On the other hand, 1,2-λ^5-azaphosphinines with alkoxy and

phenoxy groups tend to hydrolyze from their phosphonimidate form (e.g., **4**, **5**) to the considerably more stable phosphonamidate form (e.g., **6**, **8**).

Phosphonates and their analogues have seen extensive use as transition-state mimics for ester and amide hydrolysis. For instance, compound **8** has been explored recently as a bioisostere of isocarbostyril† and shows promise in pharmacological applications (**Figure 5.1 b**).[9] In addition to the ability of phosphonates/phosphonamidates to act as ester and amide bioisosteres, these compounds have relevance for a number of other health-related uses.[10] As a result, new efficient metal-free reactions to make phosphonate derivatives of common heterocyclic scaffolds, such as the quinolinone substructure, are highly desirable.[11] Herein, we describe a simple synthesis to assemble the 2-λ^5-phosphaquinoline framework in a single step from easily attainable starting materials.

RESULTS/DISCUSSION

Reaction of $P(OPh)_3$ with 2-ethynylanilines **9 a–j**, which are accessible through Sonogashira cross-coupling of known alkynes with 2-iodoaniline, furnished phosphaquinolines **10** (the imidate form; **Scheme 5.1**) along with varying amounts of phosphaquinolinones **11** (the amidate form), the latter of which arise from the partial hydrolysis of **10** by adventitious water during work-up and purification.

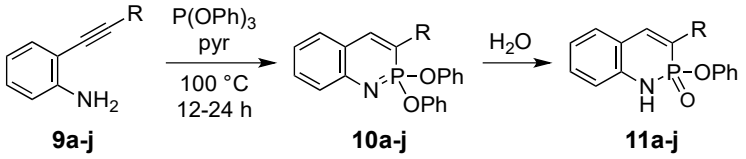

Scheme 5.1. Synthesis of 2-phosphaquinolines and 2-phosphaquinolinones

†Carbostyril and isocarbostyril are the long-standing common names of 2(1H)-quinolinone and 1(2H)-isoquinolinone, respectively, and are still used frequently in the pharmacological and fluorophore literature

The yields in **Table 5.1** reflect our best efforts to rigorously exclude (**10**) or include (**11**) water as part of the overall sequence; nonetheless, **10 a**, **d**, **i** were too labile to isolate purely as the phosphaquinoline. This cyclization is tolerant of a variety of electron-rich and electron-poor arenes, as well as alkyl functionality attached at the ethynyl group (**Table 5.1**, entry **i**). However, the reaction did not tolerate silyl-protected or terminal alkynes, and nor were ketones stable to the cyclization conditions owing to competing Kabachnik–Fields condensation,[12] all of which resulted in intractable polymers. Interestingly, ethyl ester derivative **10c** does not undergo a "traceless" Staudinger ligation.[13] This and the general stability of the phosphonimidate toward hydrolysis at room temperature once purified lends credence to the idea of increased stability from electron delocalization within the heterocycle.

Entry	R	Yield (**10**)	Yield (**11**)
a	3,5-$(CF_3)_2$Ph	---	39%
b	4-CNPh	54%	79%
c	4-CO_2EtPh	54%	74%
d	4-ClPh	80%	---
e	Ph	45%	72%
f	4-MePh	63%	82%
g	4-MeOPh	56%	66%
h	4-(NMe_2)Ph	68%	---
i	n-Pen	---	73%
j	2-pyridyl	71%	31%

Table 5.1. Reaction scope and yields of isolated product for the azaphosphinine cyclization.

Single-crystal X-ray diffraction provided the solid-state structures of **10j** (**Figure 5.2**) and **11j** (**Figure 5.3**), which allowed us to directly compare the imidate and amidate forms, respectively. The P-N bond in **10j** (1.565 Å) is much shorter than the amidate P-N bond in **11j** (1.635 Å) but is similar to the analogous bond in hexaphenoxycyclotriphosphazene (1.575

Å).[14] The imidate structure indicates some π-electron delocalization within the heterocycle, with the C(1)=C(2) double bond length (1.367 Å) intermediate between that of benzene and an isolated double bond, whereas the same bond in **11j** (1.341 Å) is nearly identical in length to the corresponding bond in carbostyril (1.343 Å) (**Table 5.2**).[15]

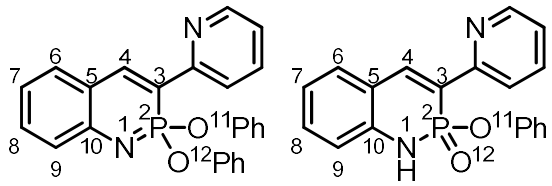

Entry	**10f**	**11f**
P^2–C^3 (Å)	**1.760(2)**	**1.780(3)**
P^2–N^1 (Å)	1.565(2)	1.635(2)
C^3–C^4 (Å)	**1.367(3)**	**1.341(4)**
C^4–C^5 (Å)	1.446(3)	1.446(4)
C^5–C^{10} (Å)	1.425(3)	1.398(5)
P^2–O^{11} (Å)	1.5945(17)	1.611(2)
P^2–O^{12} (Å)	1.5972(16)	1.4789(19)
RMSD (Å)	**0.014**	**0.066**
Torsion angle between pyridine and azaphosphinine ring (°)	4.7(2)	18.8(4)

Table 5.2. Selected structural features in phosphaquinolines and phosphaquinolinones.†

† Crystallographic data for **10 j**: $C_{25}H_{19}N_2O_2P$, M=410.39, 0.17×0.16×0.12 mm, T=173(2) K, Monoclinic, space group $P2_1/c$, a=11.0967(14) Å, b=9.6020(13) Å, c=19.319(2) Å, β=90.982(4)°, V=2058.2(5) Å^3, Z=4, ϱ_{cald}=1.324 Mg m^{-3}, μ=0.158 mm^{-1}, F(000)=856, 2 θ_{max}=50.0°, 22128 reflections, 3633 independent reflections [R_{int}=0.0525], R1=0.0428, wR2=0.0921 and GOF=1.024 for 3633 reflections (347 parameters) with I>2 σ(I), R1=0.0763, wR2=0.1078 and GOF=1.024 for all reflections, max/min residual electron density +0.290/−0.311 e Å^{-3}. Crystallographic Data for **11 j**: $C_{19}H_{15}N_2O_2P$, M=334.30, 0.12×0.09×0.04 mm, T=223(2) K, Triclinic, space group P-1, a=8.4050(3) Å, b=10.5908(4) Å, c=20.2049(7) Å, α=103.100(2)°, β=94.314(3)°, γ=109.365(2)°, V=1630.36(11) Å^3, Z=4, Z'=2, ϱ_{cald}=1.362 Mg m^{-3}, μ=1.607 mm^{-1}, F(000)=696, 2 θ_{max}=134.32°, 18 307 reflections, 5681 independent reflections [R_{int}=0.0529], R1=0.0544, wR2=0.1447 and GOF=1.050 for 5681 reflections (553 parameters) with I>2 σ(I), R1=0.0738, wR2=0.1576 and GOF=1.050 for all reflections, max/min residual electron density +0.742/−0.441 e Å^{-3}. CCDC 1416795 and 1416794 contain the supplementary crystallographic data for this paper. These data can be obtained free of charge from The Cambridge Crystallographic Data Centre via www.ccdc.cam.ac.uk/data_request/cif.

The azaphosphinine ring in **10j** shows only small deviations from planarity (RMSD 0.014 Å). Analysis of crystal structure and computational models (see the Supporting Information) indicates that the enhanced stability of **10j** to hydrolysis is likely due to coplanarity of pyridine and the azaphosphinine ring, held by a weak hydrogen bond between the hydrogen atom on C(2) and the pyridine nitrogen atom. This conformation limits water addition at phosphorus, since attack would likely occur 180° from the P=N bond. Phosphates hydrolyze via an associative mechanism, thus making a dissociative pathway unlikely.[16] Moreover, the S_N2-type displacement that is commonly found for alkyl phosphonates cannot occur with the phenyl substituents within **10**.

Interestingly, the amidate-type structures tend to crystallize as dimers between the two enantiomers, forming a complementary association between the N-H and P=O groups (**Figure 5.3, 5.4**), with correspondingly short intermolecular distances (N···O 2.837-2.840 Å in **11j**) and nearly linear N-H···O angles (164-174°). This dimer formation is mirrored in solution, since compound **11b** possesses a dimerization constant (K_{dim}) of 130±4 M^{-1} in $CDCl_3$. This corresponds to an energy of ca. 1.5 kcal mol^{-1} per H bond, which is large compared to *cis* amides such as pyrrolidone or caprolactam, which show dimerization constants in the range 1–5 M^{-1} in $CHCl_3$.[17]

Along with phosphonamidates possessing both a stronger hydrogen-bond acceptor (P=O vs. C=O) and a stronger hydrogen-bond donor (P(O)N-H vs. C(O)N-H) than amides, the non-coplanar arrangement of donor/acceptor and lower directional preference of P=O donors allow the pseudo 6-membered ring to adopt a chair conformation and minimize repulsive secondary interactions (**Figure 5.4 a,b**).[18]

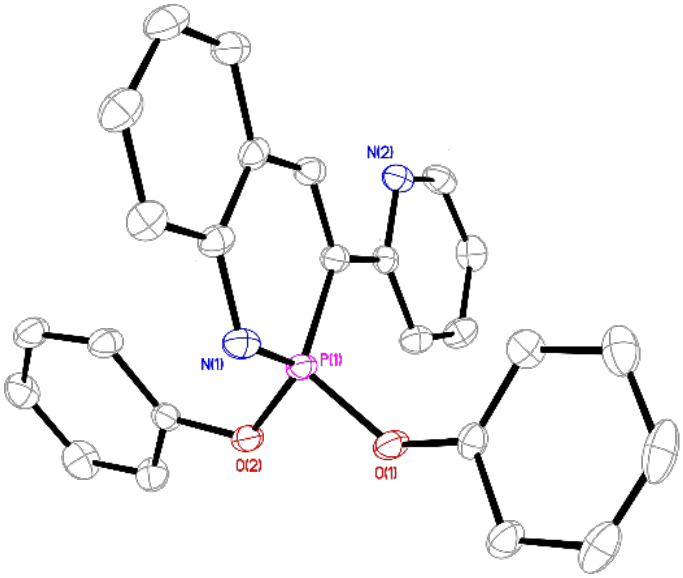

Figure 5.2. X-ray crystal structure of **10j**.

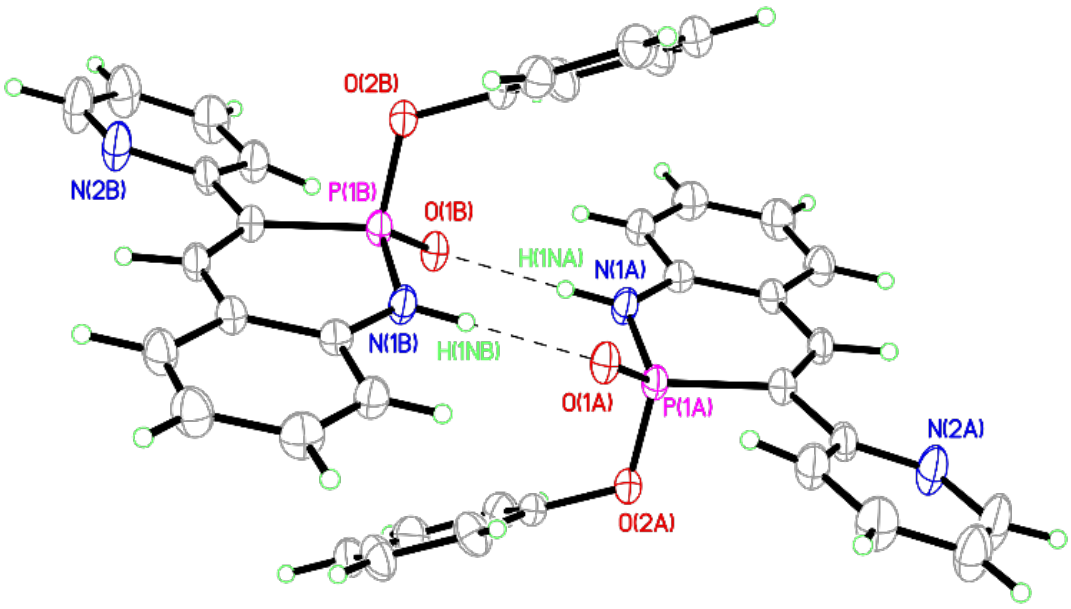

Figure 5.3. ORTEP of the dimer of **11j**.

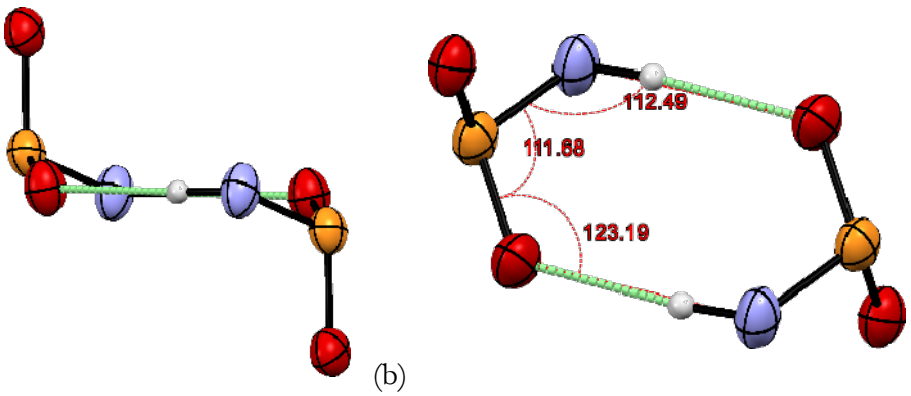

(a) (b)

Figure 5.4. (a) An angled view, with C atoms removed for clarity, shows the chair conformation of H-bonding ring. (b) A view from above the ring with relevant bond-angles demonstrates their similarity to idealized chair-conformation angles.

As a result, this dimer deviates from the trends noted by Schneider and Sartorius, where each attractive interaction gives −1.88 kcal mol^{-1} of energy to ΔG, and each repulsive secondary interaction gives +0.74 kcal mol^{-1}.[19] Following the same scheme, two repulsive secondary interactions in our dimer yield only +0.76 kcal mol^{-1} of destabilization, roughly half of what is expected.

The 2-phosphaquinolinone scaffold demonstrates a wide range of fluorescent emission wavelengths (383–554 nm), dependent on substitution and protonation state (**Figure 5.5, 5.6** and **Table 5.3**). The fluorescence behavior is similar to that of carbostyril, although somewhat red-shifted (3-phenylcarbostyril ex: 345 nm, em: 410 nm; **11e** ex: 354 nm, em: 427 nm).[22]

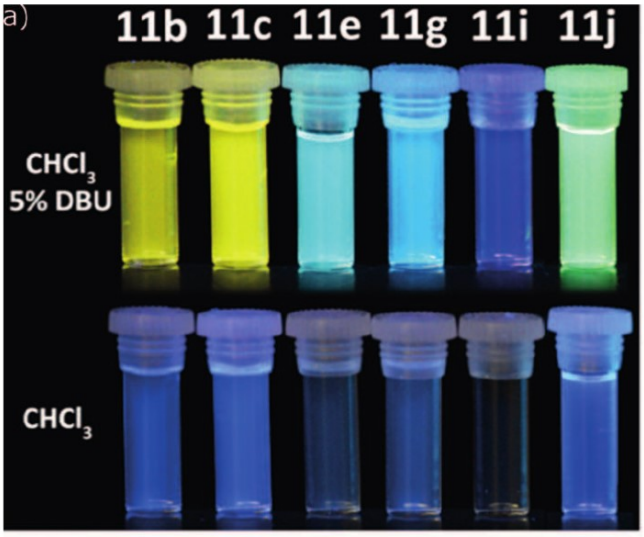

Figure 5.5. Images of the fluorescence of 2-phosphaquinolin-2-ones under neutral and basic conditions.

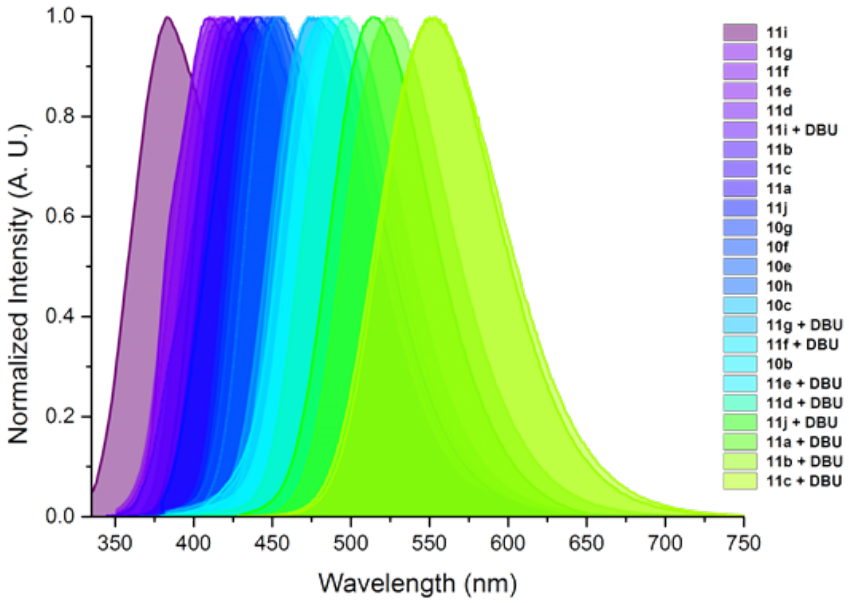

Figure 5.6. Graphical depiction of the differing emissions of 2-phosphaquinolines and 2-phosphaquinolin-2-ones in $CHCl_3$ and upon the addition of 1,8-diazabicyclo[5.4.0]undec-7-ene (DBU), demonstrating the emission range from UV to yellow.

Entry[a]	**10**	**11**	**11 + DBU**
a	---	349, 434, 85	395, 523, 128
b	400, 483, 83	349, 430, 81	417, 554, 137
c	383, 473, 90	351, 432, 81	402, 553, 151
d	---	359, 422, 63	373, 499, 126
e	373, 453, 80	342, 418, 76	364, 491, 127
f	369, 450, 81	341, 413, 72	368, 482, 114
g	369, 447, 78	339, 410, 71	366, 473, 107
h	369, 454, 85	---	---
i	---	318, 383, 65	323, 425, 102
j	388, 467, 79	363, 442, 79	412, 514, 102

[a]Each entry listed with excitation maximum, emission maximum, and Stokes shift (nm), in that order.

Table 5.3. Emissive properties of compounds 10 and 11.

Significant differences between the azaphosphinine and carbostyril include: 1) a more dramatic solvatofluorescent effect in azaphosphinines (**11b** $CHCl_3$ em: 430 nm, MeCN em: 450 nm, see Appendix C), and 2) an easily deprotonated amidate N-H, which yields a red-shifted fluorescent response, with the anion possessing a surprisingly large Stokes shift of 102–151 nm, depending upon substitution. Fluorophores possessing such a large Stokes shift are very useful owing to the lack of overlap between excitation and emission, lending promise for their use in imaging/sensing applications.[21] In addition, although the more promising red-shifted derivatives of **11** possess only modest quantum yields (ca. 4–5 %) the anions of those fluorophores show quantum yields in the range of 30–40 %, thus demonstrating their potential for use as fluorescent tags, especially if the design principles for carbostyril fluorophore development were to be followed to further red-shift emission and increase the quantum yield.[22]

CONCLUSION

In summary, we present a facile synthesis of 2-λ^5-phosphaquinoline derivatives from 2-ethynylanilines. The ease of preparation and the range of diverse structures that can be readily accessed will permit detailed examination of this rare class of heterocycles, from the fundamental perspective of the study of the delocalization of $N=P^V$ bonds to applications of the phosphaquinolinones as carbostyril mimics and as novel switchable fluorophores with high quantum yields and large Stokes shifts in the ON state. In addition, the surprisingly large dimerization constant of **11b**, a system bound by only two hydrogen bonds, hints at potential for the phosphaquinolinones as new hydrogen-bonding scaffolds in supramolecular chemistry. Our group is currently working to expand upon these varied and exciting applications.

EXPERIMENTAL

Synthesis of compounds 10b-c, e-h, j

General cyclization method. To a solution of 2-(4'-substituted phenylethynyl)aniline (0.5 mmol) in dry pyridine (1 mL) was added triphenylphosphite (0.6 mmol) under N_2 atmosphere. The reaction was heated to 100 °C for 12 h. After cooling, the volatiles were removed *in vacuo* and the crude material was then purified by preparative HPLC.

Compound 10b – Yield: 54%

^{1}H NMR (500 MHz, $CDCl_3$) δ 8.14 (d, *J* = 40.7 Hz, 1H), 7.87 (d, *J* = 8.0 Hz, 2H), 7.73 (d, *J* = 8.0 Hz, 2H), 7.41-7.35 (m, 2H), 7.23 (d, *J* = 8.2 Hz, 1H), 7.21-7.15 (m, 4H), 7.07 (t, *J* = 7.2 Hz, 2H), 6.94-6.90 (m, 5H). ^{13}C NMR (126 MHz, $CDCl_3$) δ 151.92, 150.25 (d, *J* = 5.7 Hz), 149.95 (d, *J* = 9.9 Hz), 140.54 (d, *J* = 4.2 Hz), 132.96 , 132.23 (d, *J* = 4.7 Hz), 131.59 (d, *J* =

1.7 Hz), 129.87 , 127.75 (d, *J* = 6.0 Hz), 125.42 , 124.91 (d, *J* = 26.1 Hz), 121.45 (d, *J* = 26.4 Hz), 120.66 (d, *J* = 5.2 Hz), 119.02 , 118.80 , 111.46 , 110.55 (d, *J* = 132.1 Hz). ^{31}P NMR (121 MHz, $CDCl_3$) δ 23.78 (d, *J* = 41.7 Hz). HRMS (EI+) calcd for [MH^+] 435.1262, found 435.1270.

Compound 10c – Yield: 54%

^{1}H NMR (500 MHz, $CDCl_3$) δ 8.21-8.10 (m, 3H), 7.84 (d, *J* = 8.1 Hz, 2H), 7.36 (d, *J* = 7.4 Hz, 2H), 7.23 (d, *J* = 8.5 Hz, 1H), 7.16 (t, *J* = 7.8 Hz, 4H), 7.05 (t, *J* = 7.3 Hz, 2H), 6.96-6.89 (m, 5H), 4.42 (q, *J* = 7.1 Hz, 2H), 1.43 (t, *J* = 7.1 Hz, 3H). ^{13}C NMR (126 MHz, $CDCl_3$) δ 166.39, 151.67 (d, *J* = 1.3 Hz), 150.34 (d, *J* = 5.7 Hz), 149.50 (d, *J* = 10.1 Hz), 140.20 (d, *J* = 4.2 Hz), 131.77 (d, *J* = 4.8 Hz), 131.45 (d, *J* = 1.8 Hz), 130.44, 130.05 (d, *J* = 47.4 Hz), 129.78, 127.11 (d, *J* = 6.1 Hz), 125.28 (d, *J* = 0.9 Hz), 124.79 (d, *J* = 25.9 Hz), 121.62 (d, *J* = 26.6 Hz), 120.80 (d, *J* = 5.2 Hz), 118.81, 111.47 (d, *J* = 131.0 Hz), 61.28, 14.52. ^{31}P NMR (202 MHz, $CDCl_3$) δ 24.68 (d, *J* = 41.4 Hz). HRMS (EI+) calcd for [MH^+] 482.1521, found 482.1526.

Compound 10e – Yield: 45%

^{1}H NMR (500 MHz, $CDCl_3$) δ 8.09 (d, J = 41.7 Hz, 1H), 7.75 (d, J = 8.2 Hz, 2H), 7.51 – 7.30 (m, 6H), 7.25 – 7.10 (m, 5H), 7.09 – 6.99 (m, 2H), 6.99 – 6.82 (m, 5H). ^{13}C NMR (126 MHz, $CDCl_3$) δ 151.26 , 150.48 (d, J = 5.6 Hz), 148.65 (d, J = 10.5 Hz), 135.72 (d, J = 4.2 Hz), 131.29, 131.14 (d, J = 2.44 Hz), 129.70 , 129.23 , 128.16 , 127.47 (d, J = 6.0 Hz), 125.13 (d, J = 0.8 Hz), 124.68 (d, J = 25.8 Hz), 121.81 (d, J = 26.6 Hz), 120.87 (d, J = 5.2 Hz), 118.59, 112.91 (d, J = 129.9 Hz). ^{31}P NMR (121 MHz, $CDCl_3$) δ 25.38 (d, *J* = 41.8 Hz). HRMS (EI+) calcd for [MH^+] 410.1310, found 410.1300.

Compound 10f – Yield 63%

^{1}H NMR (500 MHz, $CDCl_3$) δ = 8.07 (d, J = 42.0 Hz, 1H), 7.67 (d, J=7.8 Hz, 2H), 7.35 – 7.30 (m, 2H), 7.27 (m 1H), 7.22 (d, J = 8.3 Hz, 1H), 7.16 (t, J=7.8 Hz, 4H), 7.04 (t, J = 7.3 Hz, 2H), 6.95 (d, J = 8.5 Hz, 4H), 6.89 (t, J = 7.3 Hz, 1H), 2.41 (s, 3H). ^{13}C NMR (126 MHz, $CDCl_3$) δ = 151.06, 150.47 (d, J = 5.5 Hz), 147.91 (d, J = 10.7 Hz), 138.14, 132.68 (d, J = 4.2 Hz), 131.04 (d, J = 1.9 Hz), 130.93 (d, J = 4.7 Hz), 129.96, 129.67, 127.24 (d, J = 6.1 Hz), 125.10 (d, J = 1.1 Hz), 124.57 (d, J = 25.8 Hz), 121.86 (d, J = 26.6 Hz), 120.89 (d, J = 5.2 Hz), 118.54, 112.88 (d, J = 129.7 Hz), 21.37. ^{31}P NMR (202 MHz, CDC_3) δ 25.68 (d, J = 42.0 Hz). HRMS (EI+) calcd for [MH^+] 424.1466, found 424.1454.

Compound 10g – Yield: 56%

^{1}H NMR (500 MHz, $CDCl_3$) δ 8.00 (d, *J* = 42.0 Hz, 1H), 7.69 (d, *J* = 8.4 Hz, 2H), 7.33 (d, *J* = 7.5 Hz, 2H), 7.21 (d, *J* = 8.1 Hz, 1H), 7.15 (t, *J* = 7.7 Hz, 4H), 7.04 (t, *J* = 7.3 Hz, 2H), 6.99 (d, *J* = 8.5 Hz, 2H), 6.94 (d, *J* = 7.9 Hz, 4H), 6.88 (t, *J* = 7.2 Hz, 1H), 3.87 (s, 3H). ^{13}C NMR (126 MHz, $CDCl_3$) δ 159.72, 150.88 (d, J = 1.5 Hz), 150.48 (d, J = 5.4 Hz), 147.27 (d, J = 10.8 Hz), 130.91 (d, J = 1.9 Hz), 130.75 (d, J = 4.6 Hz), 129.69, 128.63 (d, J = 6.2 Hz), 128.03 (d, J = 4.2 Hz), 125.10 (d, J = 0.9 Hz), 121.96 (d, J = 26.7 Hz), 120.87 (d, J = 5.2 Hz), 118.53, 114.68, 112.70 (d, J = 129.3 Hz), 55.52. ^{31}P NMR (121 MHz, $CDCl_3$) δ 25.59 (d, *J* = 41.2 Hz). HRMS (EI+) calcd for [MH^+] 440.1416, found 440.1399.

Compound 10h – Yield: 68%

^{1}H NMR (500 MHz, $CDCl_3$) δ 7.98 (d, *J* = 42.6 Hz, 1H), 7.69 (d, *J* = 8.6 Hz, 2H), 7.35–7.27 (m, 2H), 7.23–7.10 (m, 5H), 7.03 (t, *J* = 7.3 Hz, 2H), 6.97 (d, *J* = 7.6 Hz, 4H), 6.86 (t, *J* = 7.2 Hz, 1H), 6.79 (d, *J* = 8.6 Hz, 2H), 3.03 (s, 6H). ^{13}C NMR (126 MHz, $CDCl_3$) δ 150.55, 150.41 (d, *J* = 24.2 Hz), 145.24 (d, *J* = 11.0 Hz), 130.94–130.46 (m), 130.17 (d, *J* = 4.8 Hz), 129.63 , 128.15 (d, *J* = 6.4 Hz), 125.00, 124.40 (d, *J* = 25.7 Hz), 123.04 (d, *J* = 3.8 Hz),

122.25 (d, *J* = 27.2 Hz), 120.98 (d, *J* = 5.1 Hz), 118.38, 113.83, 112.79 (d, *J* = 4.9 Hz), 40.49. ^{31}P NMR (121 MHz, $CDCl_3$) δ 26.73 (d, *J* = 43.4 Hz). HRMS (EI+) calcd for [MH^+] 453.1732, found 453.1718.

Compound 10j – Yield: 71%

^{1}H NMR (500 MHz, $CDCl_3$) δ 8.83 (d, *J* = 40.7 Hz, 1H), 8.71 (d, *J* = 4.2 Hz, 1H), 7.96 (d, *J* = 8.0 Hz, 1H), 7.77 (t, *J* = 8.4 Hz, 1H), 7.42 (d, *J* = 7.8 Hz, 1H), 7.36 (t, *J* = 8.1 Hz, 1H), 7.26-7.21 (m, 2H), 7.15 (t, *J* = 7.8 Hz, 4H), 7.07-6.94 (m, 6H), 6.89 (t, *J* = 7.3 Hz, 1H). ^{13}C NMR (126 MHz, $CDCl_3$) δ 153.01 (d, *J* = 7.3 Hz), 152.17 (d, *J* = 1.2 Hz), 150.36 (d, *J* = 5.4 Hz), 150.07 (d, *J* = 8.6 Hz), 149.96, 136.93, 131.87 (d, *J* = 1.9 Hz), 131.79 (d, *J* = 4.8 Hz), 129.58, 125.04, 124.55 (d, *J* = 25.8 Hz), 122.37, 121.68 (d, *J* = 2.9 Hz), 121.43 (d, *J* = 26.1 Hz), 120.78 (d, *J* = 5.2 Hz), 118.57, 110.90 (d, *J* = 133.1 Hz). ^{31}P NMR (202 MHz, $CDCl_3$) δ 25.97 (d, *J* = 40.6 Hz). HRMS (EI+) calcd for [MH^+] 411.1262, found 411.1253.

Synthesis of compounds 11a-g, i, j

To a solution of 2-(4'-substituted phenylethynyl)aniline (0.5 mmol) in dry pyridine (1 mL) was added triphenylphosphite (0.6 mmol) under an ambient atmosphere. The reaction was heated to 100 °C for 12 h. After cooling, the volatiles were removed *in vacuo* and the crude material was then purified by recrystallization from hot ethyl acetate/hexanes under ambient atmosphere to give product. Additionally, one equivalent of water can be added during recrystallization to ensure complete conversion to phosphonamidate forms.

Compound 11a – Yield: 39%

^{1}H NMR (500 MHz, $CDCl_3$) δ 8.44 (s, 1H), 8.22 (s, 2H), 7.87 (s, 1H), 7.65 (d, *J* = 38.6 Hz, 1H), 7.40-7.36 (m, 2H), 7.13-7.04 (m, 4H), 7.00 (t, *J* = 7.3 Hz, 1H), 6.91 (d, *J* = 7.7 Hz, 2H). ^{13}C NMR (126 MHz, $CDCl_3$) δ 150.13 (d, *J* = 8.9 Hz), 143.85 (d, *J* = 5.0 Hz), 140.21 (d, *J* = 1.9 Hz), 138.12 (d, *J* = 9.4 Hz), 132.31 (q, *J* = 33.3, Hz), 131.46 (d, *J* = 82.1 Hz), 129.61 ,

128.00 , 125.30 , 124.44 , 122.48 (d, J = 52.6 Hz), 122.09–121.76 (m), 121.64 , 121.41 , 121.16 (d, J = 4.1 Hz), 119.60 (d, J = 14.6 Hz), 117.77 (d, J = 9.7 Hz). ^{31}P NMR (202 MHz, $CDCl_3$) δ 10.19 (d, J = 38.7 Hz). HRMS (EI+) calcd for [MH^+] 470.0745, found 470.0761.

Compound 11b – Yield: 79%

^{1}H NMR (500 MHz, $CDCl_3$) δ 8.91 (s, 1H), 7.96 (d, J = 8.0 Hz, 1H), 7.74 (d, J = 8.1 Hz, 1H), 7.66 (d, J = 39.1 Hz, 1H), 7.32 (t, J = 9.0 Hz, 1H), 7.11–7.04 (m, 1H), 6.99 (dt, J = 19.5, 7.5 Hz, 1H), 6.89 (d, J = 7.9 Hz, 1H). ^{13}C NMR (126 MHz, $CDCl_3$) δ 150.27 (d, J = 8.6 Hz), 143.46 (d, J = 5.3 Hz), 140.44 (d, J = 9.6 Hz), 140.18, 132.79, 131.56, 131.08, 129.59, 128.42 (d, J = 6.7 Hz), 125.20, 122.88 (d, J = 159.7 Hz), 121.54, 121.17 (d, J = 4.3 Hz), 119.60 (d, J = 14.9 Hz), 118.85, 117.62 (d, J = 9.6 Hz), 111.93. ^{31}P NMR (121 MHz, $CDCl_3$) δ 10.34 (d, J = 39.0 Hz). HRMS (EI+) calcd for [MH^+] 359.0944, found 359.0949.

Compound 11c – Yield: 74%

^{1}H NMR (500 MHz, $CDCl_3$) δ 8.65 (s, 1H), 8.13 (d, J = 8.2 Hz, 2H), 7.92 (d, J = 8.0 Hz, 2H), 7.67 (d, J = 39.7 Hz, 1H), 7.35–7.27 (m, 2H), 7.12–7.02 (m, 3H), 7.02–6.94 (m, 2H), 6.90 (d, J = 7.9 Hz, 2H), 4.42 (q, J = 7.1 Hz, 2H), 1.43 (t, J = 7.1 Hz, 3H). ^{13}C NMR (126 MHz, $CDCl_3$) δ 166.46, 150.45 (d, J = 9.1 Hz), 142.80 (d, J = 5.4 Hz), 140.20 (d, J = 9.1 Hz), 140.08 (d, J = 2.0 Hz), 131.01 (d, J = 28.2 Hz), 130.26, 129.51 (d, J = 1.0 Hz), 127.80, 127.75, 125.04 (d, J = 1.3 Hz), 123.74 (d, J = 159.6 Hz), 121.32, 121.31, 121.28, 119.78 (d, J = 14.5 Hz), 117.52 (d, J = 9.5 Hz), 61.26, 14.52. ^{31}P NMR (121 MHz, $CDCl_3$) δ 10.93 (d, J = 40.2 Hz). HRMS (EI+) calcd for [MH^+] 406.1208, found 406.1227.

Compound 11d – Yield: 80%

^{1}H NMR (500 MHz, $CDCl_3$) δ 8.83 (s, 1H), 7.81 (d, J = 7.7 Hz, 2H), 7.60 (d, J = 39.9 Hz, 1H), 7.46 (d, J = 8.5 Hz, 2H), 7.37 – 7.27 (m, 3H), 7.10 (t, J = 7.9 Hz, 2H), 7.06 (d, J = 8.1 Hz, 1H), 7.03 – 6.96 (m, 2H), 6.93 (d, J = 8.3 Hz, 2H). ^{13}C NMR (126 MHz, $CDCl_3$) δ

150.35 (d, J = 9.1 Hz), 141.82 (d, J = 5.8 Hz), 139.78 (d, J = 2.4 Hz), 134.48, 134.08 (d, J = 9.1 Hz), 130.70 (d, J = 1.4 Hz), 130.53 (d, J = 2.2 Hz), 129.36 (d, J = 1.4 Hz), 129.14, 129.08 (d, J = 6.2 Hz), 124.88 (d, J = 1.9 Hz), 123.25 (d, J = 159.7 Hz), 121.15 (d, J = 4.3 Hz), 121.12, 119.65 (d, J = 14.9 Hz), 117.37 (d, J = 9.6 Hz). ^{31}P NMR (202 MHz, $CDCl_3$) δ 11.35 (d, J = 39.8 Hz). HRMS (EI+) calcd for [MH^+] 368.0607, found 368.0598.

Compound 11e – Yield: 72%

^{1}H NMR (500 MHz, DMSO-d_6) δ 9.95 (s, 1H), 7.93 – 7.81 (m, 3H), 7.47 (t, J = 7.4, 7.4 Hz, 2H), 7.40 (t, J = 7.4, 7.4 Hz, 1H), 7.30 (t, J = 7.5, 7.5 Hz, 1H), 7.20 (t, J = 7.9, 7.9 Hz, 2H), 7.15 (t, J = 7.8, 7.8 Hz, 1H), 7.05 (d, J = 7.8 Hz, 1H), 6.96 (t, J = 7.4, 7.4 Hz, 1H), 6.86 (d, J = 8.1 Hz, 2H), 6.74 (d, J = 8.5 Hz, 1H).^{13}C NMR (126 MHz, $CDCl_3$) δ 157.70, 150.84 (d, *J* = 9.1 Hz), 141.38 (d, *J* = 5.3 Hz), 140.54 (d, *J* = 2.4 Hz), 135.89 (d, *J* = 9.6 Hz), 131.11 (d, *J* = 38.4 Hz), 129.99, 129.85, 129.30, 128.71, 127.82 (d, *J* = 6.2 Hz), 125.21, 124.42 (d, *J* = 155.4 Hz), 121.31 (d, *J* = 4.3 Hz), 120.93, 119.75 (d, *J* = 14.9 Hz), 119.31, 116.76 (d, *J* = 9.6 Hz), 115.68. ^{31}P NMR (121 MHz, DMSO-d_6) δ 9.72 (d, *J* = 39.6 Hz). HRMS (EI+) calcd for [MH^+] 334.0997, found 334.0990.

Compound 11f – Yield 82%

^{1}H NMR (500 MHz, $CDCl_3$) δ 8.44 (s, 1H), 7.74 (d, J = 7.8 Hz, 2H), 7.57 (d, J = 40.5 Hz, 1H), 7.28 (d, J = 7.9 Hz, 3H), 7.23 (d, J = 7.9 Hz, 1H), 7.07 (t, J = 7.8 Hz, 2H), 7.01 (d, J = 8.1 Hz, 1H), 6.94 (dd, J = 17.5, 8.1 Hz, 4H), 2.42 (s, 3H). ^{13}C NMR (126 MHz, $CDCl_3$) δ 150.66 (d, J = 9.1 Hz), 140.92 (d, J = 6.2 Hz), 139.77 (d, J = 1.8 Hz), 138.50, 132.81 (d, J = 9.1 Hz), 130.42 (d, J = 1.2 Hz), 130.31 (d, J = 1.2 Hz), 129.80, 129.40, 127.81 (d, J = 6.6 Hz), 124.83 (d), 124.73 (d, J = 158.3 Hz), 121.41 (d, J = 4.1 Hz), 121.07, 120.08 (d, J = 14.7 Hz), 117.35 (d, J = 9.4 Hz), 21.44. ^{31}P NMR (202 MHz, $CDCl_3$) δ 11.51 (d, J = 40.6 Hz). HRMS (EI+) calcd for [MH^+] 348.1153, found 348.1155.

Compound 11g – Yield: 66%

^{1}H NMR (500 MHz, DMSO-d_6) δ 9.89 (s, 1H), 7.84–7.73 (m, 3H), 7.45 (d, *J* = 7.0 Hz, 1H), 7.28 (t, *J* = 7.9 Hz, 2H), 7.21 (t, *J* = 7.9 Hz, 1H), 7.15 (d, *J* = 7.7 Hz, 1H), 7.08–7.03 (m, 4H), 6.95 (t, *J* = 7.5 Hz, 1H), 6.87 (d, *J* = 8.1 Hz, 1H), 3.81 (s, 3H). ^{13}C NMR (126 MHz, DMSO-d_6) δ 160.01, 150.67 (d, J = 9.0 Hz), 140.27 (d, J = 6.3 Hz), 139.68 (d, J = 1.8 Hz), 130.24 (d, J = 20.3 Hz), 129.67, 129.39, 129.20 (d, J = 6.7 Hz), 128.14 (d, J = 9.1 Hz), 124.83 (d, J = 1.1 Hz), 124.15 (d, J = 158.3 Hz), 121.40 (d, J = 4.1 Hz), 121.02, 120.07 (d, J = 14.7 Hz), 117.39 (d, J = 9.6 Hz), 115.57, 114.55, 55.53.^{31}P NMR (121 MHz, DMSO-d_6) δ 9.97 (d, *J* = 40.3 Hz). HRMS (EI+) calcd for [MH^+] 364.1103, found 364.1096.

Compound 11i – Yield: 73%

^{1}H NMR (500 MHz, $CDCl_3$) δ 7.82 (s, 1H), 7.21 (q, J = 6.5, 6.5, 6.2 Hz, 3H), 7.18 – 7.13 (m, 3H), 7.02 (dd, J = 15.3, 7.7 Hz, 3H), 6.95 (t, J = 7.6, 7.6 Hz, 2H), 2.60 (dtdd, J = 40.1, 15.2, 9.3, 5.7 Hz, 2H), 1.74 (qt, *J* = 16.1, 7.4 Hz, 2H), 1.47–1.31 (m, 4H), 0.91 (t, *J* = 6.9 Hz, 3H). ^{13}C NMR (126 MHz, $CDCl_3$) δ 150.72 (d, *J* = 9.2 Hz), 140.94 (d, *J* = 7.3 Hz), 139.31 (d, *J* = 1.8 Hz), 129.80 (d, *J* = 1.4 Hz), 129.60 (d, *J* = 1.6 Hz), 129.57, 125.58, 124.73, 121.08 (d, *J* = 4.3 Hz), 121.02, 120.17 (d, *J* = 15.8 Hz), 117.31 (d, *J* = 9.1 Hz), 31.63, 31.16 (d, *J* = 8.7 Hz), 29.02 (d, *J* = 4.7 Hz), 22.62 , 14.19 . ^{31}P NMR (202 MHz, $CDCl_3$) δ 13.16 (dt, *J* = 30.3, 15.4 Hz). HRMS (EI+) calcd for [MH^+] 328.1466, found 328.1450.

Compound 11j – Yield: 31%

11j: ^{1}H NMR (500 MHz, $CDCl_3$) δ 8.71 (d, *J* = 4.1 Hz, 1H), 8.55 – 8.44 (m, 2H), 8.19 (d, *J* = 8.0 Hz, 1H), 7.78 (t, *J* = 7.7 Hz, 1H), 7.41 (d, *J* = 7.7 Hz, 1H), 7.32 – 7.27 (m, 1H), 7.22 (t, *J* = 7.8 Hz, 1H), 7.09 (m, 2H), 7.03 (d, *J* = 8.1 Hz, 1H), 7.00 – 6.95 (m, 2H), 6.90 (t, *J* = 8.1 Hz, 1H), 6.84 (d, *J* = 8.3 Hz, 1H).^{13}C NMR (126 MHz, $CDCl_3$) δ 152.64 (d, *J* = 14.4 Hz), 150.71 (d, *J* = 9.1 Hz), 150.02, 143.72 (d, *J* = 4.2 Hz), 140.70 (d, *J* = 2.4 Hz), 137.12, 131.51

(d, *J* = 1.2 Hz), 131.25 (d, *J* = 1.5 Hz), 129.48 (d, *J* = 1.2 Hz), 124.93 (d, *J* = 1.5 Hz), 123.26 (d, *J* = 2.3 Hz), 123.00, 122.68 (d, *J* = 162.0 Hz), 121.39 (d, *J* = 4.1 Hz), 121.17, 119.64 (d, *J* = 14.5 Hz), 117.40 (d, *J* = 9.6 Hz). ^{31}P NMR (202 MHz, $CDCl_3$) δ 12.40 (d, *J* = 39.2 Hz). HRMS (EI+) calcd for [MH^+] 335.0949, found 335.0959.

Synthesis of compounds 9a-b

General Sonogashira method. To a N_2 sparged 300 mM solution of bromoarene in 1:1 THF:DIPA was added 1 mol% $Pd(PPh_3)_4$ and CuI, followed by 2-ethynylaniline (1.0 equiv). Solution was heated to 50 °C for 12 hours under N_2 atmosphere, whereupon volatiles were removed under vacuum, then purified via flash chromatography.

Compound 9a – Yield: 71%

^{1}H NMR (500 MHz, $CDCl_3$) δ 7.94 (s, 2H), 7.81 (s, 1H), 7.39 (d, J = 7.9 Hz, 1H), 7.20 (t, J = 7.8 Hz, 1H), 6.82 – 6.64 (m, 2H), 5.30 (s, 2H). ^{13}C NMR (126 MHz, $CDCl_3$) δ 148.30, 132.66, 132.15 (q, J = 33.7 Hz), 131.60 – 131.18 (m), 130.96, 125.85, 123.11 (q, J = 272.8 Hz), 121.77 – 121.21 (m), 118.32, 114.76, 106.48, 91.78, 89.85. HRMS (EI+) calcd for [MH^+] 330.0717, found 330.0718.

Compound 9b – Yield: 83%

^{1}H NMR (500 MHz, $CDCl_3$) δ 7.64 (dt, J = 8.1, 1.7, 1.7 Hz, 1H), 7.59 (dd, J = 6.5, 1.8 Hz, 1H), 7.36 (dt, J = 7.9, 1.5, 1.5 Hz, 1H), 7.21 – 7.15 (m, 0H), 6.80 – 6.69 (m, 1H), 3.71 (s, 2H). ^{13}C NMR (126 MHz, $CDCl_3$) δ 148.20, 132.57, 132.23, 131.98, 130.81, 128.42, 118.67, 118.29, 114.69, 111.48, 106.88, 93.26, 90.76.

HRMS (EI+) calcd for [MH^+] 219.0922, found 219.0929.

Compounds 9c-j were synthesized as previously reported [23-27]

BRIDGE TO CHAPTER VI

In this chapter we explored the properties of the 2-λ^5-phosphaquinoline scaffold and explored the functional group tolerance of the new reaction to easily form it. We found that they display rich photophysical and supramolecular behaviors in the solid-state and in solution. In Chapter VI we explore the mechanism that the reaction undertakes in the formation of this heterocycle. In addition, the effects of the electronic modulation of the scaffold on the emissive and supramolecular properties of the scaffold are studied through Hammett correlations of both the dimerization behavior and the pK_a of the scaffold. This will allow the full use of this scaffold as both a fluorophore and a supramolecular subunit for self-assembly purposes.

CHAPTER VI

ADDITIONAL ANALYSES OF THE SYNTHESIS AND PROPERTIES OF THE AZAPHOSPHININE SCAFFOLD

Airlia Shonkwiler performed the synthesis and isolation of the new compounds disclosed within, in addition to a large portion of the supramolecular titration studies. Dr. Lev N. Zakharov solved diffraction data for the x-ray crystallographic structures disclosed. Principle investigators Prof. Darren W. Johnson and Prof. Michael M. Haley provided editorial support and enabled the research described herein.

INTRODUCTION

As seen in Chapter V, the previously reported synthesis of the 2-λ^5-azaphosphinine demonstrated the reaction scope and general tolerances by variation of the appended ethynyl arene. We found that the new reaction would tolerate a variety of functional groups present in the molecule, and behaved well for both electron-rich and electron-poor arenes, and alkyl functionality at the 3-position of the final heterocycle. What we also observed was that the fluorescence behavior of the scaffold varied greatly depending on the protonation state of the azaphosphinine functionality and the electronics of the appended arene, with electron-poor aromatic rings demonstrating significant red-shifts in the compounds' emission.

In this chapter we report further studies into the electronics of the system, substituent effects at differing positions within the ring system on the fluorescence and supramolecular behaviors of the compound. Respectful of the supramolecular chemistry, we

have determined the dimerization constants for a full range of functionalities in the appended arene beyond the initially determined dimerization constant for the 4-cyanophenyl functionality, and discuss this in context of a Hammett relationship. We determined the extent to which we can engineer the supramolecular behaviors of the system through the appended phenyl ring. The dimerization constants were then improved to a higher level through judicious choice of substituents appended to the scaffold.

Full analysis of the dimerization constants demonstrated the effects of substitution on both the donor-ability of the P=O functionality and the acidity of the N-H functionality in the azaphosphinine ring. Using the Hammett correlations, we established the ρ value for the dimerization constant. We then determined the fractional effect of the appended arene on the azaphosphinine scaffold through measurement of the pK_a of the N-H proton, established the Hammett relationship, and compared the ρ-values for dimerization and pK_a. Lastly, we have approached the mechanism of the reaction to form the azaphosphinine ring experimentally, and determined a satisfactory description of the likely mechanistic steps through a combination of rational analysis and experimental investigations.

REACTION INVESTIGATIONS

We explored the scope and the functional group tolerance of a set of substrates for this transformation in Chapter V. As discussed previously, the combination of ketones, amines, and phosphites is known as a Kabachnik-Fields condensation, which competes with the target cyclization. Nitro groups are reduced by phosphites, resulting in their incompatibility. The reaction would not tolerate either silicon-substituted substrates or terminal alkynes, however. As the transformation produces one equivalent of phenolate, the

strength of the silicon oxygen bond likely resulted in facile alkyne deprotection under the reaction conditions, forming a terminal alkyne.

This led to the question, why do terminal alkynes not form the target compounds? To answer this question, we must approach a mechanism for the transformation. The best manner of approaching this is to examine which bonds are formed and broken during the course of the reaction.

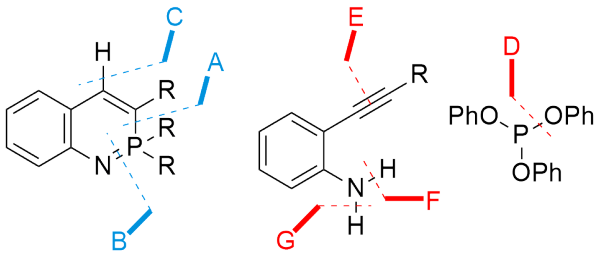

Figure 6.1. Demonstration, for the sake of discussion, which bonds are broken and formed during the course of the reaction.

The formation of bond C (**Figure 6.1**) and cleavage of bond E requires an acidic proton, of which there are none when the reaction initiates, so it cannot be the first step. The addition of the phosphorous atom to the alkyne resulting in the formation of bond A could occur prior to any other steps; however, if it were a conjugate addition, it would not preferentially occur aligned in the way it is depicted as the conjugate addition would form a negative charge next to an electron-withdrawing group, as in the case of the electron-poor arenes. Thus, the most reasonable first step is attack by nitrogen on the phosphorous atom, resulting in the initial formation of the single P-N bond, the ortho ethynyl diphenyl phosphoramidite, which requires the formation of bond B and cleavage of bond D/F. Formation of this phosphoramidite, labeled Intermediate A (**Figure 6.2**), can occur by a number of pathways.

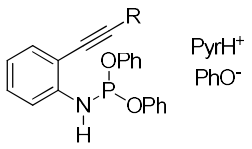

Intermediate A

Figure 6.2. The proposed intermediate species formed during the course of the reaction: a diphenyl phosphoramidite, and one equivalent of pyridinium phenolate.

As can be seen in **Figure 6.3**, the proposed pathways to form Intermediate A are as follows: the neutral aniline can attack triphenylphosphite at the phosphorous atom, either followed by an S_N2 elimination of phenolate, or formation of an -ate complex at phosphorous. The resultant ammonium phosphoramidite can then undergo deprotonation to result in Intermediate A, or the -ate complex can then be deprotonated followed by elimination of phenolate, or these steps could occur in the opposite order. These steps depicted in this figure are unlikely, due to the poor nucleophilicity of neutral anilines. Though phenolate is a proficient leaving group, it is not a good enough leaving group to activate aniline as a nucleophile; thus, the pathways depicted here can be ruled out.

A more reasonable alternative is the deprotonated aniline attacking the triphenylphosphite (**Figure 6.4**). Under basic conditions, this is more likely, as the pyridine can deprotonate a small portion of the aniline, which then undergoes nucleophilic attack on the triphenylphosphite, eliminating an equivalent of phenolate.

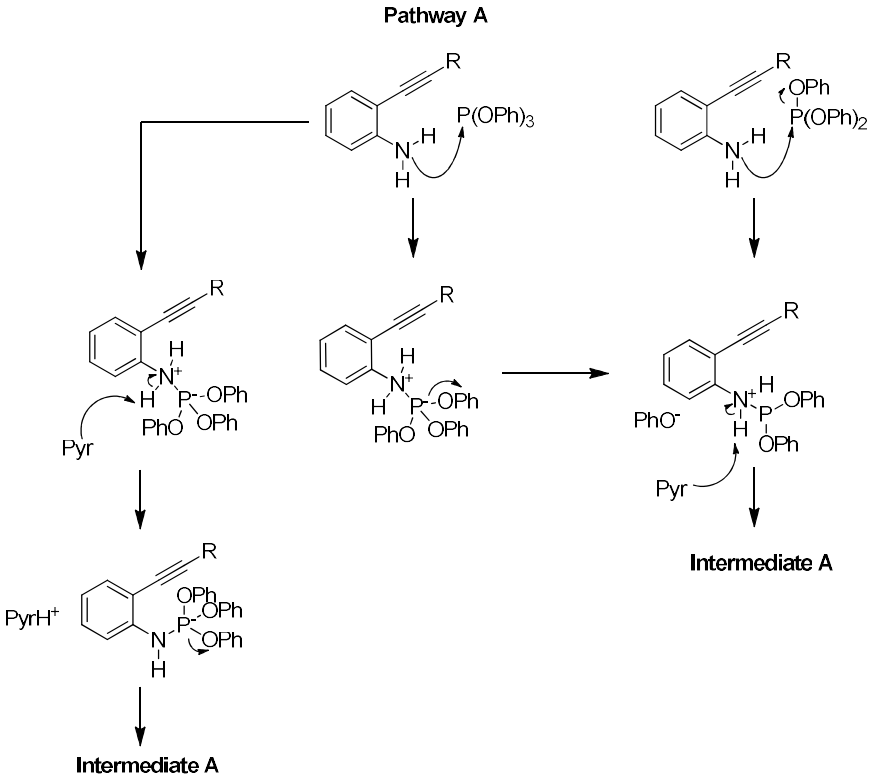

Figure 6.3. Illustration of the first mechanistic pathway that the reaction can take to form Intermediate A, involving attack of the neutral aniline on triphenylphosphite, followed by either S_N2 elimination of phenolate or formation of an ate complex, which after deprotonation results in the first proposed intermediate.

It is under dispute in the literature whether nucleophilic attack at phosphite centers results in an -ate complex followed by elimination, or simply an S_N2 mechanism, especially in the case of a mediocre leaving group like phenolate; the difference in this case, however, is trivial.

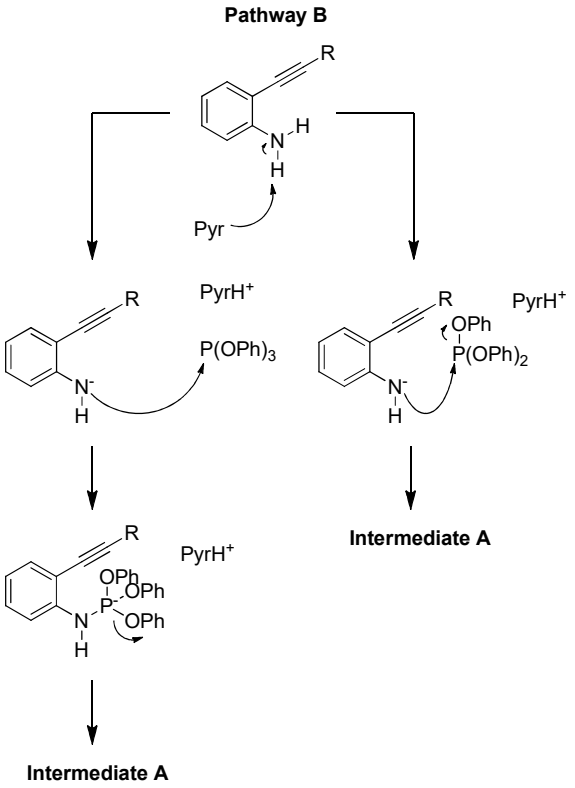

Figure 6.4. Initial deprotonation of the aniline results in a good nucleophile, which can attack the triphenylphosphite and eliminate phenolate.

This pathway does require pyridine deprotonating an aniline, which, though possible, is an unlikely occurrence from a pK_a perspective (aniline pK_a = 25, pyridinium pK_a = 9). As an alternative, the pyridine could add to triphenylphosphite, acting in a manner analogous to an acyl transfer mechanism, activating it with a better leaving group for attack by the aniline/anilide. To investigate this possibility, the same reaction was attempted utilizing a non-nucleophilic amine, N,N-diisopropylethylamine. Surprisingly, we found that the reaction only proceeded in the presence of a nucleophilic amine as N,N-diisopropylethylamine, which has too much steric bulk to act as a nucleophile, resulted in no target product. This result lends credence to the action of pyridine as a pseudo-phosphorous transfer agent during the course of the reaction. Once the resultant phosphoramidinium is formed, it is able to be

deprotonated by pyridine, much more likely than deprotonation of an aniline. This results in an initial reaction pathway as follows in **Figure 6.5**.

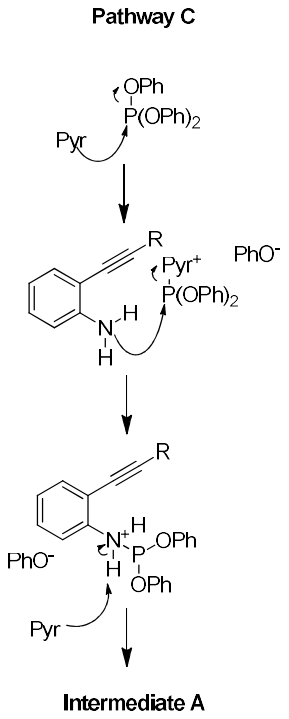

Figure 6.5. The use of a nucleophilic base, in this case pyridine, activates the triphenylphosphite toward attack by the aniline.

Intermediate A then must form one new P-C bond (**Figure 6.1**, bond A) and one new C-H bond (**Figure 6.1**, Bond C). Again, the P-C bond must form before the C-H bond, as a much stronger acid than pyridinium must be present to protonate a free alkyne. Additionally, if a carbocation were to form from protonation of the alkyne prior to the intramolecular cyclization, it would be likely to also produce an indole as the nitrogen added to the carbocation. No indoles were observed as side-products of this reaction; thus, the following pathways forward to the final product are possible (**Figure 6.6**).

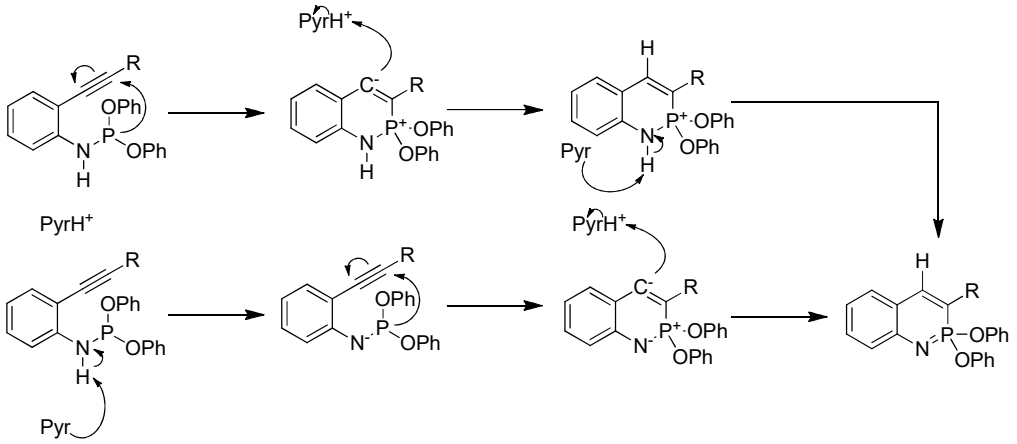

Figure 6.6. Forward reaction demonstrating the cyclization, protonation and deprotonation sequence of the final stage of the reaction.

Although pyridine could deprotonate the phosphoramidite first, increasing the nucleophilicity of the phosphorous atom, the more likely sequence is for the neutral phosphoramidite, already a good nucleophile, to attack the alkyne. Phosphoramidites are not very acidic, nor do they need activation to act as a nucleophile; in fact, the addition of phosphites to alkynes at elevated temperatures has been a known reaction for some time.[1] Additionally, the upper pathway in **Figure 6.6** develops less charge overall during the course of the reaction, making it more likely. Rationally, then, there is one dominant path for the formation of the azaphosphinine ring from o-ethynylanilines and triphenylphosphite in the presence of pyridine. (**Figure 6.7**)

To return to our initial queries as to the origin of the failure of the reaction to produce an azaphosphinine upon reaction with either terminal or silyl-protected alkynes, the mechanistic steps above must be considered.

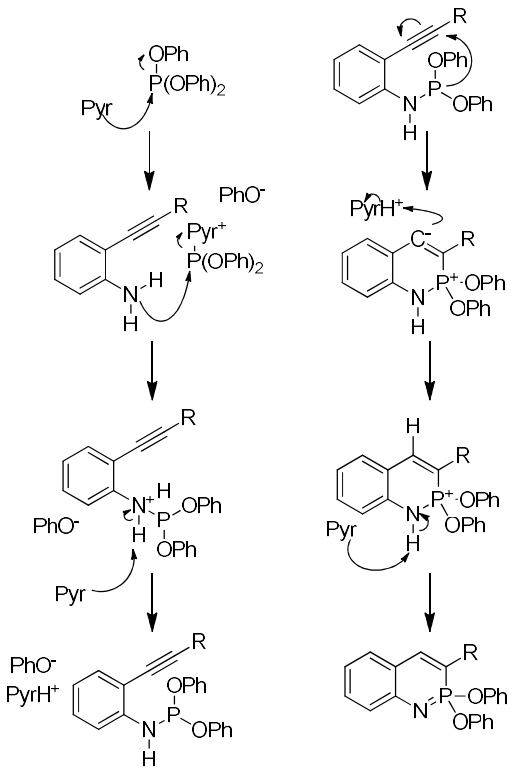

Figure 6.7. Overall mechanism of azaphosphinine cyclization reaction.

As phenolate is being produced in the reaction, the strength of the O-Si bond formed from attack of phenolate on the silicon center leads to cleavage of the sp C-Si bond, resulting in an acetylide anion. This acetylide would discourage cyclization in the final step, as the addition of a nucleophile to the terminal carbanion would be highly disfavoured. Similarly, as the pKa for terminal acetylenes (~25) and anilines (~25) is approximately the same, under conditions where the anilide can be formed, the acetylide can also be formed. As the acetylide is a proficient nucleophile which can itself add to the phosphorous center, it likely consumes some amount of triphenylphosphite[2] as well as discourages the final cyclization steps.

Overall we have broached the mechanism of this reaction experimentally through these initial investigations. The need of a nucleophilic base during the course of the reaction

enforces the presence of an activated phosphorous as the active electrophilic species in the initial addition of the aniline to the phosphorous center. We now have a passing understanding of the mechanism by which this heterocycle forms. With this knowledge, and the understanding gained through an analysis of the bond length alternation and conjugation throughout the scaffold, we turn to an understanding of the effects of differing substitution patterns on the supramolecular behavior of this scaffold.

SUPRAMOLECULAR INVESTIGATIONS

The dimerization interaction of the azaphosphinine scaffold is an intriguing one. It offers the ability to engineer materials that self-assemble based upon the induced fit of the materials with themselves, which have broad use as stimuli responsive materials as well as potential use in organic electronics. As reported in Chapter V, we found that the dimerization constant of the azaphosphinine scaffold dwarfed that of the analogous cis-amides. Amides are the dominant structural hydrogen bond donor-acceptor pair used throughout nature, and since the azaphosphinine outperformed the amide so well for dimer formation, we thought it prudent to fully understand the origins and electronic effects of substituents on the dimerization constant. Understanding what structural features increase or decrease the dimerization constant due to electronic participation would allow us to engineer this material for a variety of applications.

During our initial investigations, we synthesized a set of azaphosphinines with a range of electron-withdrawing and electron-donating substituents on the appended phenyl ring. Such a family of compounds lends itself easily to analysis through a Hammett relationship. This set of compounds could be subjected to dimerization studies in full, and then the correlation with the strength of the dimerization event with the electron-

withdrawing or -donating nature of the substituents could be related. In such a fashion, we could then understand the different conjugative pathways within the heterocycle.

The appended arene could be seen to electronically affect either the phosphorous atom or the nitrogen atom within the heterocycle. Since this dimerization is the formation of a homo-dimer, there are two factors at play, both the electron density and donor ability of the oxygen attached to the phosphorous, which if increased would enhance its propensity to act as a hydrogen bond donor; however, the nitrogen atom would strengthen the dimerization interaction if it were more acidic, and thus had less electron density. It is a delicate interplay of electron density between the two functional groups, and the Hammett correlation could help to tease this relationship out; therefore, if electron-donating groups were to decrease the dimerization constant, then we would know that the nitrogen is more in direct conjugation with the appended arene, and the phosphorous atom does not participate in the π-system dramatically. In contrast, if electron-donating groups increased the dimerization constant, then the phosphorous atom would be participating in conjugation with the π-system more than would necessarily be expected, with little contribution to resonance with the nitrogen atom.

Through the Hammett correlation of the dimerization constant, we found that the relationship follows a trend indicating an enhanced electron density on the azaphosphinine scaffold during the interaction. The correlation between dimerization constant and σ_{para} was quite good, with $r^2 = 0.88$.;therefore, the more important consideration for the dimerization interaction is not the density of electrons on the phosphorous atom, but instead the stabilization of negative charge on the nitrogen. We obtained $\varrho = 0.77$ for the Hammett correlation with the dimerization constant. Classically, this is compared to the value obtained for benzoic acid when performing Hammett correlations, which is set where $\varrho = 1$. In the

case of the azaphosphinines, the site where dimerization is occurring is somewhat removed from the rest of the scaffold compared to benzoic acid (**Figure 6.8**).

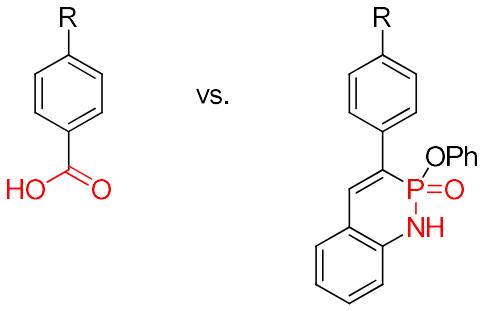

Figure 6.8. Comparison of the structure of classically utilized benzoic acid (left) with the azaphosphinine scaffold studied via Hammett correlations (right).

The nitrogen of the azaphosphinine scaffold is several carbons removed from the appended phenyl ring compared to benzoic acid, though the P=O group is in approximately the same position as the ionisable -OH group. It would be expected then that substituents would have a smaller effect than they do in benzoic acid, resulting in a smaller sensitivity constant. In addition, a formal negative charge is not developed in the dimerization reaction, contrary to the deprotonation of benzoic acid.

With $0<\rho<1$, less negative charge is formed on the azaphosphinine scaffold during the dimerization study compared to benzoic acid, though a significant partial negative charge is still formed (**Figure 6.9**). In compounds with a formal phosphorous-oxygen double bond, the back donation from n-electrons on the oxygen atom to the positively charged phosphorous atom are typically cited as having a major electronic effect on the system.[3] Interestingly, we only see a positive value of ρ in the dimerization. While hydrogen-bond formation will increase the electron density on the nitrogen atom of the azaphosphinine, it will in fact decrease the electron density on the terminal oxygen atom attached to

phosphorous, diminishing its back donation into the phosphorous orbitals. This can result in a synergistic effect between the phosphorous and the nitrogen of the azaphosphinine ring, as the electron-withdrawing capability of the phosphorous atom will increase as the back-donation from the oxide atom decreases. This will in turn stabilize the build-up of charge on the neighbouring nitrogen atom from the hydrogen bond, enhancing the acidity of the N-H group and improving its capabilities as a hydrogen bond donor.

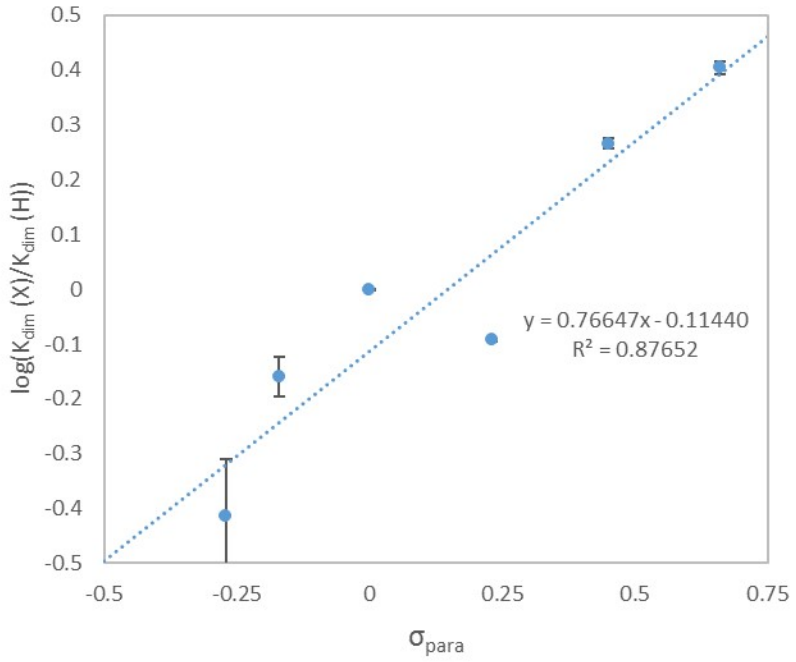

Figure 6.9. Hammett correlation between the dimerization constant of the azaphosphinine scaffold and the σ_{para} value of the substituent on the appended arene, compounds included in this plot presented in Chapter V. Error bars reported as the standard error of the measurement.

This results in a very interwoven system, with individual contributions from the substituents on the appended arene difficult to isolate. Conveniently, there is a simple

method to directly determine the acidity of the N-H proton, without interference from contribution of the P=O functionality. As seen in Chapter V, upon the addition of base, there is a dramatic spectroscopic shift, corresponding to deprotonation of the azaphosphinine scaffold. This provides us with a spectroscopic handle we can use to determine the deprotonation state. If we were to measure the emission intensity as a function of pH, then perform a nonlinear fit with the Hill equation, determination of the pK_a of the heterocycle should be trivial. This will allow us to directly measure the effects of substituents on the appended arene on the N-H group alone, without contribution from the phosphorous oxide functionality.

There is still the question, however, of whether or not there will be dimer present in the solutions where we measure the pK_a of the N-H group. To understand this, we measured the dimerization constant in a polar, competitive solvent, DMSO, in which no shift of the N-H resonance was witnessed, indicating that in more competitive solvents the dimerization is negligible. As we were able to measure the pK_a in aqueous solutions, at low analyte concentration, the amount of dimer present should be nonexistent. Unfortunately, pK_a determination of the entire set of azaphosphinine scaffolds have not yet been performed; however, a subset comprised of one electron withdrawing, one medial, and one electron donating substituent has been determined (**Figure 6.10**).

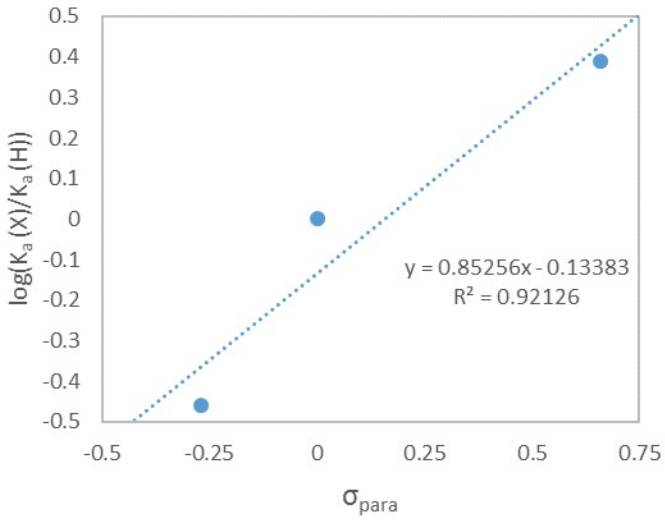

Figure 6.10. Hammett correlation of the pK_a value with the σ_{para} value of the phenyl substituent.

We find that $\rho = 0.85$ is the correlation of the pK_a of the azaphosphinine scaffold with the substituents on the azaphosphinine ring from our limited training set. As a result, we can then determine the differing ability of both the N-H functionality and the P=O functionality to electronically communicate with the groups appended to the phenyl ring in the scaffold. If we consider the ρ_{dim} value to be a linear combination of the contribution of the appended group to the electronics of both N-H hydrogen bond donor and P=O hydrogen bond acceptor, we get the following relationship:

$$\rho_{dim} = \rho_{N\text{-}H} + \rho_{P=O}$$

Where: $\rho_{P=O}$ = sensitivity constant of P=O subunit

$\rho_{N\text{-}H}$ = sensitivity constant of N-H subunit

Here, $\rho_{P=O}$ will have a negative value, as an increase in electron density of the phosphorous-oxide functionality will increase its hydrogen bond acceptor ability, the converse of the effect of substituents on the N-H group. By utilizing the results obtained from pK_a and dimerization studies, we can then determine the effects of substituents on the $\rho_{P=O}$ value, to a first approximation. This yields $\rho_{P=O}$ = -0.08 — practically zero, which is to be expected given that the hybridization of phosphorous is sp^3 in the azaphosphinine ring; as a result, there is very little conjugative communication with substituents on the appended phenyl group. In the engineering of supramolecular scaffolds with this functionality, then, it is paramount to improve the acidity of the nitrogen, whereupon the hydrogen bond acceptor ability of the phosphorous oxide will be unaffected by the changes in the electronics of the system.

With this in mind, the synthesis of an alternate structure was performed, in order to enhance both the dimerization and the pK_a of the azaphosphinine. We had reached the limit of obtaining a large dimerization constant and low pK_a for substitution at the phenyl substituents; however, substitution at the 6-position of the scaffold can then be modified to affect both the pK_a and the dimerization constant significantly, as that position is in a *para* relationship to the nitrogen atom. The 8-position could similarly affect the dimerization and acidity of the nitrogen group; however, substituents at that position could inhibit dimer formation due to steric hindrance between units. (**Figure 6.11**)

Substitution at the 6-position with electron withdrawing groups, in this case an ethyl ester group, had a dramatic effect on the dimerization constant. (**Figure 6.12, Scheme 6.1**) We were able to increase K_{dim} to 210 M^{-1} by the addition of an ethyl ester functionality at this position; similarly, the pK_a decreased to a value of 7.80 for this compound, compared to a value of 8.75 for the variant with a 4-cyanophenyl substituent.

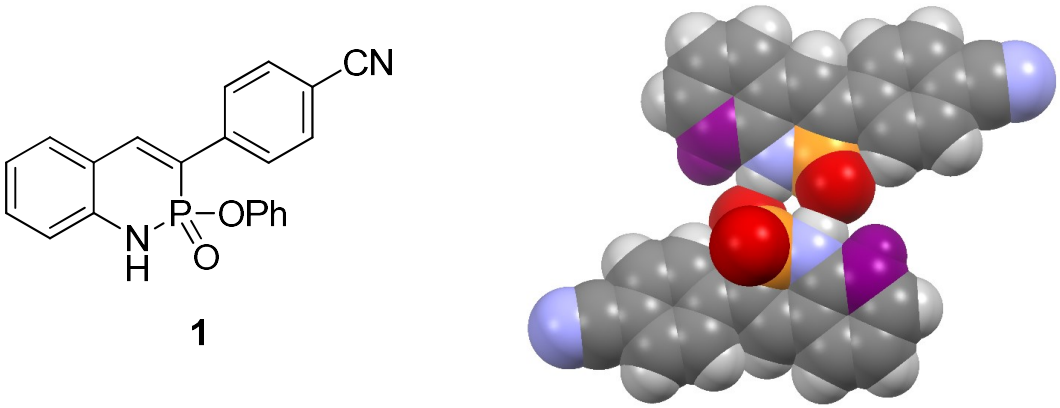

Figure 6.11. (left) Compound **1**, presented here for comparison. (right) Solid-state structure of **1**, with 8-position coloured in purple, demonstrating how steric hindrance could occur if it were to be substituted in that position. Phenoxy groups omitted for clarity, nitrogen atoms colored blue, oxygen atoms colored red, phosphorous atoms colored orange, carbon atoms colored gray, hydrogen atoms colored white.

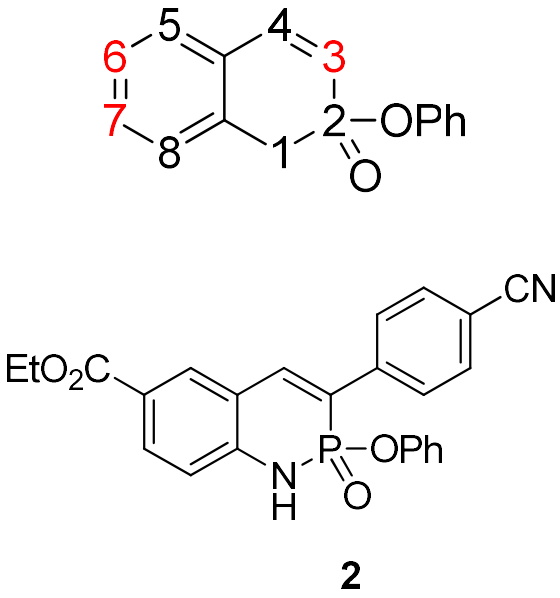

Figure 6.12. (top) Numbering scheme for azaphosphinine scaffold. Red numbers indicate positions modified during these studies. (bottom) Compound **2**, with an ethyl ester group in the 6-position.

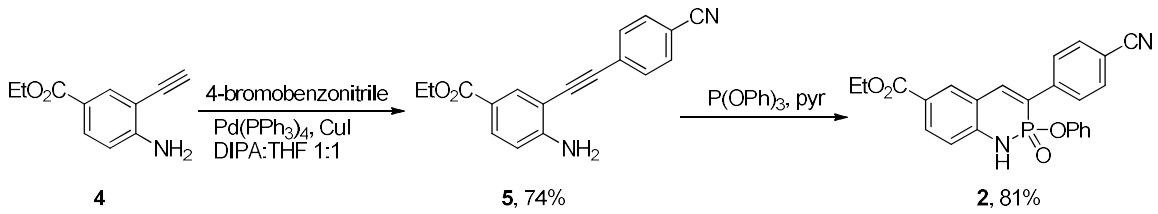

Scheme 6.1. Synthesis of Compound **2.**

Interestingly, the emission of the anion of compound **2** exhibited a 15 nm hypsochromic shift compared to the variant without a substituent at the 6-position, compound **1**. (**Figure 6.13**) Though the anionic compound still exhibited a significant Stokes' shift, as did this entire family of compounds, the difference in the optoelectronic properties were puzzling. To understand this, we turned to calculations to determine the localization of the frontier molecular orbitals. (**Figure 6.14**)

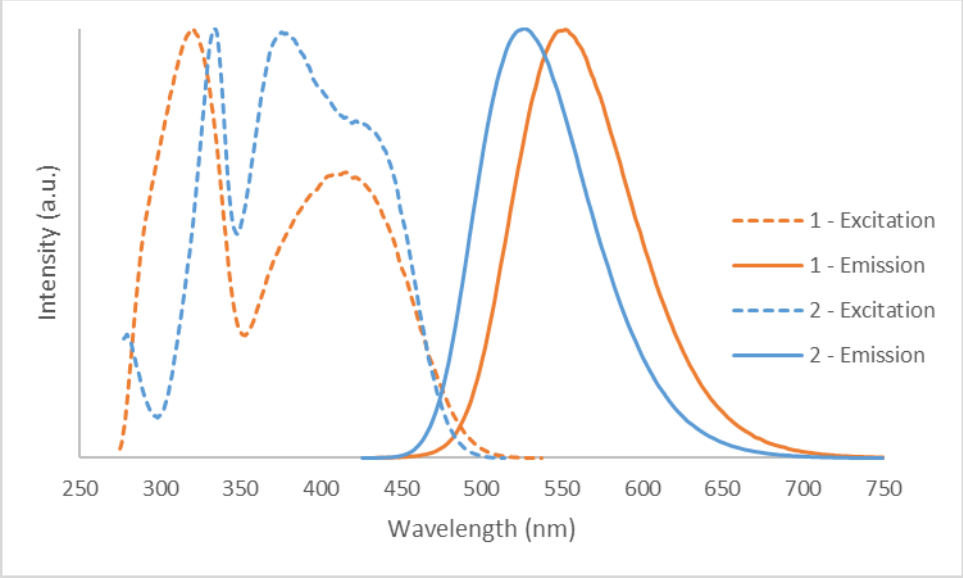

Figure 6.13. Comparison of the excitation and emission spectra of compounds **1** and **2** in $CHCl_3$ with DBU as base to generate the anion.

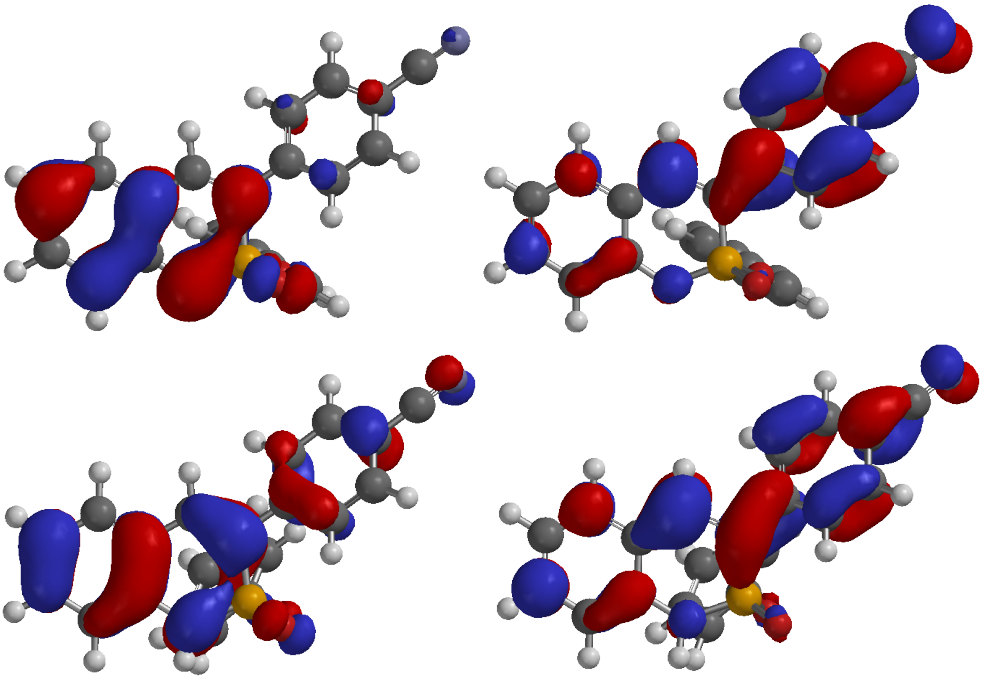

Figure 6.14. Demonstration of the localization of HOMO (left) and LUMO (right) of both neutral (bottom) and anionic (top) forms of **1**. Caclulated with DFT, at B3LYP 6-31g* level of theory.

As noted by the orbital pictures in **Figure 6.14**, position 6 of the azaphosphinine ring only affects the HOMO of the molecule. Installation of electron-withdrawing functionality there would then decrease only the HOMO energy and result in a larger energy gap and concomitant blue shifted emission. Unfortunately, as the nitrogen atom is the dominant factor in the HOMO localization, any groups that affect its acidity also detrimentally affect the HOMO levels and thus will blueshift the emission wavelengths.

This analysis is further borne out through comparison of the emissive properties of a compound synthesized with an electron-withdrawing functionality at the 6-position, and an electron-donating group in the 7-position, compound **3** (**Figure 6.15, Scheme 6.2**). As can be seen from the emission of the anionic form, the emission was further blue-shifted compared to **2** by approximately 25 nm. This result further reinforced our analysis of the frontier orbital maps, where an electron donating group at the 7-position destabilized the LUMO, causing an increase in the energy gap beyond that of **2**. Interestingly, this compound displayed an enhanced stability of the phosphonimidate form, compared to the parent compound **1**, though the phosphonamidate form was isolable.

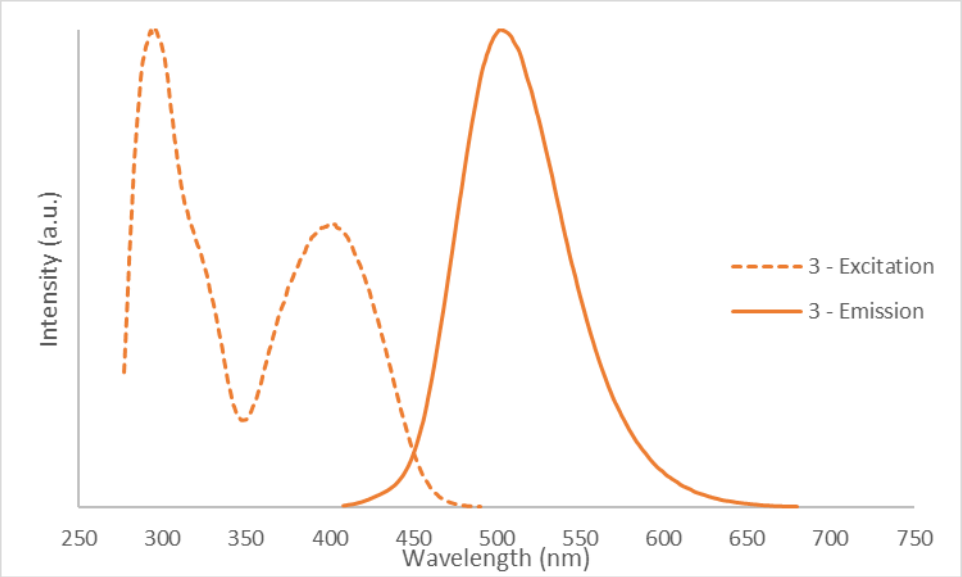

Figure 6.15. Comparison of the excitation and emission spectra of **3** in $CHCl_3$ with DBU as base to generate the anion. The emission maxima of **3** resides at 505 nm, compared to 531 nm for **2** and 551 nm for **1**.

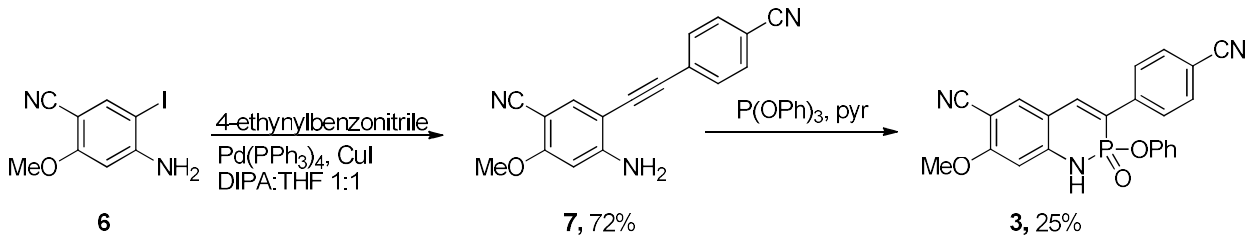

Scheme 6.2. Synthesis of compound **3.**

There are other valuable insights to be gained from the orbital maps and these analyses. In addition to the 6-position being strictly HOMO occupied, the 5- and 7-positions appear to be predominantly occupied by the LUMO, especially in the anionic form; thus, the compound with an electron-withdrawing group at the 7-position to stabilize the LUMO, and an electron-releasing group at the 6-position to destabilize the HOMO, should result in a significantly red-shifted emission compared to the parent scaffold, though the behaviour with respect to supramolecular chemistry would be diminished.

CONCLUSION

In conclusion, the mechanism of the azaphosphinine cyclization was understood to a large degree through rational analysis and experimental investigations. Due to the need for a nucleophilic base during the course of the reaction, it is likely that the pyridine solvent acts as both a base for proton transfers, and activates the phosphorous atom for nucleophilic attack. This indicates that this reaction may be made even more facile through the use of strong acyl transfer agents such as 4-(dimethylamino)pyridine in the reaction mixture.

The supramolecular behaviors of the scaffold were found to be highly dependent on the electronic effects of the ring substituents. A dual Hammett analysis was employed to deconvolute the influence of both the N-H and P=O functionality on the dimerization, and

the varying sensitivity of both members to the electronic effects of substituents. In addition, insights were gleaned as to the methods to modify the substituents to tune both the emissive properties and the supramolecular behaviors. To conclude, the potentialities of this scaffold to behave as a new fluorophore or supramolecular recognition element have been fully demonstrated, and it has now come into its own in these fields. With this understanding of this scaffold, we can then begin to develop the structure for the wide variety of applications available to it.

EXPERIMENTAL

General Cyclization Method

To a solution of 2-(4'-substituted phenylethynyl)aniline (0.5 mmol) in dry pyridine (1 mL) was added triphenylphosphite (0.6 mmol) under an ambient atmosphere. The reaction was heated to 100 °C for 12 h. After cooling, the volatiles were removed *in vacuo* and the crude material was then purified by recrystallization from hot ethyl acetate/hexanes under ambient atmosphere to give product. Additionally, one equivalent of water can be added during recrystallization to ensure complete conversion to phosphonamidate forms.

General Sonogashira Method

To a N_2 sparged 300 mM solution of haloarene in 1:1 THF:DIPA was added 1 mol% $Pd(PPh_3)_4$ and CuI, followed by arylacetylene (1.0 equiv). Solution was heated to 50 °C for 12 hours under N_2 atmosphere, whereupon volatiles were removed under vacuum, then purified via flash chromatography.

Compound 2.

Prepared by general cyclization method, to give 81% of phosphonamidate form.

^{1}H NMR (500 MHz, $CDCl_3$) δ 9.49 (s, 1H), 8.09 (d, J = 2.1 Hz, 1H), 7.99 (dt, J = 8.5, 2.1 Hz 3H), 7.80 (d, J = 8.4 Hz, 2H), 7.74 (d, J = 39.4 Hz, 1H), 7.09 (td, J = 8.3, 2.7 Hz, 3H), 7.00 (t, J = 6.8 Hz, 1H), 6.88 (d, J = 7.6 Hz, 2H), 4.40 (q, J = 7.1 Hz, 2H), 1.42 (t, J = 7.1 Hz, 3H).

^{31}P NMR (121 MHz, $CDCl_3$) δ 9.79 (d, J = 39.2 Hz)

^{13}C NMR (126 MHz, $CDCl_3$) δ 165.65, 149.95, 149.88, 143.64, 143.03, 139.79, 139.71, 132.78, 129.58, 128.31, 125.40, 123.94, 123.71, 122.66, 120.98, 118.77, 118.66, 118.54, 117.42, 112.26, 61.11.

Compound 5

Prepared by general Sonogashira method, to give 74% yield from ethyl 2-ethynyl-4-aminobenzoate and 4-bromobenzonitrile.

^{1}H NMR (300 MHz, $CDCl_3$) δ 8.11 (d, J = 2.1 Hz, 1H), 7.88 (dd, J = 8.6, 2.0 Hz, 1H), 7.67 (d, J = 8.6 Hz, 2H), 7.62 (d, J = 8.6 Hz, 2H), 6.74 (d, J = 8.6 Hz, 1H), 4.70 (s, 2H), 4.35 (q, J = 7.1 Hz, 2H), 1.39 (t, J = 7.1 Hz, 4H).

^{13}C NMR (126 MHz, $CDCl_3$) δ 162.95, 152.95, 138.25, 132.22, 131.83, 127.65, 118.39, 116.57, 111.69, 99.73, 96.11, 93.08, 91.51, 88.10, 56.20.

Compound 3

Prepared by general cyclization method, to give 25% of phosphonamidate form.

^{1}H NMR (300 MHz, $CDCl_3$) δ 9.38 (s, 1H), 7.81 (d, J = 40.7 Hz, 1H), 7.85 (d, J = 7.8 Hz, 2H), 7.77 (d, J = 8.1 Hz, 2H), 7.60 (s, 1H), 7.26 – 7.20 (m, 3H), 7.20 – 7.08 (m, 2H), 6.66 (s, 1H), 3.94 (s, 3H).

^{31}P NMR (121 MHz, $CDCl_3$) δ 9.23 (d, J = 39.5 Hz).

^{13}C NMR (126 MHz, $CDCl_3$) δ 162.84, 162.78, 157.13, 149.76, 149.71, 148.10, 139.63, 130.00, 127.47, 125.77, 120.45, 118.49, 116.79, 115.63, 115.41, 111.68, 109.76, 108.68, 94.26, 56.20.

Compound 7

Prepared by general Sonogashira method, to give 72% yield from 4-ethynylbenzonitrile and 4-amino-5-iodo-2-methoxybenzonitrile.

^{1}H NMR (500 MHz, $CDCl_3$) δ 7.67 (d, J = 8.5 Hz, 2H), 7.64 – 7.54 (m, 3H), 6.25 (s, 1H), 4.84 (s, 2H), 3.92 (s, 3H).

^{13}C NMR (126 MHz, $CDCl_3$) δ 163.7, 157, 137.8, 133.5, 133.0, 131.8, 130.1, 127.0, 118.6, 115.8, 112.3, 101.9, 99.7, 93.3, 90.8, 89.1, 55.3

CHAPTER VII

CONCLUDING REMARKS AND FUTURE DIRECTIONS

CONCLUDING REMARKS

In the first chapter of this dissertation, we demonstrated the supreme versatility of the aryl-ethynyl linkage and the myriad applications it has in the design of sensors, host molecules, and any of the wide variety of sequestration techniques. The alkyne provides an easily installed, conjugative, rigid structural unit that is matched by none. We take advantage of this rigid unit to build macrocyclic hosts with two aspects to them, a flexible portion of the macrocycle, that is able to change its cavity size to accommodate a variety of guests, and a rigid conjugated side, that defines the pocket and helps to pay the entropic cost of binding ahead of time. As a result of these structural motifs, we were able to develop a family of hosts that experienced surprisingly high association constants for chloride in very competitive media.

The overarching theme of this dissertation has been the use of alkynes in two different areas relating to fluorescent sensing molecules. In chapters II and III, we see the alkyne being employed as a structural support for the macrocyclic sensor molecules, enabling binding pocket definition and conjugative communication across the fluorescent scaffold. This yielded novel behaviors with respect to spectroscopic changes due to a variety of stimuli, from solid-state packing arrangements to the formation/cleavage of the disulfide tether.

However, as was seen in chapter IV, the alkyne is susceptible to attack by potent nucleophiles. One of the other notable uses of the alkyne can be in constructing novel heterocyclic systems, that may not be accessible through other routes. The azaphosphinine scaffold discovered in the course of our research, presented in chapter IV, displays a wide variety of unique and exciting properties.

In chapter V we performed a screen to investigate this heterocyclic scaffold and the reaction that formed it. It was found to be quite general, and enabled only through the usage of alkynes, opening access to a very underexplored heterocyclic motif from easily obtained starting materials. Using the alkyne as a heterocyclic precursor has initiated a new field of research within our labs, and the potential uses for this scaffold are very exciting, from fluorescence to supramolecular sensing to pharmaceutical applications.

In chapter VI, we then went on to explore the heterocycle more than the initial, cursory examination. We gained a new appreciation of the dimerization process, and began to understand the effects of substituents on the acidity and self-assembly capabilities of this scaffold. This can help to direct future research in this area as we now understand how to tune a variety of aspects of the azaphosphinine ring.

FUTURE DIRECTIONS

The disulfide-based macrocycles demonstrate an amazing strength of association for chloride in highly competitive solvents. Their downfall, however, is exactly the same aspect that allows for their ease of synthesis, and that is the lability of the disulfide bond. It could be possible to leverage the high yielding macrocyclization, but utilize a sulfur extrusion methodology to form a sulfide linkage as opposed to a disulfide linkage, which would be quite robust in aqueous solutions. There are a number of reactions available to perform this

transformation, and if successful, then such a scaffold could potentially be employed in remediation efforts, as the macrocycles would be highly competitive for the anionic guests, even in aqueous solutions.

The azaphosphinine scaffold, on the other hand, is an entirely new field of research. Such straightforward access to an exotic heterocycle such as this has not been possible before, and as a result this can open up a great number of avenues of research. Already in our laboratory we have begun exploring post-functionalization of the scaffold, if methodology can be developed to substitute any position on the ring, then that could allow investigations into drug discovery, as the azaphosphinine scaffold can act as a bioisostere to the carbostyril scaffold, a ubiquitous pharmacophore.

Some additional avenues of research are exploiting the self-assembly behaviors to explore the potential for crystalline domains, such as is present in liquid crystals, as their self-association constant is quite large compared to a number of other structural motifs in existence. Additionally, if it is possible to reduce the azaphosphinine ring system to the P^{III} oxidation state, this would enable the study of a novel aromatic compound, one possessing a P=N bond within the ring. Though it would not be the first preparation of such a compound, it would be the first that could be scalable, and yield facile access to the study of the aromatic properties of the ring.

Finally, the strong hydrogen-bond formation within the azaphosphinine scaffold and the spectroscopic changes upon deprotonation could lend itself well to sensing applications. If a scaffold were designed such that a specific guest, such as phosphate, could fit into the pocket and result in a deprotonation event, it would likely yield a potent anion sensor, with the desired OFF-ON response that is crucial for high sensitivity measurements.

APPENDIX A

SUPPORTING INFORMATION FOR CHAPTER II: TUNING THE SIZE OF A FLUORESCENT MACROCYCLE FOR TARGETED GUEST INCLUSION – SOLUTION STATE AND SOLID STATE INTERACTIONS

X-RAY CRYSTALLOGRAPHIC STUDIES

General Information. Diffraction intensities were collected at 150 K (**1b•HCl**), 153 K (**1a**), 173 K (**1c•HCl, 1b•H_2O**) and 200 k ((**1c•H_2O**) on a Bruker Apex2 CCD diffractometer using MoKα radiation, λ= 0.71073 Å, (**1a**) and CuKα radiation, λ= 1.54178 Å, (**1b•HCl, 1c•HCl, 1b•H_2O** and **1c•H_2O**). Space groups determined based on systematic absences (**1b•HCl, 1c•HCl** and **1c•H_2O**) and intensity statistics (**1a** and **1b•H_2O**). Absorption corrections applied by SADABS.[3] Structures solved by direct methods and Fourier techniques and refined on F^2 using full matrix least-squares procedures. All non-H atoms were refined with anisotropic thermal parameters. H atoms in **1a** and **1b•HCl** were found from the residual density maps and refined with isotropic thermal parameters except those in the t-Bu groups which were refined in calculated positions. H atoms in **1c•HCl, 1b•H_2O** and **1c•H_2O** were treated in calculated positions in a rigid group model except those at N atoms and in solvent water molecule in **1c•H_2O** involved in H-bonds. Those H atoms were found from the residual density maps and refined with isotropic thermal parameters. The structure of **1c•HCl** has four symmetrically independent structural units and five solvent molecules (CH_2Cl_2). One of the solvent molecules was refined as disordered over two

positions, another one is highly disordered and was treated by SQUEEZE;[4] correction of the X-ray data was 199 electrons/unit cell; the required value is 168 electrons/unit cell for four CH_2Cl_2 molecules in the full unit cell. Solvent molecule EtOAc in **1a** was highly disordered around an inversion center and was also treated by SQUEEZE; corrections of the X-ray data (46 electrons/cell) is close to the required value (48 electrons/cell) for one EtOAc molecule per full unit cell. Crystals of **1c•HCl** are very thin plates and reflections at high angles were very weak even with using a strong *Incoatec* Cu IμS source. The X-ray diffraction data for **1c•HCl** were collected up to $2\theta_{max} = 126.0°$, but only reflections with $2\theta_{max} = 100.0°$ were used in the final refinement. All calculations were performed by the Bruker SHELXTL (v. 6.10)[5] and SHELXL-2013 packages.[6]

Crystallographic Data for **1a**: $C_{35}H_{37}N_3O_3S_2$, M = 611.80, 0.34 x 0.28 x 0.15 mm, T = 153 K, Triclinic, space group *P*-1, $a = 9.5029(18)$ Å, $b = 12.881(2)$ Å, $c = 13.585(3)$ Å, $\alpha = 79.321(3)°$, $\beta = 86.979(3)°$, $\gamma = 88.986(3)°$, $V = 1631.8(5)$ Å^3, $Z = 2$, $D_c = 1.245$ Mg/m^3, μ(Mo) = 0.202 mm^{-1}, $F(000) = 648$, $2\theta_{max} = 56.44°$, 14264 reflections, 7398 independent reflections [$R_{int} = 0.0206$], R1 = 0.0484, wR2 = 0.1316 and GOF = 1.047 for 7398 reflections (467 parameters) with $I>2\sigma(I)$, R1 = 0.0552, wR2 = 0.1374 and GOF = 1.047 for all reflections, max/min residual electron density +0.554/-0.414 eÅ^3.

Crystallographic Data for **1b•HCl**: $C_{36}H_{40}Cl_3N_3O_2S_2$, M = 717.18, 0.45 x 0.09 x 0.07 mm, T = 150 K, Monoclinic, space group $P2_1/c$, $a = 20.457(2)$ Å, $b = 14.3758(14)$ Å, $c = 12.4644(11)$ Å, $\beta = 99.108(6)°$, $V = 3619.3(6)$ Å^3, $Z = 4$, $D_c = 1.316$ Mg/m^3, μ(Cu) = 3.653 mm^{-1}, $F(000) = 1504$, $2\theta_{max} = 134.28°$, 20657 reflections, 6395 independent reflections [$R_{int} = 0.0486$], R1 = 0.0616, wR2 = 0.1765 and GOF = 1.030 for 6395 reflections (503

parameters) with I>2σ(I), R1 = 0.0757, wR2 = 0.1890 and GOF = 1.030 for all reflections, max/min residual electron density +0.962/-0.845 eÅ^3.

Crystallographic Data for **1b•H_2O**: $C_{35}H_{39}N_3O_3S_2$, M = 613.81, 0.09 x 0.08 x 0.04 mm, T = 173 K, Triclinic, space group *P*-1, *a* = 11.4623(3) Å, *b* = 12.0360(3) Å, *c* = 13.9473(4) Å, *a* = 95.207(1)°, β = 114.090(1)°, γ = 107.307(1)°, *V* = 1626.60(8) Å^3, *Z* = 2, D_c = 1.253 Mg/m^3, μ(Cu) = 1.788 mm^{-1}, *F*(000) = 652, $2\theta_{max}$ = 133.32°, 20594 reflections, 5668 independent reflections [R_{int} = 0.0500], R1 = 0.0454, wR2 = 0.1163 and GOF = 1.078 for 5668 reflections (404 parameters) with I>2σ(I), R1 = 0.0565, wR2 = 0.1230 and GOF = 1.078 for all reflections, max/min residual electron density +0.388/-0.298 eÅ^3.

Crystallographic Data for **1c•HCl**: $C_{38.25}H_{44.5}Cl_{3.5}N_3O_2S_2$, $C_{37}H_{42}ClN_3O_2S_2$ 1.25(CH_2Cl_2), M = 766.46, 0.13 x 0.12 x 0.02 mm, T = 173 K, Monoclinic, space group $P2_1/n$, *a* = 20.7737(8) Å, *b* = 31.7155(12) Å, *c* = 24.6016(10) Å, β = 98.088(3)°, *V* = 16047.5(11) Å^3, *Z* = 16, Z'=4, D_c = 1.269 Mg/m^3, μ(Cu) = 3.627 mm^{-1}, *F*(000) = 6440, $2\theta_{max}$ = 100.0°, 101170 reflections, 16467 independent reflections [R_{int} = 0.0880], R1 = 0.1091, wR2 = 0.3280 and GOF = 1.007 for 16467 reflections (1774 parameters) with I>2σ(I), R1 = 0.1299, wR2 = 0.3530 and GOF = 1.008 for all reflections, max/min residual electron density +1.143/-0.955 eÅ^3.

Crystallographic Data for **1c•H_2O**: $C_{37}H_{43}N_3O_3S_2$, M = 641.86, 0.16 x 0.12 x 0.03 mm, T = 200 K, Monoclinic, space group $P2_1/c$, *a* = 14.0664(12) Å, *b* = 27.410(2) Å, *c* = 9.4754(7) Å, β = 107.434(5)°, *V* = 3485.5(5) Å^3, *Z* = 4, D_c = 1.223 Mg/m^3, μ(Cu) = 1.690 mm^{-1}, *F*(000) = 1368, $2\theta_{max}$ = 136.71°, 24228 reflections, 6295 independent reflections [R_{int} = 0.0605], R1 = 0.0556, wR2 = 0.1365 and GOF = 1.034 for 6295 reflections (422 parameters) with

I>2σ(I), R1 = 0.0801, wR2 = 0.1504 and GOF = 1.035 for all reflections, max/min residual electron density +0.373/-0.328 eÅ^3.

FLUORESCENCE SPECTRA IN CHLOROFORM

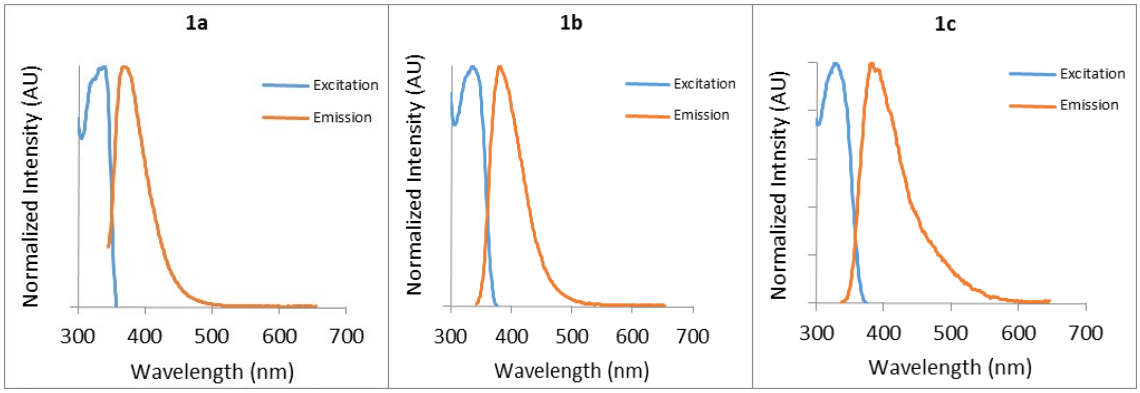

Figure A.1. Excitation and emission spectra of **1a-1c** in $CHCl_3$.

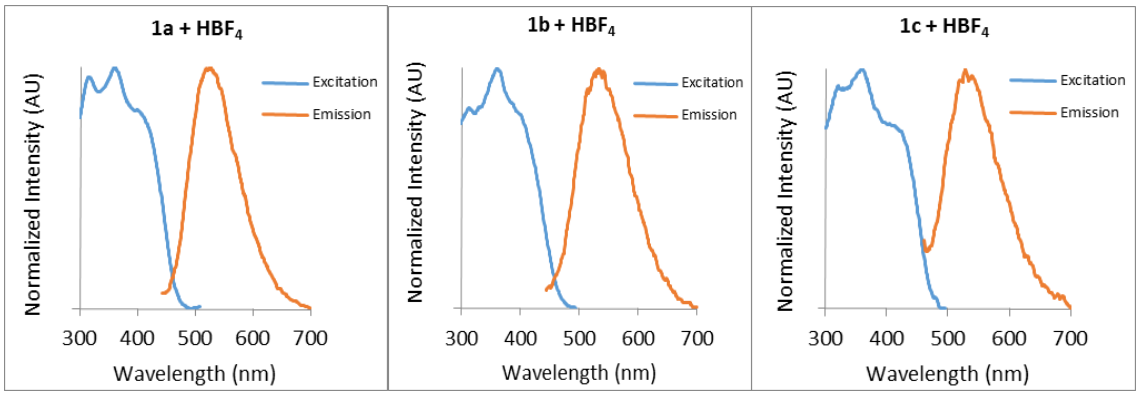

Figure A.2. Excitation and emission spectra of **1a•HBF$_4$-1c•HBF$_4$** in $CHCl_3$.

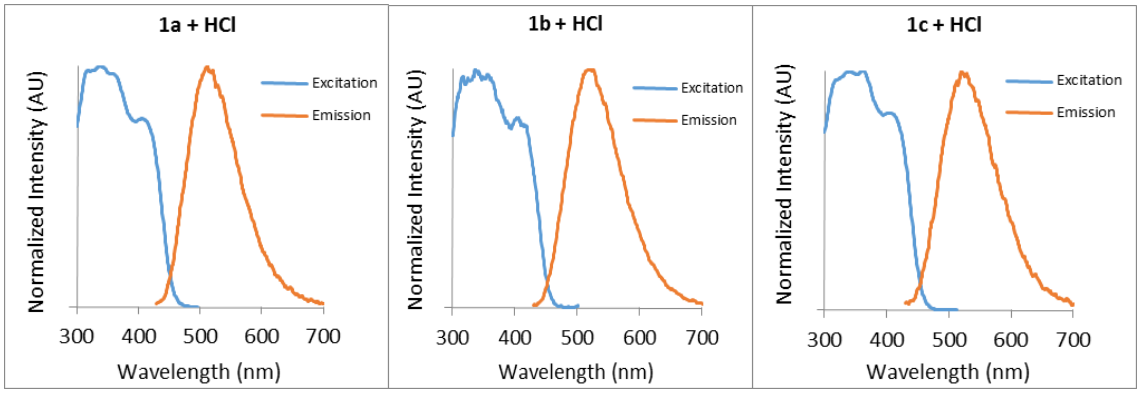

Figure A.3. Excitation and emission spectra of **1a•HCl-1c•HCl** in $CHCl_3$.

COMPUTATIONAL DATA

Job Type: Geometry Optimization
Macrocycle: **1a**
Method: B3LYP
Basis Set: 6-31G(D)

Spartan '14 output:
SPARTAN '14 MECHANICS PROGRAM: (Win/64b) Release 1.1.4
Frequency Calculation
Adjusted 11 (out of 219) low frequency modes

Reason for exit: Successful completion
Mechanics CPU Time : .45
Mechanics Wall Time: .18
SPARTAN '14 Quantum Mechanics Driver: (Win/64b) Release 1.1.4
Job type: Geometry optimization.
Method: RB3LYP
Basis set: 6-31G(D)
Number of shells: 228
Number of basis functions: 674
Multiplicity: 1
Parallel Job: 4 threads
SCF model:
A restricted hybrid HF-DFT SCF calculation will be
performed using Pulay DIIS + Geometric Direct Minimization

Optimization:
Step Energy Max Grad. Max Dist.
1 -2388.424990 0.000555 0.013394

2 -2388.424999 0.000451 0.004827
3 -2388.425000 0.000446 0.006776
4 -2388.425003 0.000409 0.024798
5 -2388.425011 0.000397 0.030259
6 -2388.425012 0.000408 0.022695
7 -2388.425026 0.000417 0.101237
8 -2388.425038 0.001722 0.043441
9 -2388.425066 0.000908 0.015456
10 -2388.425081 0.001020 0.048058
11 -2388.425094 0.001278 0.011616
12 -2388.425109 0.001063 0.022132
13 -2388.425127 0.000582 0.016708
14 -2388.425133 0.000533 0.007519
15 -2388.425140 0.000457 0.023940
16 -2388.425149 0.000409 0.020361
17 -2388.425158 0.000544 0.044999
18 -2388.425173 0.000598 0.031047
19 -2388.425186 0.000334 0.012611
20 -2388.425198 0.000228 0.006638
21 -2388.425200 0.000188 0.006359
22 -2388.425202 0.000175 0.005436
23 -2388.425202 0.000164 0.009416

Reason for exit: Successful completion
Quantum Calculation CPU Time : 1:23:32.81
Quantum Calculation Wall Time: 1:54:52.06
SPARTAN '14 Semi-Empirical Program: (Win/64b) Release 1.1.4
Semi-empirical Property Calculation
M0000
Guess from Archive
Energy Due to Solvation
Solvation Energy SM5.4/A -36.553
Memory Used: 30.244 Mb
Reason for exit: Successful completion
Semi-Empirical Program CPU Time : 1.81
Semi-Empirical Program Wall Time: 1.52
SPARTAN '14 Properties Program: (Win/64b) Release 1.1.4
Reason for exit: Successful completion
Properties CPU Time : 9.02
Properties Wall Time: 8.74
Atomic Coordinates:
C -1.145262 -3.982755 0.938775
C -1.257835 -2.635196 0.552008
N -0.192879 -1.827309 0.356792
C 1.031364 -2.356219 0.543622
C 1.234330 -3.696479 0.933506
C 0.126528 -4.512032 1.131207
C -2.541058 -2.048066 0.335738

C	2.180771	-1.533299	0.321323
C	-3.621097	-1.522903	0.136157
C	3.242009	-0.962594	0.146389
C	-4.754438	-0.710339	-0.140760
C	4.518722	-0.372687	-0.079481
C	-6.062104	-1.214625	-0.103583
C	-7.177070	-0.413847	-0.375026
C	-6.927508	0.929074	-0.693085
C	-5.640597	1.466824	-0.741324
C	-4.536237	0.659146	-0.463991
C	4.707574	1.034449	-0.105142
C	5.992226	1.531072	-0.348757
C	7.059670	0.657817	-0.556901
C	6.908973	-0.735670	-0.530578
C	5.621245	-1.219710	-0.285552
C	-8.591392	-1.017974	-0.322586
C	-9.683536	0.032547	-0.601386
C	-8.848781	-1.616437	1.080423
C	-8.713995	-2.135834	-1.384968
C	8.073706	-1.719666	-0.740611
C	8.280604	-2.546623	0.550886
C	7.746402	-2.676370	-1.911448
C	9.393718	-0.997575	-1.068909
N	-3.208456	1.107945	-0.476977
N	3.587053	1.854312	0.114075
C	-2.720450	2.356707	-0.766918
C	-1.205191	2.460287	-0.613460
O	-3.397289	3.322222	-1.091765
S	-0.865720	3.488105	0.901239
C	3.552525	3.223563	0.225550
O	4.523748	3.958808	0.131721
C	2.160567	3.838932	0.417233
S	1.021210	2.839385	1.482893
H	-2.039362	-4.580651	1.078169
H	2.243833	-4.067502	1.072554
H	0.253077	-5.548444	1.431203
H	-6.186669	-2.263718	0.146024
H	-7.753889	1.595460	-0.912388
H	-5.483132	2.507433	-0.989169
H	6.145998	2.600124	-0.369030
H	8.033902	1.095840	-0.743718
H	5.436227	-2.288545	-0.251296
H	-9.585946	0.470584	-1.601232
H	-9.665815	0.846368	0.132734
H	-10.670865	-0.439450	-0.545361
H	-9.857194	-2.044536	1.130670
H	-8.138117	-2.414042	1.322118
H	-8.765330	-0.848021	1.857262

H	-8.545510	-1.739315	-2.392656
H	-7.988457	-2.938933	-1.215940
H	-9.716254	-2.580537	-1.356408
H	7.380044	-3.109212	0.819377
H	8.534178	-1.896880	1.396195
H	9.097919	-3.265424	0.415864
H	6.844548	-3.267847	-1.720437
H	8.574473	-3.378219	-2.067328
H	7.590650	-2.120350	-2.842867
H	9.313963	-0.399329	-1.983774
H	9.714435	-0.338122	-0.254501
H	10.187279	-1.736890	-1.224831
H	-2.528970	0.400227	-0.219405
H	2.708173	1.361621	0.248025
H	-0.714010	1.492213	-0.484904
H	-0.802412	2.970020	-1.491837
H	1.695088	3.952367	-0.567278
H	2.308158	4.830374	0.846291

Job Type: Geometry Optimization
Macrocycle: **1a + H_2O**
Method: B3LYP
Basis Set: 6-31G(D)

Spartan '14 output:
SPARTAN '14 MECHANICS PROGRAM: (Win/64b) Release 1.1.4
Frequency Calculation
Adjusted 11 (out of 228) low frequency modes

Reason for exit: Successful completion
Mechanics CPU Time : .39
Mechanics Wall Time: .15
SPARTAN '14 Quantum Mechanics Driver: (Win/64b) Release 1.1.4
Job type: Geometry optimization.
Method: RB3LYP
Basis set: 6-31G(D)
Number of shells: 236
Number of basis functions: 693
Multiplicity: 1
Parallel Job: 4 threads
SCF model:
A restricted hybrid HF-DFT SCF calculation will be
performed using Pulay DIIS + Geometric Direct Minimization

Optimization:
Step Energy Max Grad. Max Dist.
1 -2464.842421 0.023340 0.088706
2 -2464.851727 0.005387 0.096647

3 -2464.853178 0.003613 0.101451
4 -2464.853960 0.002546 0.102741
5 -2464.854384 0.001142 0.101390
6 -2464.854607 0.001241 0.085830
7 -2464.854747 0.000999 0.084279
8 -2464.854961 0.001143 0.091483
9 -2464.855189 0.002007 0.106637
10 -2464.855467 0.002387 0.110845
11 -2464.855792 0.002550 0.119181
12 -2464.856204 0.003167 0.112232
13 -2464.856723 0.003670 0.104084 1
14 -2464.851217 0.025547 0.099719
15 -2464.857780 0.003848 0.108434
16 -2464.858798 0.003581 0.088331
17 -2464.859910 0.002624 0.101096
18 -2464.860856 0.002454 0.079623
19 -2464.861737 0.002843 0.086775
20 -2464.862393 0.001932 0.094931
21 -2464.862863 0.001203 0.108966
22 -2464.863184 0.000965 0.114569
23 -2464.863456 0.001012 0.112192
24 -2464.863689 0.000697 0.125233
25 -2464.863803 0.000593 0.101520
26 -2464.863844 0.000602 0.031316
27 -2464.863873 0.000784 0.021350
28 -2464.863889 0.000548 0.014605
29 -2464.863899 0.000731 0.013821
30 -2464.863905 0.000682 0.005836
31 -2464.863911 0.000620 0.008816
32 -2464.863916 0.000602 0.009168
33 -2464.863922 0.000398 0.018810
34 -2464.863932 0.000409 0.013900
35 -2464.863942 0.000231 0.011466
36 -2464.863947 0.000146 0.009643
37 -2464.863951 0.000124 0.005945
38 -2464.863952 0.000090 0.008866

Reason for exit: Successful completion
Quantum Calculation CPU Time : 2:38:31.42
Quantum Calculation Wall Time: 3:38:06.30
SPARTAN '14 Semi-Empirical Program: (Win/64b) Release 1.1.4
Semi-empirical Property Calculation
M0000
Guess from Archive
Energy Due to Solvation
Solvation Energy SM5.4/A -138.953
Memory Used: 33.080 Mb

Reason for exit: Successful completion
Semi-Empirical Program CPU Time : 2.56
Semi-Empirical Program Wall Time: 2.26
SPARTAN '14 Properties Program: (Win/64b) Release 1.1.4
Reason for exit: Successful completion
Properties CPU Time : 9.67
Properties Wall Time: 9.40

Atomic Coordinates:

C	-1.293884	-4.314710	0.608772
C	-1.263664	-2.936381	0.332872
N	-0.104094	-2.270103	0.147438
C	1.064009	-2.937198	0.237211
C	1.112506	-4.316179	0.513749
C	-0.085451	-5.000404	0.696742
C	-2.450933	-2.155046	0.235763
C	2.251420	-2.177028	0.034102
C	-3.418713	-1.421827	0.153616
C	3.267404	-1.527040	-0.131579
C	-4.553589	-0.571775	0.065557
C	4.472509	-0.798138	-0.317434
C	-5.814613	-1.149854	-0.165834
C	-6.986335	-0.394822	-0.239728
C	-6.847188	0.990607	-0.068481
C	-5.613757	1.599796	0.156944
C	-4.440171	0.838321	0.225615
C	4.464676	0.586712	-0.643253
C	5.696962	1.231529	-0.803432
C	6.890466	0.526422	-0.656489
C	6.930155	-0.840418	-0.342958
C	5.697766	-1.473831	-0.174486
C	-8.336281	-1.089092	-0.491039
C	-9.502091	-0.085269	-0.551637
C	-8.618619	-2.094954	0.650460
C	-8.284056	-1.849467	-1.837407
C	8.237774	-1.633761	-0.171599
C	8.355666	-2.115382	1.294358
C	8.230583	-2.861646	-1.112646
C	9.478652	-0.782880	-0.501616
N	-3.172052	1.401548	0.443993
N	3.228545	1.234140	-0.797723
C	-2.903257	2.672190	0.913890
C	-1.420927	2.965708	1.115769
O	-3.751709	3.518013	1.161530
S	-0.931902	4.309984	-0.075776
C	3.003395	2.556318	-1.134158
O	3.885840	3.382443	-1.315684
C	1.532250	2.924999	-1.270209
S	1.142108	4.240981	-0.012986

H	-2.244658	-4.815765	0.752022
H	2.070505	-4.819714	0.578572
H	-0.077132	-6.065429	0.910409
H	-5.850178	-2.228293	-0.283667
H	-7.719706	1.633179	-0.113826
H	-5.549452	2.669610	0.291435
H	5.708345	2.284198	-1.044987
H	7.813665	1.077970	-0.796202
H	5.652840	-2.528672	0.076017
H	-9.369807	0.640655	-1.361692
H	-9.616815	0.465848	0.388630
H	-10.440523	-0.619453	-0.736727
H	-9.576937	-2.602303	0.484610
H	-7.842437	-2.865339	0.715662
H	-8.665814	-1.585451	1.619590
H	-8.092695	-1.161405	-2.668710
H	-7.497904	-2.612538	-1.846314
H	-9.239278	-2.354375	-2.026592
H	7.507677	-2.745043	1.585087
H	8.391706	-1.264586	1.984228
H	9.271576	-2.703588	1.430125
H	7.390824	-3.533363	-0.904794
H	9.154149	-3.440176	-0.989254
H	8.159805	-2.553581	-2.162102
H	9.455525	-0.412209	-1.532747
H	9.572815	0.077047	0.170810
H	10.383027	-1.390805	-0.387522
H	-2.359676	0.818424	0.235182
H	2.407100	0.656221	-0.653969
H	-1.279909	3.337843	2.133093
H	-0.789456	2.097483	0.932109
H	0.861297	2.079698	-1.107227
H	1.375599	3.346353	-2.266726
H	-0.786251	0.259901	-1.510486
O	-0.475187	0.374942	-0.599104
H	-0.275160	-0.551265	-0.292065

Job Type: Geometry Optimization
Macrocycle: **1a + HCl**
Method: B3LYP
Basis Set: 6-31G(D)

Spartan '14 output:
SPARTAN '14 MECHANICS PROGRAM: (Win/64b) Release 1.1.4
Frequency Calculation
Adjusted 8 (out of 225) low frequency modes

Reason for exit: Successful completion

Mechanics CPU Time : .45
Mechanics Wall Time: .17
SPARTAN '14 Quantum Mechanics Driver: (Win/64b) Release 1.1.4
Job type: Geometry optimization.
Method: RB3LYP
Basis set: 6-31G(D)
Number of shells: 235
Number of basis functions: 695
Multiplicity: 1
Parallel Job: 4 threads
SCF model:
A restricted hybrid HF-DFT SCF calculation will be
performed using Pulay DIIS + Geometric Direct Minimization

Optimization:
Step Energy Max Grad. Max Dist.
1 -2849.238303 0.024256 0.087216
2 -2849.249725 0.006567 0.070943
3 -2849.252225 0.003263 0.109006
4 -2849.253306 0.001798 0.160034
5 -2849.253800 0.001160 0.186539
6 -2849.254015 0.000927 0.110815
7 -2849.254074 0.001542 0.058476
8 -2849.254148 0.001279 0.030269
9 -2849.254193 0.001294 0.051137
10 -2849.254260 0.001348 0.023353
11 -2849.254281 0.001054 0.013943
12 -2849.254297 0.000712 0.021817
13 -2849.254312 0.000742 0.012205
14 -2849.254325 0.000749 0.018526
15 -2849.254340 0.000519 0.020903
16 -2849.254354 0.000365 0.018758

Reason for exit: Aborted by user
Quantum Calculation CPU Time : 1:43:28.66
Quantum Calculation Wall Time: 2:47:03.37
SPARTAN '14 Quantum Mechanics Driver: (Win/64b) Release 1.1.4
Job type: Geometry optimization.
Method: RB3LYP
Basis set: 6-31G(D)
Number of shells: 235
Number of basis functions: 695
Multiplicity: 1
Parallel Job: 4 threads
SCF model:
A restricted hybrid HF-DFT SCF calculation will be
performed using Pulay DIIS + Geometric Direct Minimization

2 -2849.254360 0.000295 0.001918 Restart with RIC
3 -2849.254362 0.000277 0.001331
4 -2849.254363 0.000261 0.040230
5 -2849.254382 0.000283 0.020114
6 -2849.254394 0.000457 0.010482
7 -2849.254399 0.000133 0.012335
8 -2849.254401 0.000123 0.027803
9 -2849.254404 0.000137 0.003996
10 -2849.254406 0.000077 0.003718
11 -2849.254407 0.000076 0.007191
12 -2849.254407 0.000064 0.005889

Reason for exit: Successful completion
Quantum Calculation CPU Time : 41:16.97
Quantum Calculation Wall Time: 48:33.56
SPARTAN '14 Properties Program: (Win/64b) Release 1.1.4
Reason for exit: Successful completion
Properties CPU Time : 8.72
Properties Wall Time: 8.42
Atomic Coordinates:

C	-1.144237	-4.456587	-0.793484
C	-1.207696	-3.109393	-0.412291
N	-0.042093	-2.442896	-0.188957
C	1.192572	-2.993238	-0.336395
C	1.277835	-4.340143	-0.724228
C	0.104968	-5.058853	-0.941269
C	-2.397236	-2.370991	-0.259328
C	2.305378	-2.167392	-0.096789
C	-3.355328	-1.630813	-0.116775
C	3.243060	-1.411297	0.096210
C	-4.479282	-0.783315	0.017149
C	4.411203	-0.637265	0.274599
C	4.396654	0.754177	0.580883
C	5.645824	1.396502	0.685194
C	6.828581	0.694874	0.504519
C	6.870804	-0.682688	0.211656
C	5.642691	-1.318052	0.103884
C	-5.742206	-1.372514	0.254853
C	-6.905868	-0.618002	0.344582
C	-6.763164	0.774713	0.183185
C	-5.538631	1.388687	-0.043902
C	-4.361701	0.627300	-0.125719
N	-3.103638	1.197152	-0.352876
N	3.184487	1.427582	0.766986
C	3.022996	2.788054	1.007390
C	-2.855801	2.426502	-0.939907
C	8.216376	-1.400963	0.023126
C	8.038561	-2.900202	-0.280013

C	9.056816	-1.263370	1.314819
C	8.980147	-0.754956	-1.157072
C	-8.291970	-1.233897	0.598823
C	-9.227039	-0.899554	-0.587605
C	-8.886171	-0.644401	1.899936
C	-8.230189	-2.765242	0.746428
C	-1.380583	2.715028	-1.181225
O	-3.725145	3.218687	-1.274024
C	1.585479	3.255639	1.166082
O	3.945326	3.588502	1.072790
S	1.144889	4.240739	-0.356528
S	-0.929538	4.292614	-0.306416
H	-0.096306	-1.443818	0.202325
Cl	-0.142281	0.225384	1.066293
H	-2.064385	-4.998340	-0.974297
H	2.254035	-4.792840	-0.846970
H	0.164627	-6.101698	-1.238506
H	5.667103	2.452612	0.905027
H	7.757455	1.251354	0.597931
H	5.583043	-2.375582	-0.124212
H	-5.769489	-2.450405	0.361128
H	-7.640921	1.411789	0.243205
H	-5.475797	2.459737	-0.169406
H	-2.286167	0.673590	-0.031659
H	2.326513	0.872353	0.744594
H	7.474932	-3.065509	-1.205681
H	7.525292	-3.424381	0.534701
H	9.020789	-3.368840	-0.405240
H	10.022226	-1.770349	1.197365
H	9.259162	-0.215069	1.558623
H	8.538222	-1.711305	2.169969
H	8.415744	-0.854550	-2.091246
H	9.161657	0.311683	-0.989091
H	9.953440	-1.241734	-1.293576
H	-8.842976	-1.323432	-1.522555
H	-9.334498	0.180932	-0.729474
H	-10.227541	-1.313111	-0.411785
H	-8.991283	0.443980	1.842788
H	-8.250536	-0.874903	2.762281
H	-9.881176	-1.065666	2.086550
H	-7.847285	-3.247363	-0.160642
H	-7.600465	-3.070115	1.590401
H	-9.236316	-3.158611	0.928189
H	-0.731877	1.919212	-0.813695
H	-1.234135	2.861973	-2.254823
H	1.541923	3.921499	2.030262
H	0.872307	2.438556	1.275741

Job Type: Geometry Optimization
Macrocycle: **1b**
Method: B3LYP
Basis Set: 6-31G(D)

Spartan '14 output:
SPARTAN '14 MECHANICS PROGRAM: (Win/64b) Release 1.1.4
Frequency Calculation
Adjusted 10 (out of 237) low frequency modes

Reason for exit: Successful completion
Mechanics CPU Time : .39
Mechanics Wall Time: .17
SPARTAN '14 Quantum Mechanics Driver: (Win/64b) Release 1.1.4
Job type: Geometry optimization.
Method: RB3LYP
Basis set: 6-31G(D)
Number of shells: 244
Number of basis functions: 712
Multiplicity: 1
Parallel Job: 4 threads
SCF model:
A restricted hybrid HF-DFT SCF calculation will be
performed using Pulay DIIS + Geometric Direct Minimization
Optimization:
Step Energy Max Grad. Max Dist.
1 -2467.048848 0.024268 0.077537
2 -2467.058226 0.005198 0.101891
3 -2467.059285 0.002173 0.093416
4 -2467.059596 0.001523 0.094757
5 -2467.059736 0.001189 0.142367
6 -2467.059860 0.001489 0.142543
7 -2467.059969 0.001332 0.156307
8 -2467.060026 0.000862 0.131367
9 -2467.060111 0.001041 0.124210
10 -2467.060168 0.001383 0.046971
11 -2467.060229 0.001421 0.035965
12 -2467.060268 0.001170 0.040431
13 -2467.060293 0.001153 0.035464
14 -2467.060307 0.001144 0.039809
15 -2467.060315 0.001148 0.053375
16 -2467.060318 0.001154 0.052230
17 -2467.060331 0.001004 0.048792
18 -2467.060339 0.000765 0.055981
19 -2467.060361 0.000673 0.122882
20 -2467.060391 0.000807 0.109173

21 -2467.060362 0.001042 0.125678
22 -2467.060438 0.000898 0.053711
23 -2467.060485 0.000670 0.030106
24 -2467.060512 0.000575 0.044068
25 -2467.060512 0.000400 0.014342
26 -2467.060526 0.000425 0.010896
27 -2467.060532 0.000317 0.014508
28 -2467.060533 0.000322 0.008300
29 -2467.060533 0.000187 0.003481

Reason for exit: Successful completion
Quantum Calculation CPU Time : 2:00:38.67
Quantum Calculation Wall Time: 2:52:57.92
SPARTAN '14 Semi-Empirical Program: (Win/64b) Release 1.1.4
Semi-empirical Property Calculation
M0000
Guess from Archive
Energy Due to Solvation
Solvation Energy SM5.4/A -40.041
Memory Used: 36.087 Mb

Reason for exit: Successful completion
Semi-Empirical Program CPU Time : 2.28
Semi-Empirical Program Wall Time: 1.99
SPARTAN '14 Properties Program: (Win/64b) Release 1.1.4
Reason for exit: Successful completion
Properties CPU Time : 11.16
Properties Wall Time: 11.24
Atomic Coordinates:

C	-1.268459	-3.913883	-1.953413
C	-1.142279	-2.691206	-1.264082
N	0.047868	-2.154643	-0.932863
C	1.157635	-2.848233	-1.257838
C	1.124259	-4.078313	-1.940932
C	-0.112755	-4.607755	-2.294393
C	-2.320476	-1.991403	-0.855253
C	2.406502	-2.281360	-0.855358
C	-3.361722	-1.488109	-0.475087
C	3.467500	-1.821879	-0.474892
C	-4.571781	-0.911835	0.001814
C	4.642453	-1.169517	-0.009699
C	-5.730449	-1.710120	0.083742
C	-6.940371	-1.217247	0.568351
C	-6.954005	0.128758	0.976341
C	-5.833538	0.948956	0.905276
C	-4.622602	0.443761	0.412582
C	4.626256	0.235717	0.188280
C	5.787156	0.859555	0.662486

C	6.923146	0.102068	0.927074
C	6.972587	-1.291507	0.740832
C	5.812372	-1.902108	0.266581
C	-8.215488	-2.073166	0.665189
C	-9.323410	-1.441087	-0.210157
C	-8.691809	-2.124434	2.136397
C	-7.985398	-3.517356	0.183599
C	8.259464	-2.070320	1.063588
C	8.115425	-3.577745	0.781998
C	8.605199	-1.888918	2.560745
C	9.423279	-1.526188	0.201567
N	-3.455364	1.215131	0.280584
N	3.442072	0.921040	-0.123714
C	-3.262150	2.536167	0.615513
O	-4.112384	3.243881	1.140080
C	-1.878770	3.094822	0.266776
C	-2.049690	4.467879	-0.386252
S	-0.522383	5.449736	-0.688312
C	3.191505	2.273134	-0.079663
O	3.995139	3.112151	0.305823
C	1.804292	2.674274	-0.587198
C	1.948821	3.802240	-1.610762
S	0.386714	4.482989	-2.311189
H	-2.253815	-4.294091	-2.200051
H	2.051143	-4.589146	-2.178431
H	-0.175059	-5.553136	-2.826009
H	-5.641903	-2.738776	-0.243900
H	-7.871384	0.562972	1.363668
H	-5.878943	1.979363	1.226744
H	5.782634	1.929447	0.815483
H	7.802017	0.625096	1.292964
H	5.776102	-2.972064	0.100647
H	-9.025427	-1.418794	-1.264674
H	-9.547222	-0.413481	0.094891
H	-10.250572	-2.021784	-0.130590
H	-9.606879	-2.723298	2.220605
H	-7.928462	-2.576511	2.779811
H	-8.910565	-1.126027	2.529628
H	-7.672318	-3.552853	-0.866174
H	-7.228871	-4.032762	0.786356
H	-8.917947	-4.086363	0.267656
H	7.894344	-3.775124	-0.273310
H	7.324669	-4.032695	1.389515
H	9.053269	-4.089489	1.025335
H	7.803037	-2.278091	3.198076
H	8.757349	-0.835727	2.819260
H	9.527676	-2.429113	2.805950
H	9.208775	-1.641009	-0.867146

H	9.609310	-0.464147	0.393225
H	10.348629	-2.071536	0.423777
H	-2.667909	0.722176	-0.125527
H	2.688560	0.325136	-0.448215
H	-1.319241	2.421333	-0.391030
H	-1.312049	3.196627	1.200731
H	-2.594315	4.383332	-1.331016
H	-2.643442	5.108997	0.273050
H	1.258936	1.826352	-1.016530
H	1.229761	3.042074	0.271490
H	2.480301	3.450946	-2.503978
H	2.534463	4.616507	-1.180201

Job Type: Geometry Optimization
Macrocycle: **1b + H_2O**
Method: B3LYP
Basis Set: 6-31G(D)

Spartan '14 output:
SPARTAN '14 MECHANICS PROGRAM: (Win/64b) Release 1.1.4
Frequency Calculation
Adjusted 15 (out of 246) low frequency modes

Reason for exit: Successful completion
Mechanics CPU Time : .44
Mechanics Wall Time: .20
SPARTAN '14 Quantum Mechanics Driver: (Win/64b) Release 1.1.4
Job type: Geometry optimization.
Method: RB3LYP
Basis set: 6-31G(D)
Number of shells: 252
Number of basis functions: 731
Multiplicity: 1
Parallel Job: 4 threads
SCF model:
A restricted hybrid HF-DFT SCF calculation will be
performed using Pulay DIIS + Geometric Direct Minimization

Optimization:
Step Energy Max Grad. Max Dist.
1 -2543.452578 0.031206 0.090346
2 -2543.464638 0.017618 0.101598
3 -2543.472143 0.010592 0.112225
4 -2543.477746 0.006690 0.114285
5 -2543.482020 0.004094 0.115093
6 -2543.485395 0.003049 0.110765
7 -2543.488096 0.002359 0.103686
8 -2543.490069 0.002268 0.069763

9 -2543.491364 0.002514 0.091779
10 -2543.492290 0.002506 0.097741
11 -2543.492782 0.001435 0.105562
12 -2543.493191 0.003686 0.081504
13 -2543.493309 0.001624 0.141630
14 -2543.493538 0.002929 0.176142
15 -2543.493902 0.001844 0.098356
16 -2543.494065 0.001622 0.097830
17 -2543.494143 0.001539 0.108429
18 -2543.494178 0.002992 0.106621
19 -2543.494412 0.002183 0.052067
20 -2543.494505 0.002415 0.110139
21 -2543.494658 0.002454 0.083933
22 -2543.494818 0.002583 0.087240
23 -2543.495083 0.003146 0.092934
24 -2543.495347 0.003479 0.084632
25 -2543.495548 0.003703 0.105141
26 -2543.495808 0.003137 0.110575
27 -2543.496037 0.002177 0.097183
28 -2543.496137 0.002084 0.065565
29 -2543.496329 0.001123 0.108702
30 -2543.496415 0.001424 0.105922
31 -2543.496508 0.001000 0.042765
32 -2543.496552 0.001106 0.029142
33 -2543.496561 0.000967 0.020117
34 -2543.496577 0.000515 0.009257
35 -2543.496586 0.000321 0.009774
36 -2543.496595 0.000355 0.025073
37 -2543.496611 0.000425 0.026099
38 -2543.496620 0.000451 0.020377
39 -2543.496626 0.000485 0.008254
40 -2543.496629 0.000214 0.006846
41 -2543.496635 0.000102 0.004629
42 -2543.496635 0.000116 0.002709

Reason for exit: Successful completion
Quantum Calculation CPU Time : 3:08:29.89
Quantum Calculation Wall Time: 4:21:50.52
SPARTAN '14 Properties Program: (Win/64b) Release 1.1.4
Reason for exit: Successful completion
Properties CPU Time : 11.59
Properties Wall Time: 11.31
Atomic Coordinates:

C	-1.087681	-4.498425	-0.802761
C	-1.080969	-3.114797	-0.545776
N	0.064835	-2.406627	-0.437357
C	1.241954	-3.056458	-0.548594
C	1.315032	-4.438753	-0.803941

C	0.130391	-5.156211	-0.936405
C	-2.293459	-2.392992	-0.364645
C	2.431990	-2.292855	-0.372737
C	-3.310453	-1.763132	-0.142352
C	3.475106	-1.697149	-0.173679
C	-4.525008	-1.084479	0.133979
C	4.685768	-0.999596	0.079602
C	-5.729855	-1.807016	-0.015071
C	-6.972887	-1.253006	0.269696
C	-6.971607	0.080429	0.719206
C	-5.808348	0.822729	0.873789
C	-4.552748	0.262959	0.579290
C	4.695450	0.410084	0.239682
C	5.920740	1.038254	0.507672
C	7.085106	0.285741	0.607342
C	7.108804	-1.112694	0.450231
C	5.888555	-1.728334	0.185942
C	-8.293921	-2.025437	0.122175
C	-9.219139	-1.282915	-0.871032
C	-8.990409	-2.115143	1.500948
C	-8.078174	-3.457235	-0.403316
C	8.432903	-1.885545	0.571351
C	8.241051	-3.402317	0.383659
C	9.042486	-1.643107	1.972257
C	9.418152	-1.382752	-0.510283
N	-3.356206	0.995653	0.671513
N	3.482161	1.100395	0.107141
C	-3.191736	2.207962	1.316909
O	-4.066390	2.755926	1.977471
C	-1.837055	2.888841	1.112142
C	-2.106638	4.320752	0.634396
S	-0.647266	5.418577	0.387916
C	3.256887	2.461077	0.193708
O	4.130967	3.282025	0.438338
C	1.811171	2.881071	-0.062543
C	1.796356	4.076246	-1.015930
S	0.140397	4.764417	-1.440689
H	-2.031919	-5.024780	-0.885934
H	2.283540	-4.918412	-0.889985
H	0.157359	-6.223820	-1.135408
H	-5.644359	-2.830546	-0.359460
H	-7.913449	0.566935	0.957052
H	-5.855565	1.838729	1.235589
H	5.941596	2.111032	0.633418
H	8.009676	0.816818	0.817089
H	5.825109	-2.801984	0.055869
H	-8.749681	-1.199369	-1.857963
H	-9.458287	-0.270795	-0.528250

H	-10.164384	-1.826577	-0.989078
H	-9.939680	-2.657907	1.414065
H	-8.360083	-2.645357	2.223972
H	-9.208195	-1.124044	1.912533
H	-7.604762	-3.459996	-1.391861
H	-7.459055	-4.054046	0.276449
H	-9.045655	-3.963205	-0.496898
H	7.843328	-3.643819	-0.608937
H	7.564313	-3.823697	1.136150
H	9.204439	-3.914697	0.484033
H	8.369633	-1.999223	2.760604
H	9.236471	-0.580816	2.153954
H	9.996051	-2.175949	2.071976
H	9.013780	-1.547480	-1.515495
H	9.625073	-0.312557	-0.405184
H	10.373755	-1.915993	-0.435408
H	-2.517741	0.593444	0.243666
H	2.673179	0.519069	-0.081095
H	-1.207964	2.337464	0.410944
H	-1.321911	2.918317	2.079801
H	-2.679226	4.318005	-0.297910
H	-2.709087	4.848439	1.380359
H	1.195543	2.059413	-0.441439
H	1.382441	3.190925	0.899362
H	2.194700	3.798101	-2.000142
H	2.429600	4.873338	-0.622469
H	-0.727201	0.404409	-1.506799
O	-0.570005	0.358493	-0.551341
H	-0.276353	-0.576156	-0.402836

Job Type: Geometry Optimization
Macrocycle: **1b + HCl**
Method: B3LYP
Basis Set: 6-31G(D)

Spartan '14 output:
SPARTAN '14 Quantum Mechanics Driver: (Win/64b) Release 1.1.4
Job type: Geometry optimization.
Method: RB3LYP

Basis set: 6-31G(D)
Number of shells: 251
Number of basis functions: 733
Multiplicity: 1
Parallel Job: 4 threads
SCF model:
A restricted hybrid HF-DFT SCF calculation will be
performed using Pulay DIIS + Geometric Direct Minimization

Optimization:
Step Energy Max Grad. Max Dist.
1 -2927.889771 0.000093 0.001602
2 -2927.889772 0.000059 0.000874

Reason for exit: Successful completion
Quantum Calculation CPU Time : 11:19.47
Quantum Calculation Wall Time: 18:11.53
SPARTAN '14 Properties Program: (Win/64b) Release 1.1.4
Reason for exit: Successful completion
Properties CPU Time : 13.42
Properties Wall Time: 13.72

Atomic Coordinates:

C	-1.243841	-4.506966	-1.175346
C	-1.201030	-3.162074	-0.774283
N	0.012180	-2.572545	-0.604912
C	1.196601	-3.214594	-0.790664
C	1.177836	-4.559886	-1.187813
C	-0.049001	-5.192899	-1.377193
C	2.372826	-2.479426	-0.556722
C	-2.345465	-2.387273	-0.517520
C	3.353768	-1.803296	-0.300381
C	-3.318923	-1.704803	-0.247559
C	-4.512191	-1.016431	0.060432
C	4.531041	-1.083189	-0.000478
C	4.557859	0.337525	0.057062
C	5.795435	0.943259	0.342139
C	6.929724	0.175977	0.565558
C	6.926670	-1.232634	0.522685
C	5.708842	-1.832546	0.234180
C	-5.703999	-1.783030	0.044246
C	-6.947028	-1.238644	0.331551
C	-6.959742	0.134506	0.645959
C	-5.816102	0.919019	0.671368
C	-4.551409	0.370930	0.378555
N	-3.375658	1.128584	0.384005
N	3.388428	1.073575	-0.162803
C	3.324489	2.418855	-0.502537
C	1.911312	2.967876	-0.680527
O	4.315032	3.121702	-0.654180
C	-3.283379	2.506746	0.548841
C	-1.870978	3.081996	0.464919
O	-4.252894	3.228994	0.741509
C	-1.940489	4.605530	0.506897
C	1.963754	4.373761	-1.268170
S	0.343262	5.219125	-1.502422
S	-0.339709	5.516092	0.462738

H	0.033781	-1.547870	-0.260840
C	-8.251672	-2.052154	0.323567
C	-9.242019	-1.425935	-0.686419
C	-8.877874	-2.026844	1.738282
C	-8.018776	-3.520673	-0.075296
C	8.216064	-2.024405	0.792216
C	7.995794	-3.546124	0.696612
C	8.730247	-1.697230	2.214211
C	9.291736	-1.625844	-0.246132
Cl	0.037331	0.210244	0.373154
H	-2.206091	-4.983813	-1.315473
H	2.117144	-5.077086	-1.339857
H	-0.073869	-6.233814	-1.685998
H	5.852804	2.020604	0.374657
H	7.853839	0.701760	0.790455
H	5.619760	-2.911026	0.181343
H	-5.601600	-2.832490	-0.204838
H	-7.902261	0.620261	0.883644
H	-5.882011	1.968225	0.912409
H	-2.486759	0.636421	0.261794
H	2.490812	0.591224	-0.067869
H	1.313617	2.289559	-1.297770
H	1.417926	2.981882	0.299067
H	-1.384100	2.732795	-0.451480
H	-1.265513	2.681413	1.285943
H	-2.573517	4.987180	-0.296879
H	-2.392746	4.945598	1.444283
H	2.383951	4.362033	-2.280373
H	2.610147	5.017154	-0.669184
H	-8.834836	-1.452765	-1.703527
H	-9.466322	-0.382119	-0.444041
H	-10.189340	-1.978481	-0.683640
H	-9.820320	-2.587843	1.747327
H	-8.203854	-2.481195	2.473583
H	-9.093536	-1.005518	2.069457
H	-7.599750	-3.608013	-1.084454
H	-7.345210	-4.030528	0.623202
H	-8.972103	-4.060737	-0.065546
H	7.661657	-3.847849	-0.303025
H	7.258505	-3.899007	1.427111
H	8.937032	-4.068263	0.901047
H	9.660363	-2.241509	2.417803
H	8.936891	-0.628799	2.337785
H	7.993978	-1.984194	2.973485
H	8.954485	-1.846983	-1.265112
H	9.528877	-0.557925	-0.197898
H	10.219919	-2.181791	-0.065814

Job Type: Geometry Optimization
Macrocycle: **1c**
Method: B3LYP
Basis Set: 6-31G(D)

Spartan '14 output:
SPARTAN '14 MECHANICS PROGRAM: (Win/64b) Release 1.1.4
Frequency Calculation
Adjusted 12 (out of 255) low frequency modes

Reason for exit: Successful completion
Mechanics CPU Time : .52
Mechanics Wall Time: .25
SPARTAN '14 Quantum Mechanics Driver: (Win/64b) Release 1.1.4
Job type: Geometry optimization.
Method: RB3LYP
Basis set: 6-31G(D)
Number of shells: 260
Number of basis functions: 750
Multiplicity: 1
Parallel Job: 4 threads
SCF model:
A restricted hybrid HF-DFT SCF calculation will be
performed using Pulay DIIS + Geometric Direct Minimization
Reason for exit: Aborted by user
Quantum Calculation CPU Time : 10.17
Quantum Calculation Wall Time: 22.51
SPARTAN '14 Quantum Mechanics Driver: (Win/64b) Release 1.1.4
Job type: Geometry optimization.
Method: RB3LYP
Basis set: 6-31G(D)
Number of shells: 260
Number of basis functions: 750
Multiplicity: 1
Parallel Job: 4 threads

SCF model:
A restricted hybrid HF-DFT SCF calculation will be
performed using Pulay DIIS + Geometric Direct Minimization
Reason for exit: Aborted by user
Quantum Calculation CPU Time : 8.78
Quantum Calculation Wall Time: 16.78
SPARTAN '14 Quantum Mechanics Driver: (Win/64b) Release 1.1.4
Job type: Geometry optimization.
Method: RB3LYP
Basis set: 6-31G(D)
Number of shells: 260
Number of basis functions: 750

Multiplicity: 1
Parallel Job: 4 threads
SCF model:
A restricted hybrid HF-DFT SCF calculation will be
performed using Pulay DIIS + Geometric Direct Minimization
Optimization:
Step Energy Max Grad. Max Dist.
1 -2545.676157 0.022010 0.060604
2 -2545.684770 0.004833 0.102531
3 -2545.685783 0.003509 0.074696
4 -2545.686010 0.002420 0.078644
5 -2545.686412 0.001956 0.088181
6 -2545.686621 0.001230 0.099094
7 -2545.686810 0.001670 0.100827
8 -2545.686964 0.001042 0.101874
9 -2545.687046 0.001257 0.073162
10 -2545.687114 0.000576 0.022500
11 -2545.687146 0.000408 0.032657
12 -2545.687177 0.000355 0.058906
13 -2545.687201 0.000537 0.041508
14 -2545.687221 0.000331 0.049369
15 -2545.687241 0.000535 0.019752
16 -2545.687260 0.000414 0.029766
17 -2545.687273 0.000234 0.039551
18 -2545.687272 0.000632 0.024653
19 -2545.687285 0.000371 0.008411
20 -2545.687286 0.000200 0.014411
Reason for exit: Successful completion
Quantum Calculation CPU Time : 1:30:38.28
Quantum Calculation Wall Time: 2:06:34.56
SPARTAN '14 Properties Program: (Win/64b) Release 1.1.4
Reason for exit: Successful completion
Properties CPU Time : 12.75
Properties Wall Time: 12.46

Atomic Coordinates:

C	1.579453	3.437746	2.445222
C	1.421302	2.362135	1.548101
N	0.219138	1.942512	1.108173
C	-0.868303	2.613452	1.534941
C	-0.801605	3.698727	2.430175
C	0.445599	4.107005	2.890439
C	2.592431	1.711811	1.043183
C	-2.146349	2.223615	1.016809
C	3.654171	1.284508	0.627590
C	-3.263359	2.015197	0.580312
C	4.903555	0.828991	0.118561
C	-4.560144	1.778268	0.038577
C	5.974708	1.740985	0.026432

C	7.220530	1.377076	-0.479677
C	7.364698	0.041103	-0.894988
C	6.334789	-0.888800	-0.813000
C	5.083707	-0.511667	-0.304264
C	-5.083495	0.464907	-0.049424
C	-6.354831	0.286689	-0.611892
C	-7.076708	1.386216	-1.062449
C	-6.591549	2.703628	-0.979750
C	-5.324983	2.868354	-0.421002
C	8.397051	2.360206	-0.604812
C	8.787102	2.499925	-2.095597
C	9.609147	1.825116	0.193167
C	8.049378	3.759415	-0.063089
C	-7.440403	3.876134	-1.499867
C	-6.757646	5.237296	-1.271712
C	-7.679419	3.699784	-3.018097
C	-8.802094	3.895332	-0.765696
N	3.998005	-1.392590	-0.182033
N	-4.297278	-0.586190	0.448290
C	3.957092	-2.745509	-0.450732
C	-4.591971	-1.930855	0.500113
O	-5.620147	-2.427536	0.059896
O	4.906034	-3.383688	-0.884875
C	2.605546	-3.396802	-0.153200
C	-3.524038	-2.793508	1.169408
C	2.688449	-4.922526	-0.265709
C	-3.064379	-3.926922	0.235597
C	1.412550	-5.656051	0.154872
C	-2.244878	-4.982276	0.975932
S	0.037247	-5.352134	-1.050644
S	-1.566609	-6.304481	-0.122131
H	2.573921	3.727118	2.767410
H	-1.713755	4.196848	2.740325
H	0.532897	4.939468	3.583079
H	5.787138	2.753870	0.361720
H	8.314968	-0.294958	-1.300785
H	6.483109	-1.908835	-1.136160
H	-6.760098	-0.712153	-0.687486
H	-8.056710	1.201152	-1.492941
H	-4.881130	3.852590	-0.329143
H	7.950845	2.895549	-2.683260
H	9.074651	1.537389	-2.531767
H	9.635961	3.185684	-2.206770
H	10.453990	2.519416	0.109558
H	9.363510	1.715449	1.255748
H	9.944892	0.849372	-0.173892
H	7.219919	4.218285	-0.613296
H	7.781869	3.728007	0.999252

H	8.917569	4.419538	-0.166705
H	-5.800608	5.310112	-1.800978
H	-6.575505	5.426760	-0.207608
H	-7.401830	6.041372	-1.644785
H	-8.195143	2.760050	-3.242823
H	-8.295289	4.520358	-3.406178
H	-6.730851	3.697516	-3.567110
H	-9.364966	2.967883	-0.916106
H	-8.664307	4.030047	0.313174
H	-9.421363	4.721478	-1.135661
H	3.148752	-0.967920	0.175023
H	-3.403255	-0.297000	0.827722
H	1.855184	-2.993033	-0.846293
H	2.274827	-3.104942	0.854285
H	-2.665957	-2.199689	1.508644
H	-3.993792	-3.222593	2.064795
H	2.970264	-5.199057	-1.287381
H	3.505553	-5.279893	0.371860
H	-2.465729	-3.507360	-0.581839
H	-3.947420	-4.391439	-0.214042
H	1.080746	-5.328622	1.146252
H	1.588652	-6.734355	0.193660
H	-1.410702	-4.537186	1.529489
H	-2.865918	-5.523717	1.701059

Job Type: Geometry Optimization
Macrocycle: **1c + H_2O**
Method: B3LYP
Basis Set: 6-31G(D)

Spartan '14 output:
SPARTAN '14 MECHANICS PROGRAM: (Win/64b) Release 1.1.4
Frequency Calculation
Adjusted 12 (out of 264) low frequency modes

Reason for exit: Successful completion
Mechanics CPU Time : .45
Mechanics Wall Time: .22
SPARTAN '14 Quantum Mechanics Driver: (Win/64b) Release 1.1.4
Job type: Geometry optimization.
Method: RB3LYP
Basis set: 6-31G(D)
Number of shells: 268
Number of basis functions: 769
Multiplicity: 1
Parallel Job: 4 threads
SCF model:
A restricted hybrid HF-DFT SCF calculation will be

performed using Pulay DIIS + Geometric Direct Minimization

Optimization:
Step Energy Max Grad. Max Dist.
1 -2622.106710 0.021400 0.091242
2 -2622.116206 0.005819 0.079372
3 -2622.117875 0.002700 0.085042
4 -2622.118756 0.002644 0.079277
5 -2622.119276 0.002426 0.078581
6 -2622.119578 0.002391 0.090116
7 -2622.119746 0.002135 0.082643
8 -2622.119813 0.001914 0.069642
9 -2622.119850 0.001691 0.061742
10 -2622.119912 0.001414 0.038154
11 -2622.119956 0.001334 0.040295
12 -2622.119997 0.001424 0.033370
13 -2622.120027 0.001471 0.015740
14 -2622.120049 0.001407 0.031905
15 -2622.120084 0.001227 0.029906
16 -2622.120120 0.000977 0.050682
17 -2622.120184 0.000747 0.045772
18 -2622.120238 0.000915 0.018872
19 -2622.120274 0.000560 0.017323
20 -2622.120293 0.000331 0.009448
21 -2622.120299 0.000275 0.009037
22 -2622.120303 0.000194 0.007007
23 -2622.120304 0.000191 0.006216
24 -2622.120304 0.000096 0.003454

Reason for exit: Successful completion
Quantum Calculation CPU Time : 1:54:08.88
Quantum Calculation Wall Time: 2:36:40.40
SPARTAN '14 Properties Program: (Win/64b) Release 1.1.4
Reason for exit: Successful completion
Properties CPU Time : 13.53
Properties Wall Time: 13.30
Atomic Coordinates:

C	1.507243	3.609253	2.525117
C	1.441059	2.516361	1.639565
N	0.267633	2.016987	1.188994
C	-0.874320	2.615716	1.584101
C	-0.887992	3.710621	2.467951
C	0.323249	4.203419	2.943491
C	2.635366	1.917329	1.148908
C	-2.115597	2.151952	1.042697
C	3.656052	1.452111	0.678655
C	-3.226419	1.915561	0.603898
C	4.854054	0.945235	0.110546

C	-4.528109	1.683358	0.071854
C	5.975314	1.801374	0.054962
C	7.193256	1.400723	-0.484564
C	7.253701	0.084212	-0.977039
C	6.170713	-0.784966	-0.940540
C	4.940538	-0.378110	-0.395529
C	-5.115539	0.394946	0.094185
C	-6.405309	0.240978	-0.434422
C	-7.076346	1.335885	-0.966482
C	-6.518498	2.626495	-1.009640
C	-5.239271	2.769541	-0.476181
C	8.425522	2.318867	-0.555907
C	8.859617	2.482661	-2.032002
C	9.584331	1.688616	0.251828
C	8.143677	3.718886	0.020423
C	-7.314790	3.798853	-1.607803
C	-6.502383	5.107494	-1.623736
C	-7.717954	3.464362	-3.063341
C	-8.591799	4.027950	-0.764831
N	3.815701	-1.216425	-0.334790
N	-4.373138	-0.656834	0.651428
C	3.827476	-2.596516	-0.422222
C	-4.741124	-1.977394	0.809640
O	-5.825808	-2.430967	0.471547
O	4.833160	-3.255842	-0.657572
C	2.478201	-3.265234	-0.156311
C	-3.669488	-2.871811	1.424650
C	2.522796	-4.751019	-0.528603
C	-3.206478	-3.929453	0.403942
C	1.303394	-5.556750	-0.073948
C	-2.335412	-5.007636	1.042989
S	-0.172348	-5.179584	-1.130808
S	-1.684814	-6.241964	-0.168638
H	2.474510	3.967521	2.859506
H	-1.835136	4.151689	2.757398
H	0.342337	5.046379	3.628502
H	5.847588	2.799930	0.455458
H	8.179082	-0.282857	-1.412896
H	6.265109	-1.790845	-1.320662
H	-6.865006	-0.736711	-0.418533
H	-8.074279	1.168983	-1.362467
H	-4.744156	3.733405	-0.470840
H	8.059580	2.937831	-2.627032
H	9.110858	1.521055	-2.491630
H	9.744431	3.127388	-2.100374
H	10.478348	2.321587	0.193457
H	9.312587	1.579454	1.308033
H	9.852929	0.696773	-0.126726

H	7.347067	4.234157	-0.528560
H	7.858523	3.673172	1.077566
H	9.047356	4.334032	-0.052109
H	-5.583730	5.009279	-2.213880
H	-6.228282	5.432761	-0.613432
H	-7.100384	5.907199	-2.074664
H	-8.336061	2.562351	-3.117952
H	-8.297220	4.289528	-3.495015
H	-6.833980	3.303312	-3.690708
H	-9.227425	3.136529	-0.744830
H	-8.337007	4.280763	0.270682
H	-9.182431	4.852047	-1.183048
H	2.902919	-0.777394	-0.168468
H	-3.446841	-0.398551	0.970084
H	1.673961	-2.726235	-0.667838
H	2.260314	-3.156257	0.916828
H	-2.812665	-2.297034	1.797568
H	-4.134039	-3.367045	2.286271
H	2.666993	-4.861322	-1.610547
H	3.412057	-5.195859	-0.069553
H	-2.643070	-3.437926	-0.398625
H	-4.089352	-4.389862	-0.050831
H	1.051983	-5.332421	0.968210
H	1.500192	-6.629151	-0.155372
H	-1.484423	-4.577756	1.581932
H	-2.911342	-5.606513	1.760207
H	0.616801	0.396118	0.156794
O	0.945229	-0.347557	-0.399822
H	0.892054	0.001593	-1.302192

Job Type: Geometry Optimization
Macrocycle: **1c + HCl**
Method: B3LYP
Basis Set: 6-31G(D)

Spartan '14 output:
SPARTAN '14 MECHANICS PROGRAM: (Win/64b) Release 1.1.4
Frequency Calculation
Adjusted 10 (out of 261) low frequency modes

Reason for exit: Successful completion
Mechanics CPU Time : .52
Mechanics Wall Time: .21
SPARTAN '14 Quantum Mechanics Driver: (Win/64b) Release 1.1.4
Job type: Geometry optimization.
Method: RB3LYP
Basis set: 6-31G(D)
Number of shells: 267

Number of basis functions: 771
Multiplicity: 1
Parallel Job: 4 threads
SCF model:
A restricted hybrid HF-DFT SCF calculation will be
performed using Pulay DIIS + Geometric Direct Minimization

Optimization:
Step Energy Max Grad. Max Dist.
1 -3006.497086 0.027030 0.070942
2 -3006.509393 0.008185 0.073402
3 -3006.511674 0.002980 0.101007
4 -3006.512480 0.002171 0.130487
5 -3006.513016 0.002295 0.136165
6 -3006.513416 0.002125 0.147310
7 -3006.513739 0.001924 0.141779
8 -3006.514035 0.001673 0.142057
9 -3006.514284 0.001914 0.145327
10 -3006.514531 0.001928 0.146261
11 -3006.514810 0.001894 0.152215
12 -3006.515084 0.002593 0.151743
13 -3006.515318 0.002223 0.139305
14 -3006.515456 0.003336 0.124797
15 -3006.515657 0.001741 0.102100
16 -3006.515790 0.001301 0.053100
17 -3006.515875 0.001325 0.051738
18 -3006.515885 0.000938 0.034981
19 -3006.515919 0.000636 0.013493
20 -3006.515937 0.000603 0.021922
21 -3006.515945 0.000804 0.016071
22 -3006.515950 0.000735 0.013272
23 -3006.515954 0.000763 0.011202
24 -3006.515956 0.000605 0.013852
25 -3006.515955 0.000469 0.014264
26 -3006.515956 0.000381 0.010457
27 -3006.515951 0.000355 0.008032
28 -3006.515953 0.000403 0.013375
29 -3006.515948 0.000469 0.016873
30 -3006.515950 0.000467 0.019869
31 -3006.515951 0.000363 0.006005
32 -3006.515956 0.000232 0.005978
33 -3006.515958 0.000116 0.002944
34 -3006.515961 0.000061 0.002387
35 -3006.515960 0.000075 0.000743

Reason for exit: Successful completion
Quantum Calculation CPU Time : 2:54:38.33
Quantum Calculation Wall Time: 4:02:50.83

SPARTAN '14 Properties Program: (Win/64b) Release 1.1.4
Reason for exit: Successful completion
Properties CPU Time : 14.45
Properties Wall Time: 14.40

Atomic Coordinates:

C	-0.927825	-4.662119	1.007917
C	-0.997324	-3.302342	0.668965
N	0.159641	-2.603091	0.513357
C	1.392384	-3.160610	0.652655
C	1.485110	-4.517165	1.003847
C	0.319583	-5.256651	1.179316
C	2.527446	-2.365514	0.410760
C	-2.217434	-2.630482	0.467294
C	3.555326	-1.762984	0.151504
C	-3.288669	-2.088648	0.259831
C	-4.555785	-1.516901	0.003755
C	4.775698	-1.122046	-0.154337
C	4.823766	0.132438	-0.822562
C	6.095122	0.649202	-1.133805
C	7.245892	-0.039704	-0.778671
C	7.226667	-1.276669	-0.102786
C	5.972878	-1.793724	0.192481
C	-5.608540	-2.390030	-0.340852
C	-6.900373	-1.940527	-0.602271
C	-7.106353	-0.554604	-0.499228
C	-6.091920	0.336496	-0.160108
C	-4.788786	-0.115328	0.097985
N	-3.737822	0.743463	0.437194
N	3.637089	0.802339	-1.125683
C	3.496943	1.945431	-1.911530
C	2.108908	2.556895	-1.888827
O	4.422873	2.461395	-2.520563
C	-3.868229	2.036707	0.930445
C	-2.553780	2.759955	1.178912
O	-4.951408	2.567402	1.135112
C	-2.675501	3.774323	2.320343
C	2.086145	3.709562	-0.859419
C	0.686277	4.309350	-0.729425
C	-1.438151	4.660298	2.488233
H	0.089322	-1.545455	0.281620
C	-8.007773	-2.940422	-0.978863
C	-9.361493	-2.244286	-1.214710
C	-8.186837	-3.969527	0.162029
C	-7.609697	-3.680921	-2.277248
C	8.541144	-1.980970	0.271310
C	8.299412	-3.327415	0.979343
C	9.354006	-1.071917	1.223346
C	9.364406	-2.250642	-1.010222

S	0.728993	5.688450	0.507263
S	-1.256744	5.886055	1.097260
Cl	-0.068701	0.295938	-0.027414
H	-1.848559	-5.218185	1.133692
H	2.465748	-4.962179	1.118567
H	0.384070	-6.307207	1.446832
H	6.157522	1.588995	-1.661464
H	8.199272	0.410859	-1.039448
H	5.870603	-2.743445	0.703558
H	-5.373084	-3.448089	-0.399128
H	-8.089386	-0.138686	-0.691217
H	-6.303326	1.392035	-0.079218
H	-2.785834	0.388536	0.339906
H	2.778431	0.430039	-0.723185
H	1.909738	2.948930	-2.891320
H	1.339818	1.821186	-1.633436
H	-2.305451	3.291447	0.249101
H	-1.736243	2.052225	1.351666
H	-3.568943	4.387076	2.161526
H	-2.837876	3.241465	3.267857
H	2.814560	4.472429	-1.159673
H	2.399413	3.328543	0.120053
H	0.325853	4.700316	-1.686183
H	-0.011634	3.546277	-0.375682
H	-0.517249	4.070870	2.517911
H	-1.503898	5.233406	3.418135
H	-9.314763	-1.528610	-2.043328
H	-9.707212	-1.712669	-0.320993
H	-10.120829	-2.992995	-1.466122
H	-8.972010	-4.690727	-0.095615
H	-7.267071	-4.534084	0.350733
H	-8.473195	-3.474783	1.097028
H	-7.474238	-2.975262	-3.104555
H	-6.674424	-4.238626	-2.156896
H	-8.389656	-4.396501	-2.564848
H	7.745995	-4.028933	0.344102
H	7.747029	-3.204864	1.918443
H	9.260486	-3.792635	1.224378
H	10.302917	-1.552011	1.491230
H	9.588355	-0.106370	0.763034
H	8.797889	-0.875415	2.147060
H	8.814966	-2.901515	-1.699712
H	9.604955	-1.325452	-1.544419
H	10.311467	-2.742535	-0.757797

SOLUTION STATE TITRATION DATA

NMR titration data is not presented here due to an inability to obtain reliable fits to the data, however, example fits from treatment of **1b•TFA** with TBACl in acetonitrile with 15% H_2O are presented.

1b•TFA was prepared through dissolution of **1b** in CH_2Cl_2 and then bubbling TFA vapors through the solution. This was then dried under vacuum, and the solid remaining was used to prepare solutions of **1b•TFA** for analysis.

2.4mg **1b•TFA** was dissolved in 3 mL acetonitrile with 15% H_2O, and the UV/Vis absorption spectrum was measured after every addition of a stock solution of TBACl (16.9 mM in acetonitrile with 15% H_2O).

The results obtained from these studies yielded variable association constants depending on the period of time the solutions stood prior to analysis, leading us to believe the macrocycles were structurally dynamic in the partially aqueous solutions. These titrations presented here are the result of the measurement occurring as quickly as possible after solution preparation.

The highest quality fits for association in solution resulted from calculation as a 2:1 host:guest ratio.

The relative amounts of host and guest were correlated to the absorbance values of a peak at 255 nm, and fitted with the Thordarson host-guest association program provided at http://supramolecular.org/.

The result of the titrations and the fitting are provided below.

Titration 1

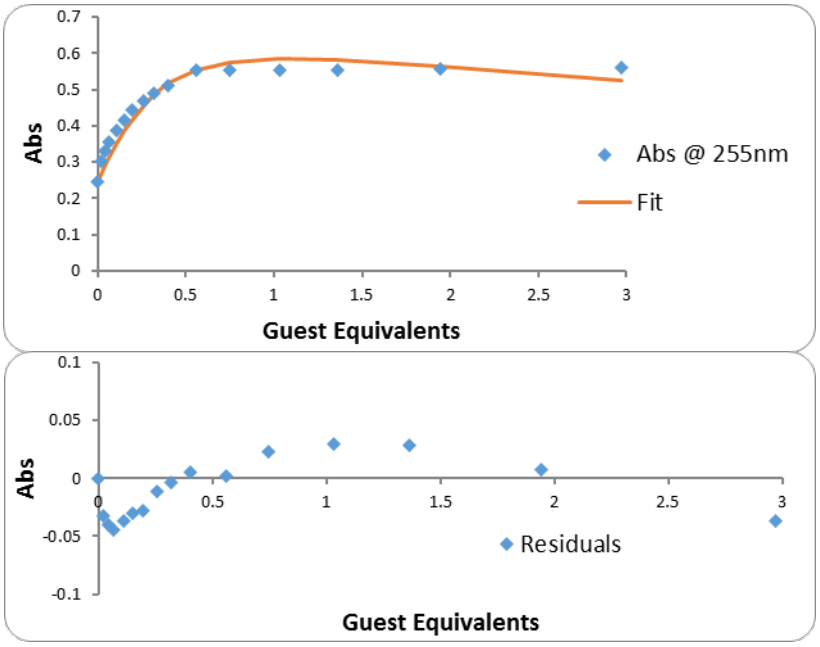

Figure A.4. Titration fit results for **1b•TFA** + TBACl.

K_{11}	7.30621474
K_{21}	1.2292E+10
RMS:	0.02672682
Covariance:	0.05909585

Table A.1. Results from titration of 1b•TFA + TBACl.

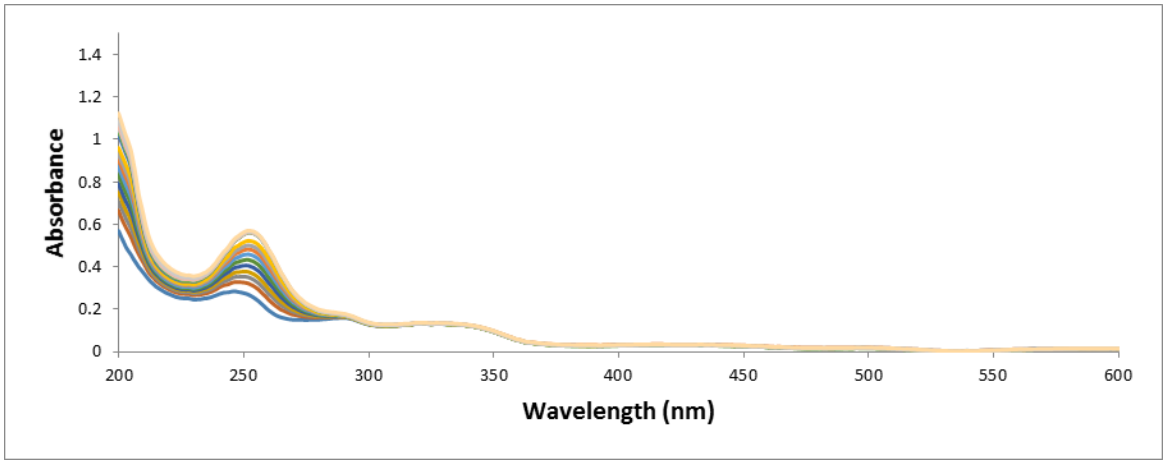

Figure A.5. Stacked UV/Vis absorption plots of titration of **1b•TFA** with TBACl.

Titration 2

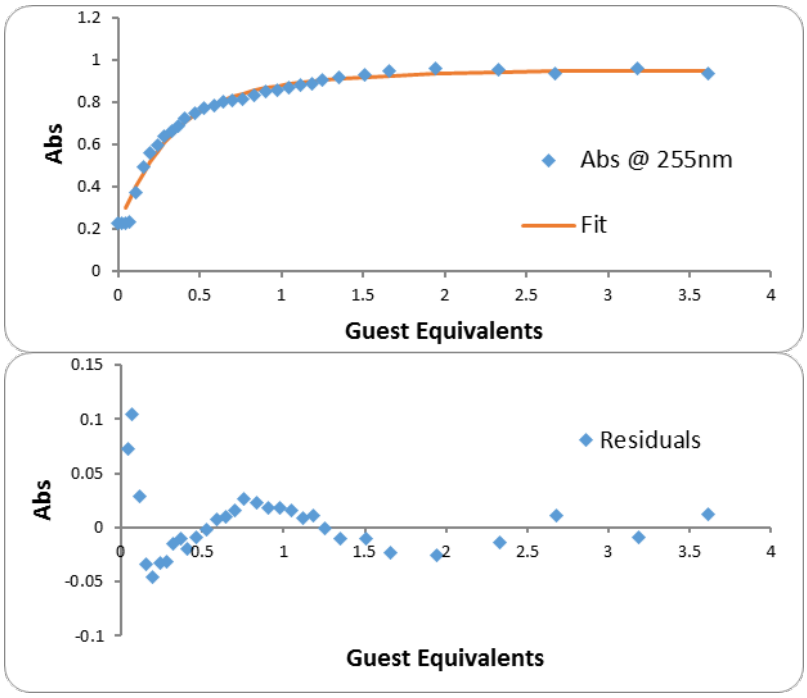

Figure A.6. Titration fit results for **1b•TFA** + TBACl.

K_{11}	11.9227657
K_{21}	1.0748E+10
RMS:	0.03001286
Covariance:	0.02217114

Table A.2. Results from titration of 1b•TFA + TBACl.

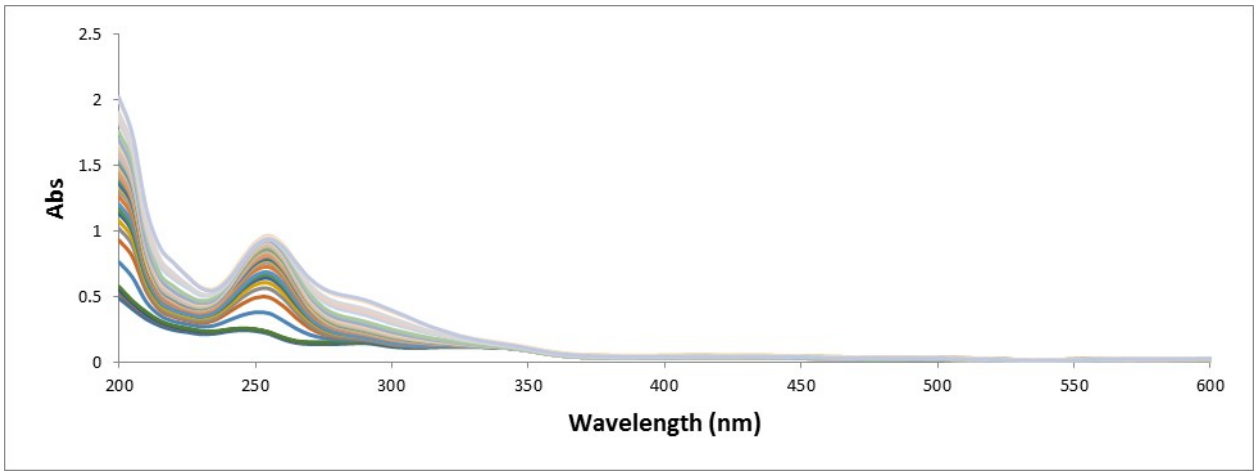

Figure A.7. Stacked UV/Vis absorption plots of titration of **1b•TFA** with TBACl.

APPENDIX B

SUPPORTING INFORMATION FOR CHAPTER III: ELECTROCHEMICAL DETERMINATION OF DISULFIDE REDOX POTENTIALS: A CORRELATED STUDY RELATING IRREVERSIBLE NON-NERNSTIAN TWO-ELECTRON PROCESSES TO STANDARD DISULFIDE REDOX POTENTIALS

Cyclic Voltammetry

All electrochemical experiments were conducted in a traditional 3- electrode geometry with a Biologic SP-50. Electrolyte solutions (0.1 M) were prepared from HPLC-grade DMSO/MeOH and anhydrous Bu_4NBF_4, and the solutions were extensively sparged with N_2 prior to analysis, and held under N_2 atmosphere for the duration of the experiment. The working electrode was a glassy carbon electrode (3-mm diameter), with a Pt coil counter electrode and Ag wire pseudo reference. The ferrocene/ferrocenium (Fc/Fc^+) couple was used as an internal standard following each experiment. Potential values were referenced to NHE using Fc/Fc^+(DMSO) = +0.482 V[1]. Cyclic voltammetry experiments were conducted at sweep rates of 50 (reported), 75, 100, 125 and 150 mV s^{-1}. The anodic peak current increases linearly with the square root of the scan rate in the range 50 to 125 mV s^{-1}, indicating a diffusion-controlled process. Analyte concentrations were ca. 1-5 mM.

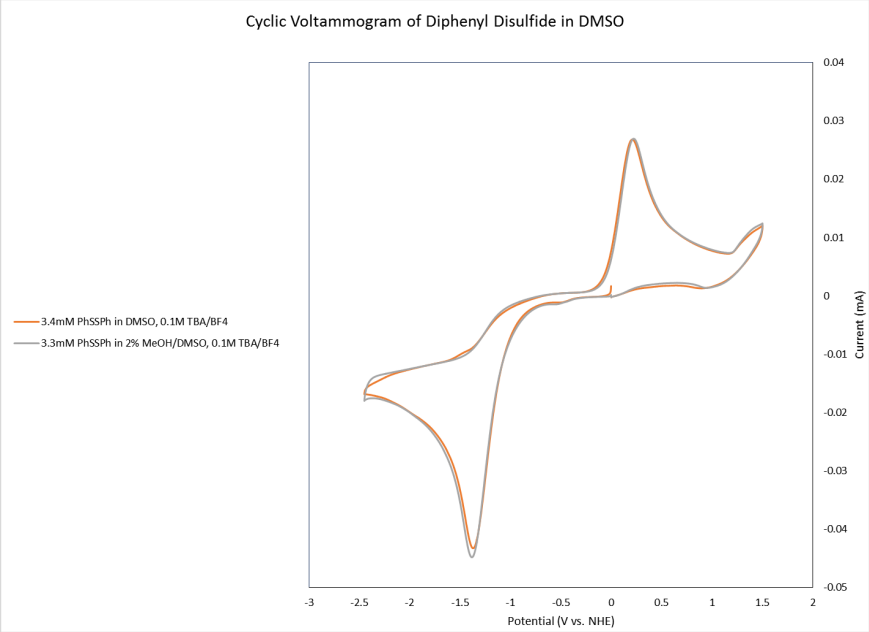

Figure B.1. Cyclic voltammogram of diphenyl disulphide in DMSO and 2%MeOH/DMSO.

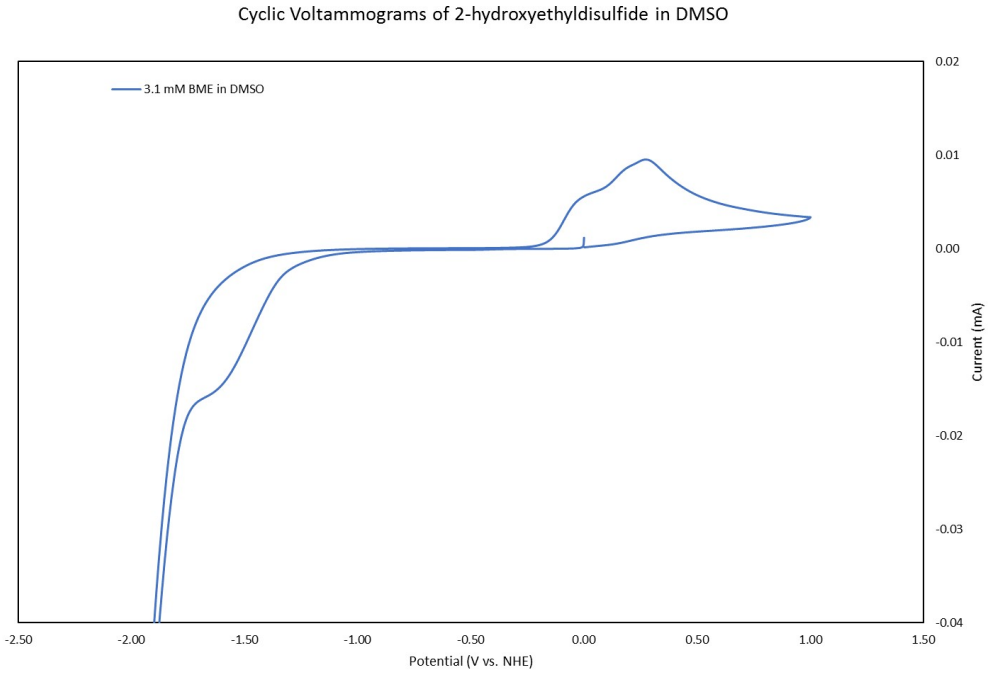

Figure B.2. Cyclic voltammogram of 2-hydroxyethyl disulfide in DMSO.

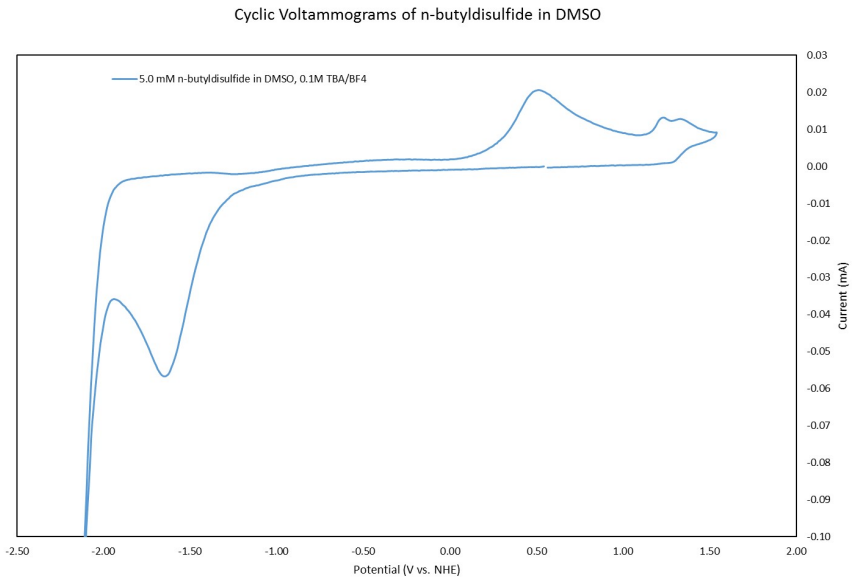

Figure B.3. Cyclic voltammogram of 2-hydroxyethyl disulfide in DMSO.

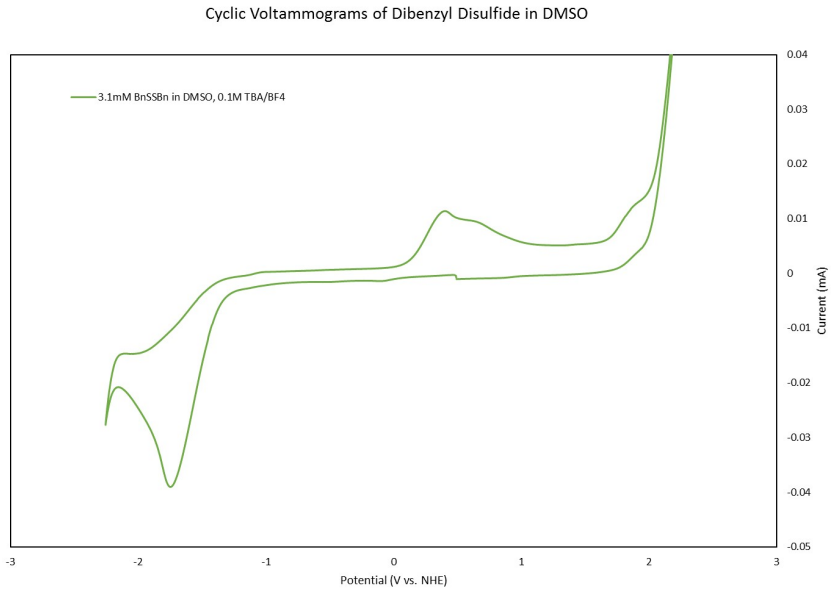

Figure B.4. Cyclic voltammogram of benzyl disulfide in DMSO.

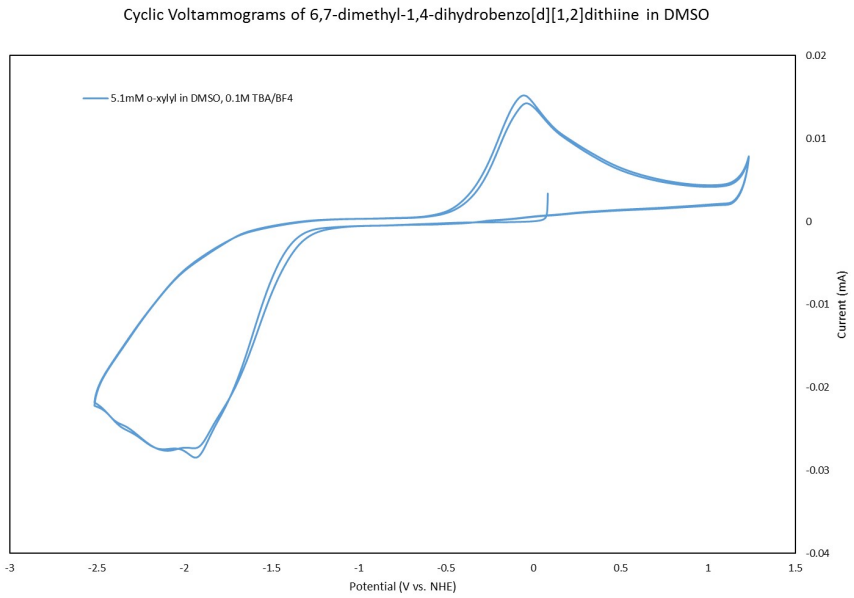

Figure B.5. Cyclic voltammogram of 6,7-dimethyl-1,4-dihydrobenzo[b][1,2]dithiine in DMSO.

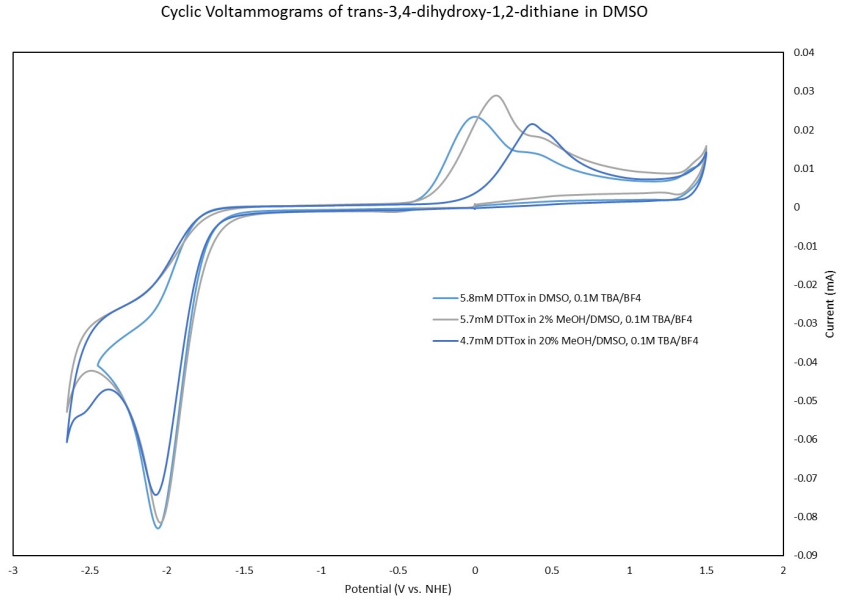

Figure B.6. Cyclic voltammogram of trans-3,4-dihydroxy-1,2-dithiane in DMSO.

Determination of redox potentials via solution equilibration

An equimolar (5mM) amount of DTT and target sensor were combined in N_2 sparged 1:1 DMF-d7 and CD_3OD in triplicate in septa-capped NMR tubes. The ratio of reduced and oxidized DTT was then measured via NMR periodically for a total time period of 48 hours. The redox potential was determined by use of the Nernst equation to relate the reduction potential of the disulphide under query to that of the known DTT/DTT^{ox} redox couple. See **Figure B.7** for a plot of the ratio of DTT/DTT^{ox} as a function of time.

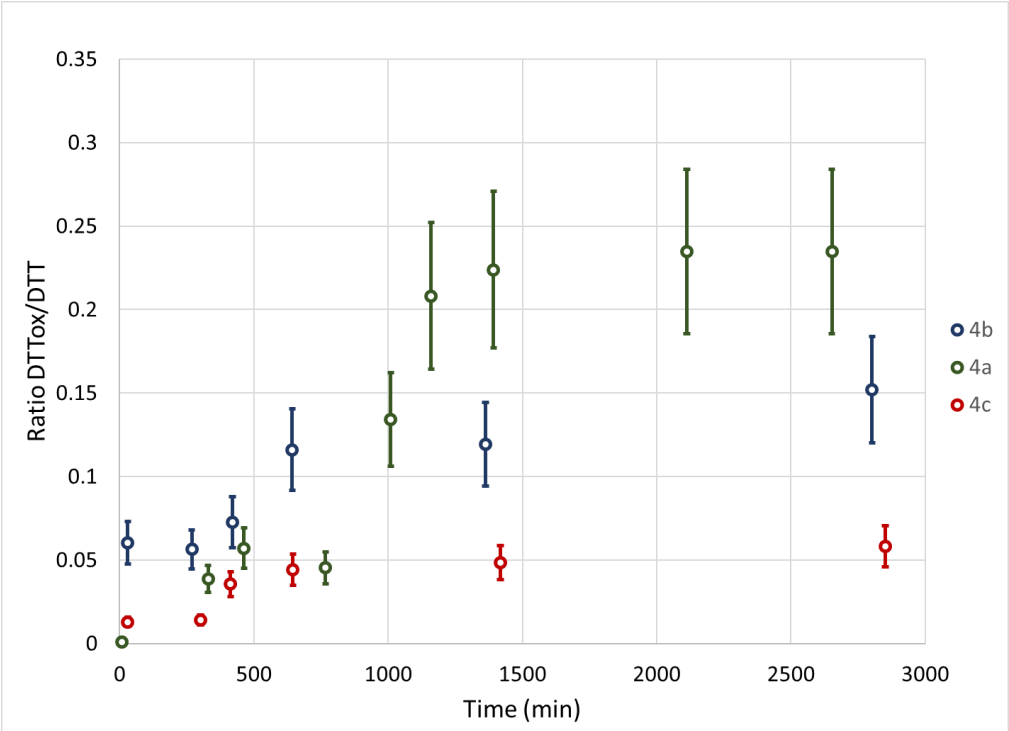

Figure B.7. A plot of the ratio of DTT/DTT^{ox} as a function of time in the presence of disulfides **4a^{ox}-4c^{ox}**.

APPENDIX C

SUPPORTING INFORMATION FOR CHAPTER V: INITIAL INVESTIGATIONS INTO THE FORMATION AND APPLICATIONS OF 2-Λ^5-PHOSPHAQUINOLINES

DETERMINATION OF DIMERIZATION CONSTANTS

Azaphosphinine (~22.5 μmol) was dissolved in $CDCl_3$ (900 μL) saturated with H_2O (H_2O saturated $CDCl_3$ prepared by mixing equal parts (v/v) $CDCl_3$ and H_2O for 10 min followed by separation of the two layers). H_2O saturated $CDCl_3$ aliquots were added to the initial solution (25 mM) until the titration end point was reached (minimal chemical shift change per $CDCl_3$ aliquot). All additions performed through septa via Hamilton gas tight microsyringe at room temperature. ^1H NMR spectra recorded after each addition on a Varian 500 MHz spectrometer. Proton signals were referenced to residual $CHCl_3$ signal. The dimerization constant (K_{dim}) was calculated by plotting the change in shift of the phosphonamidate proton versus total concentration and resulting data was fit to a 1:1 dimerization with non-linear regression curve fitting software Hyperquad2006, χ^2 of fit reported in each section and all regressions fell within the 95% confidence interval. Dimerization constant determination performed in triplicate, K_{dim} reported as mean, error reported as standard error.

$$Standard\ error = \frac{\sqrt{\Sigma(x-\bar{x})^2}}{\sqrt{N}}$$

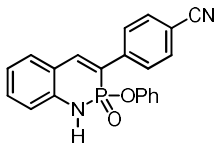

Figure C.1. Compound **11b**.

$$K_{dim} = 130 \pm 4\ M^{-1}$$

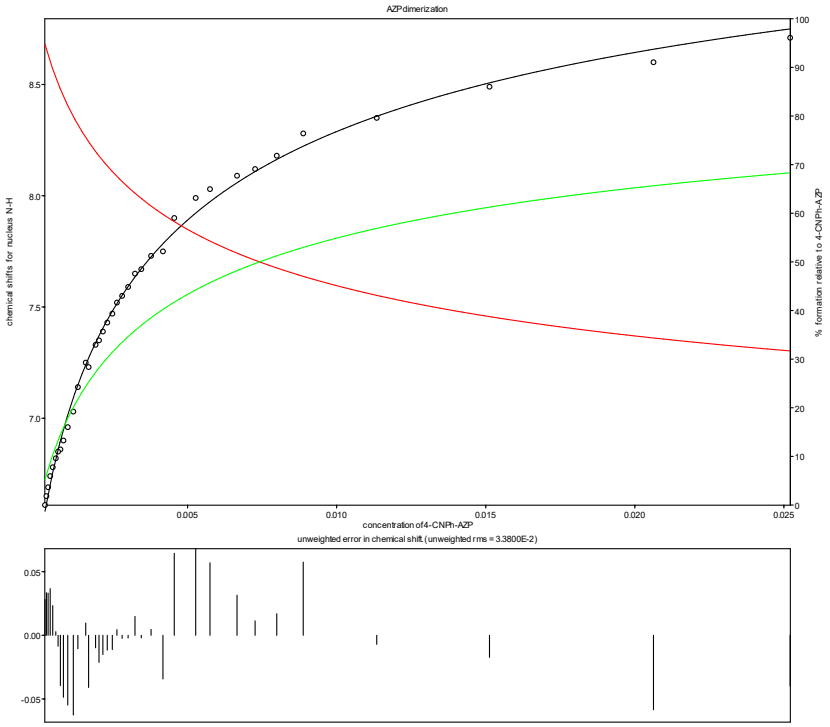

Figure C.2. Representative dimerization fit of Compound **11b.**

Solvent: water saturated $CDCl_3$ Results page - HypNMR version: 16.04.2006. Hqdll version: 09/05/2006. 3 iterations Refinement converged successfully			
sigma = 0.03524434951		RMS weighted residual = 0.03378532460	Chi-squared = 5.59 Chi-squared should be less than 12.60 at the 95% confidence level
Beta 2 refined	value	rSD	SD
	1.3374E+002	0.0637	0.0277

Table C.1. Results of dimerization fit of Compound **11b.**

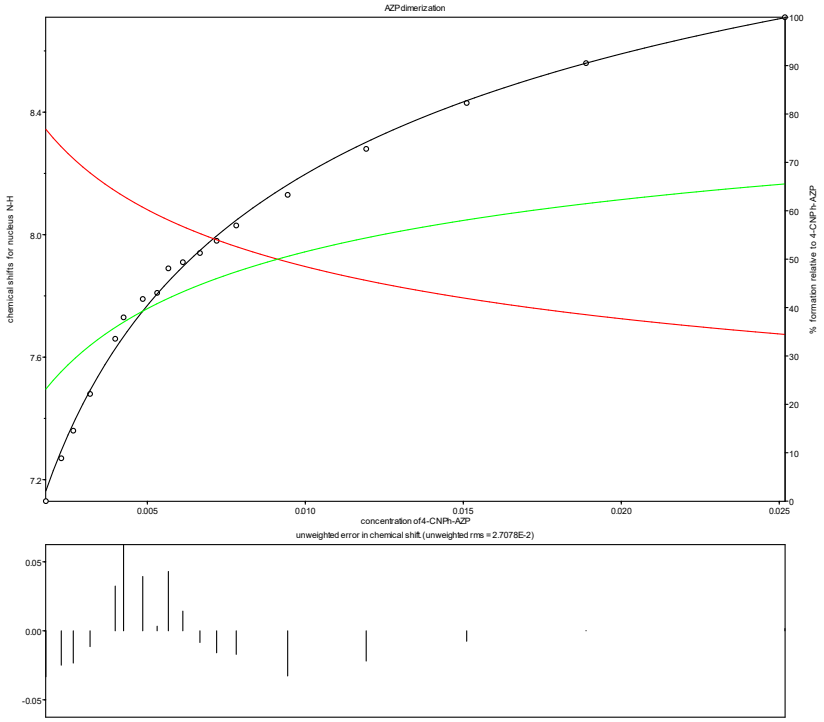

Figure C.3. Representative dimerization fit of Compound **11b.**

Solvent: water saturated $CDCl_3$ Results page - HypNMR version: 16.04.2006. Hqdll version: 09/05/2006. 4 iterations Refinement converged successfully			
sigma = 0.02686072296		RMS weighted residual 0.02452037312	Chi-squared = 4.22 Chi-squared should be less than 12.60 at the 95% confidence level
Beta 2 refined	value	rSD	SD
	1.5329E+002	0.0144	0.0062

Table C.2. Results of dimerization fit of Compound **11b.**

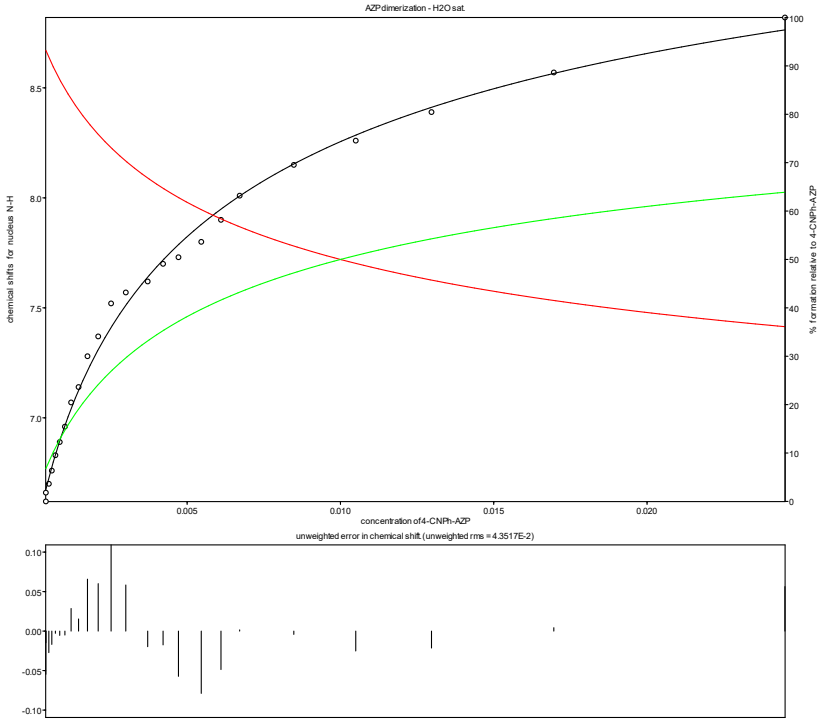

Figure C.4. Representative dimerization fit of Compound **11b.**

Solvent: water saturated $CDCl_3$ Results page - HypNMR version: 16.04.2006. Hqdll version: 09/05/2006. 3 iterations Refinement converged successfully			
sigma = 0.04592437076		RMS weighted residual 0.04295831527	Chi-squared = 7.33 Chi-squared should be less than 12.60 at the 95% confidence level
Beta 2 refined	value	rSD	SD
	1.0906E+002	0.1109	0.0482

Table C.3. Results of dimerization fit of Compound **11b.**

Dimerization data for compound 10b					
Raw data for trial 1		Raw data for trial 2		Raw data for trial 3	
conc. (M)	ppm	conc. (M)	ppm	conc. (M)	ppm
0.02521	8.71	0.025179	8.71	0.024496	8.82
0.020626	8.6	0.018884	8.56	0.016959	8.57
0.015126	8.49	0.015107	8.43	0.012969	8.39
0.011344	8.35	0.011927	8.28	0.010498	8.26
0.008878	8.28	0.009442	8.13	0.00848	8.15
0.00799	8.18	0.007814	8.03	0.006713	8.01
0.007264	8.12	0.007194	7.98	0.006103	7.9
0.006659	8.09	0.006665	7.94	0.00546	7.8
0.005751	8.03	0.006125	7.91	0.004716	7.73
0.005271	7.99	0.005665	7.89	0.004214	7.7
0.004553	7.9	0.005311	7.81	0.003712	7.62
0.004173	7.75	0.004856	7.79	0.002998	7.57
0.003776	7.73	0.004249	7.73	0.002519	7.52
0.003447	7.67	0.003983	7.66	0.002099	7.37
0.003236	7.65	0.003187	7.48	0.001749	7.28
0.003005	7.59	0.002656	7.36	0.001458	7.14
0.002805	7.55	0.002276	7.27	0.001215	7.07
0.00263	7.52	0.001788	7.13	0.001012	6.96
0.002475	7.47			0.000844	6.89
0.002306	7.43			0.000703	6.83
0.002159	7.39			0.000586	6.76
0.002029	7.35			0.000488	6.7
0.001915	7.33			0.000391	6.66
0.00168	7.23			0.000391	6.62
0.001583	7.25				
0.001321	7.14				
0.001168	7.03				
0.00098	6.96				
0.000835	6.9				
0.000735	6.86				
0.000656	6.85				
0.00058	6.82				
0.000477	6.78				
0.000392	6.74				
0.000322	6.69				
0.000264	6.65				
0.000217	6.61				
0.000677	6.69				
0.000599	6.65				
0.000537	6.62				
0.000426	6.55				

Table C.4. Table of raw ^{1}H NMR ppm and concentration values for dimerization fit of Compound **11b.**

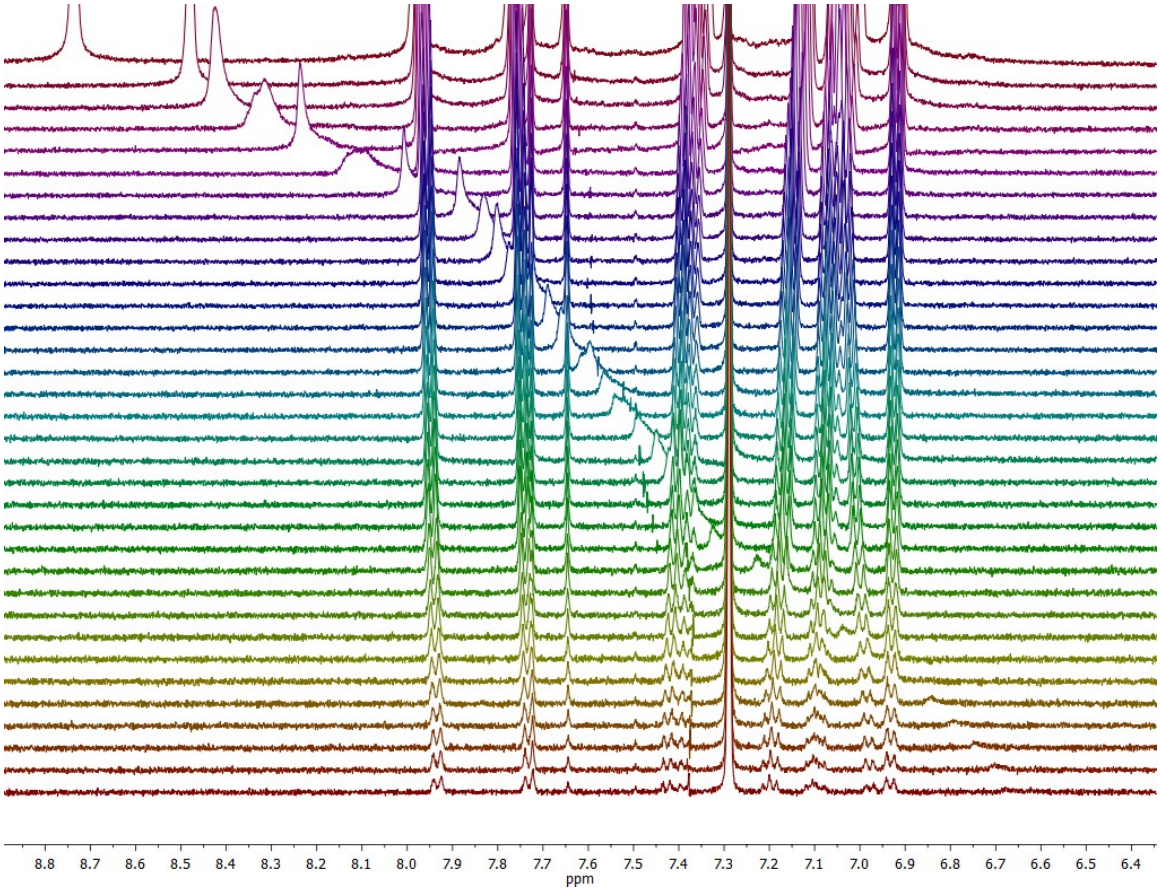

Figure C.5. Representative stacked ^{1}H NMR plot from dimerization experiment of Compound **11b.**

FLUORESCENCE SPECTRA

Phosphonimidate Species in $CHCl_3$

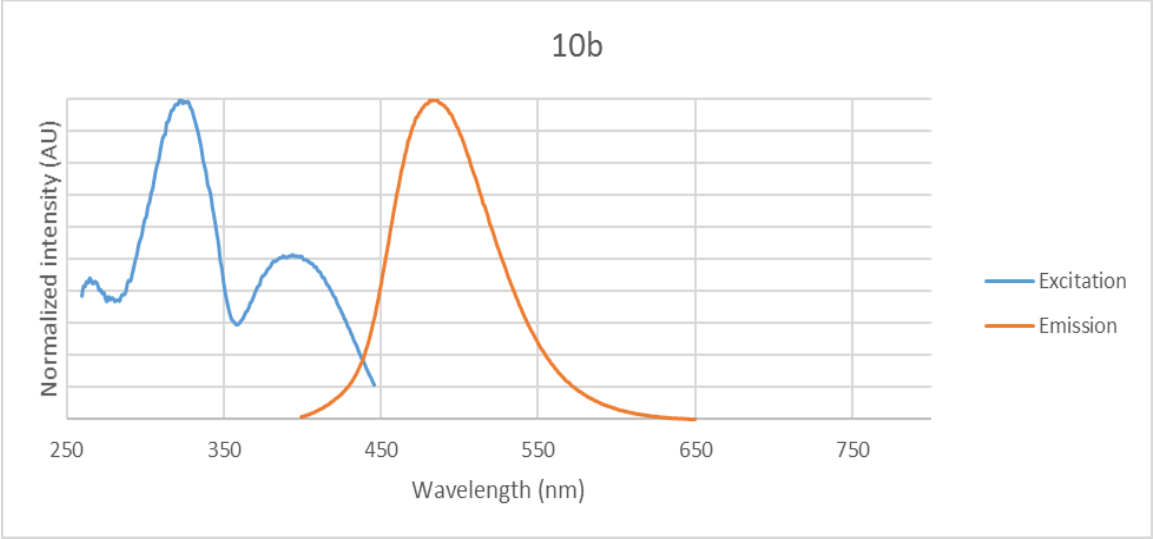

Figure C.6. Excitation and emission spectra of compound **10b** in $CHCl_3$**.**

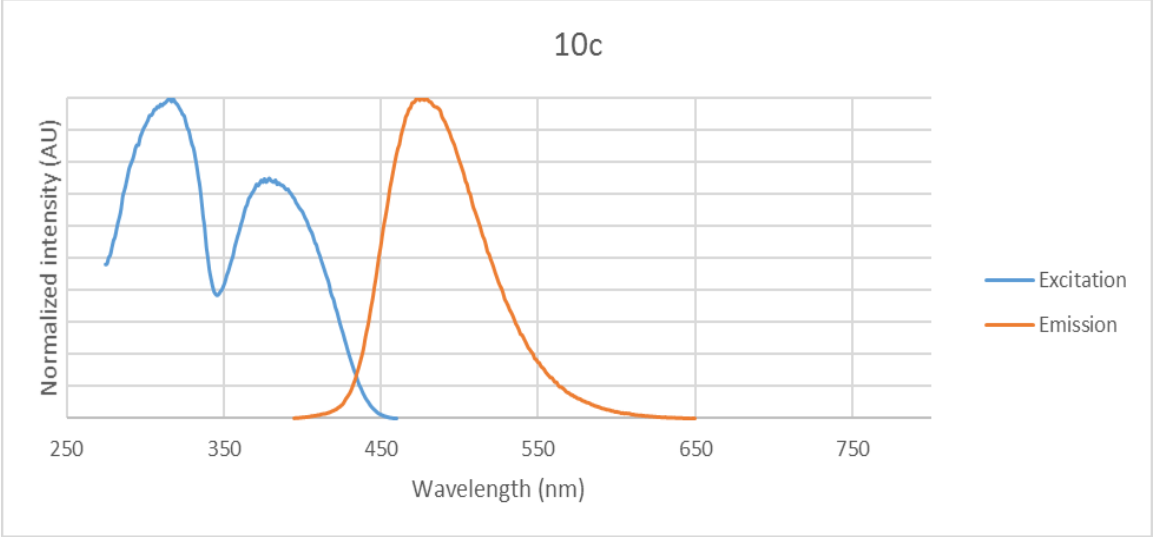

Figure C.7. Excitation and emission spectra of compound **10c** in $CHCl_3$**.**

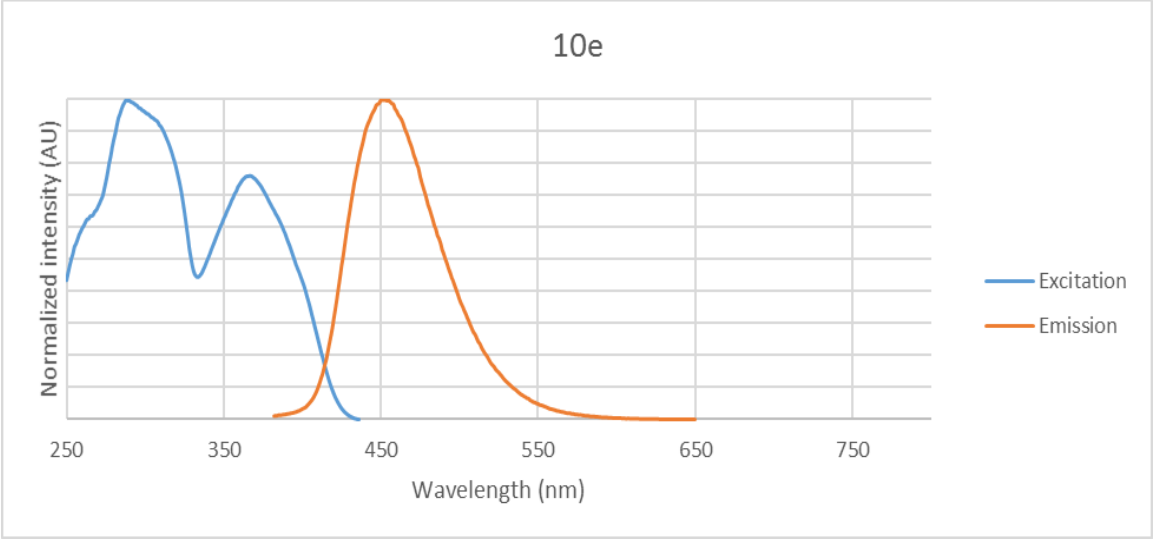

Figure C.8. Excitation and emission spectra of compound **10e** in $CHCl_3$**.**

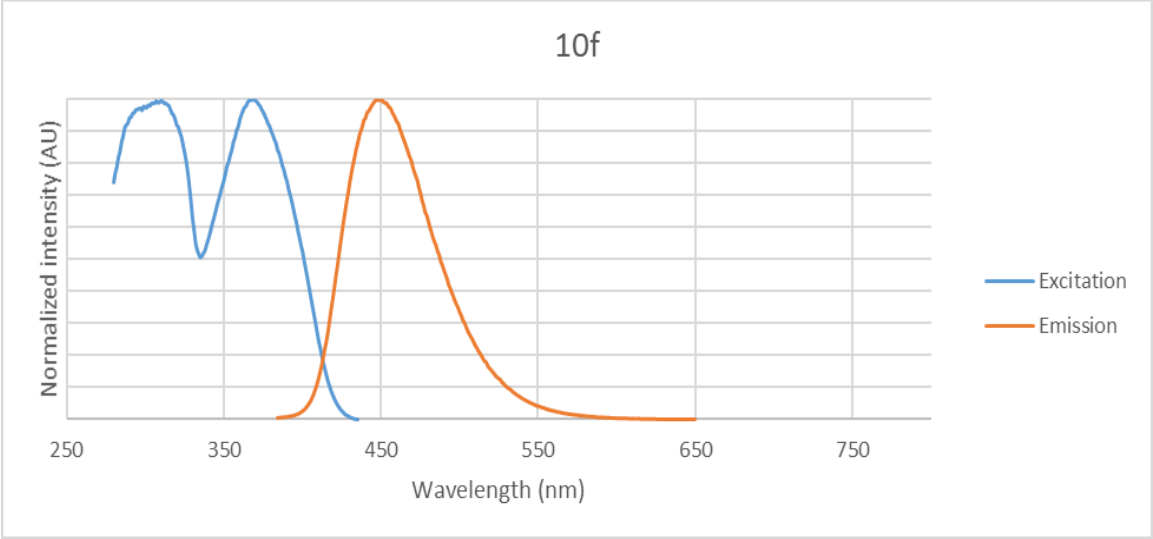

Figure C.9. Excitation and emission spectra of compound **10f** in $CHCl_3$**.**

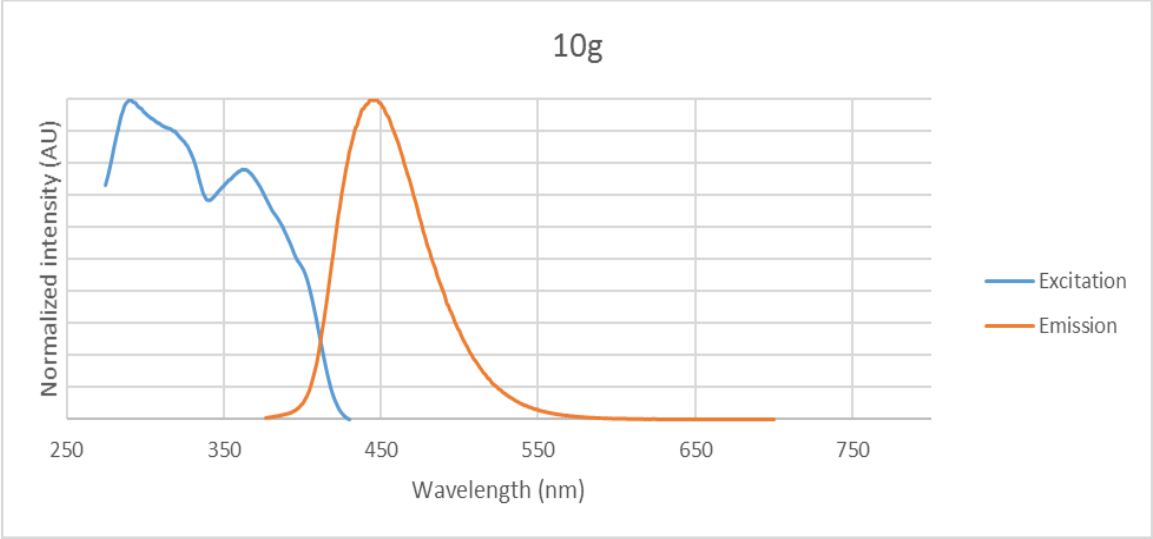

Figure C.10. Excitation and emission spectra of compound **10g** in $CHCl_3$**.**

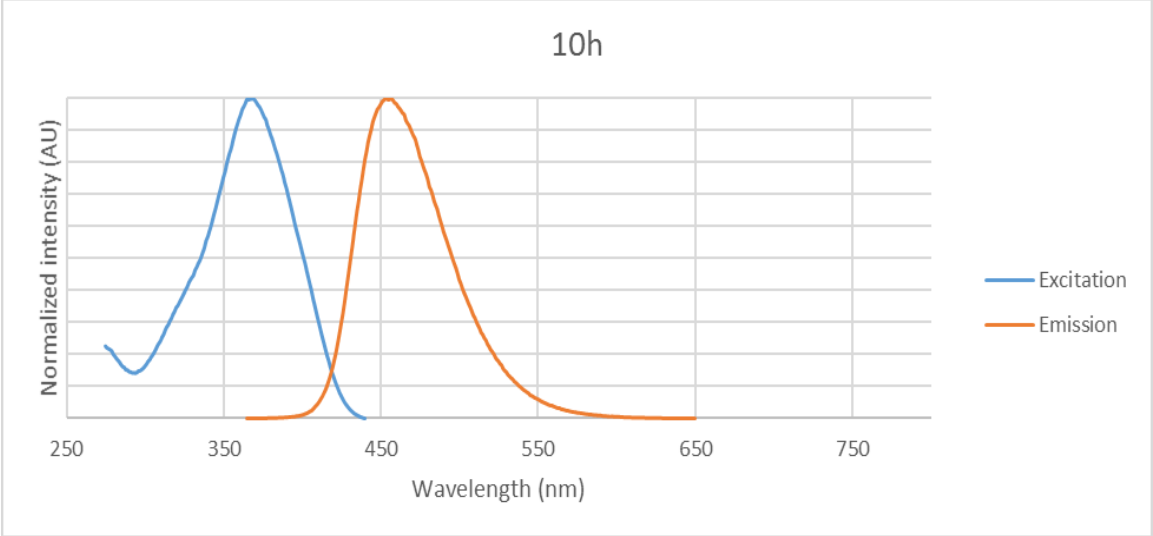

Figure C.11. Excitation and emission spectra of compound **10h** in $CHCl_3$**.**

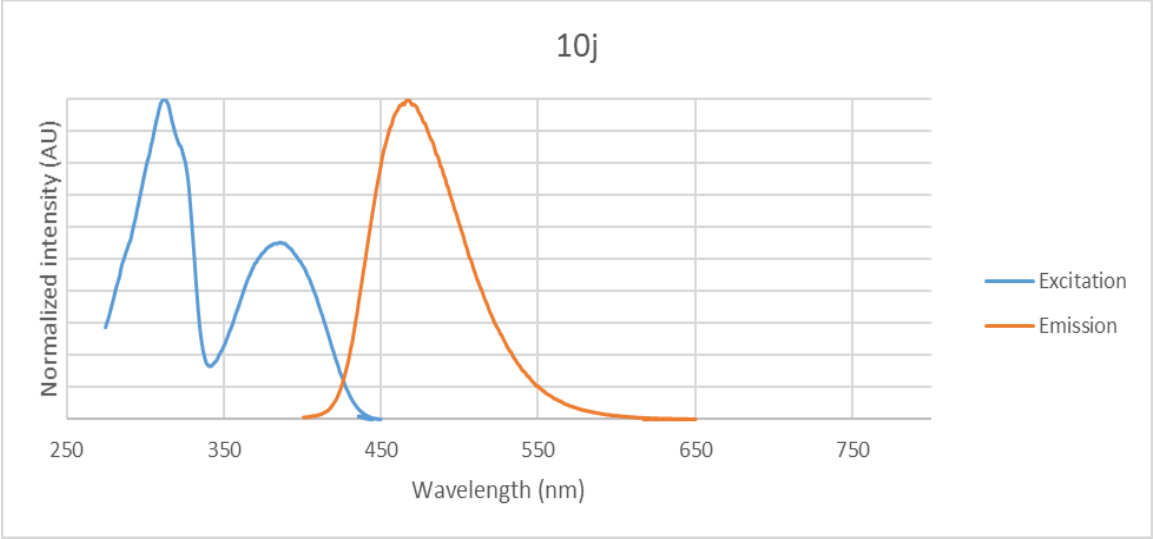

Figure C.12. Excitation and emission spectra of compound **10j** in $CHCl_3$.

Phosphonamidate Species in $CHCl_3$

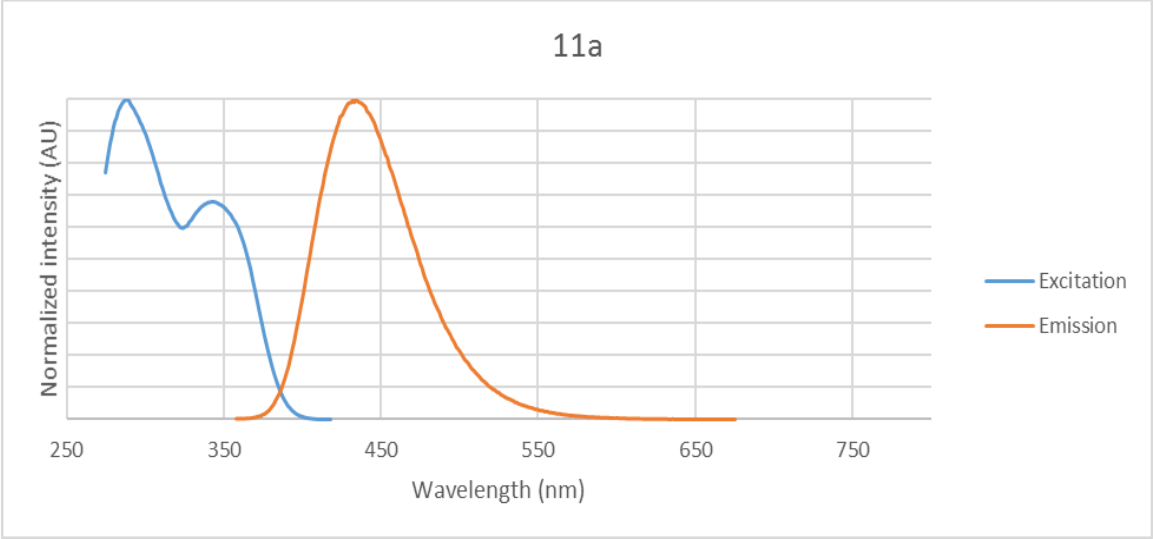

Figure C.13. Excitation and emission spectra of compound **11a** in $CHCl_3$.

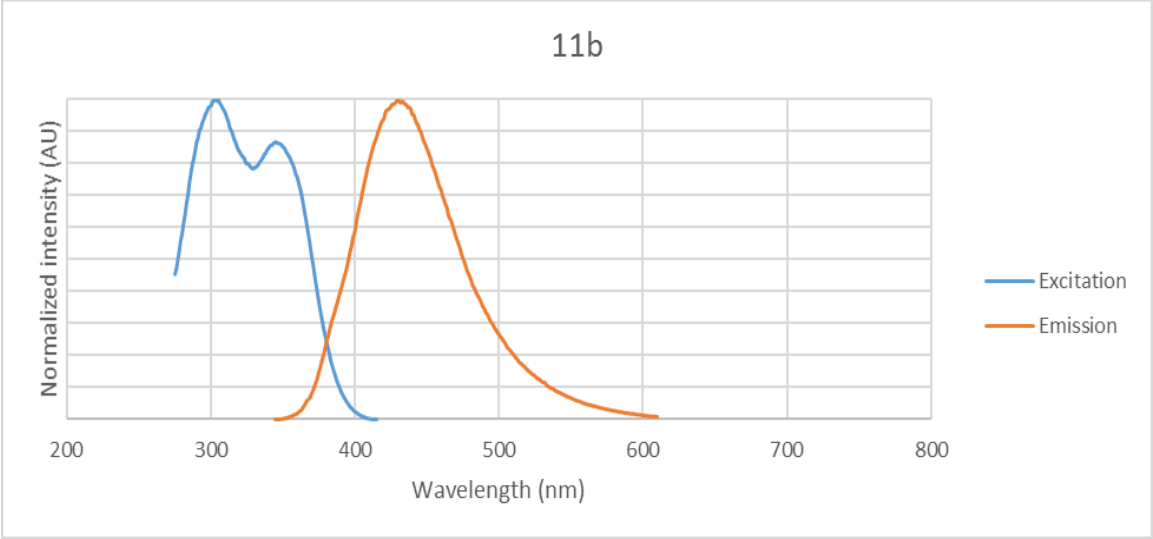

Figure C.14. Excitation and emission spectra of compound **11b** in $CHCl_3$.

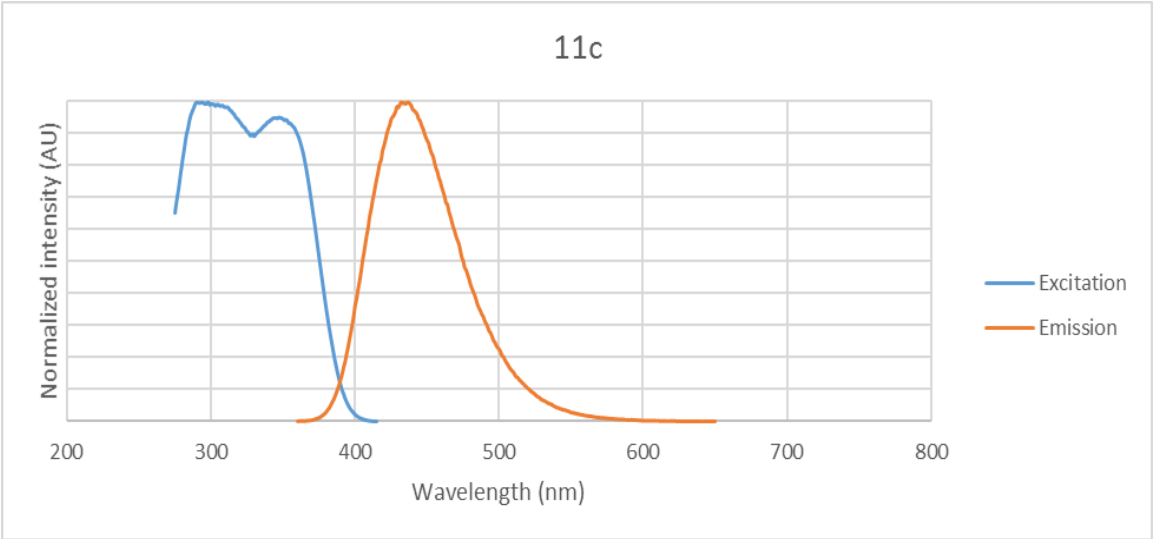

Figure C.15. Excitation and emission spectra of compound **11c** in $CHCl_3$.

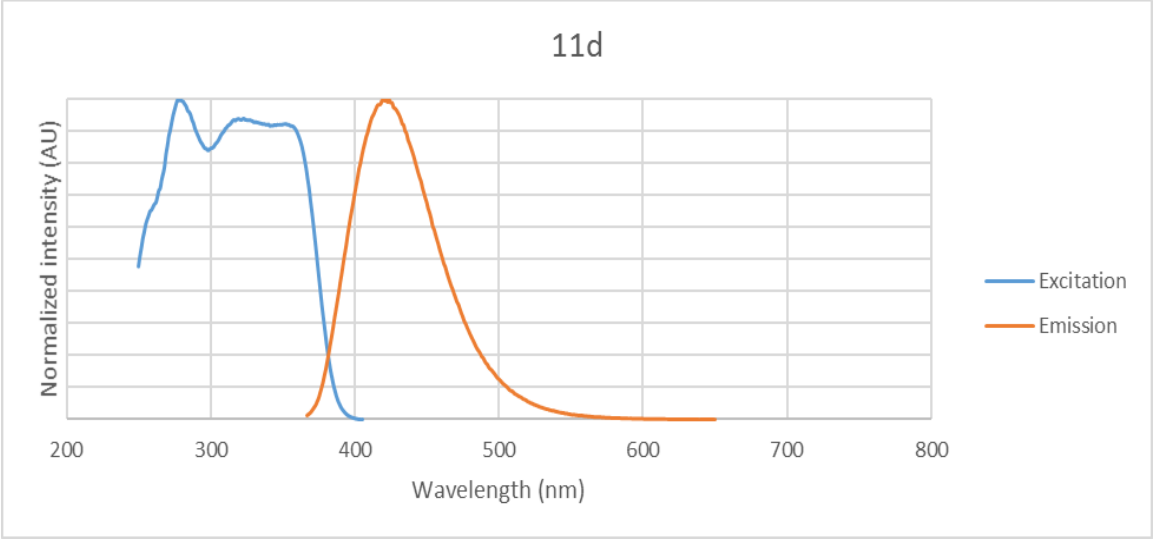

Figure C.16. Excitation and emission spectra of compound **11d** in $CHCl_3$.

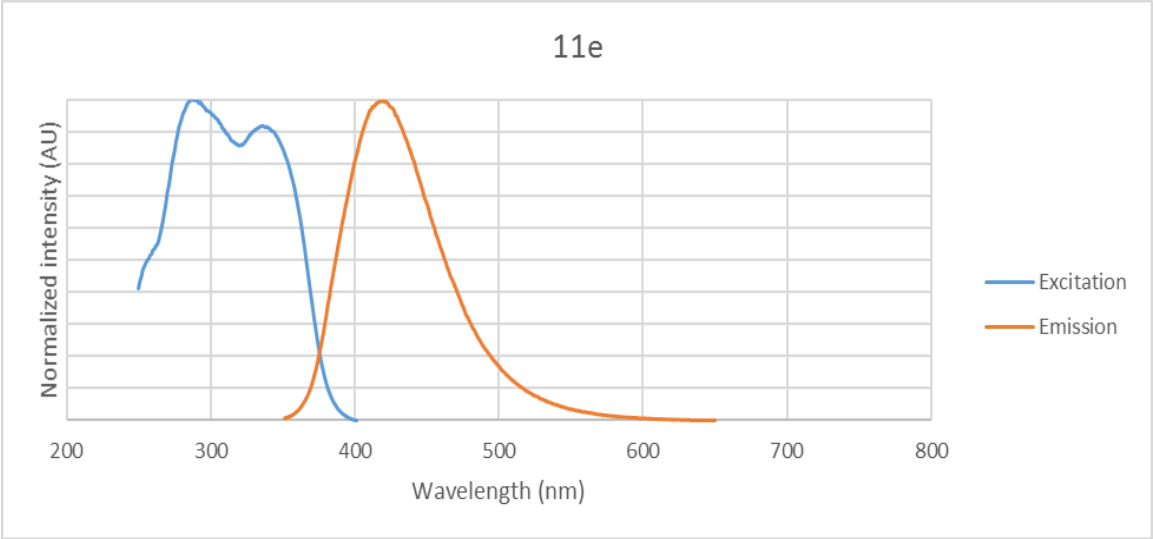

Figure C.17. Excitation and emission spectra of compound **11e** in $CHCl_3$.

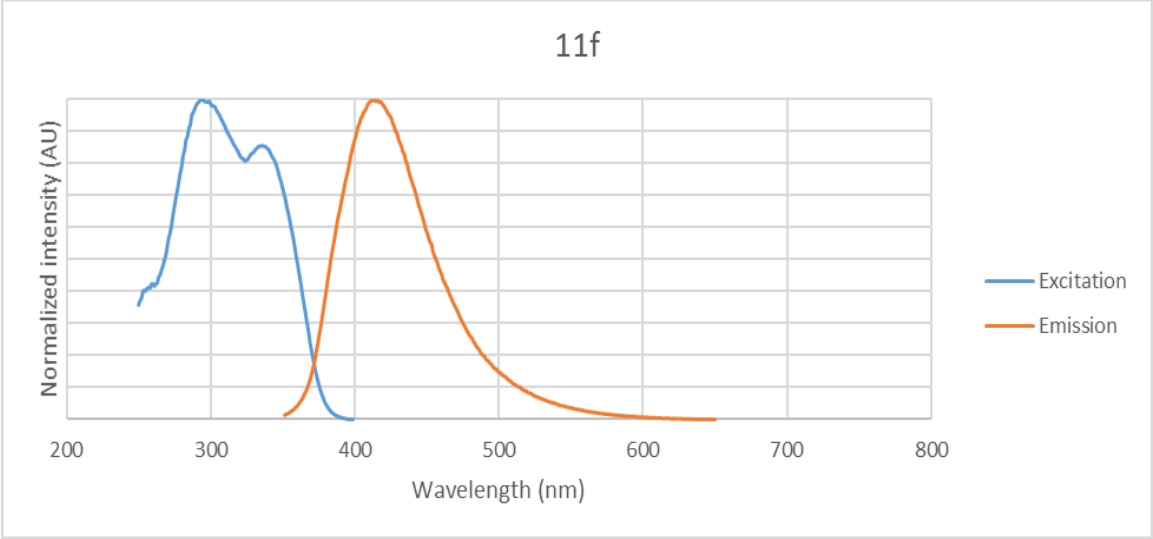

Figure C.18. Excitation and emission spectra of compound **11f** in $CHCl_3$**.**

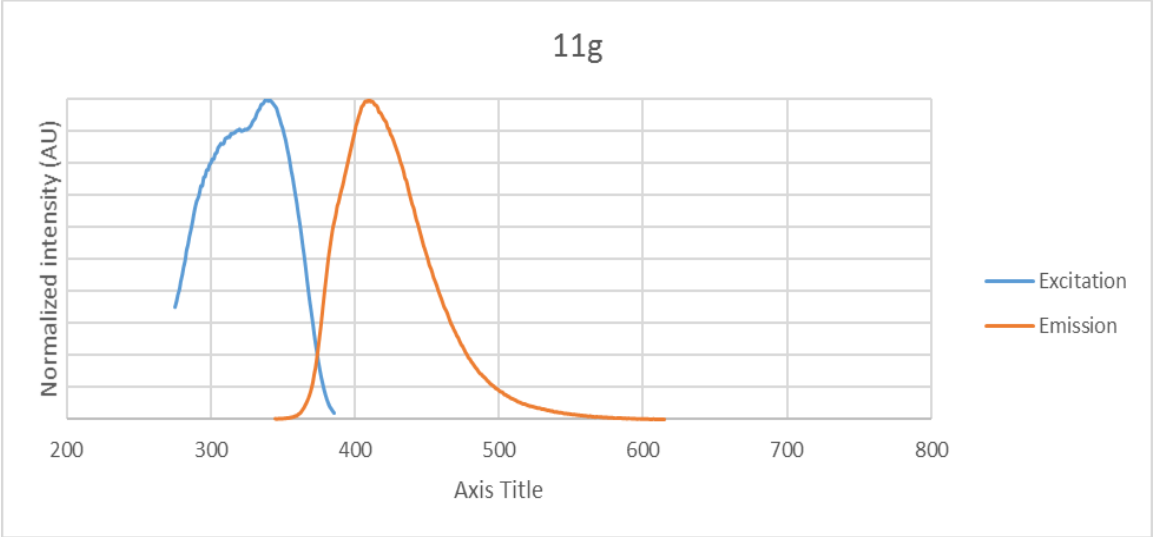

Figure C.19. Excitation and emission spectra of compound **11g** in $CHCl_3$**.**

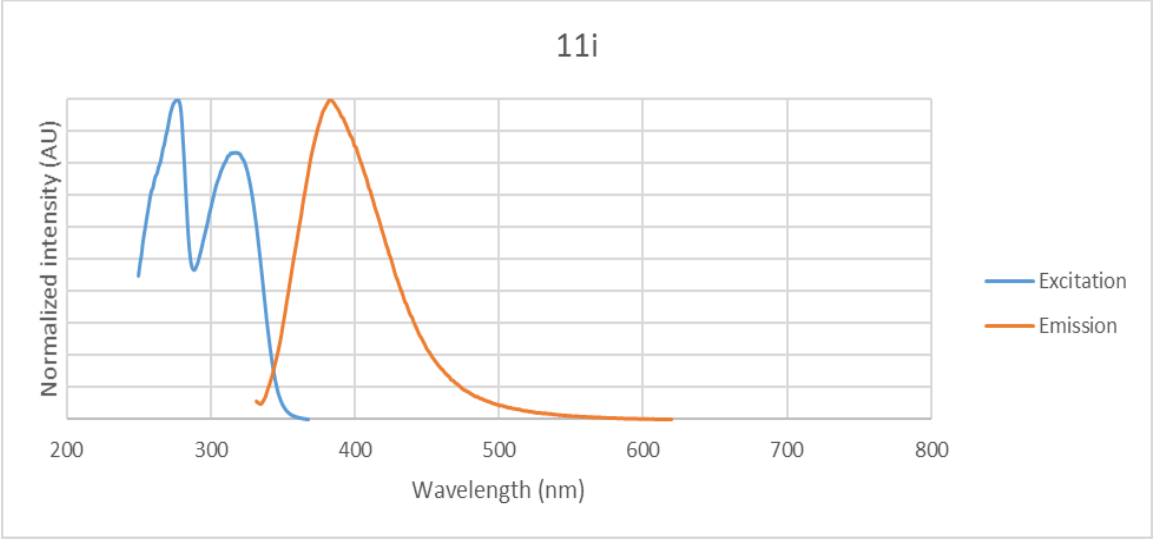

Figure C.20. Excitation and emission spectra of compound **11i** in $CHCl_3$.

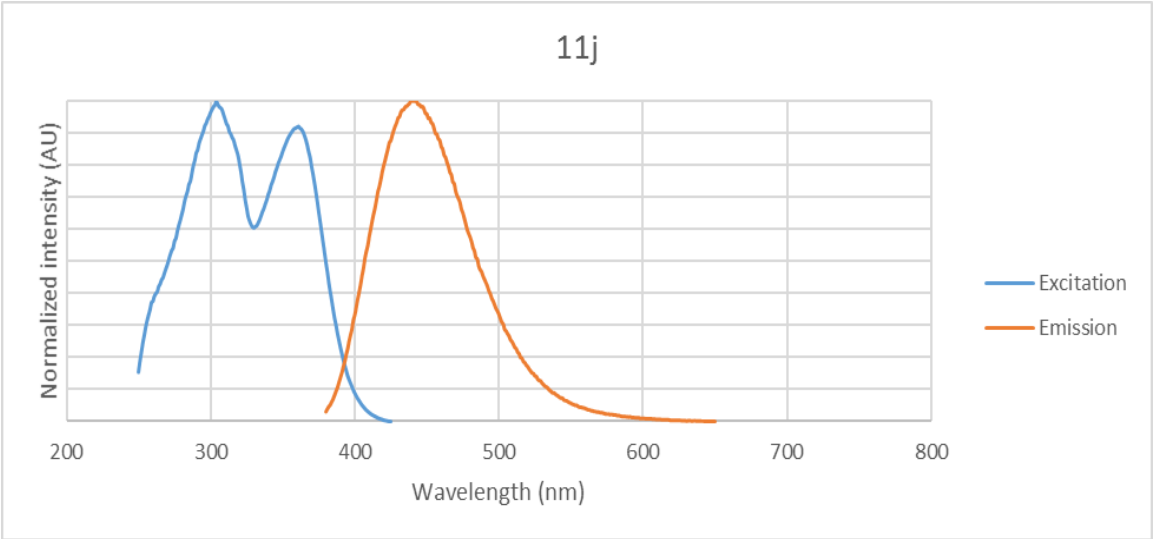

Figure C.21. Excitation and emission spectra of compound **11j** in $CHCl_3$.

Phosphonamidate Species in $CHCl_3$ + 5% DBU

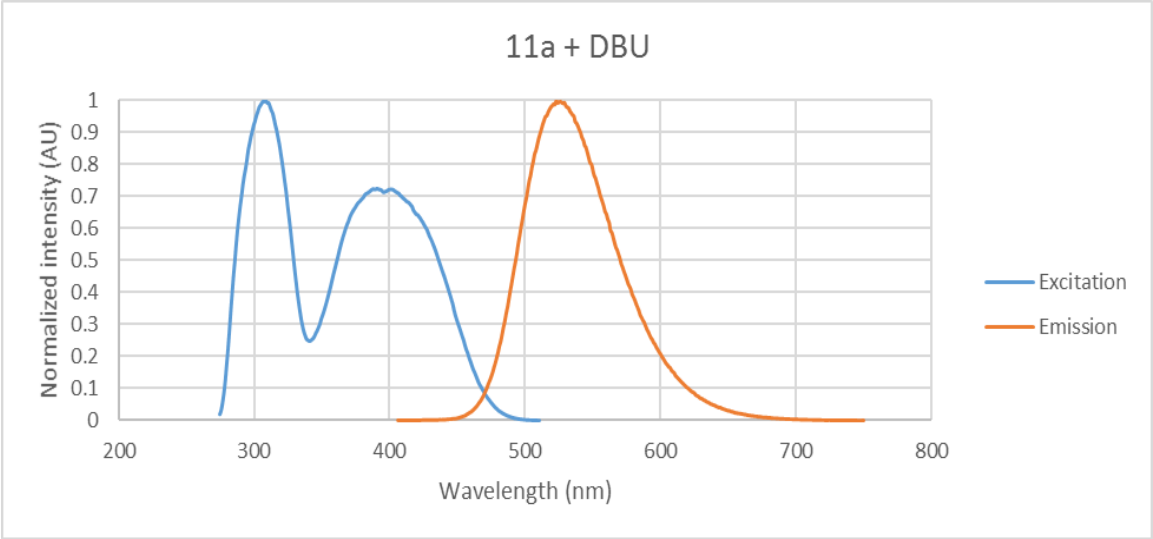

Figure C.22. Excitation and emission spectra of compound **11a** in $CHCl_3$/5%DBU.

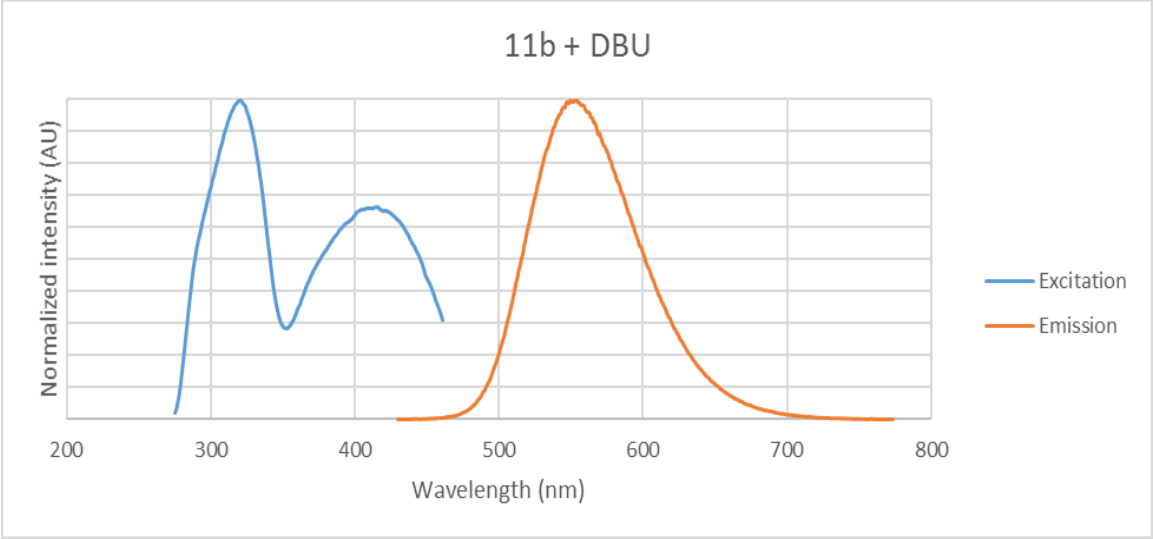

Figure C.23. Excitation and emission spectra of compound **11b** in $CHCl_3$/5%DBU.

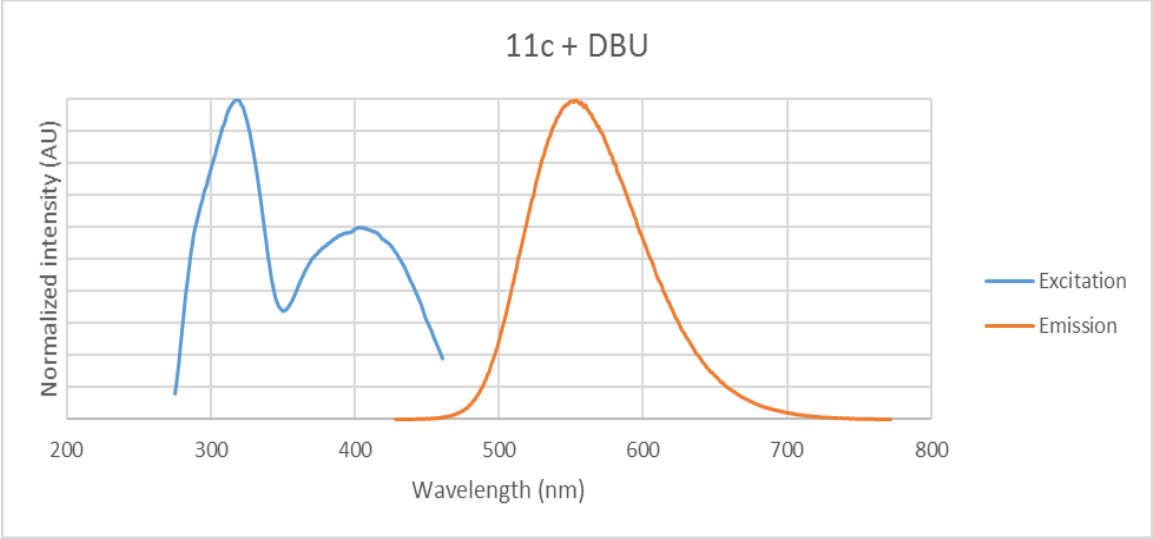

Figure C.24. Excitation and emission spectra of compound **11c** in $CHCl_3$/5%DBU.

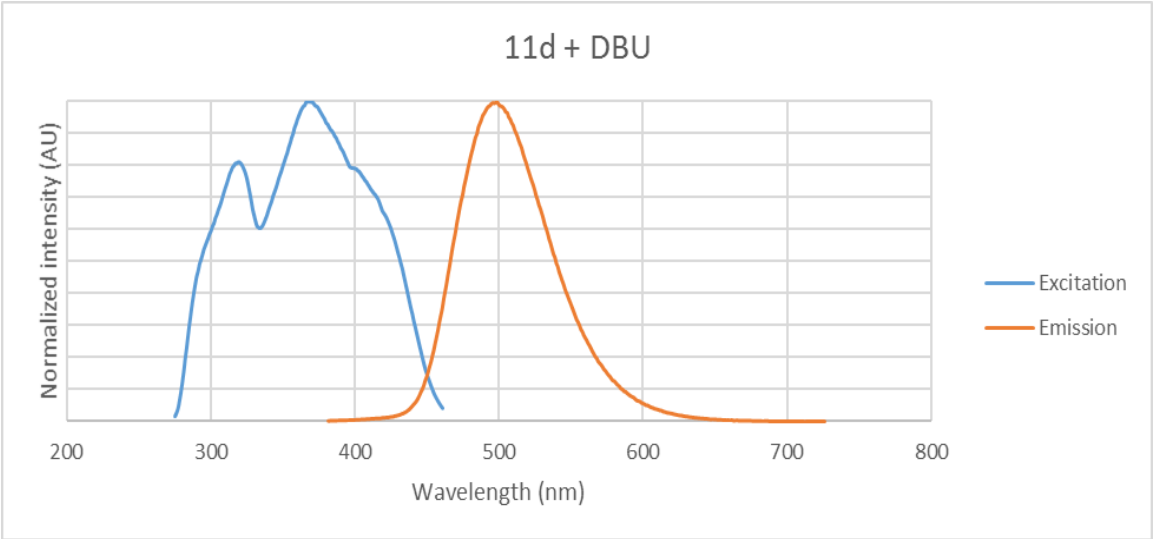

Figure C.25. Excitation and emission spectra of compound **11d** in $CHCl_3$/5%DBU.

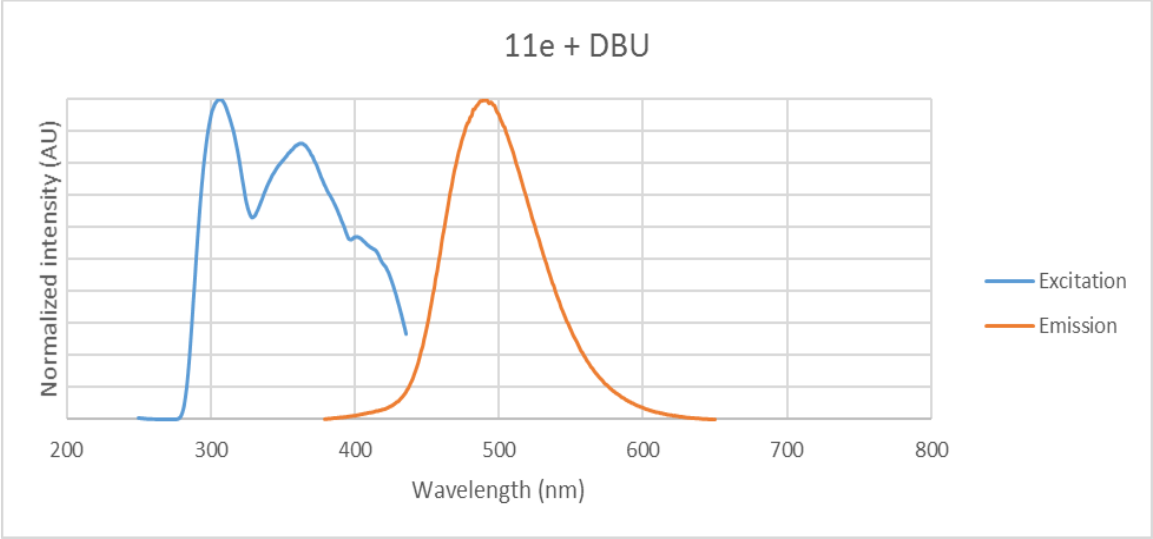

Figure C.26. Excitation and emission spectra of compound **11e** in $CHCl_3$/5%DBU.

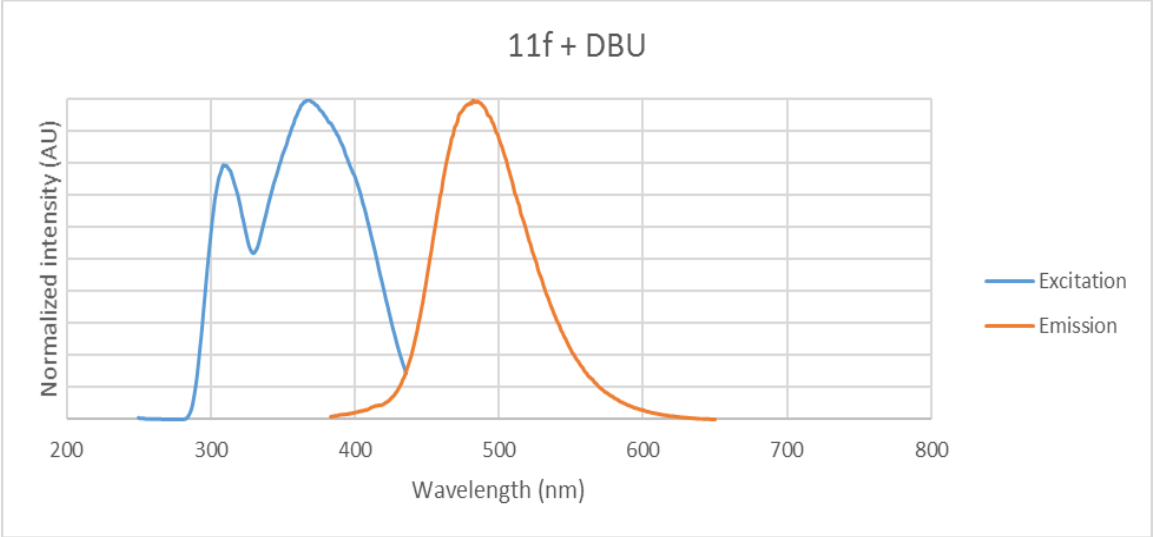

Figure C.27. Excitation and emission spectra of compound **11f** in $CHCl_3$/5%DBU.

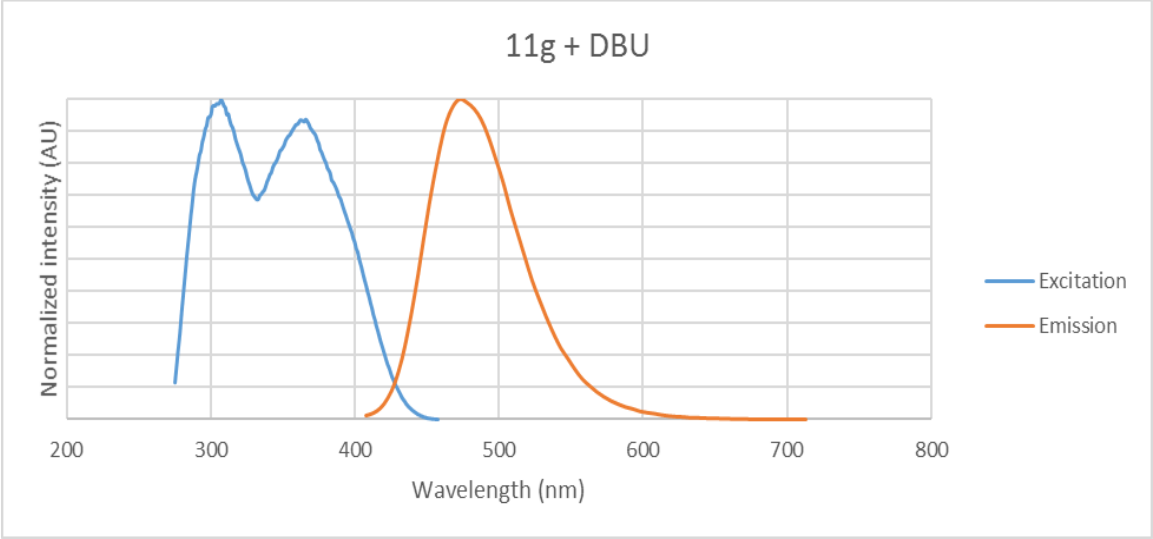

Figure C.28. Excitation and emission spectra of compound **11g** in $CHCl_3$/5%DBU.

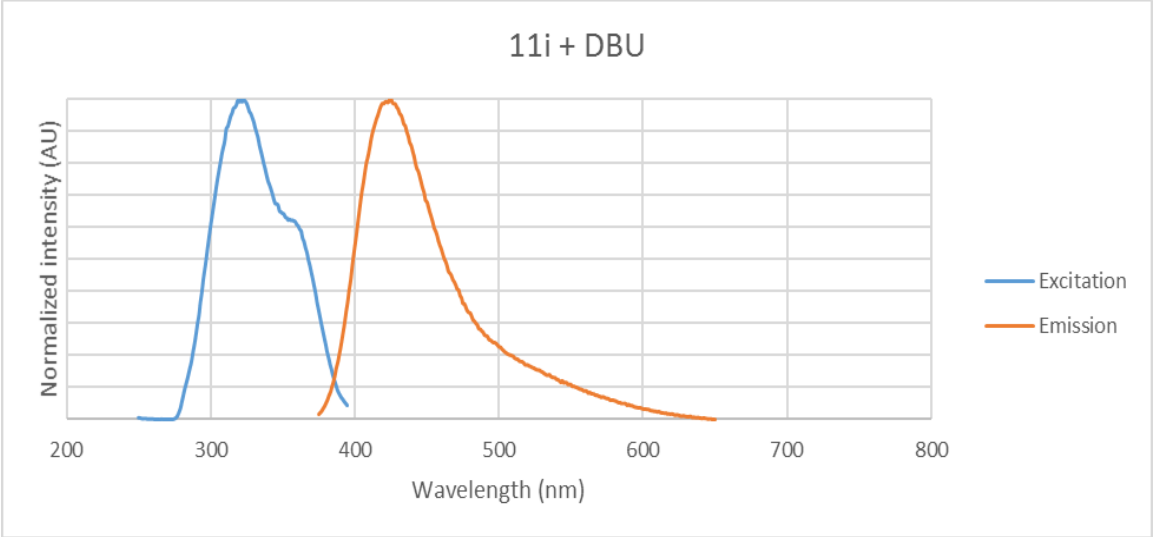

Figure C.29. Excitation and emission spectra of compound **11i** in $CHCl_3$/5%DBU.

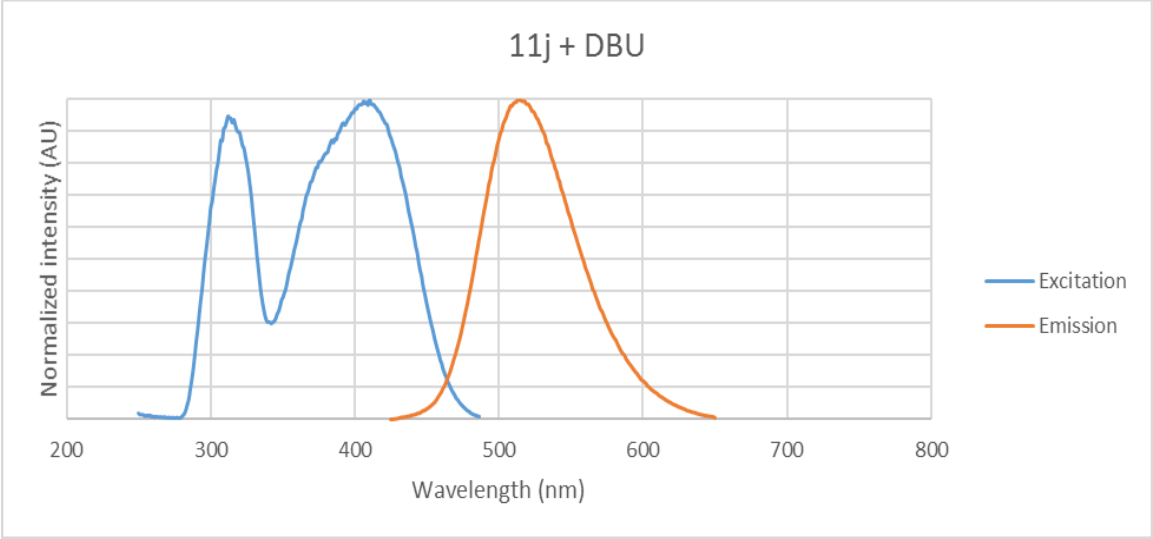

Figure C.30. Excitation and emission spectra of compound **11j** in $CHCl_3$/5%DBU.

Selected Phosphonamidates in MeCN

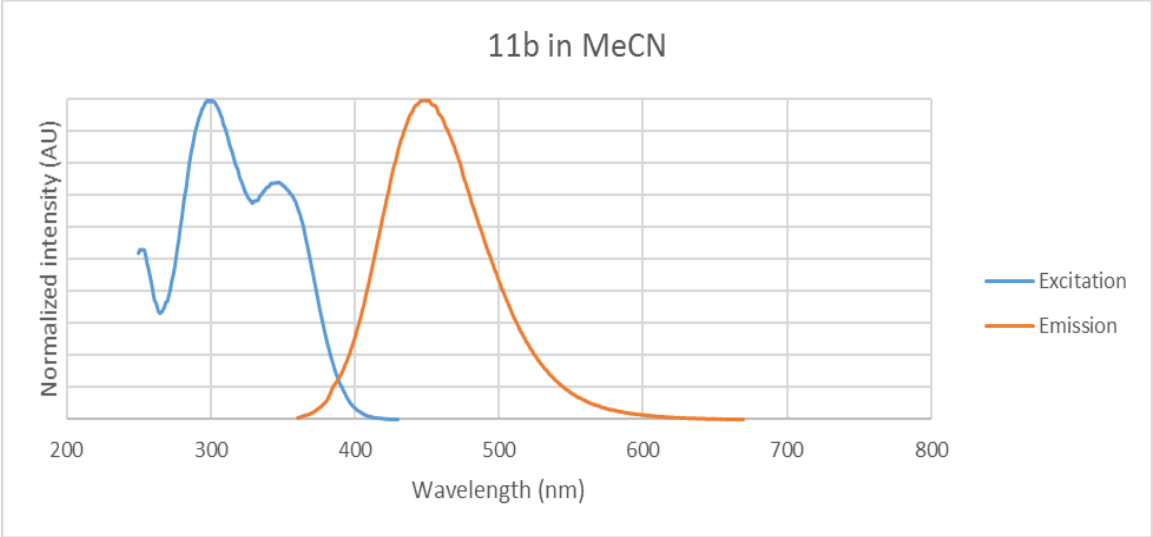

Figure C.31. Excitation and emission spectra of compound **11b** in MeCN.

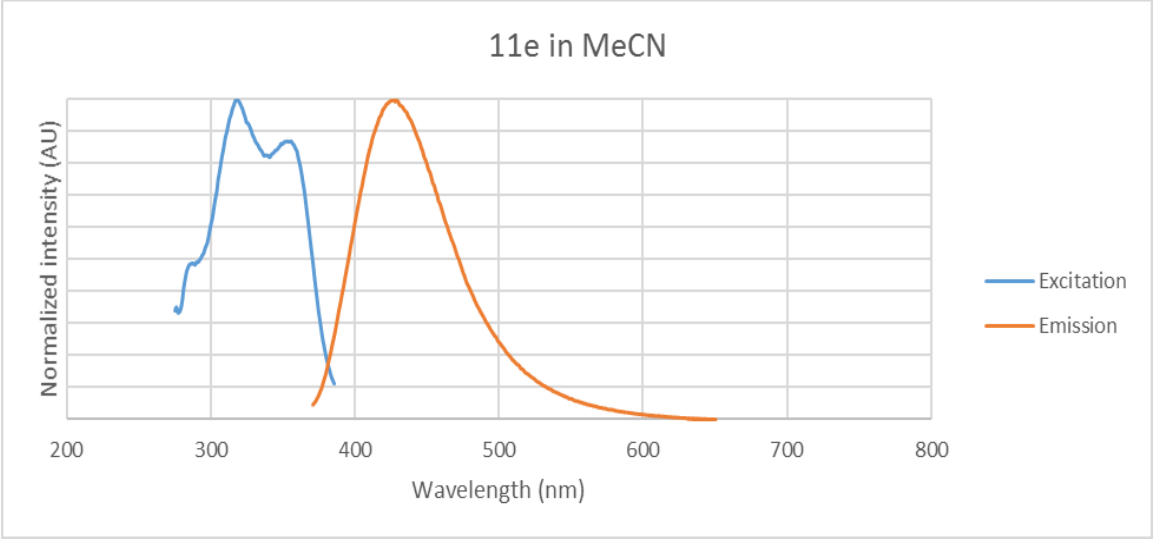

Figure C.32. Excitation and emission spectra of compound **11e** in MeCN.

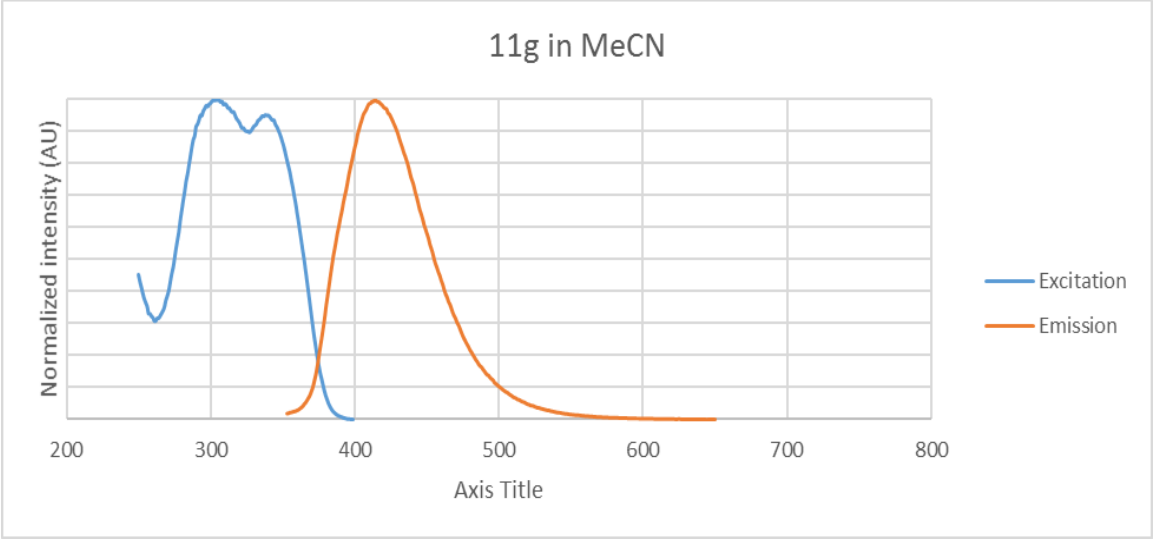

Figure C.33. Excitation and emission spectra of compound **11g** in MeCN.

COMPUTATIONAL DATA

Job type: Geometry optimization.

Method: RB3LYP
Basis set: 6-31G(D)
Number of shells: 159
Number of basis functions: 492

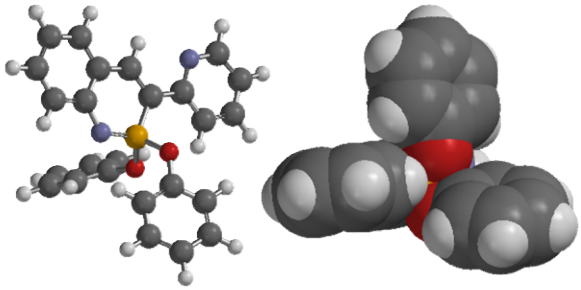

Figure C.34. Ball-and-stick model of calculated geometry (B3LYP, 6-311g*), shows the same conformation as in solid state (left). A space-filling model of this structure, viewed 180° from the P=N bond, shows an inaccessible phosphorus for water addition (right).

Optimization:

Step	Energy	Max Grad.	Max Dist.
1	-1565.409701	0.044845	0.082638
2	-1565.426555	0.019685	0.092526
3	-1565.430288	0.008615	0.094381
4	-1565.431821	0.003579	0.113407
5	-1565.432443	0.005768	0.087080
6	-1565.432734	0.005654	0.114185
7	-1565.433042	0.003193	0.081673
8	-1565.433163	0.001196	0.026906
9	-1565.433214	0.001128	0.040564
10	-1565.433276	0.001902	0.124118
11	-1565.433454	0.001770	0.134196
12	-1565.433569	0.003771	0.141819

13	-1565.433894	0.005848	0.194493	1
14	-1565.434520	0.004020	0.187465	
15	-1565.435158	0.006094	0.200523	
16	-1565.435663	0.006182	0.078187	
17	-1565.435860	0.002149	0.145918	
18	-1565.435994	0.001223	0.027730	
19	-1565.436062	0.001145	0.016318	
20	-1565.436083	0.000633	0.022577	
21	-1565.436088	0.000304	0.005584	
22	-1565.436090	0.000180	0.002404	
23	-1565.436091	0.000075	0.002045	

Coordinates:

C	-0.717660	-5.197190	0.978681
C	-1.702368	-4.549634	1.753089
C	-1.883873	-3.181168	1.675310
C	-1.087494	-2.389505	0.814579
C	-0.085568	-3.043434	0.025793
C	0.073234	-4.447556	0.131783
N	-1.299601	-1.035736	0.774914
P	-0.478264	-0.069155	-0.164080
C	0.740982	-0.940843	-1.085480
C	0.757444	-2.300290	-0.856491
C	1.695274	-0.308532	-2.028576
N	2.536569	-1.142831	-2.672001
C	3.421810	-0.628767	-3.525697
C	3.537342	0.735137	-3.799925
C	2.671407	1.601918	-3.136120
C	1.739746	1.082260	-2.241819
O	-1.363533	0.770039	-1.239677

C	-2.283473	1.782070	-0.952377
C	-3.151848	1.714693	0.137376
C	-4.067237	2.751139	0.329110
C	-4.124250	3.827116	-0.558518
C	-3.256101	3.867619	-1.651353
C	-2.329700	2.844696	-1.852513
O	0.123794	1.225203	0.641063
C	0.894666	1.077998	1.800058
C	0.281866	0.783580	3.017109
C	1.069495	0.709697	4.166720
C	2.446546	0.931414	4.098098
C	3.042138	1.226284	2.870153
C	2.267585	1.299852	1.711810
H	-0.584843	-6.272564	1.049642
H	-2.329100	-5.134112	2.422390
H	-2.639995	-2.677639	2.269753
H	0.839400	-4.926099	-0.474520
H	1.505735	-2.857142	-1.417304
H	4.076157	-1.346557	-4.018995
H	4.277830	1.097997	-4.505936
H	2.717134	2.673842	-3.310201
H	1.062538	1.745859	-1.717443
H	-3.109251	0.865165	0.810319
H	-4.744352	2.708906	1.177966
H	-4.842638	4.626572	-0.401687
H	-3.295680	4.698022	-2.351030
H	-1.646470	2.854416	-2.695800
H	-0.787369	0.609643	3.048599
H	0.601252	0.478680	5.119546
H	3.052873	0.874297	4.997652

H	4.113083	1.399241	2.809173
H	2.710718	1.528121	0.74777

X-RAY CRYSTALLOGRAPHY

Diffraction intensities were collected at 173(2) (**10j**) and 223 K (**11j**) on a Bruker Apex2 Due CCD diffractometer using MoKα radiation, λ= 0.71073 Å, (**10j**) and CuKα radiation, λ= 1.54178 Å, (**11j**). Space groups were determined based on systematic absences (**10j**) and intensity statistics (**11j**). Absorption corrections were applied by SADABS.[6] Structures were solved by direct methods and Fourier techniques and refined on F^2 using full matrix least-squares procedures. All non-H atoms were refined with anisotropic thermal parameters. H atoms in both structures were found on the residual density maps and refined with isotropic thermal parameters. The data for **10j** were collected up to $2\theta_{max}$ = 56.0°, but only the data up to $2\theta_{max}$ = 50.0° have been used in the final refinement. The crystal structure of **11j** has two symmetrically independent molecules. All calculations were performed by the Bruker Apex2/SHELXL-2013 package.

Crystallographic Data for **10j**: $C_{25}H_{19}N_2O_2P$, M = 410.39, 0.17 x 0.16 x 0.12 mm, T = 173(2) K, Monoclinic, space group $P2_1/c$, a = 11.0967(14) Å, b = 9.6020(13) Å, c = 19.319(2) Å, β = 90.982(4)°, V = 2058.2(5) $Å^3$, Z = 4, D_c = 1.324 Mg/m^3, μ = 0.158 mm^{-1}, $F(000)$ = 856, $2\theta_{max}$ = 50.0°, 22128 reflections, 3633 independent reflections [R_{int} = 0.0525], R1 = 0.0428, wR2 = 0.0921 and GOF = 1.024 for 3633 reflections (347 parameters) with I>2σ(I), R1 = 0.0763, wR2 = 0.1078 and GOF = 1.024 for all reflections, max/min residual electron density +0.290/-0.311 $eÅ^3$.

Crystallographic Data for **11j**: $C_{19}H_{15}N_2O_2P$, M = 334.30, 0.12 x 0.09 x 0.04 mm, T = 223(2) K, Triclinic, space group *P*-1, a = 8.4050(3) Å, b = 10.5908(4) Å, c = 20.2049(7) Å, α = 103.100(2)°, β = 94.314(3)°, γ = 109.365(2)°, V = 1630.36(11) Å^3, Z = 4, Z' = 2, D_c = 1.362 Mg/m^3, μ = 1.607 mm^{-1}, $F(000)$ = 696, $2\theta_{max}$ = 134.32°, 18307 reflections, 5681 independent reflections [R_{int} = 0.0529], R1 = 0.0544, wR2 = 0.1447 and GOF = 1.050 for 5681 reflections (553 parameters) with $I>2\sigma(I)$, R1 = 0.0738, wR2 = 0.1576 and GOF = 1.050 for all reflections, max/min residual electron density +0.742/-0.441 eÅ^3.

APPENDIX D

SUPPORTING INFORMATION FOR CHAPTER VI: ADDITIONAL ANALYSES OF THE SYNTHESIS AND PROPERTIES OF THE AZAPHOSPHININE SCAFFOLD

DIMERIZATION STUDIES

Azaphosphinine (~22.5 μmol) was dissolved in $CDCl_3$ (900 μL) saturated with H_2O (H_2O saturated $CDCl_3$ prepared by mixing equal parts (v/v) $CDCl_3$ and H_2O for 10 min followed by separation of the two layers). H_2O saturated $CDCl_3$ aliquots were added to the initial solution (25 mM) until the titration end point was reached (minimal chemical shift change per $CDCl_3$ aliquot). All additions performed through septa via Hamilton gas tight microsyringe at room temperature. ^1H NMR spectra recorded after each addition on a Varian 500 MHz spectrometer. Proton signals were referenced to residual $CHCl_3$ signal. The dimerization constant (K_{dim}) was calculated by plotting the change in shift of the phosphonamidate proton versus total concentration and resulting data was fit to a 1:1 dimerization with non-linear regression curve fitting software Hyperquad2006, χ^2 of fit reported in each section and all regressions fell within the 95% confidence interval. Dimerization constant determination performed in a minimum of triplicate, K_{dim} reported as mean, error reported as standard error of the measurement.

$$K_{dim} = 36 \pm 8\ M^{-1}$$

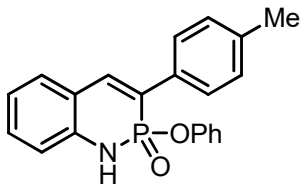

Figure D.1. Compound **11f** from Chapter V.

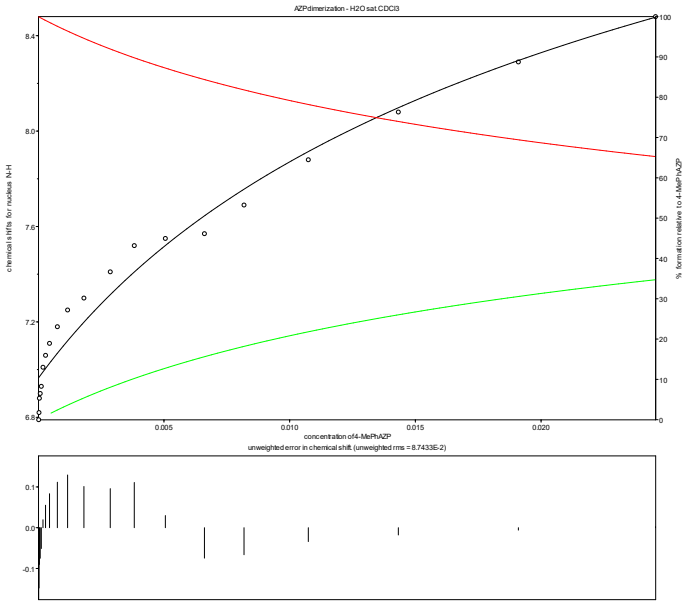

Figure D.2. Representative dimerization fit of Compound **11f.**

Solvent: water saturated $CDCl_3$ Results page - HypNMR version: 16.04.2006. Hqdll version: 09/05/2006. 5 iterations Refinement converged successfully				
sigma = 0.08907362557		RMS weighted residual = 0.08212182509		Chi-squared = 7.20 Chi-squared should be less than 12.60 at the 95% confidence level
Beta 2 refined	value	rSD	Log beta	SD
	2.9763E+001	0.3097	1.4737	0.1345

Table D.1. Results of dimerization fit of Compound **11f.**

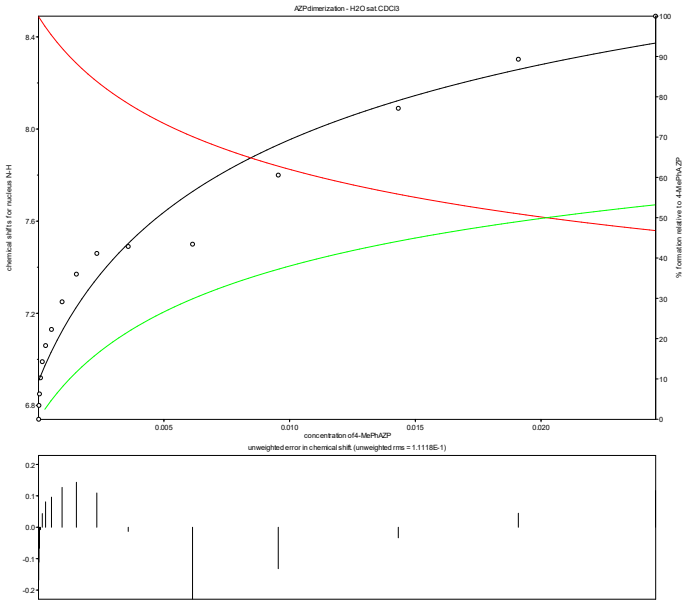

Figure D.3. Representative dimerization fit of Compound **11f.**

Solvent: water saturated $CDCl_3$ Results page - HypNMR version: 16.04.2006. Hqdll version: 09/05/2006. 5 iterations Refinement converged successfully				
sigma = 0.12333122781		RMS weighted residual = 0.11116926643		Chi-squared = 6.00 Chi-squared should be less than 12.60 at the 95% confidence level
Beta 2 refined	value	rSD	Log beta	SD
	4.9249E+001	0.0101	1.6924	0.0044

Table D.2. Results of dimerization fit of Compound **11f.**

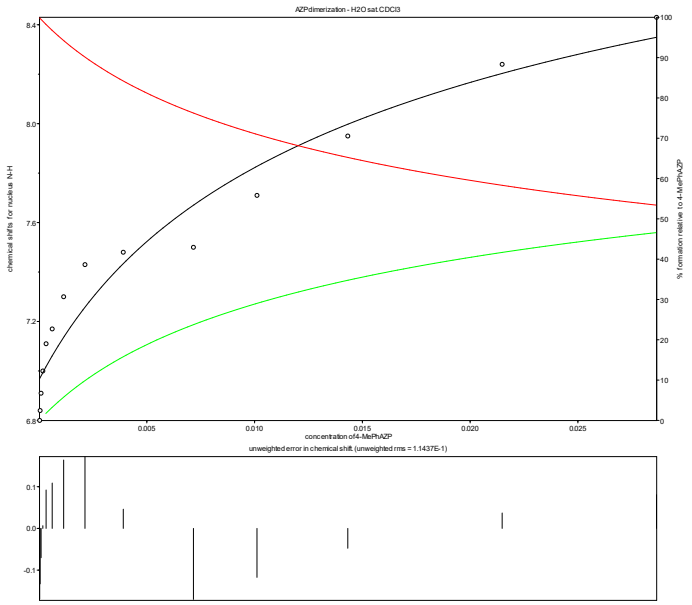

Figure D.4. Representative dimerization fit of Compound **11f.**

Solvent: water saturated $CDCl_3$ Results page - HypNMR version: 16.04.2006. Hqdll version: 09/05/2006. 7 iterations Refinement converged successfully				
sigma = 0.12901442760		RMS weighted residual = 0.11435906730		Chi-squared = 2.00 Chi-squared should be less than 12.60 at the 95% confidence level
Beta 2 refined	value	rSD	Log beta	SD
	2.8508E+001	0.5606	1.4550	15.9816

Table D.3. Results of dimerization fit of Compound **11f.**

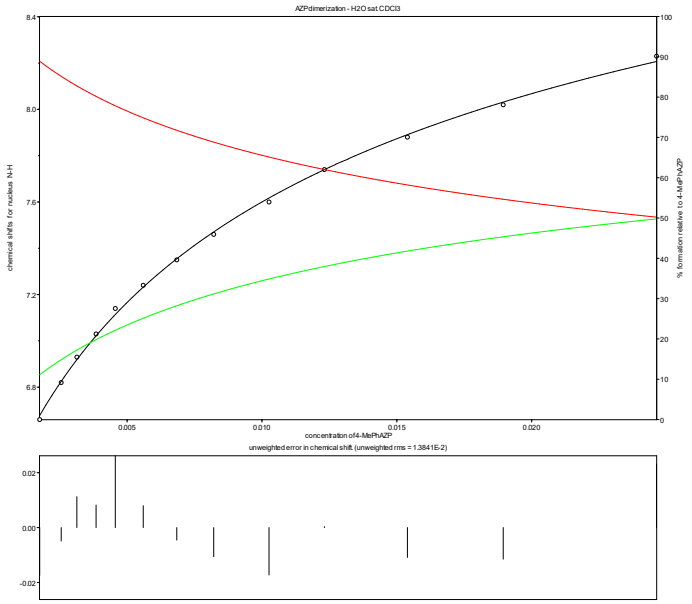

Figure D.5. Representative dimerization fit of Compound **11f.**

Solvent: water saturated $CDCl_3$ Results page - HypNMR version: 16.04.2006. Hqdll version: 09/05/2006. 4 iterations Refinement converged successfully				
sigma = 0.01576635418		RMS weighted residual = 0.01382800737		Chi-squared = 6.08 Chi-squared should be less than 12.60 at the 95% confidence level
Beta 2 refined	value	rSD	Log beta	SD
	4.0070E+001	0.0950	1.6028	0.0413

Table D.4. Results of dimerization fit of Compound **11f.**

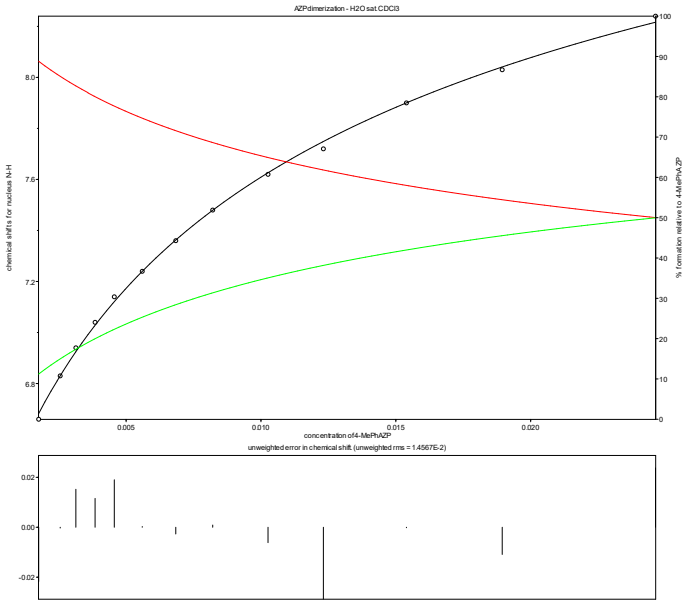

Figure D.6. Representative dimerization fit of Compound **11f.**

Solvent: water saturated $CDCl_3$ Results page - HypNMR version: 16.04.2006. Hqdll version: 09/05/2006. 4 iterations Refinement converged successfully				
sigma = 0.01576635418		RMS weighted residual = 0.01382800737		Chi-squared = 6.08 Chi-squared should be less than 12.60 at the 95% confidence level
Beta 2 refined	value	rSD	Log beta	SD
	4.0532E+001	0.0997	1.6078	0.0433

Table D.5. Results of dimerization fit of Compound **11f.**

$$K_{dim} = 52 \pm 5\ M^{-1}$$

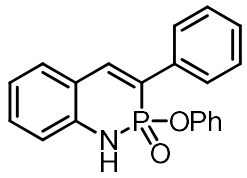

Figure D.7. Compound **11e** from Chapter V.

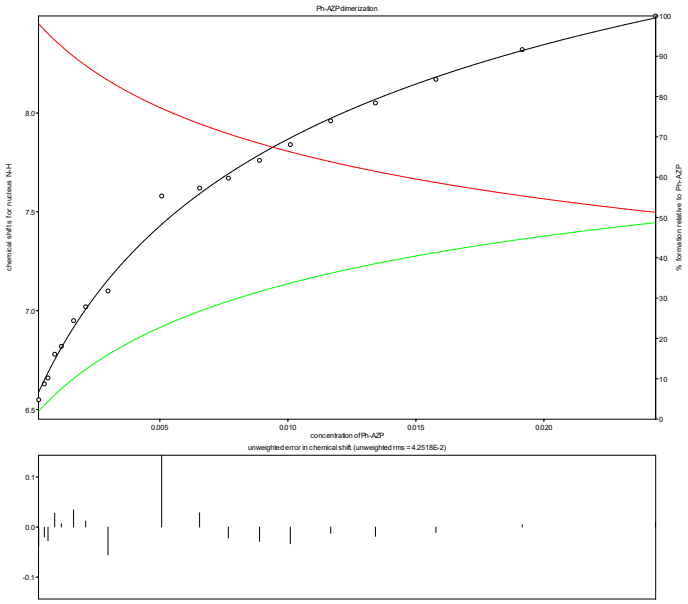

Figure D.8. Representative dimerization fit of Compound **11e.**

Solvent: water saturated $CDCl_3$ Results page - HypNMR version: 16.04.2006. Hqdll version: 09/05/2006. 3 iterations Refinement converged successfully				
sigma = 0.04506630728		RMS weighted residual = 0.04113972180		Chi-squared = 3.33 Chi-squared should be less than 12.60 at the 95% confidence level
Beta 2 refined	value	rSD	Log beta	SD
	4.4001E+001	0.1407	1.6435	0.0611

Table D.6. Results of dimerization fit of Compound **11e.**

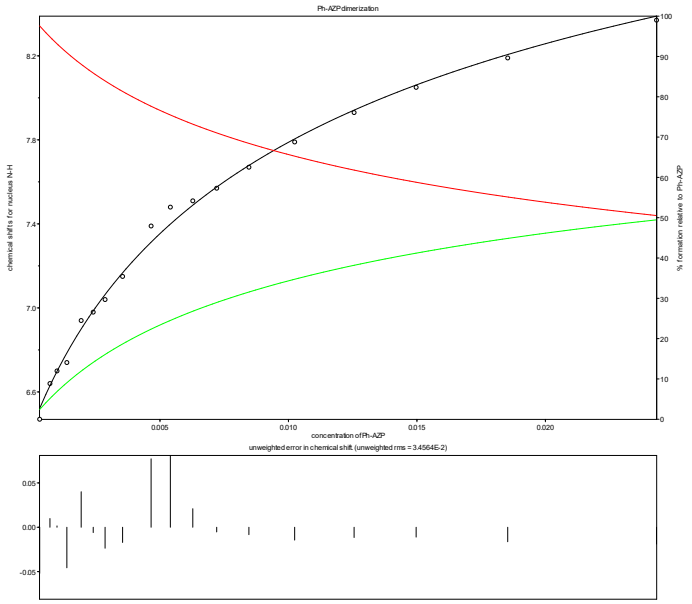

Figure D.9. Representative dimerization fit of Compound **11e.**

Solvent: water saturated $CDCl_3$ Results page - HypNMR version: 16.04.2006. Hqdll version: 09/05/2006. 3 iterations Refinement converged successfully				
sigma = 0.03281660362		RMS weighted residual = 0.02995732344		Chi-squared = 7.78 Chi-squared should be less than 12.60 at the 95% confidence level
Beta 2 refined	value	rSD	Log beta	SD
	5.0071E+001	0.1018	1.6996	0.0442

Table D.7. Results of dimerization fit of Compound **11e.**

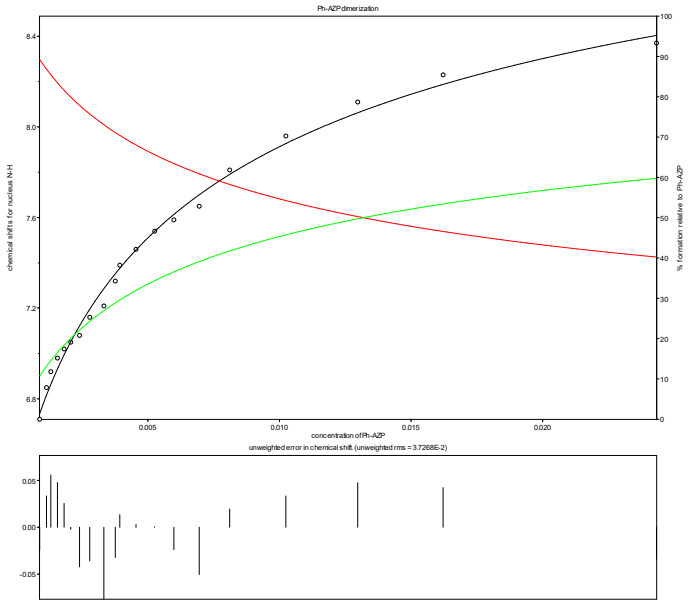

Figure D.10. Representative dimerization fit of Compound **11e.**

Solvent: water saturated $CDCl_3$ Results page - HypNMR version: 16.04.2006. Hqdll version: 09/05/2006. 3 iterations Refinement converged successfully				
sigma = 0.03862796500		RMS weighted residual = 0.03561322406		Chi-squared = 6.40 Chi-squared should be less than 12.60 at the 95% confidence level
Beta 2 refined	value	rSD	Log beta	SD
	6.2603E+001	0.1522	1.7966	0.0661

Table D.8. Results of dimerization fit of Compound **11e.**

$$K_{dim} = 42 \pm 1\ M^{-1}$$

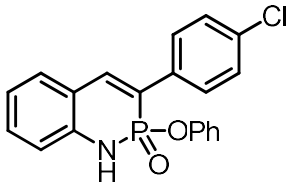

Figure D.11. Compound **11d** from Chapter V.

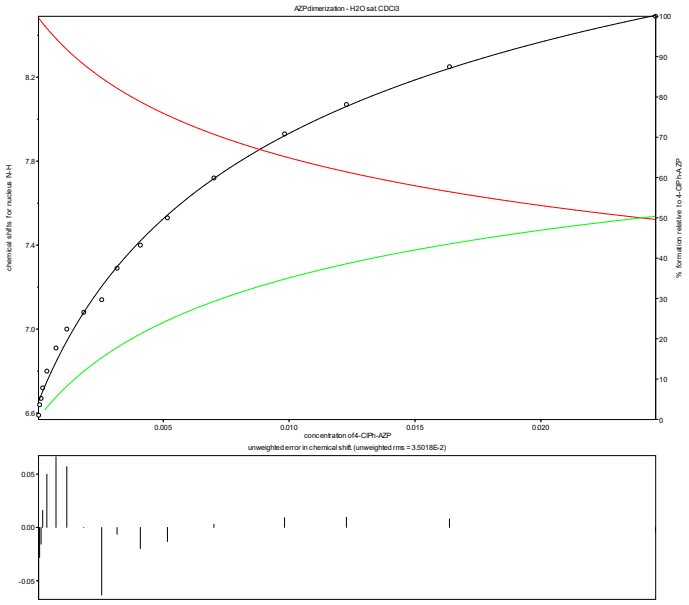

Figure D.12. Representative dimerization fit of Compound **11d.**

Solvent: water saturated $CDCl_3$ Results page - HypNMR version: 16.04.2006. Hqdll version: 09/05/2006. 5 iterations Refinement converged successfully				
sigma = 0.03857540366		RMS weighted residual = 0.03500660841		Chi-squared = 7.94 Chi-squared should be less than 12.60 at the 95% confidence level
Beta 2 refined	value	rSD	Log beta	SD
	4.1461E+001	0.1076	1.6176	0.0467

Table D.9. Results of dimerization fit of Compound **11d.**

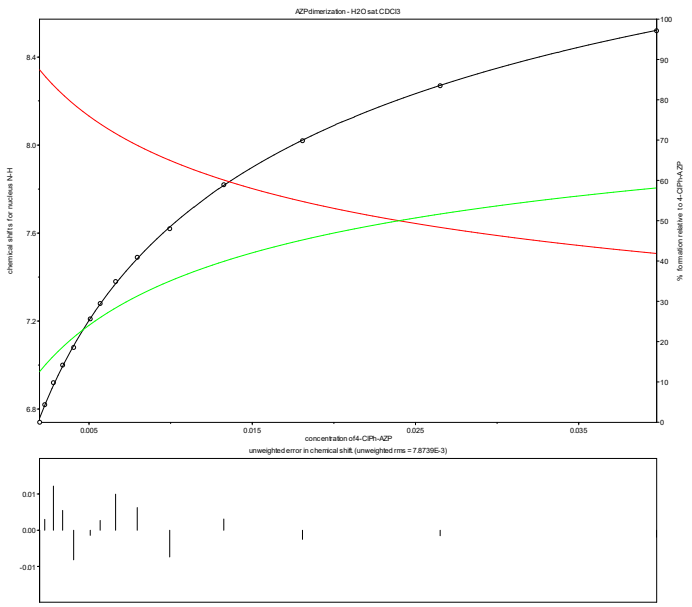

Figure D.13. Representative dimerization fit of Compound **11d.**

Solvent: water saturated $CDCl_3$ Results page - HypNMR version: 16.04.2006. Hqdll version: 09/05/2006. 3 iterations Refinement converged successfully				
sigma = 0.00842687788		RMS weighted residual = 0.00746962888		Chi-squared = 4.29 Chi-squared should be less than 12.60 at the 95% confidence level
Beta 2 refined	value	rSD	Log beta	SD
	4.3504E+001	0.0388	1.6385	0.0168

Table D.10. Results of dimerization fit of Compound **11d.**

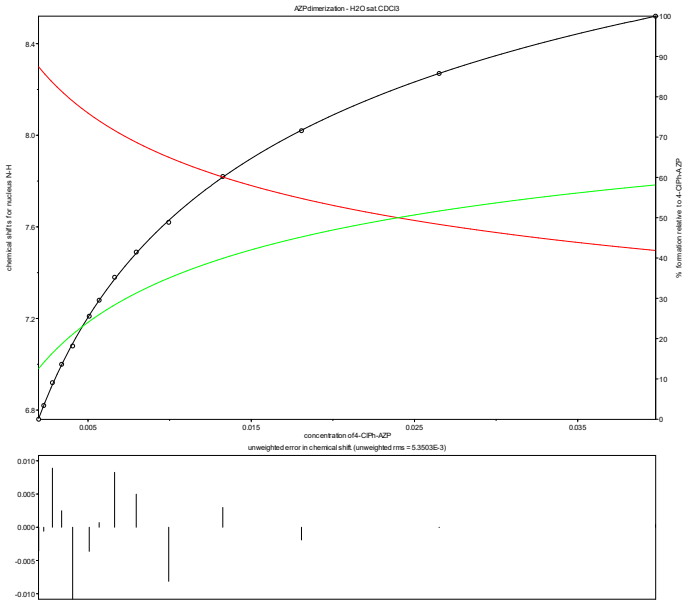

Figure D.14. Representative dimerization fit of Compound **11d.**

Solvent: water saturated $CDCl_3$ Results page - HypNMR version: 16.04.2006. Hqdll version: 09/05/2006. 3 iterations Refinement converged successfully				
sigma = 0.00603287042		RMS weighted residual = 0.00534756807		Chi-squared = 4.29 Chi-squared should be less than 12.60 at the 95% confidence level
Beta 2 refined	value	rSD	Log beta	SD
	4.1789E+001	0.0277	1.6211	0.0120

Table D.11. Results of dimerization fit of Compound **11d.**

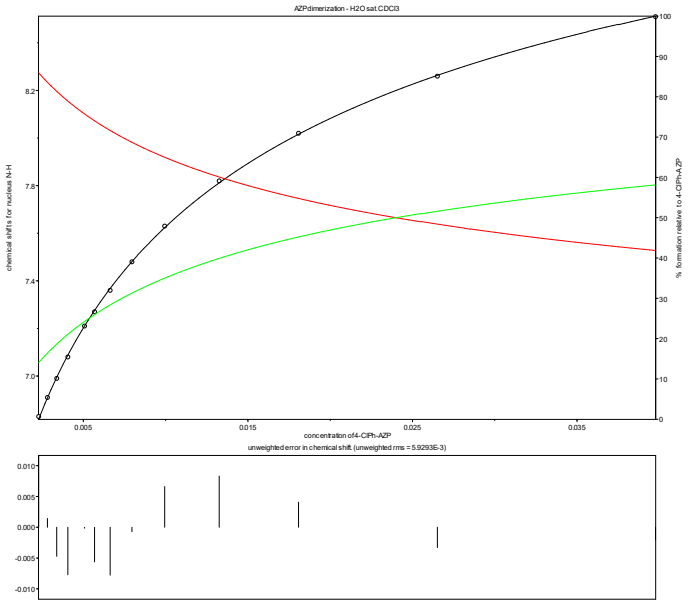

Figure D.15. Representative dimerization fit of Compound **11d.**

Solvent: water saturated $CDCl_3$ Results page - HypNMR version: 16.04.2006. Hqdll version: 09/05/2006. 2 iterations Refinement converged successfully				
sigma = 0.00603287042		RMS weighted residual = 0.00534756807		Chi-squared = 4.85 Chi-squared should be less than 12.60 at the 95% confidence level
Beta 2 refined	value	rSD	Log beta	SD
	4.1182E+001	0.0352	0.0352	1.6147

Table D.12. Results of dimerization fit of Compound **11d.**

$$K_{dim} = 20 \pm 5\ M^{-1}$$

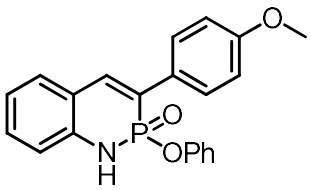

Figure D.16. Compound **11g** from Chapter V.

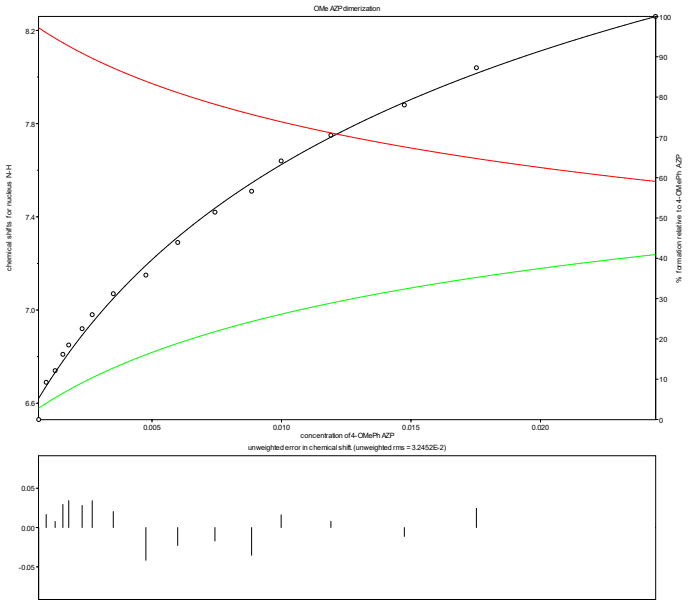

Figure D.17. Representative dimerization fit of Compound **11g.**

Solvent: water saturated $CDCl_3$ Results page - HypNMR version: 16.04.2006. Hqdll version: 09/05/2006. 5 iterations Refinement converged successfully				
sigma = 0.03573923843		RMS weighted residual = 0.03243283040		Chi-squared = 7.94 Chi-squared should be less than 12.60 at the 95% confidence level
Beta 2 refined	value	rSD	Log beta	SD
	2.4207E+001	0.1503	1.3839	0.0653

Table D.13. Results of dimerization fit of Compound **11g.**

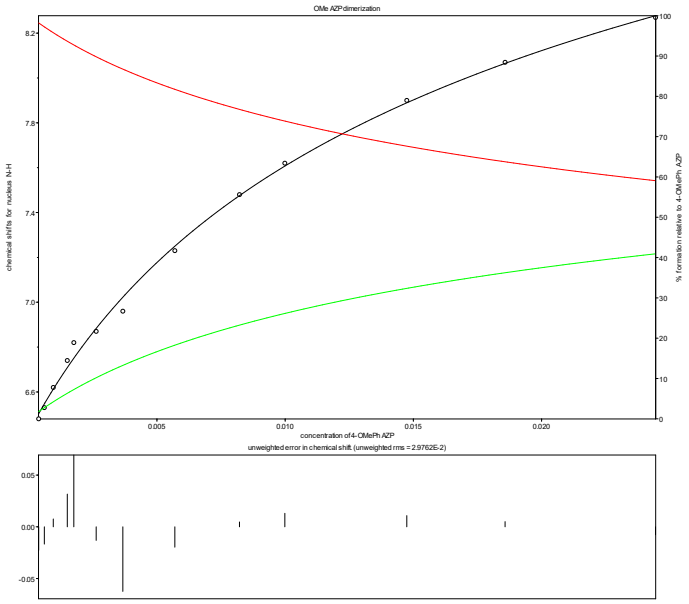

Figure D.18. Representative dimerization fit of Compound **11g.**

Solvent: water saturated $CDCl_3$ Results page - HypNMR version: 16.04.2006. Hqdll version: 09/05/2006. 5 iterations Refinement converged successfully				
sigma = 0.03387623761		RMS weighted residual = 0.02971142586		Chi-squared = 3.62 Chi-squared should be less than 12.60 at the 95% confidence level
Beta 2 refined	value	rSD	Log beta	SD
	2.3443E+001	0.1371	1.3700	0.0596

Table D.14. Results of dimerization fit of Compound **11g.**

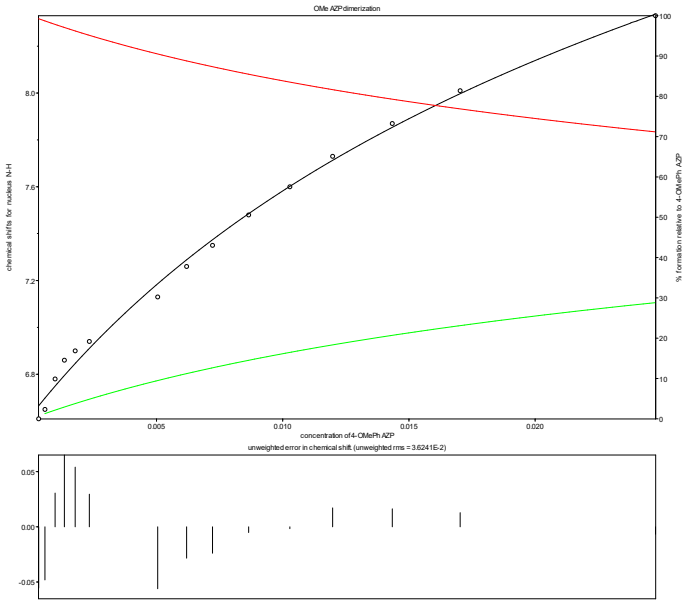

Figure D.19. Representative dimerization fit of Compound **11g.**

Solvent: water saturated $CDCl_3$ Results page - HypNMR version: 16.04.2006. Hqdll version: 09/05/2006. 5 iterations Refinement converged successfully				
sigma = 0.04046148665		RMS weighted residual = 0. 03618985384		Chi-squared = 2.60 Chi-squared should be less than 12.60 at the 95% confidence level
Beta 2 refined	value	rSD	Log beta	SD
	1.1076E+001	0.1922	1.0444	0.0835

Table D.15. Results of dimerization fit of Compound **11g.**

$$K_{dim} = 96 \pm 3\ M^{-1}$$

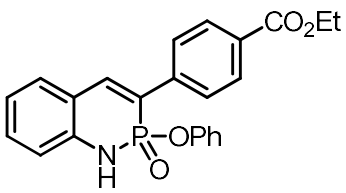

Figure D.20. Compound **11c** from Chapter V.

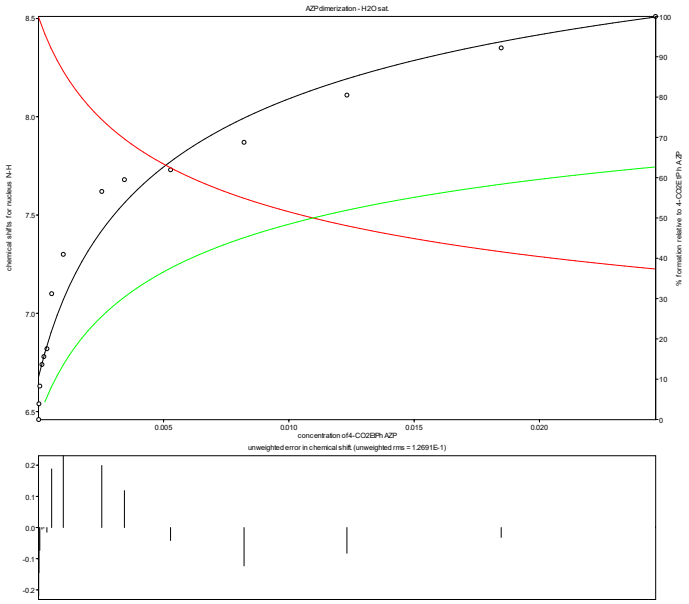

Figure D.21. Representative dimerization fit of Compound **11c.**

Solvent: water saturated $CDCl_3$ Results page - HypNMR version: 16.04.2006. Hqdll version: 09/05/2006. 4 iterations Refinement converged successfully				
sigma = 0.02133479466		RMS weighted residual = 0.0187489734821		Chi-squared = 8.14 Chi-squared should be less than 12.60 at the 95% confidence level
Beta 2 refined	value	rSD	Log beta	SD
	9.101E+001	0.0859	1.9591	0.0284

Table D.16. Results of dimerization fit of Compound **11c.**

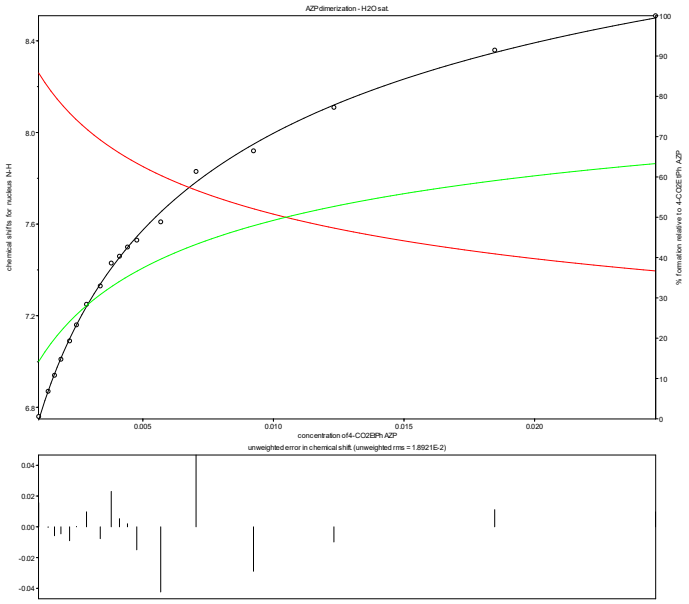

Figure D.22. Representative dimerization fit of Compound **11c.**

Solvent: water saturated $CDCl_3$ Results page - HypNMR version: 16.04.2006. Hqdll version: 09/05/2006. 4 iterations Refinement converged successfully				
sigma = 0.02038889466		RMS weighted residual = 0.01861242921		Chi-squared = 7.78 Chi-squared should be less than 12.60 at the 95% confidence level
Beta 2 refined	value	rSD	Log beta	SD
	9.791E+001	0.0859	1.9532	0.0373

Table D.17. Results of dimerization fit of Compound **11c.**

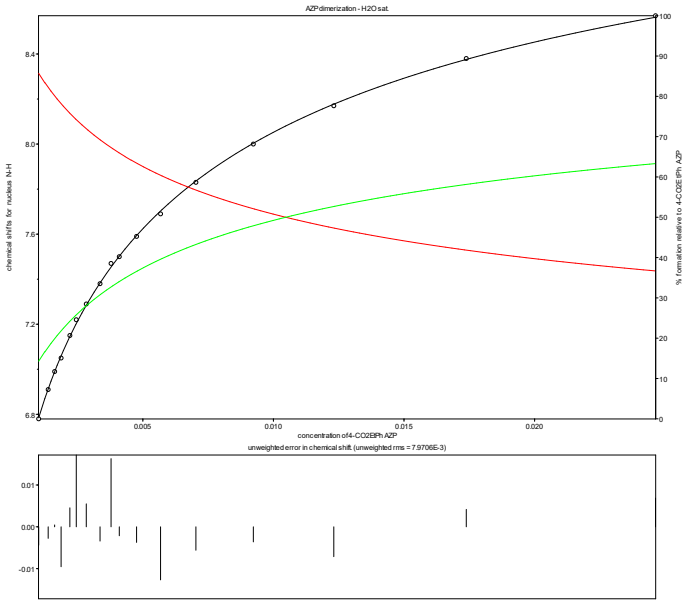

Figure D.23. Representative dimerization fit of Compound **11c.**

Solvent: water saturated $CDCl_3$ Results page - HypNMR version: 16.04.2006. Hqdll version: 09/05/2006. 2 iterations Refinement converged successfully				
sigma = 0.00877825075		RMS weighted residual = 0.00796613276		Chi-squared = 9.82 Chi-squared should be less than 12.60 at the 95% confidence level
Beta 2 refined	value	rSD	Log beta	SD
	9.5033E+001	0.0385	1.9779	0.0167

Table D.18. Results of dimerization fit of Compound **11c.**

pK_a Determinations

A series of solutions were prepared ranging from pH=5 up to pH=8 in phosphate, citrate, or carbonate buffer, as necessary. These buffers were used to compose solutions of azaphosphinine compounds at constant molarity (~200 μM). The emission of each solution when excited at the redshifted excitation wavelength to selectively excite the anionic form was then measured, and plotted as a function of pH. These data were then fit via GraphPad Prism to find the pK_a of the scaffold in question.

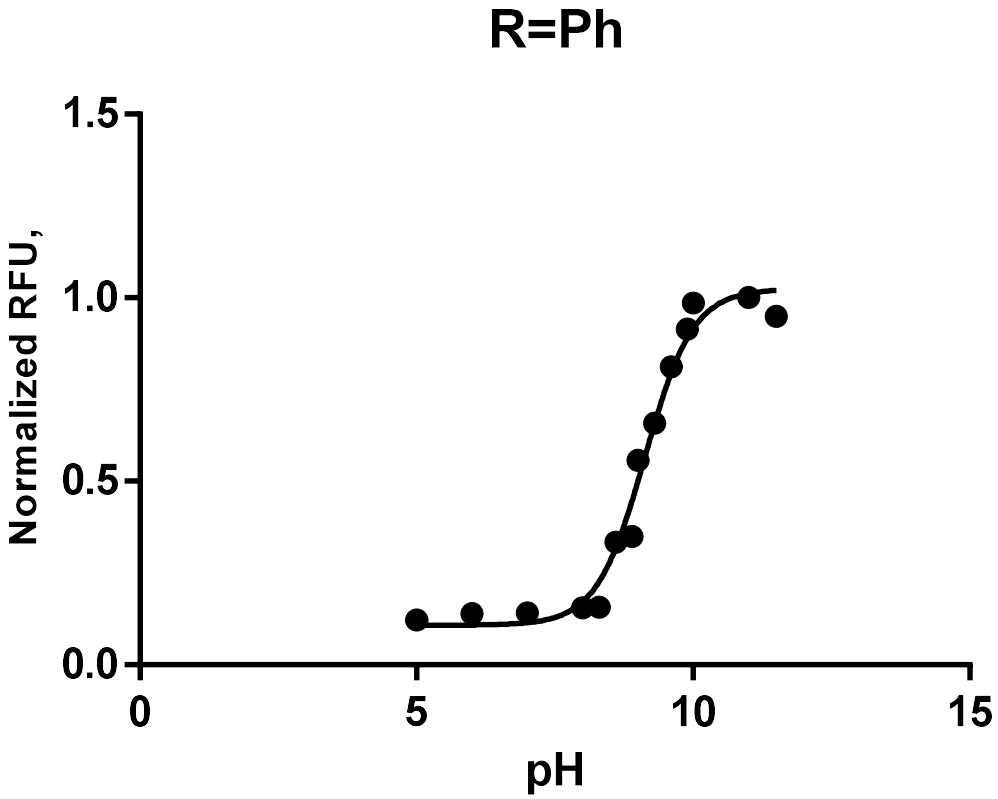

Best-fit values	
Bottom	0.1080
Top	1.024
LogEC50	9.129
EC50	1.345e+009
Span	0.9158
Std. Error	
Bottom	0.02654
Top	0.03227
LogEC50	0.07417
Span	0.03853
95% Confidence Intervals	
Bottom	0.04955 to 0.1664
Top	0.9528 to 1.095
LogEC50	8.966 to 9.292
EC50	9.239e+008 to 1.959e+009
Span	0.8310 to 1.001
Goodness of Fit	
Degrees of Freedom	11
R square	0.9813
Absolute Sum of Squares	0.03119
Sy.x	0.05325
Number of points	
Analyzed	14

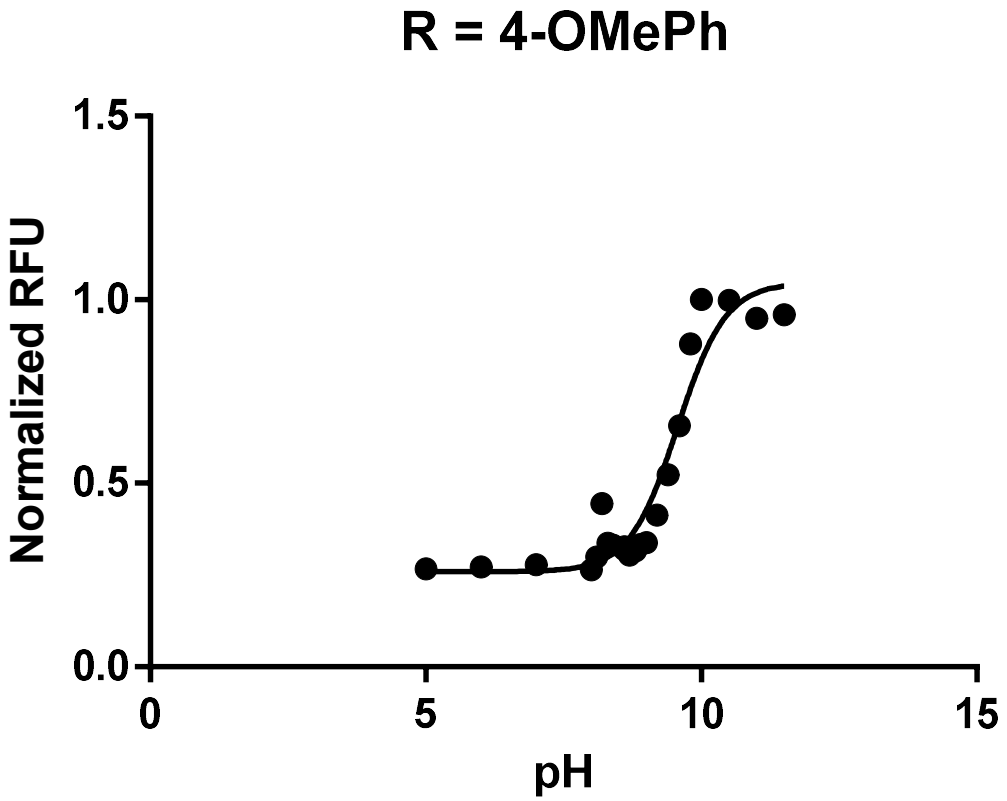

Best-fit values	
Bottom	0.2610
Top	1.091
LogEC50	9.617
EC50	4.139e+009
Span	0.8300
Std. Error	
Bottom	0.02620
Top	0.06452
LogEC50	0.1197
Span	0.06357
95% Confidence Intervals	
Bottom	0.2059 to 0.3160
Top	0.9554 to 1.227
LogEC50	9.365 to 9.868
EC50	2.319e+009 to 7.386e+009
Span	0.6965 to 0.9636
Goodness of Fit	
Degrees of Freedom	18
R square	0.9264
Absolute Sum of Squares	0.09985
Sy.x	0.07448
Number of points	
Analyzed	21

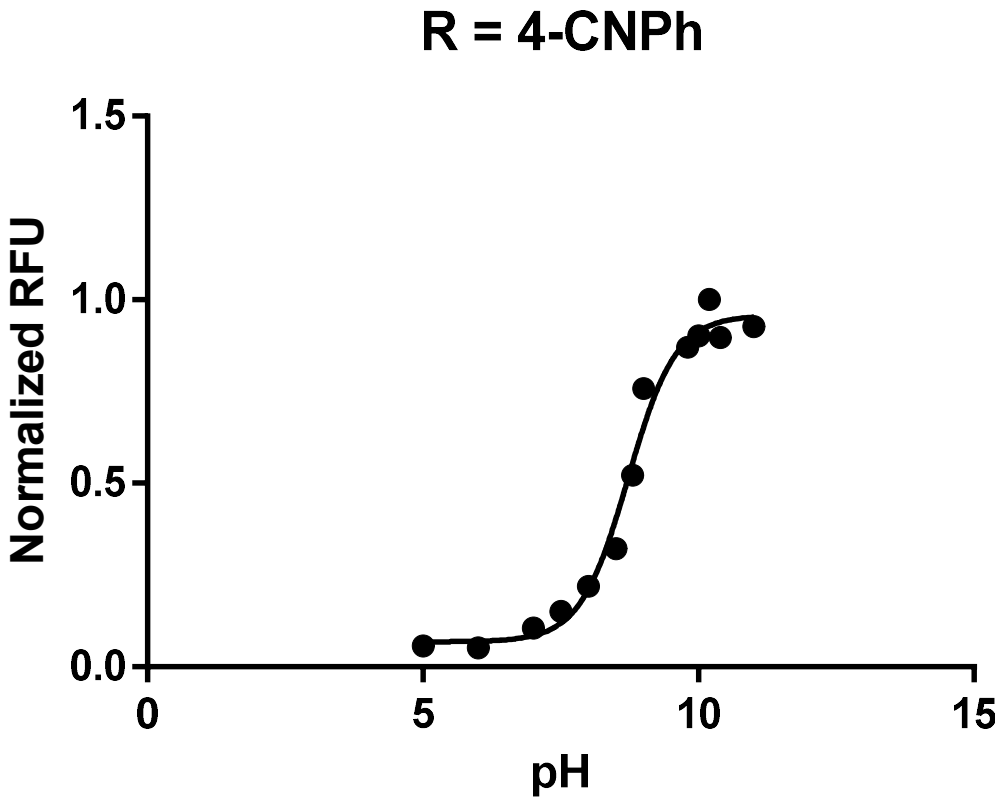

Best-fit values	
Bottom	0.06822
Top	0.9577
LogEC50	8.721
EC50	5.255e+008
Span	0.8894
Std. Error	
Bottom	0.02745
Top	0.02717
LogEC50	0.08049
Span	0.03650
95% Confidence Intervals	
Bottom	0.007067 to 0.1294
Top	0.8971 to 1.018
LogEC50	8.541 to 8.900
EC50	3.478e+008 to 7.942e+008
Span	0.8081 to 0.9708
Goodness of Fit	
Degrees of Freedom	10
R square	0.9834
Absolute Sum of Squares	0.02874
Sy.x	0.05361
Number of points	
Analyzed	13

REFERENCES CITED

CHAPTER I

1. J. Szejtli, *Chem. Rev.* **1998***, 98,* 1743-1754.

2. J. F. Stoddart, *Annu. Rep. Sect. B* **1983***, 80,* 353-378.

3. S. Leininger, B. Olenyuk, P. J. stang, *Chem. Rev.* **2000**, *100*, 853-908.

4. C. N. Carroll, J. J. Naleway, M. M. Haley, D. W. Johnson, *Chem. Soc. Rev.* **2010***, 39,* 3875-3888.

5. D. Habrant, V. Rauhala, A. M. P. Koskinen, *Chem. Soc. Rev.* **2010***, 39,* 2007-2017.

6. S. D. Zanatta, *Aust. J. Chem.* **2007***, 60,* 963-964.

7. R. Chinchilla, C. Nájera, *Chem. Soc. Rev.* **2011***, 40,* 5084-5121.

8. R. Chinchilla, C. Nájera, *Chem. Rev.* **2007,** *107*, 874-922.

9. J. A. Marsden, M. M. Haley in *Metal-Catalyzed Cross-Coupling Reactions*, 2nd ed. (Eds.: A. de Meijere, F. Diederich), Wiley-VCH, Weinheim, **2004,** pp. 317-394.

10. S. W. Thomas, G. D. Joly, T. M. Swager, *Chem. Rev.* **2007,** *107*, 1339- 1388.

11. N. M. Sangeetha, U. Maitra, *Chem. Soc. Rev.* **2005***, 34,* 821-836.

12. S. E. Kudaibergenov, N. Nuraje, V. V. Khutoryanskiy, *Soft Matter* **2012***, 8,* 9302-9321.

13. J. Hu, G. Zhang, S. Liu, *Chem. Soc. Rev.* **2012***, 41,* 5933-5949.

14. C. Wolf, K. W. Bentley, *Chem. Soc. Rev.* **2013***, 42,* 5408-5424.

15. A. P. de Silva, H. Q. N. Gunaratne, T. Gunnlaugsson, A. J. M. Huxley, C. P. McCoy, J. T. Rademacher, T. E. Rice, *Chem. Rev.* **1997***, 97,* 1515-1566.

16. Y. Yang, Q. Zhao, W. Feng, F. Li, *Chem. Rev.* **2013***, 113,* 192-270.

17. T. Terai, T. Nagano, Pflüg. *Arch. Eur. J. Physiol.* **2013***, 465,* 347-359.

18. Z. R. Grabowski, K. Rotkiewicz, W. Rettig, *Chem. Rev.* **2003***, 703,* 3899-4032.

19. Y. Hong, J. W. Y. Lam, B. Z. Tang, *Chem. Commun.* **2009,** 4332-4353.

20. J. Wu, W. Liu, J. Ge, H. Zhang, P. Wang, *Chem. Soc. Rev.* **2011***, 40,* 3483- 3495.

21. D. Ding, K. Li, B. Liu, B. Z. Tang, *Acc. Chem. Res.* **2013***, 46,* 2441 -2453.

22. S. Menning, M. Krämer, A. Duckworth, F. Rominger, A. Beeby, A. Dreuw, U. H. F. Bunz, *J. Org. Chem.* **2014***, 79,* 6571 -6578.

23. E. V. Anslyn, *J. Org. Chem.* **2007***, 72,* 687-699.

24. K. Rurack, U. Resch-Genger, *Chem. Soc. Rev.* **2002***, 31,* 116-127.

25. J. M. Engle, C. N. Carroll, D. W. Johnson, M. M. Haley, *Chem. Sci.* **2012***, 3,* 1105-1110.

26. C. N. Carroll, O. B. Berryman, C. A. Johnson, L. N. Zakharov, M. M. Haley, D. W. Johnson, *Chem. Commun.* **2009,** 2520-2522.

27. J. M. Engle, P. S. Lakshminarayanan, C. N. Carroll, L. N. Zakharov, M. M. Haley, D. W. Johnson, *Cryst Growth Des.* **2011***, 11,* 5144-5152.

28. C. A. Johnson, O. B. Berryman, A. C. Sather, L. N. Zakharov, M. M. Haley, D. W. Johnson, *Cryst Growth Des.* **2009***, 9,* 4247-4249.

29. J. V. Gavette, N. S. Mills, L. N. Zakharov, C. A. Johnson, D. W. Johnson, M. M. Haley, *Angew. Chem. Int. Ed.* **2013***, 52,* 10270- 10274; *Angew. Chem.* **2013***, 125,* 10460-10464.

30. Z. Liu, W. He, Z. Guo, *Chem. Soc. Rev.* **2013***, 42,* 1568-1600.

31. K. P. Carter, A. M. Young, A. E. Palmer, *Chem. Rev.* **2014***, 114,* 45644601.

32. G. Aragay, J. Pons, A. Merkoçi, *Chem. Rev.* **2011***, 111,* 3433-3458.

33. N. Kaur, S. Kumar, *Tetrahedron* **2011***, 67,* 9233-9264.

34. K. Kaur, R. Saini, A. Kumar, V. Luxami, N. Kaur, P. Singh, S. Kumar, *Coord. Chem. Rev.* **2012***, 256,* 1992-2028.

35. B. Valeur, l. Leray, *Coord. Chem. Rev.* **2000***, 205,* 3-40.

36. K. Deibler, P. Basu, *Eur. J. Inorg. Chem.* **2013,** 1086-1096.

37. M. Formica, V. Fusi, L. Giorgi, M. Micheloni, *Coord. Chem. Rev.* **2012***, 256,* 170-192.

38. A. de Los Rios, P. Mal, A. J. Meixner, D. Khoptyar, M. Schmittel, *Bull. Chem. Soc. Jpn.* **2011***, 84,* 620-622.

39. Y.-P. Zhao, L.-Z. wu, G. Si, Y. Liu, H. Xue, L.-P. Zhang, C.-H. Tung, *J. Org. Chem.* **2007***, 72,* 3632-3639.

40. M. Shao, P. Dongare, L. N. Dawe, D. W. Thompson, Y. Zhao, *Org. Lett.* **2010***, 12,* 3050-3053.

41. A. P. de Silva, B. McCaughan, B. O. F. McKinney, M. Querol, *Dalton Trans.* **2003,** 1902-1913.

42. L. Li, N. She, Z. Fei, P. So, Y. Wang, L. Cao, A. Wu, Z. Yao, *J. Fluoresc.* **2011***, 21,* 1103-1110.

43. A. J. Zucchero, P. L. McGrier, U. H. F. Bunz, *Acc. Chem. Res.* **2010***, 43,* 397-408.

44. J. N. Wilson, U. H. F. Bunz, *J. Am. Chem. Soc.* **2005***, 127,* 4124-4125.

45. P. L. McGrier, K. M. Solntsev, A. J. Zucchero, O. R. Miranda, V. M. Rotello, L. M. Tolbert, U. H. F. Bunz, *Chem. Eur. J.* **2011***, 17,* 3112-3119.

46. A. J. Zucchero, J. N. Wilson, U. H. F. Bunz, *J. Am. Chem. Soc.* **2006***, 128,* 11872-11881.

47. A. Mangalum, R. J. G. Jr, J. M. Hanley, A. M. Parker, R. C. Smith, *Org. Biomol. Chem.* **2010***, 8,* 5620-5627.

48. E. L. Spitler, L. D. Shirtcliff, M. M. Haley, *J. Org. Chem.* **2007***, 72,* 86-96.

49. E. L. Spitler, C. A. Johnson, M. M. Haley, *Chem. Rev.* **2006***, 106,* 53445386.

50. J. A. Marsden, J. J. Miller, L. D. Shirtcliff, M. M. Haley, *J. Am. Chem. Soc.* **2005***, 127,* 2464-2476.

51. P. N. W. Baxter, J.-P. Gisselbrecht, L. Karmazin-Brelot, A. Varnek, L. Allouche, *Chem. Eur. J.* **2013***, 19,* 12336- 12349.

52. A. Al Ouahabi, P. Baxter, C. Mathis, M. Bernard, B. Vileno, J.-P. Gisselbrecht, P. Turek, J.-M. Mouesca, S. Choua, *ChemPhysChem* **2013***, 14,* 958-969.

53. G. W. Gokel, W. M. Leevy, M. E. Weber, *Chem. Rev.* **2004***, 104,* 27232750.

54. J. L. Sessler, P. A. Gale, W.-S. Cho, *Anion Receptor Chemistry*, Royal Society of Chemistry, Cambridge, 2006.

55. V. Amendola, M. Bonizzoni, D. Esteban-Gómez, L. Fabbrizzi, M. Licchelli, F. Sancenón, A. Taglietti, *Coord. Chem. Rev.* **2006***, 250,* 1451 -1470.

56. O. B. Berryman, V. S. Bryantsev, D. P. Stay, D. W. Johnson, B. P. Hay, *J. Am. Chem. Soc.* **2007***, 129,* 48-58.

57. L. E. Santos-Figueroa, M. E. Moragues, E. Climent, A. Agostini, R. Martínez-Máñez, F. Sancenón, *Chem. Soc. Rev.* **2013***, 42,* 3489-3613.

58. P. A. Gale, N. Busschaert, C. J. E. Haynes, L. E. Karagiannidis, l. L. Kirby, *Chem. Soc. Rev.* **2014***, 43,* 205-241.

59. N. H. Evans, P. D. Beer, *Angew. Chem. Int. Ed.* **2014***, 53,* 11716- 111754; *Angew. Chem.* **2014***, 126,* 11908- 11948.

60. W. N. George, M. Giles, l. McCulloch, J. H. G. Steinke, J. C. deMello, *ChemPhysChem* **2011***, 12,* 765-768.

61. M. Cametti, K. Rissanen, *Chem. Soc. Rev.* **2013***, 42,* 2016-2038.

62. H. Sun, X. Dong, S. Liu, Q. Zhao, X. Mou, H. Y. Yang, W. Huang, *J. Phys. Chem. C* **2011***, 115,* 19947- 19955.

63. R. C. Ling, H. T. M. Le, O. S. Miljanié, *Chem. Commun.* **2013***, 49,* 4304-

64. J. Lim, D. Nam, O. S. Miljanié, *Chem. Sci.* **2012***, 3,* 559-563.

65. J. Lim, O. S. Miljanié, *Chem. Commun.* **2012***, 48,* 10301 -10303.

66. A. N. Swinburne, M. J. Paterson, A. Beeby, J. W. Steed, *Chem. Eur. J.* **2010***, 16,* 2714-2718.

67. l. M. Jones, A. D. Hamilton, *Angew. Chem. Int. Ed.* **2011***, 50,* 4597-4600; *Angew. Chem.* **2011***, 123,* 4693-4696.

68. A. B. Wolk, E. Garand, l. M. Jones, A. D. Hamilton, M. A. Johnson, *J. Phys. Chem. A* **2013***, 117,* 5962-5969.

69. D. M. Jessen, A. N. Wercholuk, B. Xiong, A. L. Sargent, W. E. Allen, *J. Org. Chem.* **2012***, 77,* 6615-6619.

70. N.-K. Kim, K.-J. Chang, D. Moon, M. S. Lah, K.-S. Jeong, *Chem. Commun.* **2007,** 3401 -3403.

71. S. Freye, J. Hey, A. Torras-Galán, D. Stalke, R. Herbst-lrmer, M. John, G. H. Clever, *Angew. Chem. Int. Ed.* **2012***, 51,* 2191 -2194; *Angew. Chem.* **2012***, 124,* 2233-2237.

72. S. Freye, R. Michel, D. Stalke, M. Pawliczek, H. Frauendorf, G. H. Clever, *J. Am. Chem. Soc.* **2013***, 135,* 8476-8479.

73. M. Han, R. Michel, B. He, Y.-S. Chen, D. Stalke, M. John, G. H. Clever, *Angew. Chem. Int. Ed.* **2013***, 52,* 1319-1323; *Angew. Chem.* **2013***, 125,* 1358-1362.

74. V. Valderrey, E. C. Escudero-Adán, P. Ballester, *Angew. Chem. Int. Ed.* **2013***, 52,* 6898-6902; *Angew. Chem.* **2013***, 725,* 7036-7040.

75. V. Valderrey, E. C. Escudero-Adán, P. Ballester, *J. Am. Chem. Soc.* **2012***, 134,* 10733-10736.

76. H. J. Kim, J.-M. Suk, K.-S. Jeong, *Supramol. Chem.* **2013***, 25,* 46-53.

77. O. B. Berryman, C. A. Johnson, L. N. Zakharov, M. M. Haley, D. W. Johnson, *Angew. Chem. Int. Ed.* **2008***, 47,* 1 17- 120; *Angew. Chem.* **2008***, 120,* 123-126.

78. M. M. Watt, L. N. Zakharov, M. M. Haley, D. W. Johnson, *Angew. Chem. Int. Ed.* **2013***, 52,* 10275-10280; *Angew. Chem.* **2013***, 125,* 1046510470.

79. B. W. Tresca, L. N. Zakharov, C. N. Carroll, D. W. Johnson, M. M. Haley, *Chem. Commun.* **2013***, 49,* 7240-7242.

80. J. V. Gavette, C. J. Evoniuk, L. N. Zakharov, M. E. Carnes, M. M. Haley, D. W. Johnson, *Chem. Sci.* **2014***, 5,* 2899-2905.

81. H. Maeda, K. Kitaguchi, Y. Haketa, *Chem. Commun.* **2011***, 47,* 9342- 9344.

82. G. Wei, S. Zhang, C. Dai, Y. Quan, Y. Cheng, C. Zhu, *Chem. Eur. J.* **2013***, 19,* 16066-16071.

83. W. Makiguchi, S. Kobayashi, Y. Furusho, E. Yashima, *Angew. Chem. Int. Ed.* **2013***, 52,* 5275-5279; *Angew. Chem.* **2013***, 125,* 5383-5387.

84. Y. Nakatani, Y. Furusho, E. Yashima, *Org. Biomol. Chem.* **2013***, 11,* 16141623.

85. Y. Wu, H. Guo, X. Zhang, T. D. James, J. Zhao, *Chem. Eur. J.* **2011***, 17,* 7632-7644.

86. D. P. Iwaniuk, C. Wolf, *J. Am. Chem. Soc.* **2011***, 133,* 2414-2417.

87. D. P. Iwaniuk, C. Wolf, *Chem. Commun.* **2012***, 48,* 11226- 11228.

88. D. P. Iwaniuk, C. Wolf, *Org. Lett.* **2011***, 13,* 2602-2605.

89. D. A. Kim, P. Kang, M.-G. Choi, K-. S. Jeong, *Chem. Commun.* **2013***, 49,* 9743-9745.

90. M. J. Kim, Y. R. Choi, H.-G. Jeon, P. Kang, M.-G. Choi, K.-S. Jeong, *Chem. Commun.* **2013***, 49,* 11412- 11414.

91. H.-G. Jeon, M. J. Kim, K.-S. Jeong, *Org. Biomol. Chem.* **2014***, 12,* 54645468.

92. Y. R. Choi, M. K. Chae, D. Kim, M. S. Lah, K.-S. Jeong, *Chem. Commun.* **2012***, 48,* 10346-10348.

93. T. Muraoka, T. Shima, T. Hamada, M. Morita, M. Takagi, K. V. Tabata, H. Noji, K. Kinbara, *J. Am. Chem. Soc.* **2012***, 134,* 19788-19794.

94. J. M. Heemstra, J. S. Moore, *J. Org. Chem.* **2004***, 69,* 9234-9237.

95. H. Abe, H. Machiguchi, S. Matsumoto, M. Inouye, *J. Org. Chem.* **2008***, 73,* 4650-4661.

96. F. Kayamori, H. Abe, M. Inouye, *Eur. J. Org. Chem.* **2013,** 1677-1682.

97. H. Abe, K. Okada, H. Makida, M. Inouye, *Org. Biomol. Chem.* **2012***, 10,* 6930-6936.

98. J. Dash, Z. A. E. Waller, G. D. Pantos, S. Balasubramanian, *Chem. Eur. J.* **2011***, 17,* 4571-4581.

99. S. Shanmugaraju, S. A. Joshi, P. S. Mukherjee, *Inorg. Chem.* **2011***, 50,* 11736-11745.

100. M. Wang, V. Vajpayee, S. Shanmugaraju, Y.-R. Zheng, Z. Zhao, H. Kim, P. S. Mukherjee, K.-W. Chi, P. J. Stang, *Inorg. Chem.* **2011***, 50,* 15061512.

101. S. Li, T. Leng, H. Zhong, C. Wang, Y. Shen, *J. Heterocycl. Chem.* **2012***, 49,* 64-70.

102. A. Wild, A. Winter, M. D. Hager, U. S. Schubert, *Chem. Commun.* **2012***, 48,* 964-966.

103. D. M. D'Alessandro, B. Smit, J. R. Long, *Angew. Chem. Int. Ed.* **2010***, 49,* 6058-6082; *Angew. Chem.* **2010***, 122,* 6194-6219.

104. Y. Jin, B. A. Voss, A. Jin, H. Long, R. D. Noble, W. Zhang, *J. Am. Chem. Soc.* **2011***, 133,* 6650-6658.

105. Y. Jin, B. A. Voss, R. McCaffrey, C. T. Baggett, R. D. Noble, W. Zhang, *Chem. Sci.* **2012***, 3,* 874-877.

CHAPTER II

1. E. M. Driggers, S. P. Hale, J. Lee, N. K. Terrett, *Nat. Rev. Drug Discov.* **2008**, *7*, 608–624.

2. C. Heinis, *Nat. Chem. Biol.* **2014**, *10*, 696–698.

3. J. Levin, Ed. , *Macrocycles in Drug Discovery,* The Royal Society of Chemistry, **2015.**

4. E. A. Villar, D. Beglov, S. Chennamadhavuni, J. A. P. Jr, D. Kozakov, S. Vajda, A. Whi tty, *Nat. Chem. Biol.* **2014**, *10*, 723–731.

5. S. W. Sisco, B. M. Larson, J. S. Moore, *Macromolecules* **2014**, *47*, 3829–3836.

6. H. S. G. Beckmann, F. Nie, C. E. Hagerman, H. Johansson, Y. S. Tan, D. Wilcke, D. R. Spring, *Nat. Chem.* **2013**, *5*, 861–867.

7. J. Xie, N. Bogliotti, *Chem. Rev.* **2014**, *114*, 7678–7739.

8. V. Martí-Centelles, M. D. Pandey, M. I. Burguete, S. V. Luis, *Chem. Rev.* **2015**, *115*, 8736–8834.

9. S. Lee, C.-H. Chen, A. H. Flood, *Nat. Chem.* **2013**, *5*, 704–710.

10. O. B. Berryman, C. A. Johnson II, L. N. Zakharov, M. M. Haley, D. W. Johnson, *Angew. Chem. Int. Ed.* **2008**, *47*, 117–120.

11. J. M. Engle, P. S. Singh, C. L. Vonnegut, L. N. Zakharov, D. W. Johnson, M. M. Haley, *CrystEngComm* **2014**, *16*, 3703–3706.

12. C. N. Carroll, O. B. Berryman, C. A. Johnson, L. N. Zakharov, M. M. Haley, D. W. Johnson, *Chem. Commun.* **2009**, 2520–2522.

13. C. N. Carroll, J. J. Naleway, M. M. Haley, D. W. Johnson, *Chem. Soc. Rev.* **2010**, *39*, 3875–3888.

14. C. N. Carroll, B. A. Coombs, S. P. McClintock, C. A. Johnson II, O. B. Berryman, D. W. Johnson, Michael M. Haley, *Chem. Commun.* **2011**, *47*, 5539.

15. J. M. Engle, C. N. Carroll, D. W. Johnson, M. M. Haley, *Chem. Sci.* **2012**, *3*, 1105.

16. J. M. Engle, P. S. Lakshminarayanan, C. N. Carroll, L. N. Zakharov, M. M. Haley, D. W. Johnson, *Cryst. Growth Des.* **2011**, *11*, 5144–5152.

17. M. M. Haley, *Angew. Chem. Int. Ed.* **2013**, *52*, 10270–10274.

18. C. A. Johnson, O. B. Berryman, A. C. Sather, L. N. Zakharov, M. M. Haley, D. W. Johnson, *Cryst. Growth Des.* **2009**, *9*, 4247–4249.

19. O. B. Berryman, C. A. Johnson, C. L. Vonnegut, K. A. Fajardo, L. N. Zakharov, D. W. Johnson, M. M. Haley, *Cryst. Growth Des.* **2015**, *15*, 1502–1511.

20. J. V. Gavette, C. J. Evoniuk, L. N. Zakharov, M. E. Carnes, M. M. Haley, D. W. Johnson, *Chem. Sci.* **2014**, *5*, 2899–2905.

21. B. W. Tresca, L. N. Zakharov, C. N. Carroll, D. W. Johnson, M. M. Haley, *Chem. Commun.* **2013**, *49*, 7240–7242.

22. O. B. Berryman, V. S. Bryantsev, D. P. Stay, D. W. Johnson, B. P. Hay, *J. Am. Chem. Soc.* **2007**, *129*, 48–58.

23. Z. S. Derewenda, L. Lee, U. Derewenda, *J. Mol. Biol.* **1995**, *252*, 248–262.

24. S. Horowitz, R. C. Trievel, *J. Biol. Chem.* **2012**, *287*, 41576–41582.

25. D. E. Koshland, *Angew. Chem. Int. Ed. Engl.* **1995**, *33*, 2375–2378.

26. J. A. Burns, G. M. Whitesides, *J. Am. Chem. Soc.* **1990**, *112*, 6296–6303.

27. A. K. Chamberlain, J. U. Bowie, *J. Mol. Biol.* **2002**, *322*, 497–503.

28. M. C. Wahl, M. Sundaralingam, *Trends Biochem. Sci.* **1997**, *22*, 97–102.

29. P. Thordarson, *Chem. Soc. Rev.* **2011**, *40*, 1305–1323.

30. U. Rösch, S. Yao, R. Wortmann, F. Würthner, *Angew. Chem.* **2006**, *118*, 7184–7188.

31. R. Thomas, S. Varghese, G. U. Kulkarni, *J. Mater. Chem.* **2009**, *19*, 4401–4406

CHAPTER III

1. Finkel, T. *Curr Opin Cell Biol* **2003**, *15*, 247–254.

2. Lu, T.; Pan, Y.; Kao, S.-Y.; Li, C.; Kohane, I.; Chan, J.; Yankner, B. A. *Nature* **2004**, *429*, 883–891.

3. Balaban, R. S.; Nemoto, S.; Finkel, T. *Cell* **2005**, *120*, 483–495.

4. Østergaard, H.; Henriksen, A.; Hansen, F. G.; Winther, J. R. *EMBO J.* **2001**, *20*, 5853–5862.

5. Cline, D. J.; Thorpe, C.; Schneider, J. P. *Anal. Biochem.* **2004**, *325*, 144–150.

6. Xu, K.; Chen, H.; Tian, J.; Ding, B.; Xie, Y.; Qiang, M.; Tang, B. *Chem. Commun.* **2011**, *47*, 9468.

7. Haugland, R. P. *The Handbook: A Guide to Fluorescent Probes and Labeling Technologies*, 10th ed.; Molecular Probes/Invitrogen, 2005.

8. Woolley, J. F.; Stanicka, J.; Cotter, T. G. *Trends Biochem. Sci.* **2013**, *38*, 556–565.

9. Pedersen, C. J. *J. Am. Chem. Soc.* **1967**, *89*, 7017–7036.

10. Park, C. H.; Simmons, H. E. *J. Am. Chem. Soc.* **1968**, *90* (9), 2431–2432.

11. Vonnegut, C. L.; Tresca, B. W.; Johnson, D. W.; Haley, M. M. *Chem. – Asian J.* **2015**, *10*, 522–535.

12. Engle, J. M.; Carroll, C. N.; Johnson, D. W.; Haley, M. M. *Chem. Sci.* **2012**, *3*, 1105.

13. Engle, J. M.; Lakshminarayanan, P. S.; Carroll, C. N.; Zakharov, L. N.; Haley, M. M.; Johnson, D. W. *Cryst. Growth Des.* **2011**, *11*, 5144–5152.

14. Engle, J. M.; Singh, P. S.; Vonnegut, C. L.; Zakharov, L. N.; Johnson, D. W.; Haley, M. M. *CrystEngComm* **2014**, *16*, 3703–3706.

15. Carroll, C. N.; Berryman, O. B.; Johnson, C. A.; Zakharov, L. N.; Haley, M. M.; Johnson, D. W. *Chem. Commun.* **2009**, 2520–2522.

16. Carroll, C. N.; Naleway, J. J.; Haley, M. M.; Johnson, D. W. *Chem. Soc. Rev.* **2010**, *39*, 3875–3888.

17. Carroll, C. N.; Coombs, B. A.; McClintock, S. P.; Johnson II, C. A.; Berryman, O. B.; Johnson, D. W.; Michael M. Haley. *Chem. Commun.* **2011**, *47* (19), 5539.

18. Tresca, B. W.; Zakharov, L. N.; Carroll, C. N.; Johnson, D. W.; Haley, M. M. *Chem. Commun.* **2013**, *49* (65), 7240–7242.

19. Gavette, J. V.; Mills, N. S.; Zakharov, L. N.; Johnson, C. A.; Johnson, D. W.; Haley, M. M. *Angew. Chem. Int. Ed.* **2013**, *52* (39), 10270–10274.

20. Gavette, J. V.; Klug, C. M.; Zakharov, L. N.; Shores, M. P.; Haley, M. M.; Johnson, D. W. *Chem. Commun.* **2014**, *50* (54), 7173–7175.

21. Gavette, J. V.; Evoniuk, C. J.; Zakharov, L. N.; Carnes, M. E.; Haley, M. M.; Johnson, D. W. *Chem. Sci.* **2014**, *5* (7), 2899–2905.

22. Watt, M. M.; Zakharov, L. N.; Haley, M. M.; Johnson, D. W. *Angew. Chem. Int. Ed.* **2013**, n/a – n/a.

23. Lamoureux, G. V.; Whitesides, G. M. *J. Org. Chem.* **1993**, *58* (3), 633–641.

24. Koide, Y.; Kawaguchi, M.; Urano, Y.; Hanaoka, K.; Komatsu, T.; Abo, M.; Terai, T.; Nagano, T. *Chem. Commun.* **2012**, *48* (25), 3091.

25. Miller, E. W.; Bian, S. X.; Chang, C. J. *J. Am. Chem. Soc.* **2007**, *129* (12), 3458–3459.

26. Yu, F.; Li, P.; Li, G.; Zhao, G.; Chu, T.; Han, K. *J Am Chem Soc* **2011**, *133*, 11030–11033.

27. Cheruku, P.; Huang, J.-H.; Yen, H.-J.; Iyer, R. S.; Rector, K. D.; Martinez, J. S.; Wang, H.-L. *Chem. Sci.* **2015**, *6* (2), 1150–1158.

28. Han, R.; Yang, X.; Zhang, D.; Fan, M.; Ye, Y.; Zhao, Y. *New J. Chem.* **2012**, *36*, 1961–1965.

29. Manjare, S. T.; Kim, Y.; Churchill, D. G. *Acc. Chem. Res.* **2014**, *47* (10), 2985–2998.

30. Hanson, G. T.; Aggeler, R.; Oglesbee, D.; Cannon, M.; Capaldi, R. A.; Tsien, R. Y.; Remington, S. J. *J. Biol. Chem.* **2004**, *279* (13), 13044–13053.

31. Lohman, J. R.; Remington, S. J. *Biochemistry (Mosc.)* **2008**, *47* (33), 8678–8688.

32. Massey, V. *Biochim. Biophys. Acta* **1960**, *37* (2), 314–322.

33. K, B.; T. H., W. *Biochem. J.* **1953**, *54*, 86–94.

34. Antonello, S.; Daasbjerg, K.; Jensen, H.; Taddei, F.; Maran, F. *J. Am. Chem. Soc.* **2003**, *125* (48), 14905–14916.

35. Antonello, S.; Benassi, R.; Gavioli, G.; Taddei, F.; Maran, F. *J. Am. Chem. Soc.* **2002**, *124* (25), 7529–7538.

36. Fernandes, P. A.; Ramos, M. J. *Chem. – Eur. J.* **2004**, *10* (1), 257–266.

37. Lees, W. J.; Whitesides, G. M. *J. Org. Chem.* **1993**, *58* (3), 642–647.

CHAPTER IV

1. G. K. S. Prakash, A. K. Yudin, *Chem. Rev.* **1997**, *97*, 757–786.

2. M. Liu, S. J. Visco, L. C. De Jonghe, *J. Electrochem. Soc.* **1989**, *136*, 2570–2575.

3. P. Zhou, F. Tian, F. Lv, Z. Shang, *Proteins Struct. Funct. Bioinforma.* **2009**, *76*, 151–163.

4. M. M. Khalifa, M. J. Bodner, J. A. Berglund, M. M. Haley, *Tetrahedron Lett.* **2015**, *56*, 4109–4111.

5. E. Potteau, L. Nicolle, E. Levillain, Jean-Pierre Lelieur, *Electrochem. Commun.* **1999**, *1*, 360–364.

6. M. Hoffmann, J. O. Edwards, *Inorg. Chem.* **1977**, *16*, 3333–3338.

7. P. W. Preisler, L. Berger, *J. Am. Chem. Soc.* **1947**, *69*, 322–325.

8. P. W. Preisler, *J. Am. Chem. Soc.* **1949**, *71*, 2849–2852.

9. V. M. Shul'man, S. V. Larionov, T. V. Kramareva, T. D. Efremova, *Bull. Acad. Sci. USSR Div. Chem. Sci.* **1965**, *14*, 1216–1217.

CHAPTER V

1. G. Märkl, D. Matthes, *Angew. Chem. Int. Ed. Engl.* **1972,** *11*, 1019–1020;

2a. G. Märkl, G. Dorfmeister, *Tetrahedron Lett.* **1987,** *28*, 1093–1096;

2b. C. Bourdieu, A. Foucaud, *Tetrahedron Lett.* **1987,** *28*, 4673–4674.

3. "Product Class 13: 1-λ^3-Phosphinines": F. Mathey, P. le Floch in *Science of Synthesis*, Vol. 15 (Ed.: D. StC. Black) Georg Thieme, Stuttgart, **2005**, pp. 1097–1155.

4. C. Bedel, A. Foucaud, *Tetrahedron Lett.* **1991,** *32*, 2619–2620.

5a. M. J. S. Dewar, V. P. Kubba, *J. Am. Chem. Soc.* **1960,** *82*, 5685–5688;

5b. I. G. M. Campbell, J. K. Way, *J. Chem. Soc.* **1960,** 5034–5041;

5c. I. G. M. Campbell, J. K. Way, *J. Chem. Soc.* **1961,** 2133–2141.

6a. T. Kobayashi, M. Nitta, *Chem. Lett.* **1985,** *14*, 1459–1462;

6b. N. G. Khusainova, Z. A. Bredikhina, A. D. Sinitsa, V. I. Kal'chenko, A. N. Pudovik, *J. Gen. Chem. USSR Engl. Transl.* **1982,** *52*, 789–795;

6c. Z. A. Bredikhina, N. G. Khusainova, Y. Y. Efremov, R. L. Korshunov, A. N. Pudovik, *J. Gen. Chem. USSR. Engl. Transl.* **1985,** *55*, 1710–1718;

6d. G. Veneziani, R. Reau, F. Dahan, G. Bertrand, *J. Org. Chem.* **1994,** *59*, 5927–5929;

6e. A. Foucaud, C. Bedel, Tetrahedron **1995***, 51,* 9625–9632*;*

6f. A. D. Averin, N. V. Lukashev, A. A. Borisenko, M. A. Kazankova, I. P. Beletskaya, Russ. *J. Org. Chem.* **1996,** *32*, 415–426;

6g. M. Nitta, H. Yamamoto, T. Kobayashi, *Heterocycles* **1998**, *48*, 1903;

6h. Y. V. Svyaschenko, D. M. Volochnyuk, A. N. Kostyuk, *Tetrahedron Lett.* **2010,** *51*, 6316–6318;

6i. D. Aguilar, R. Bielsa, T. Soler, E. P. Urriolabeitia, *Organometallics* **2011**, *30*, 642–648;

6j. N. Avarvari, P. Le Floch, F. Mathey, *J. Am. Chem. Soc.* **1996,** 118, 11978–11979.

7a. B. Dishon, *J. Am. Chem. Soc.* **1949,** *71*, 2251–2251;

7b. M. J. S. Dewar, E. C. Lucken, M. A. Whitehead, *J. Chem. Soc.* **1960,** 2423–2429;

7c. L. Nyulászi, *Chem. Rev.* **2001,** 101, 1229–1246;

7d. A. B. Chaplin, J. A. Harrison, P. J. Dyson, *Inorg. Chem.* **2005,** *44*, 8407–8417;

7e. J. J. Torres-Vega, A. Vásquez-Espinal, J. Caballero, M. L. Valenzuela, L. Alvarez-Thon, E. Osorio, W. Tiznado, *Inorg. Chem.* **2014,** *53*, 3579–3585.

8a. J. H. Gladstone, J. D. Holmes, *J. Chem. Soc.* **1864,** *17*, 225–237;

8b. J. Liebig, F. Woehler, *Justus Liebigs Ann. Chem.* **1834,** *11*, 139–150.

9a. W. Tang, Y. X. Ding, *J. Org. Chem.* **2006,** *71*, 8489–8492;

9b. W. Tang, Y. Ding, Y. X. Ding, *Tetrahedron* **2008**, *64*, 10507–10511;

9c. J. Yan, Q. Li, J. A. Boutin, M. P. Renard, Y. Ding, X. Hao, W. Zhao, M. Wang, *Acta Pharmacol. Sin.* **2008,** *29*, 752–758;

9d. S. Park, B. Seo, S. Shin, J.-Y. Son, P. H. Lee, *Chem. Commun.* **2013,** *49*, 8671–8673;

9e. D. Zhao, C. Nimphius, M. Lindale, F. Glorius, *Org. Lett***. 2013,** *15*, 4504–4507.

10a. J. W. Darrow, D. G. Drueckhammer, *Bioorg. Med. Chem***. 1996,** *4,* 1341–1348;

10b. D. J. Tantillo, K. N. Houk, *J. Org. Chem.* **1999,** *64*, 3066–3076;

10c. V. Ferro, L. Weiler, S. G. Withers, H. Ziltener, *Can. J. Chem***. 1998,** *76*, 313–318;

10d. H. Kakinuma, K. Shimazaki, N. Takahashi, K. Takahashi, S. Niihata, Y. Aoki, K. Hamada, H. Matsushita, Y. Nishi, *Tetrahedron* **1999**, *55*, 2559–2572;

10e. M. Mikolajczyk, P. Balczewski in *New Aspects in Phosphorus Chemistry II* (Ed.: D. J. P. Majoral), Springer, Berlin, **2003**, pp. 161–214;

10f. A. Y. Peng, Y. X. Ding, *J. Am. Chem. Soc.* **2003,** *125*, 15006–15007;

10g. B. Li, B. Zhou, H. Lu, L. Ma, A.-Y. Peng, *Eur. J. Med. Chem***. 2010,** *45*, 1955–1963;

10h. J. W. McGrath, J. P. Chin, J. P. Quinn, *Nat. Rev. Microbiol***. 2013,** *11*, 412–419;

10i. J. J. Shie, J.-M. Fang, *J. Chin. Chem. Soc***. 2014,** *61*, 127–141.

11a. C. Y. Hong, S. H. Kim, Y. K. Kim, *Bioorg. Med. Chem. Lett.* **1997,** *7*, 1875–1878;

11b. Y. Oshiro, S. Sato, N. Kurahashi, T. Tanaka, T. Kikuchi, K. Tottori, Y. Uwahodo, T. Nishi, *J. Med. Chem***. 1998,** *41*, 658–667;

11c. T. S. Harrison, C. M. Perry, *Drugs* **2004**, *64*, 1715–1736;

11d. S. Heeb, M. P. Fletcher, S. R. Chhabra, S. P. Diggle, P. Williams, M. Cámara, *FEMS Microbiol. Rev***. 2011,** *35*, 247–274;

11e. G. A. Lemieux, J. Liu, N. Mayer, R. J. Bainton, K. Ashrafi, Z. Werb, *Nat. Chem. Biol***. 2011,** *7*, 206–213.

12. S. Bhagat, A. K. Chakraborti, *J. Org. Chem.* **2007,** *72*, 1263–1270.

13. E. Saxon, C. R. Bertozzi, *Science* **2000**, *287*, 2007–2010.

14. W. C. Marsh, J. Trotter, *J. Chem. Soc.* A **1971**, 169–173.

15. M. Ikbal, R. Banerjee, S. Atta, A. Jana, D. Dhara, A. Anoop, N. D. P. Singh, *Chem. Eur. J***. 2012,** *18*, 11968–11975.

16. R. Hirschmann, K. M. Yager, C. M. Taylor, J. Witherington, P. A. Sprengeler, B. W. Phillips, W. Moore, A. B. Smith, *J. Am. Chem. Soc.* **1997,** *119*, 8177–8190.

17. S. E. Krikorian, *J. Phys. Chem***. 1982,** *86*, 1875–1881.

18. W. L. Jorgensen, J. Pranata, *J. Am. Chem. Soc.* **1990,** *112*, 2008–2010.

19. J. Sartorius, H.-J. Schneider, *Chem. Eur. J***. 1996,** *2*, 1446–1452.

20. W. M. F. Fabian, K. S. Niederreiter, G. Uray, W. Stadlbauer, *J. Mol. Struct***. 1999,** *477*, 209–220.

21. J. F. Araneda, W. E. Piers, B. Heyne, M. Parvez, R. McDonald, *Angew. Chem. Int. Ed***. 2011,** *50*, 12214–12217;

22. G. Uray, K. S. Niederreiter, F. Belaj, W. M. F. Fabian, *Helv. Chim. Acta* **1999**, *82,* 1408–1417.

23. C. Peng, Y. Wang, L. Liu, H. Wang, J. Zhao, Q. Zhu, *Eur. J. Org. Chem*. **2010**, 818 – 822.

24. A. Wetzel, F. Gagosz, *Angew. Chem. Int. Ed.* **2011**, *50*, 7354 – 7358.

25. R. Cano, M. Yus, D. J. Ramon, *Tetrahedron* **2012**, *68,* 1393 – 1400.

26. J. E. Perea-Buceta, T. Wirtanen, O.-V. Laukkanen, M. K. Maekelae, M. Nieger, M. Melchionna, N. Huittinen, J. A. Lopez-Sanchez, J. Helaja, *Angew. Chem. Int. Ed.* **2013**, *52*, 11835 – 11839.

27. E. Kumaran, W. K. Leong, *Tetrahedron Lett.* **2014**, *55*, 5495 – 5498.

CHAPTER VI

1. C. E. Griffin, T. D. Mitchell, *J. Org. Chem.* **1965**, *30*, 1935–1939.

2. N. Ashkenazi, Y. Karton, Y. Segall, *Tetrahedron Lett.* **2004**, *45*, 8003–8006.

3. T. Baumgartner, *Acc. Chem. Res.* **2014**, *47*, 1613–1622.